DIE STRESS AND FRICTION BEHAVIOUR ANALYSIS
IN BOLT FORMING

A THESIS SUBMITTED TO
THE GRADUATE SCHOOL OF NATURAL AND APPLIED SCIENCES
OF
MIDDLE EAST TECHNICAL UNIVERSITY

BY

MERT AYGEN

IN PARTIAL FULLFILLMENT OF THE REQUIREMENTS
FOR
THE DEGREE OF MASTER OF SCIENCE
IN
MECHANICAL ENGINEERING

DECEMBER 2006

Approval of the Graduate School of Natural and Applied Sciences

_____

Prof. Dr. Canan Özgen
Director

I certify that this thesis satisfies all the requirements as a thesis for the degree of Master of Science

_____

Prof. Dr. Kemal İder
Head of Department

This is to certify that we have read this thesis and that in our opinion it is fully adequate, in scope and quality, as a thesis for the degree of Master of Science

_____   _____

Prof. Dr.-Ing. A. Erman Tekkaya   Prof. Dr. S. Engin Kılıç

Co-Supervisor   Supervisor

Examining Committee Members

Prof. Dr. Mehmet Çalışkan   (METU, ME) _____

Prof. Dr. S. Engin Kılıç   (METU, ME) _____

Prof. Dr. –Ing. A. Erman Tekkaya (Atılım Unv., MFGE) _____

Assoc. Prof. Dr. Suat Kadıoğlu   (METU, ME) _____

Assoc. Prof. Dr. C. Hakan Gür   (METU, METE) _____

I hereby declare that all information in this document has been obtained and presented in accordance with academic rules and ethical conduct. I also declare that, as required by these rules and conduct, I have fully cited and referenced all material and results that are not original to this work.

Mert AYGEN

ABSTRACT

DIE STRESS AND FRICTION BEHAVIOUR ANALYSIS
IN BOLT FORMING

Aygen, Mert

M.S., Department of Mechanical Engineering

Supervisor: Prof. Dr. S. Engin Kılıç

Co-Supervisor: Prof. Dr.-Ing A. Erman Tekkaya

December 2006, 272 pages

In cold forming operations, tool geometry has a direct influence on the product quality, forming force, load acting on dies and tool life. Finite element method provides a means to analyse these parameters to predict forming defects and die failures.

In this study, shrink fitting the components of a bolt forming die is modelled and the finite element results are compared with the analytical solutions and experiments. In order to perform die stress analyses, deformable die models are implemented in the forging simulations. Furthermore, effect of using rigid and deformable dies on the stress distributions in the tools, forming force and product dimensions are examined. Some applications of tool geometry improvements and optimization of prestressing are presented in the case studies.

In the second part of the study, the appropriate friction model for the cold forming operation of bolts is investigated. For this purpose, ring compression and forward

rod extrusion tests are conducted. Dimensional variations and deformation forces are compared with the finite element simulations performed for different friction models and constants.

The results of shrink fit analyses of die prestressing are in good agreement with the elasticity formulations and real applications. In the studied bolt production cases, after improving the die stress distributions by using FE simulations, longer tool lives are achieved. Finally, for more accurate results, Coulomb friction model is determined as an appropiate model for bolt forming analyses.

Keywords: Bolt Production, Cold Forging, Shrink Fit, Friction, Finite Element Method

ÖZ

CIVATA ŞEKİLLENDİRMEDE KALIP GERİLME VE SÜRTÜNME DAVRANIŞ ANALİZLERİ

Aygen, Mert

Yüksek Lisans, Makina Mühendisliği Bölümü

Tez Yöneticisi: Prof. Dr. S. Engin Kılıç

Ortak Tez Yöneticisi: Prof. Dr.-Ing A. Erman Tekkaya

Aralık 2006, 272 Sayfa

Soğuk dövme işlemlerinde, kalıp geometrisinin, dövülen parçanın kalitesi, dövme kuvveti, kalıplara etki eden yükler ve kalıp ömrü üzerinde doğrudan etkisi bulunmaktadır. Sonlu elemanlar yöntemi, şekillendirme kusurları ve kalıp kırılmalarının önceden tespit edilmesi için, bu parametrelerin analiz edilebileceği bir çözüm yöntemidir.

Bu çalışmada cıvata şekillendirmede kullanılan sıkı geçmeli kalıplar modellenerek, analitik ve deneysel sonuçlar ile karşılaştırılmıştır. Kalıp gerilme analizlerinin yapılabilmesi için, deforme olabilen kalıp modelleri, dövme simulasyonlarına eklenmiştir. Ayrıca rijit ve deforme olabilen kalıp modellerinin kullanılmasının, kalıplardaki gerilme dağılımı, dövme yükü ve ürün ölçüleri üzerindeki etkileri incelenmiştir. Kalıp geometri iyileştirmeleri ve öngerilme optimizasyonu ile ilgili uygulamalar, örnek çalışmalar içerisinde sunulmuştur.

Çalışmanın ikinci bölümünde cıvataların soğuk şekillendirmesi için uygun olan sürtünme modeli araştırılmıştır. Bu amaçla halka şişirme ve ileri çubuk akıtma

testleri yapılmıştır. Boyutsal değişimler ve deformasyon kuvvetleri değişik sürtünme modelleri ve katsayıları ile yapılmış sonlu elemanlar analizleri ile karşılaştırılmıştır.

Kalıp öngerilmesi için gerçekleştirilen sıkı geçme analizleri, elastisite denklemleri ve gerçek uygulamalar ile çok yakın sonuçlar vermiştir. Üzerinde çalışılan cıvata üretim uygulamalarında, sonlu elemanlar simülasyonları yardımıyla kalıp gerilme dağılımlarında yapılan iyileştirmeler sonunda daha uzun kalıp ömürleri elde edilmiştir. Son olarak, daha doğru sonuçlar elde etmek için, cıvata şekillendirme analizlerinde, Coulomb sürtünme modelinin kullanılmasının daha uygun olduğu belirlenmiştir.

Anahtar Kelimeler: Cıvata Üretimi, Soğuk Dövme, Sıkı Geçme, Sürtünme, Sonlu Eleman Metodu

To the memory of my grandmother Saliha BALCIL...

ACKNOWLEDGMENTS

TABLE OF CONTENTS

xiii

LIST OF TABLES

LIST OF FIGURES

xvi

xix

CHAPTER 1

INTRODUCTION

Mechanical fastening is the act of joining parts with the aid of devices such as screws, rivets, bolts and pins. Fasteners are inserted into overlapping holes in separate parts to create compressive or frictional bond. They may be the smallest component of any manufactured product, but fasteners and fixings are perhaps the most important since nothing would be built without them.

Most early threaded fasteners were made by hand, by forging the head, cutting the slot with a saw and fashioning the thread with a file. As the geometry of the fasteners became more complicated, with the improvements in manufacturing methods, material characterization techniques and computer technology, high speed formers with high-tech tooling systems were developed. Moreover, some numerical techniques like finite element and finite volume methods started being used to visualize the processes on a virtual environment and perform analyses to improve process parameters.

This chapter gives the general concept about the production of mechanical fasteners and importance of design of bolt forming tools by the aid of computer simulations to describe the motivation underlying this study. In the coming sections; production of mechanical fasteners, an overview of cold forging, cold forging dies, motivation and aim and scope of the study is explained.

1.1 Production of Mechanical Fasteners

Threaded fasteners are widely used fastener types for their ease of use and disassembling. They may be used many times if fatigue strength is not a criterion to think about. Threaded fasteners contain a lot of different types, but in a simple manner they can be described as: A threaded shank passing through drilled (sometimes drilled & threaded) holes on members that is desired to be clamped [1].

There are different manufacturing methods to produce a fastener, for instance a bolt, like casting, (primary formation), deforming (upsetting or extrusion), turning (separation) or joining (welding) [2] (Fig. 1.1).
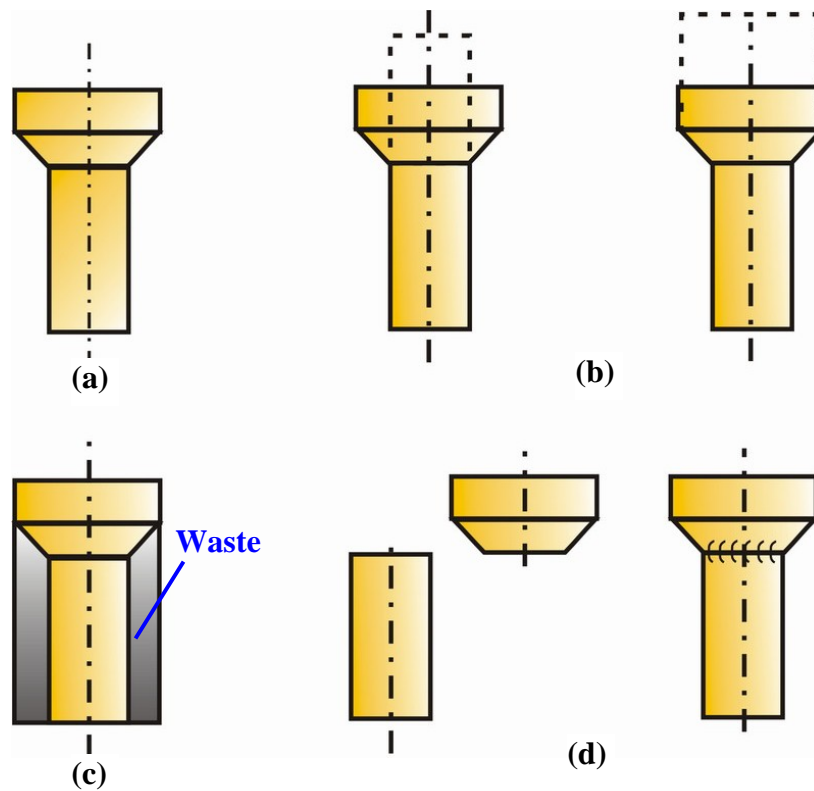
Figure 1.1. Methods of manufacturing bolt **a)** Primary formation **b)** Deformation **c)** Separation **d)** Joining [2]

Among these methods, fasteners are preferred to be produced by deforming the material to meet strength and economical requirements. One of the most important benefits of deforming is to the enhanced grain flow in forged parts which lead to longer fatigue life and higher ductility. In casting there is a risk of formation of porosities in the material (Fig. 1.2a). Similarly during metal cutting operations flow lines are intersecting the surface and cause micro gaps and cracks (Fig.1.2b). However metal forming provides homogenous and uniform grain flow over the entire part (Fig. 1.2c).

(a)   **(b)**   **(c)**
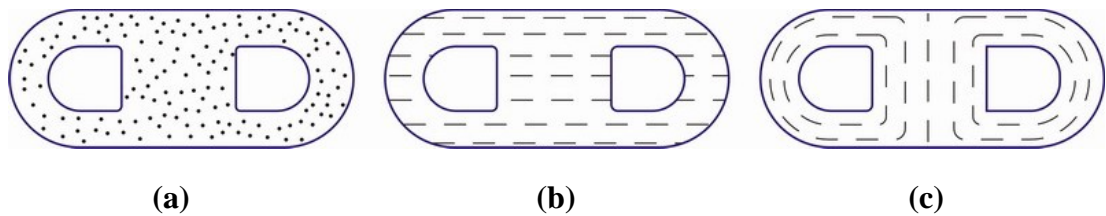
Figure 1.2. Grain flow **a)** Casting **b)** Machining **c)** Forging

Major outcome of cold bulk metal forming in the economical aspect is the elimination of scrap and secondary operations which leads to significant cost reduction. Also forming machines provide higher production rates than metal cutting tools and high production capacities can be achieved.

1.2 An Overview of Cold Forging

Metal forming processes can be defined as manufacturing by plastic deformation (permanent change) of a solid body by preserving both the mass and the cohesion [3] and can be classified into three categories according to the forming temperature as cold, warm and hot forging (Fig. 1.3).
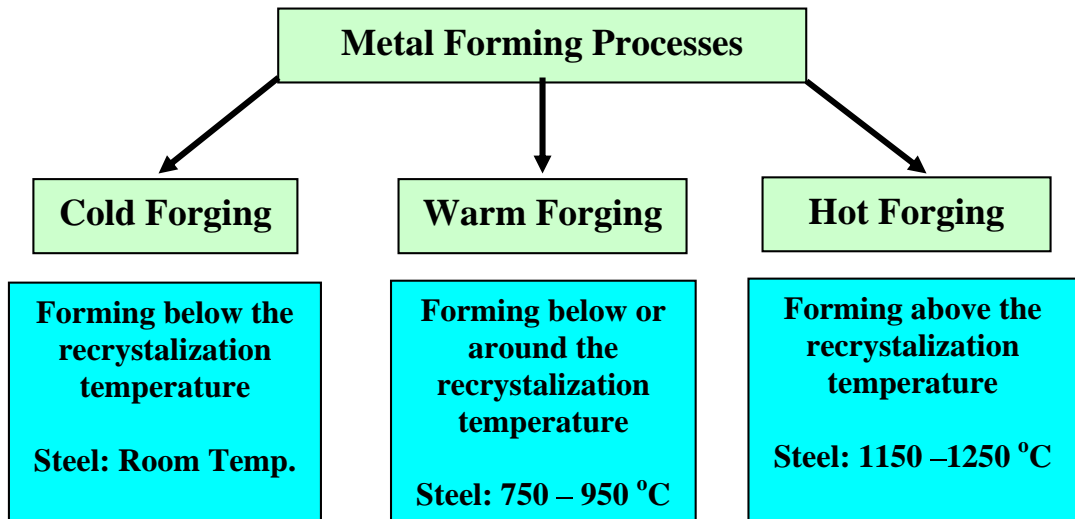
Figure 1.3. Classification of metal forming processes [4]

Cold forging of fasteners encompasses many processes; cold drawing, cold heading, open and closed die forward extrusions, backward can extrusion and more, to yield a diverse range of part shapes (Fig. 1.4.).

(a)

(b)

(c)
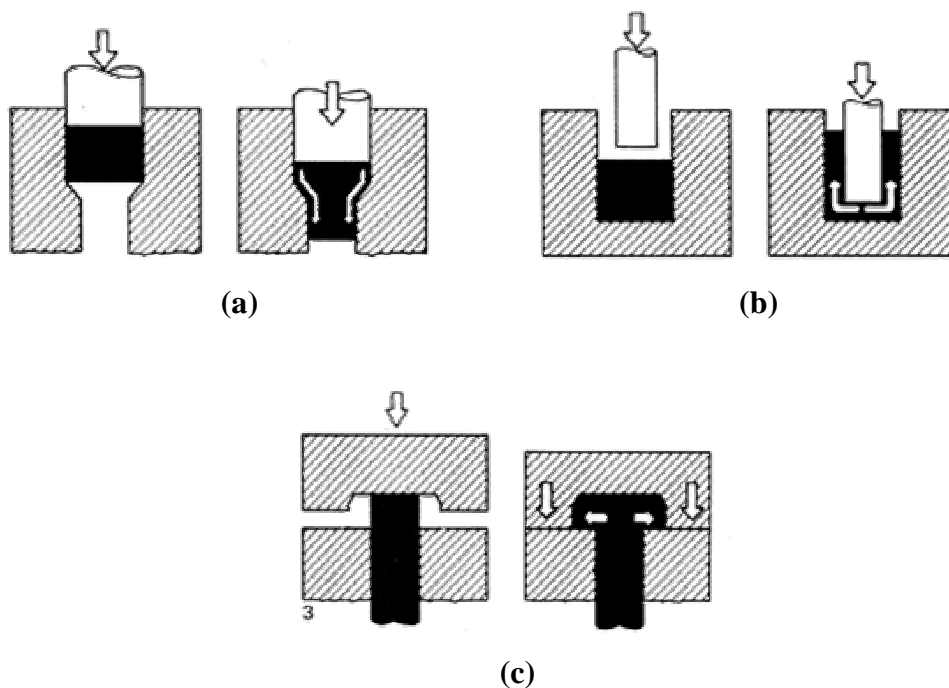
Figure 1.4. Examples of cold forging processes **a)** Forward rod extrusion **b)** Backward can extrusion **c)** Heading

Deformation methods can be classified into five groups based on differences in effective stresses [2];

- ➢ Compressive forming
- ➢ Combined tensile and compressive forming
- ➢ Tensile forming
- ➢ Forming by bending
- ➢ Forming by shearing

No simple descriptions of stress states are possible since different stress states may occur simultaneously or change during deforming operation. Therefore predominant stresses are chosen as the classification criteria. Bolt forming process can be classified as compressive forming since the material is mostly pushed into the dies to take the shape of the die geometry.

Typical parts produced by cold forging are most cost-effective in the range of 5 kg or less; symmetrical parts up to 3 kg, readily lend themselves to automated processing. Material options for cold forging range from lower-alloy and carbon steels to 300 and 400 series stainless, selected aluminum alloys, brass and bronze [5].

Cold forming is generally chosen for producing parts when following parameters are taken into consideration;

- Superior dimensional control
- Improved strength, fatigue and wear properties are as a result of strain hardening
- Better surface finish
- High production rates

1.3 Cold Forging Dies

Dies are tools which completely or in part contain the negative contour of the workpiece and transmit this to workpiece during deformation [6]. In the forming system, all interactions take place between workpiece and die. Due to this direct contact, stresses are exerted on dies, which are caused by forces, heat and material movement (resulting in frictional wear and surface erosion). According to the amount of stress and material strength limit, the die withstands the working conditions or fails.

In cold forming of fasteners, productivity of the part is depending on die design and production of it as well as forging sequence design. If the tooling dimensions, material selection or heat treatment of tools are not correctly performed, failure under the loading will be inevitable. Also the production parameters, like surface finish, directly affects formed part surface quality.

Another consideration of dies is the effect on the cost of the product. In bolt forming, die cost constitutes approximately 20% of total cost. Moreover, in case of die failure, the stoppage of production during replacement also affects the production efficiency and results time waste and cause indirect cost increase. So it is essential to keep tool life as long as possible to obtain maximum economical benefit.

1.4 Motivation

In fastener production which includes almost all processes of cold bulk metal forming processes such as wire drawing, open die and close die extrusion, heading and close die forging, die design has a crucial role affecting the soundness of the product. Some of the fastener manufacturers through out the world focus on the geometry of product and design the forging sequence to obtain required geometry without considering the forming forces and the stresses exerted on the dies. With such an approach, due to deficient analyses of forming process, die failures are the

6

most common problems encountered during the production. In Figure 1.5 a wheel bolt die is shown which fails frequently during the production and requires modification in the design.

Proper die design not only prevents die failure but also prohibits formation of any defects on the product like cracks and internal fracture which are strictly related with material flow.

(a)   **(b)**
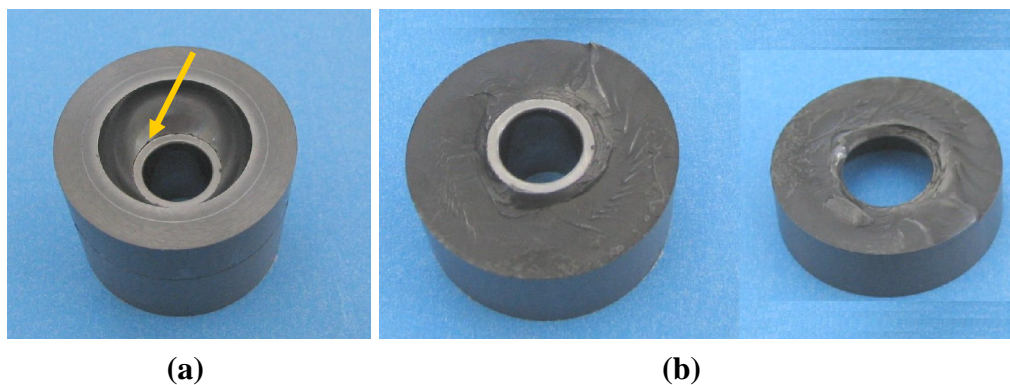
Figure 1.5. Sample die failure of a wheel bolt **a)** Crack initiation location **b)** Completely fractured die. *Courtesy: Norm Fasteners Co.*

When such a die failure occurs, in the companies which are incapable of executing a scientific approach, trial - error method is preferred to eliminate the problems. In this method, successive modifications on dies are performed till the proper product within dimensional tolerances is obtained without breaking dies. However, this is a time consuming method causing material waste which increases the cost significantly. Besides, due to idle time while disassembling, proceeding the modification and reassembling the dies, the production may not be managed to complete till delivery date.

In some cases where proper solution can not be achieved after a number of attempts, production is usually annulled and new product geometry is offered to customer with some modifications on the part where forming problems occur. This situation mostly ends with a requirement of a machining process to produce demanded part by customer or the loss of order.

In industry, products can be classified in two types. First types can be named as standard parts which have simpler geometry defined by international norms and easier to produce compared to the second type, named as special parts, which are special for the customer and have more complicated shapes. As the demand for standard parts is decreasing, demand for special parts increases. So that performing correct die design and producing defect free products with the lowest possible cost become an obligation.

Another need for proper die designs is development of more and more complicated parts with closer tolerances. Achieving production of parts with these tolerances is too difficult by using only the experience based approach without considering thermal effects, die material selection, elastic behaviour of die and friction condition.

In some cases although correct die design have been made, minor changes in forming process may lead parts with failure. In bolt production, forming always begins with the wire drawing process for straightening the raw material to eliminate the ovalities. The diameter of the raw material is selected according to the design of the forming sequence. However, in the absence of raw material in stock with required diameter, usually materials with bigger diameters are used by performing two or more drawing processes to reduce the diameter to the design value. Due to low reduction rates in these drawing processes, possibilities of formation of internal defects like Chevron cracks are present (Fig. 1.6).

Figure 1.6. Central burst in extrusion (Chevron crack) [7]

Due to the reasons mentioned above, new metal forming processes are initiated for development and advanced tools are being designed to produce complicated parts by using numerical analysis techniques. These also create an environment for solving problems confronted during production in shorter time and obtaining more reliable results than those by empirical methods.

Finite Element Method is the most effective tool to determine material flow, stress-strain distributions on both workpiece and dies, temperature distribution, die deformation, material spring back and defects inside or on the surface of the formed part in cold forging. In order to obtain accurate results by performing computer simulations, all the related input data have to be defined precisely. Otherwise simulated part geometry and colorful graphs developed in the virtual environment will orient the engineer in a wrong way.

In order to perform the numerical analyses of cold forging of fasteners, material properties of workpiece and tools must be precisely defined with the correct boundary conditions like temperature and friction between mating surfaces. This study focuses on implementation of prestressed cold forging die models into finite element analyses to perform stress analyses and predict die failures. Different types of friction models are also investigated to determine the appropriate friction model giving the most accurate results.

During this study, all practical studies are conducted in collaboration with Norm Fasteners Co. that gives the opportunity to observe the problems faced during fastener production. Also, it provides production of dies designed by using computer simulations to perform tests for investigating tool lives.

1.5 Aim and Scope of the Study

In bolt forming processes, forging sequence designs are usually made without considering possibility of defect formation and stress distributions on dies and in case of a tool failure or a forging defect, problem is preferred to solve by experience rather than rely on calculations.

Aim of this thesis is to analyse the forging process and tools in bolt forming to predict die failures before production to provide an environment for improving process and die design. In order to reach this aim, shrink fit application is analysed to obtain a proper method for modeling dies with stress rings. Results are also verified with closed form solutions and experiments. In addition, results of bolt forming simulations are compared between rigid and deformable die models.

Furthermore to perform accurate force calculations especially for forward rod extrusion process, friction coefficient between tool and workpiece is investigated by making several ring compression and extrusion tests.

Scope of this thesis is focused on bolt forming analyses and experiments for modeling of shrink fitted cold forming dies to investigate stress distributions on tools during forging and predict possible die failures caused by overloading or fatigue by including determination of appropriate friction factor.

All the simulations are performed by using the commercial finite element program MSC. Superform Version 2005. Simulation results are verified by conducting experiments where applicable.

This thesis can be divided mainly into 6 chapters. Upcoming chapter deals with the previous studies in the literature about research related with tool design, prestressing and friction. Chapter 3 covers general information about the production of bolt forming dies. In Chapter 4 prestressing and die stress analyses which are performed by FEM are explained. Chapter 5 includes the results of ring upsetting and forward rod extrusion experiments that are conducted to determine friction coefficient in cold forming operations. The discussions, conclusions and further recommendations are given in the last chapter of the disertation.

CHAPTER 2

LITERATURE SURVEY

2.1 Introduction

In this chapter, relevant literature is discussed by subdividing it into two main topics; cold forging tools and friction. Moreover, since the forging tools cover a large number of topics with different area of interest, they are also grouped under the titles of tool life, die prestressing, elastic characteristics of dies and optimization of shrink fit interference.

2.2 Cold Forging Tools

Near net shape production, new materials and forming techniques are the new challenges in metal forming [8]. Due to the intermediate position between machine and workpiece, tools represent the interface of the forging process. A wide range of parameters in bulk metal forming like dimensional accuracy, product quality, process efficiency and cost are directly influenced by the quality of the tools. Moreover, tooling system stores most of the information related to the shape and property transformation resulting from the deformation of the material [9]. Therefore, correct decisions made about selecting and designing of the tools will yield in an effective production process.

In this section related studies about tool life, die prestressing, elastic characteristics of dies and optimization of prestressing are reviewed.

2.2.1 Tool Life

In bulk metal forming operations, tool life is mainly constrained by three causes [10];

- Plastic deformation
- Fracture
- Wear
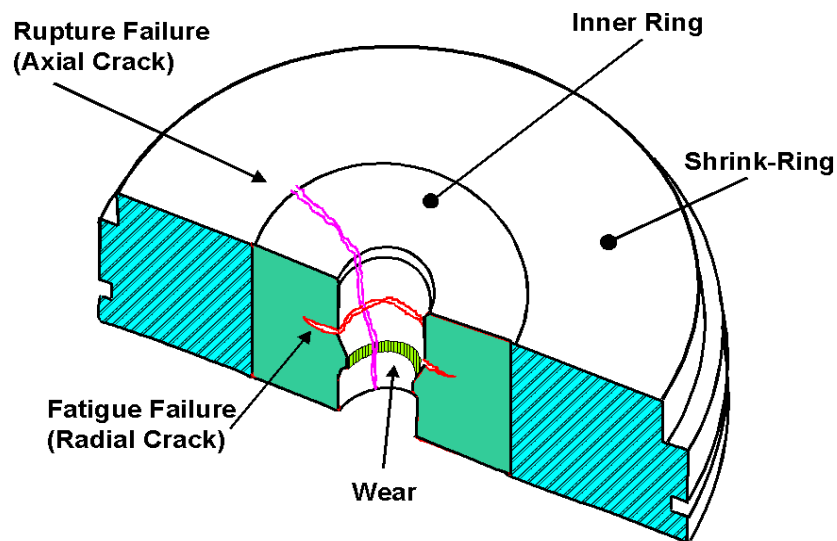
Figure 2.1. Typical tool failures in cold forming

The classical division of factors influencing tool life distinguishes between tool specific and application specific failure reasons. However they cover a much more complicated network of factors as shown in Figure 2.2

Depending on the type of process and deformation behaviour, failure mode and the frequency of the tool damage differs. Fracture is the main reason for failure where high forming loads are present whereas wear arises on parts having excess sliding over tool.
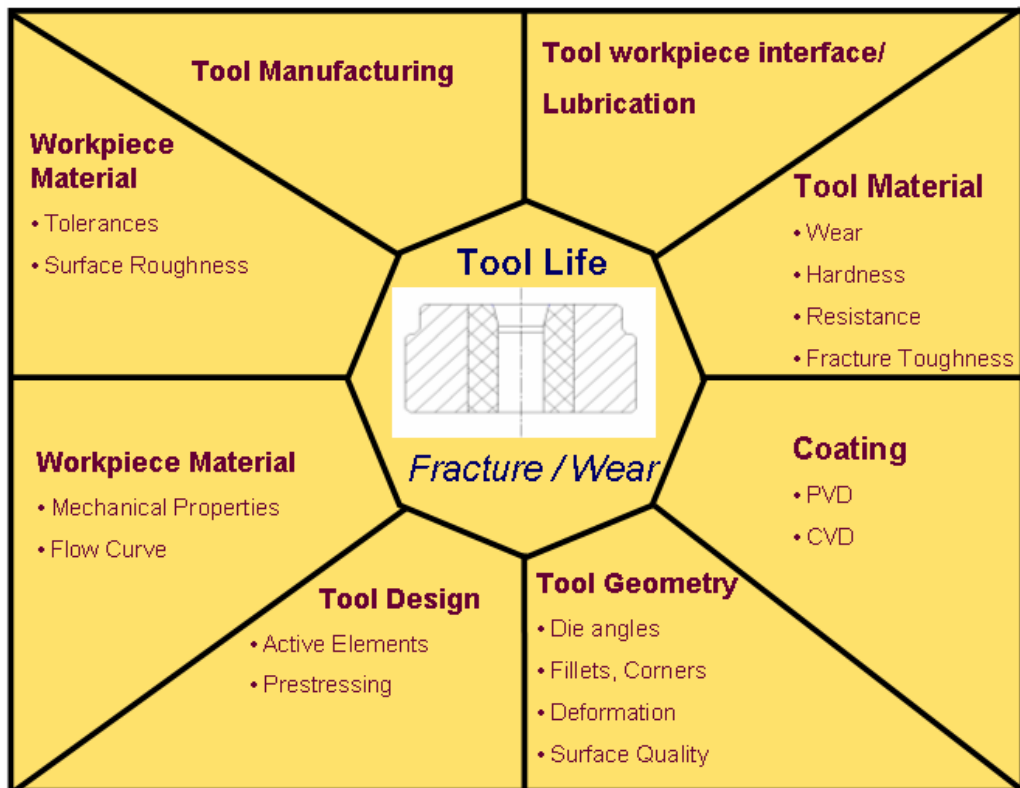
Figure 2.2. Different aspects of tool, workpiece and forming process, affecting wear and fracture behaviour of tool [8]

Since wear is the main kind of surface damage, it is the principal reason for scrapping the tools used in bulk forming processes because of large influence on the surface quality and tolerances of forged part and thereby tool life. It is generally accepted that this phenomenon is very complicated and a number of mechanisms and factors are involved [11], [12].

14

Tool fracture is the main danger in cold forming production because of the high costs arising not only from tool replacement but also from the damage which may be caused by the broken tool in an automatic press environment. Overload fracture can be avoided by using modern techniques of stress and strain estimation, like FEM, but fatigue fracture always occurs in highly loaded tools. For both fracture types, fatigue and overload, failure takes place when the sum of mechanical and thermal load exceeds a critical value [13].

Die failures mostly occur due to propagation of imperfections in the die material. Voids and surface fissures (micro cracks) formed during machining due to abrasion or thermal effects. These defects can act as stress concentrators and create large stresses on the die when the tool is subjected to the forming load. These cracks and voids propogate along the highly stressed regions up to a limit depending on material strength and result in fracture.

Tool life can be predicted by measuring the propagation speed of the cracks and voids however this process requires significant effort. Two types of methods have been reported for investigating the crack initiation and propagation [14], [15]. Eddy current testing is used to determine crack initiation and ultrasonic testing method monitors crack growth. Both methods have enormous importance for providing theoretical consideration of fracture simulation and on-line monitoring (Fig. 2.3).
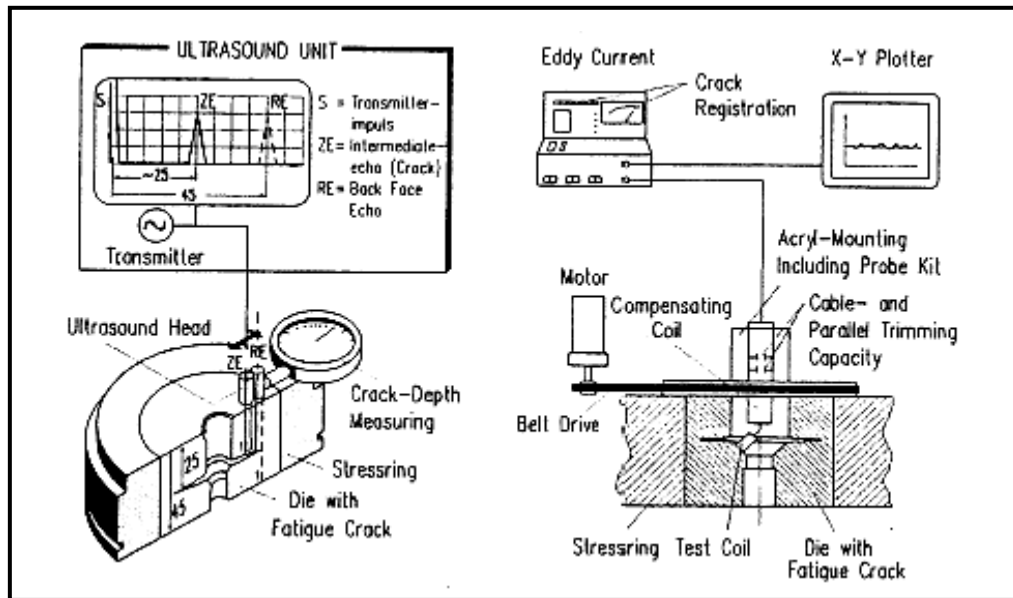
Figure 2.3. Systems, measuring initiation and propagation of cracks in a cold extrusion die [14], [15]

The combination of fracture mechanics with FEM enables the computer simulation of crack propagation to produce results that agree well with the results of practical measurements [16]-[18]. A.E. Tekkaya et al. [19], [20] investigated the crack growth behaviour and service life of an extrusion die. By using the linear elastic fracture mechanics theory and FEM simulations crack growth behaviour is investigated and computed effective stress intensity factors, after crack initiation, stable-unstable-stable growth phases are observed. In Figure 2.4 effective stress intensity factor as a function of the crack length is shown where;

> ➢ Phase A: Crack free phase
> ➢ Phase B: Crack initiation
> ➢ Phase C: Stable crack propagation
> ➢ Phase D: Unstable crack propagation
> ➢ Phase E: Stable crack propagation
> ➢ Phase F: Unstable crack propagation and rupture

16
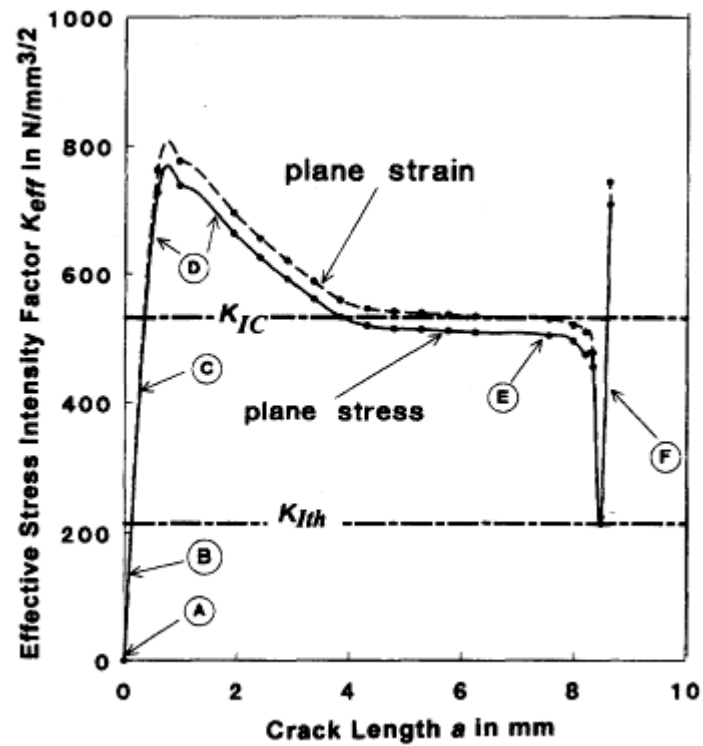
Figure 2.4. Effective stress intensity factor as a function of the crack length [19]

Finite element analyses showed that the reason for the second stable phase during the crack propagation is due to the reduction of von Misses stresses at the crack tip with increasing crack length. Figure 2.5 shows the von Misses stress distribution in a die insert without crack (Fig. 2.5a), with crack length 3 mm (Fig. 2.5b), 6 mm (Fig. 2.5c) and 9 mm (Fig. 2.5d). However, the numerical analyses are found to underestimate the crack length up to rupture. Basic source for this deviation is definitely the ignored wedge effect of lubricant and workpiece material penetrating into the crack.
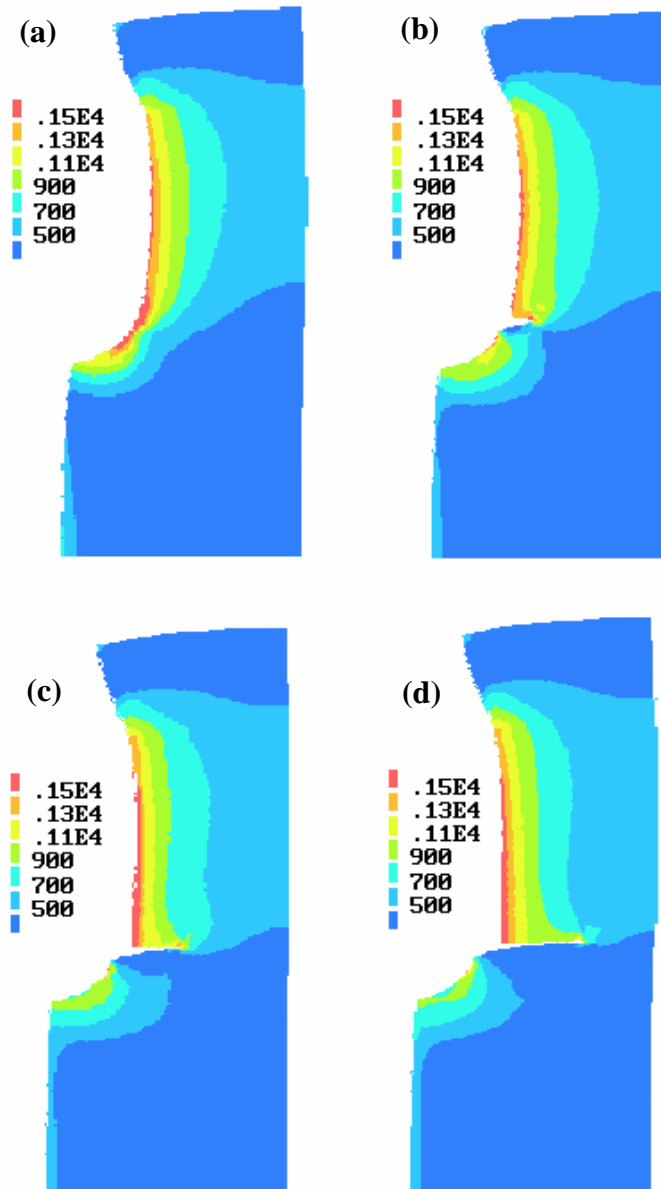
Figure 2.5. von Misses stress distribution in the die for various crack lengths (Enlarged deformations by a factor of 50) [19]

2.2.2 Die Prestressing

In cold forging, the die is subject to high loads that cause high tensile and compressive stresses depending on the material deformation. In order to reduce the

tensile stresses and thus the risk of cracks, the die is prestressed to a more compressive stress state by shrink or press fitting it in a prestressing system. Conventional prestressing systems consist of one or more stress rings of hot working or construction steel. The loadability, i.e. the ability of the rings to withstand a certain pressure on the inner bore, can be improved by increasing the number of stress rings, however the degree of improvement declines rapidly. Therefore the number of rings in a conventional system is usually limited to maximum three.
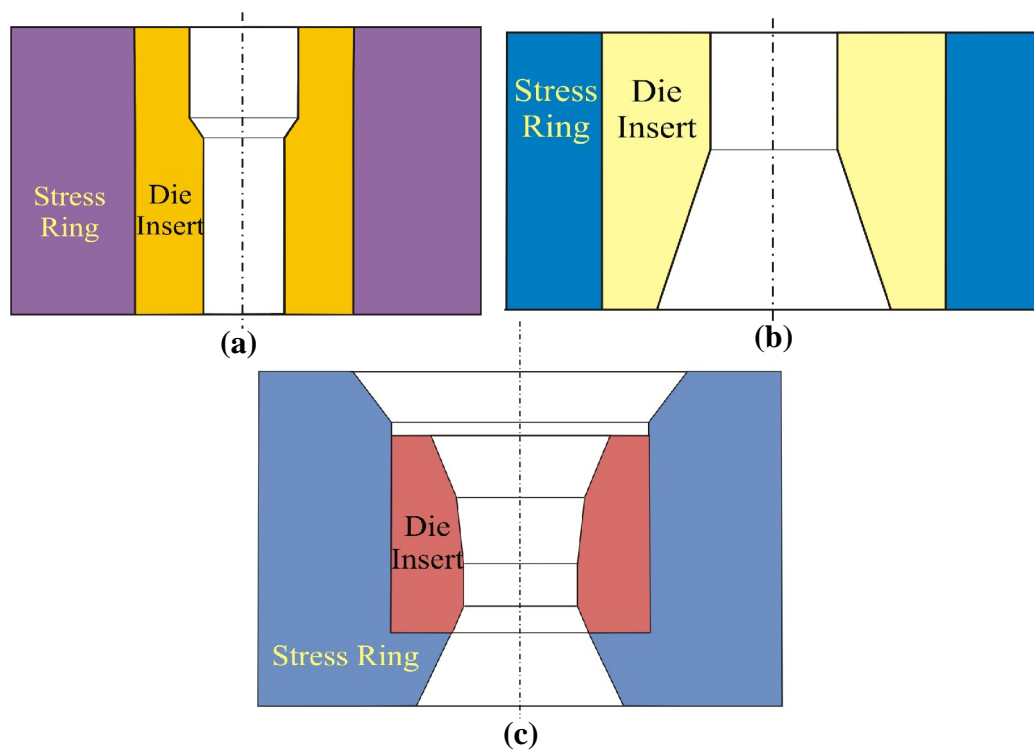
Figure 2.6. Dies with varying profile **a)** Extrusion **b)** Head Preform **c)** Wire Drawing

Die stress distribution after prestressing can be calculated analytically considering a plane strain problem of thick walled cylinders which is explained detailed in Chapter 4. However this approach is limited to cases with uniform inner section profile and

loading along the thickness. In many cold forming processes like drawing, extrusion and preform heading, dies with varying profile are used (Fig. 2.6) causing non uniform contact pressure. These nonlinear contact problems should be solved by using numerical methods like FEM.

Joun et al. [21] proposed a varying penalty method for solving the contact problem iteratively based on finite element method. Contacting objects have the same normal vector n_i along the interface where boundaries denoted as Γ_c^+ and Γ_c^- (Fig. 2.7).

(a)   **(b)**
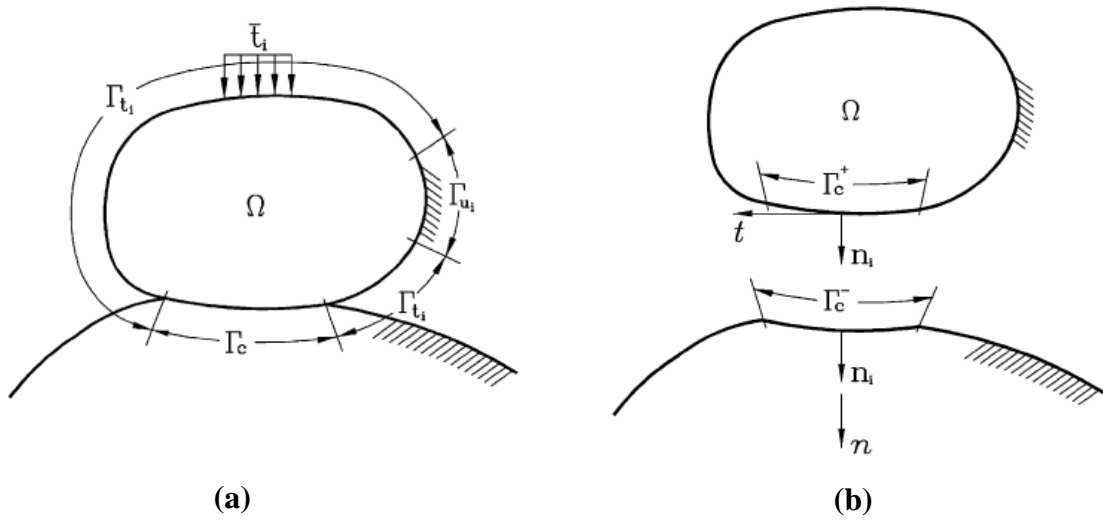
Figure 2.7. Definition of contact problem and the local coordinate system **a)** Contact problem **b)** Local coordinate system defined on contacting interfaces [21]

Under the assumption that the interface obeys the law of Coulomb friction, the geometrical and mechanical boundary conditions on Γ_c are as follows;

In the normal direction,

$$u_n^{+c} = u_n^{-c} \text{ if } \sigma_n^{+c} = -\sigma_n^{-c} < 0 \tag{2.1}$$

$$u_n^{+c} = 0 \text{ if } u_n^{+c} - u_n^{-c} < 0 \tag{2.2}$$

and in tangential direction,

$$\sigma_t^{+c} = -\sigma_t^{-c} = \mu \left| \sigma_n^{+c} \right| \frac{\left(u_t^{-c} - u_t^{+c} \right)}{\left| u_t^{-c} - u_t^{+c} \right|} \text{ if } u_t^{+c} \neq u_t^{-c} \tag{2.3}$$

$$u_t^{+c} = u_t^{-c} \text{ if } \left| \sigma_t^{+c} \right| = \mu \left| \sigma_n^{+c} \right| \tag{2.4}$$

where μ is the Coulomb friction coefficient and subscripts n and t denote normal and tangential component in the local coordinate system. Superscripts +c and −c specify related values on Γ_c^+ and Γ_c^-.

Using a penalty method Eqn. (2.1) and Eqn (2.4) are imbedded into the virtual work principle.

$$\int_\Omega \sigma_{ij} \delta \varepsilon_{ij} d\Omega - \int_\Omega f_i \delta u_i d\Omega - \sum \int_{\Gamma_{ti}} \bar{t}_i \delta u_i d\Gamma + \int_{\Gamma_{cn}} \beta_n \left(u_n^{+c} - u_n^{-c} \right) \left(\delta u_n^{+c} - \delta u_n^{-c} \right) d\Gamma$$
$$+ \int_{\Gamma_{ct}} \beta_t \left(u_t^{+c} - u_t^{-c} \right) \left(\delta u_t^{+c} - \delta u_t^{-c} \right) d\Gamma - \int_{\Gamma_{cs}} \sigma_t^{+c} \delta u_t^{+c} d\Gamma = 0 \tag{2.5}$$

β_n and β_t are large positive constants of which physical meanings are expressed as,

$$\sigma_n^{+c} = -\beta_n \left(u_n^{+c} - u_n^{-c} \right) \tag{2.6a}$$

$$\sigma_t^{+c} = -\beta_t \left(u_t^{+c} - u_t^{-c} \right) \tag{2.6b}$$

The die material is assumed to be linearly elastic and isotropic where stress-strain relation can be expressed as,

$$\sigma_{ij} = \frac{E}{1+v} \varepsilon_{ij} + \frac{vE}{(1+v)(1-2v)} \varepsilon_{kk} \delta_{ij} - \frac{\alpha E}{1-2v} \Delta T \delta_{ij} \tag{2.7}$$

21

where E, ν and α are Young's modulus, Poisson's ratio and coefficient of thermal expansion, respectively. ΔT is temperature difference and δ_{ij} is Kronecker delta.

In order to find the unknown boundaries Γ_{cn}, Γ_{ct} and Γ_{cs}, the problem is solved by an iterative method. This approach is verified by solving the problem presented by Takahashi and Brebbia [22] by the variable penalty method. In this case two hollow steel cylinders are prestressed by the interference, $\delta = 0.3$ mm, and internal pressure of 5000 MPa is exerted on the inner surface. Under these conditions $\Delta T = -625\,^{o}C$ equivalent to the interference $\delta = 0.3$ mm, was imposed to outer cylinder. Predicted results of radial and circumferential stresses are compared with their exact solution and results are in well agreement (Fig. 2.8).
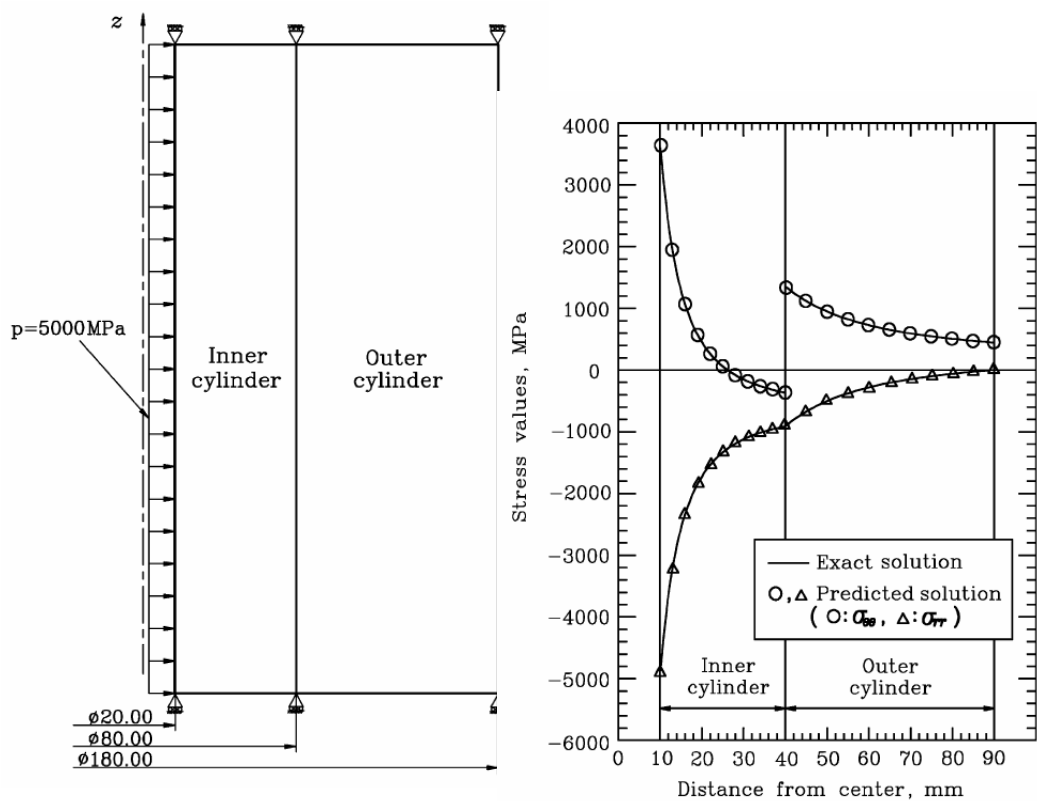
Figure 2.8. a) Analyses information for the test example **b)** Comparison of predicted results with the analytical ones [22]

Two different types of prestressing can be applied on the dies according to forging load and pressure acting on the die insert which are in radial and axial directions. An example of the method for applying radial prestressing is using a stress ring shrink fitting over the die insert as explained above. For axial prestressing there exist two common methods [23]. One of them is using a variable interference between insert and die (Fig. 2.9) to create a bending effect and produce compressive stresses along axial direction [24]. Other method is to use a threaded casing with a nut at the end to compress the dies assembled inside the case by tightening two parts.
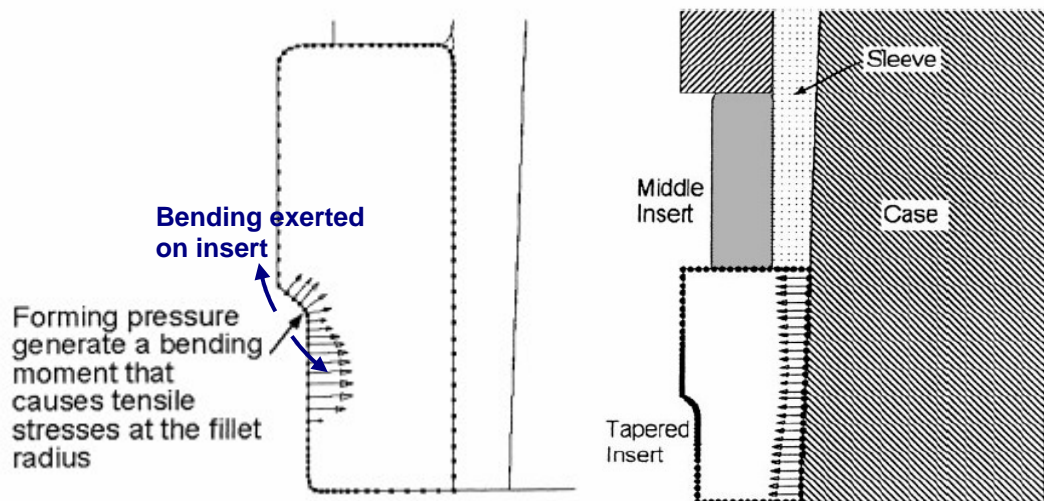
Figure 2.9. Tapered insert design with varying interference [24]

Goh [25] performed two dimensional axisymmetric finite element analyses consisting of die, die ring, punch, die support prestressed in different conditions. Figure 2.10 shows the components of the tooling.

The material constants of the tool steel (die, die ring, punch and die support) and low carbon steel (billet) are presented in Table 2.1.
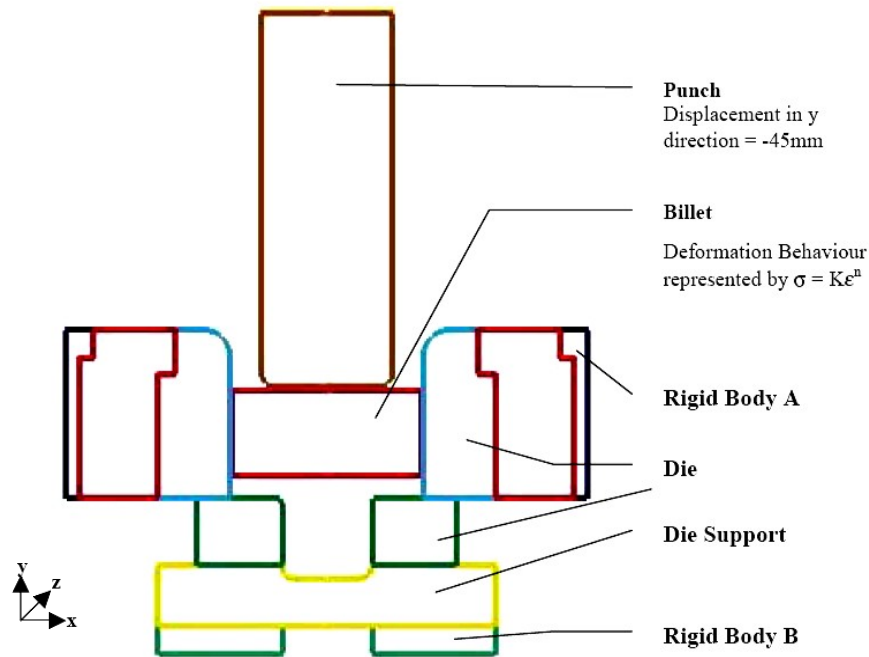
Figure 2.10. Configuration of the die set up for axial and radial prestressing [25]

Table 2.1. Material Properties of Tool Steel and Low Carbon Steel [25]

Material	Density (Kg/mm³)	Young's Modulus (MPa)	Posion's Ratio	Yield Stress (MPa)
Tool Steel	0.785×10^{-8}	210,000	0.3	1100
Low Carbon Steel	0.785×10^{-8}	210,000	0.3	220

To create compressive stresses on the die insert and ring, rigid body A is moved radially by 0.4% of the diameter of the die. Also, upward compressive stresses are applied to close the gaps between dies and prevent flash formation during forging by movement of rigid body B along positive y direction. To compare of effect of prestressing in radial and axial directions, different prestressing conditions are applied on die. Radial, axial and hoop stresses on the inner side of the die after prestressing and at the final stage of forming are tabulated in Table 2.2. As it can be

24

seen from the table, in presence of the prestressing, tensile stress generation on the die insert is prevented.

Table 2.2. Pressures and Stresses in X, Y and Z direction along Die Wall [25]

Prestressing Condition	σ_x (Radial Stress)		σ_y (Axial Stress)		σ_z (Hoop Stress)	
	Before Forming	End of Forming	Before Forming	End of Forming	Before Forming	End of Forming
Axial and Radial Prestressing	-112.6	-102.2	-412.9	-247.3	-936.6	-833.0
Only Axial Prestressing	-27.1	-49.4	-302.6	-214.4	-281.7	-75.5
No Prestressing	0	-14.7	0	47.4	0	108.3

The loadability of conventional prestressing system is mainly restricted by the material properties of the stress ring materials. The following figure shows that typical stress ring steels start to yield around 1000 MPa and this value depends on hardness (Fig. 2.11).
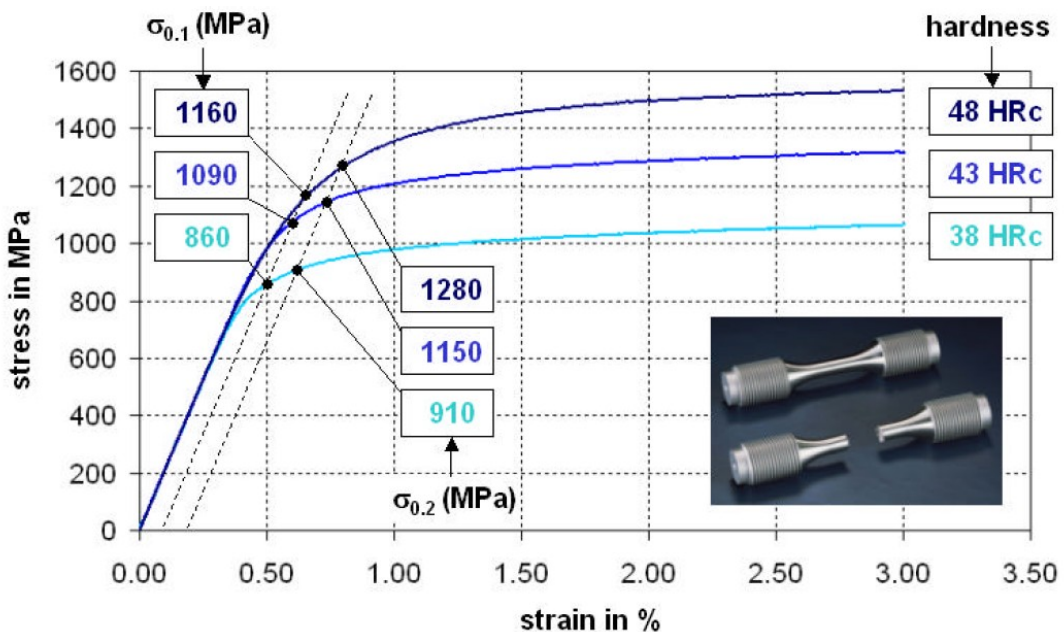
Figure 2.11. Flow curves of typical stress ring steels, derived from uniaxial tensile tests [26]

Since tool cost is one of the major factors in the industry, it is being studied to reduce by developing new techniques in die design. The strip wound containers are one of the unique elements replacing conventional multiple stress rings in tools for cold forming [27]. These strip wound containers are manufactured by winding a thin strip of high strength steel around tool steel or tungsten carbide (Fig. 2.12). During the winding process, strip is preloaded with a controlled tension.
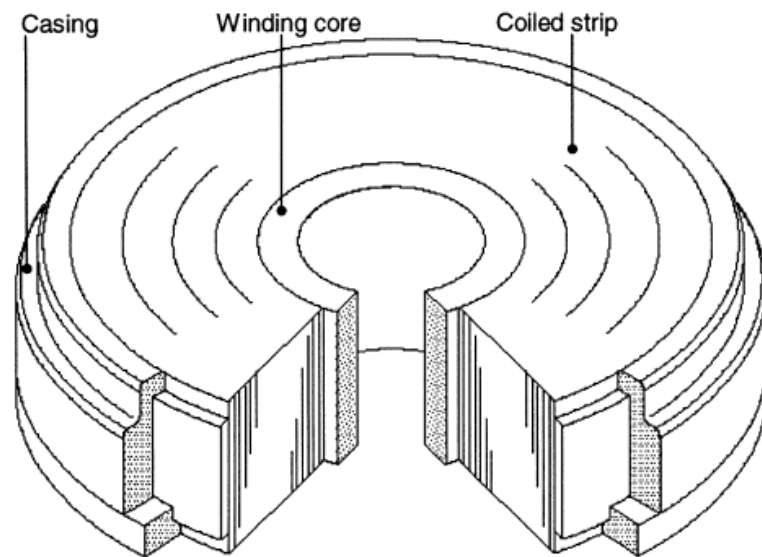
Figure 2.12. Layout of strip wound prestressed container [27]

Optimum stress distribution is obtained by varying the winding tension from layer to layer. The prestressed condition in the strip is equal to "several hundreds" of conventional stress rings. Another type of strip-wound container which is shown in Figure 2.13 has a very thick winding core made of tungsten carbide (WC). Since the Young's Modulus of tungsten carbide is around 500 GPa, total stiffness of the container is increased to 400 GPa or higher.
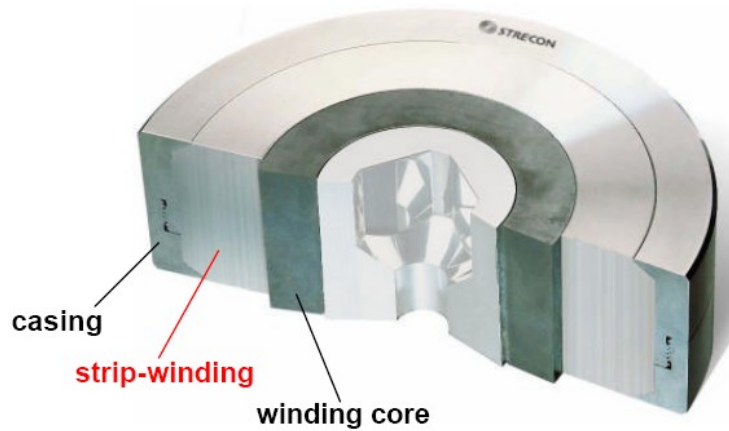
Figure 2.13. Layout of Strip-wound container with a tungsten carbide winding core, *Courtesy: Strecon A/S*

Analysis of a bevel gear die (Fig. 2.14) performed with different prestressed dies shows that with an increase in prestressing on the container, maximum tangential stresses reduce and this results in an increase in the tool life (Fig. 2.15). According to the stress – strain relations along the critical edge in the first load cycle of three different designs, cyclic fatigue tests are performed until fracture according to [28]. Conventionally assembled die failed after 400 cycles while normal strip wound die ruptured after 4700 and strip wound die with tungsten carbide winding core after 70000 cycles.
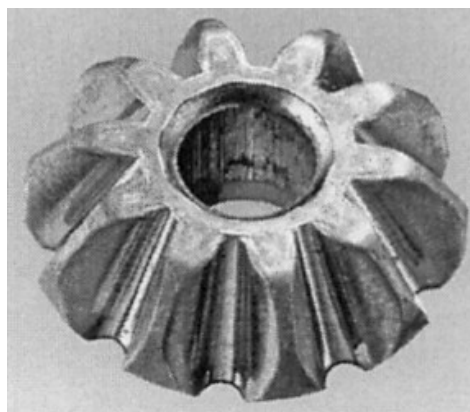
Figure 2.14. Cold Forged Bevel Gear
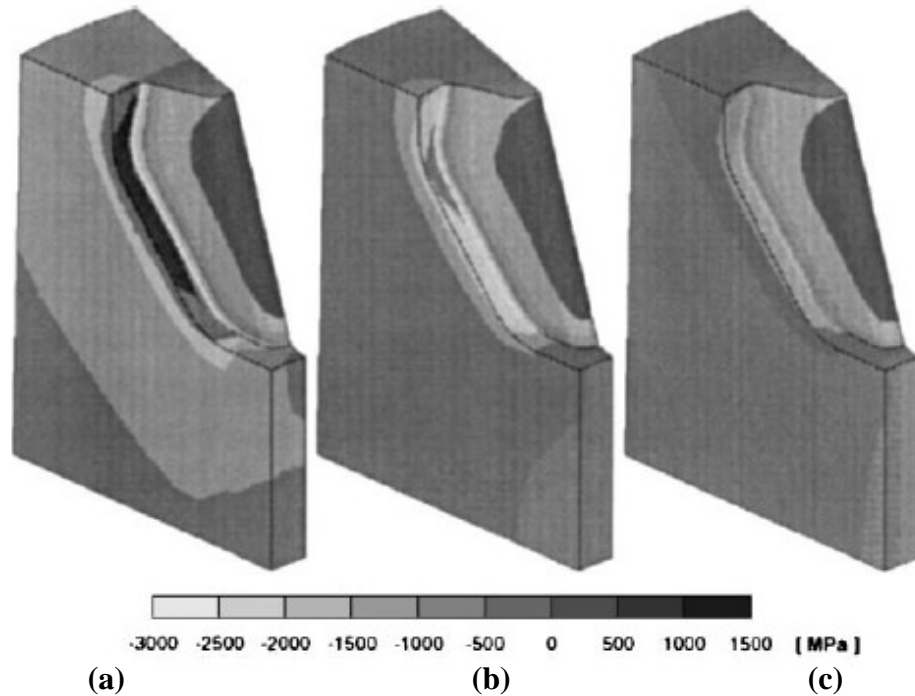
Figure 2.15. Tangential operational stress distribution **a)** Conventional die **b)** Normal strip wound die **c)** Strip wound die with tungsten carbide winding core [27]

2.2.3 Elastic Characteristics of Dies

In cold forging process, dies are expected to withstand high forming loads and produce small deflections during the forming operation. This can be only achieved by making proper die design by considering die structural analysis. However this is a very complicated task since it does not only involves elastic and plastic deformations together with complex contact problems, but it is also directly related to the forging analysis problem.

During investigation of the forming problems, dies are mostly regarded as rigid bodies. Hence, elastic properties are ignored. The effect of this elastic behaviour on the material flow during forming process is usually negligible as compared to the size of the workpiece. However, if the working conditions of the forming process are

extreme, such as high frictional constraints at the die-workpiece interface, the geometrical ratios, involving high local pressure, the elastic deflection of the die may considerably influence the local stress and strain of the deforming body due to the elastic effects. Thus, rigid die analysis is inadequate for forming operations if very high pressure is involved or where precision parts with close tolerances are demanded [29].

Since the forging tools are elastically deformed under cold forging pressure, this deformation behaviour should be analyzed to improve the dimensional accuracy of forged part. Lin [29] investigated upsetting of a cylinder between elastic dies for determination of spring-back of the end surfaces of the billet and elastic deflection of the dies by utilizing a thermo-elastic-plastic coupled model. Figure 2.16 shows the configuration of the die and the specimen and initial finite element mesh.
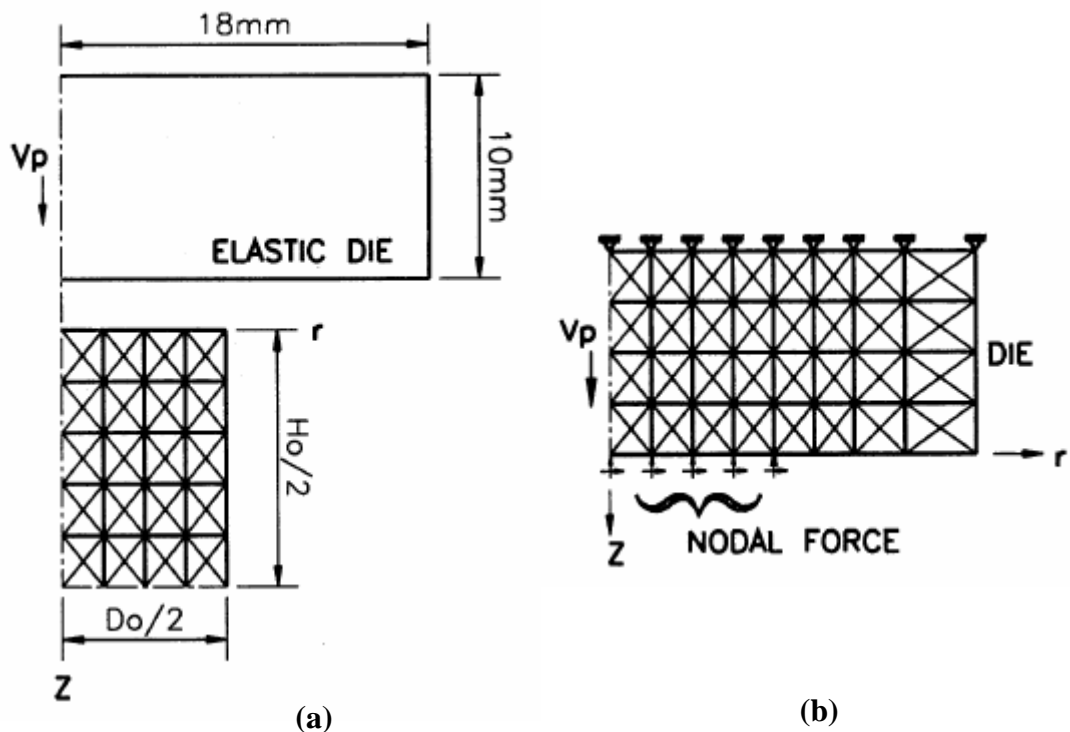
Figure 2.16. a) Dimensions of the die and the specimen and the initial mesh of the billet **b)** Initial mesh pattern and boundary conditions of the die [29]

The nodal forces are reacting at the die-workpiece interface at each small deformation step which are prescribed on the corresponding boundary of the die and cause the die to deform elastically. Since the level of spring-back of the end surface of the workpiece must be identical to the amount of small deformation of the die, to maintain die – workpiece contact at each step, unloading process has been performed on the elements of the billet to account for this spring back characteristic.

Comparison of load displacement curve and spring back of the end of the billet between experimental measurement and FE analyse results (Fig. 2.17) is showing that surface asperities obtained by using deformable die models are consistent with experiments (Fig. 2.18).
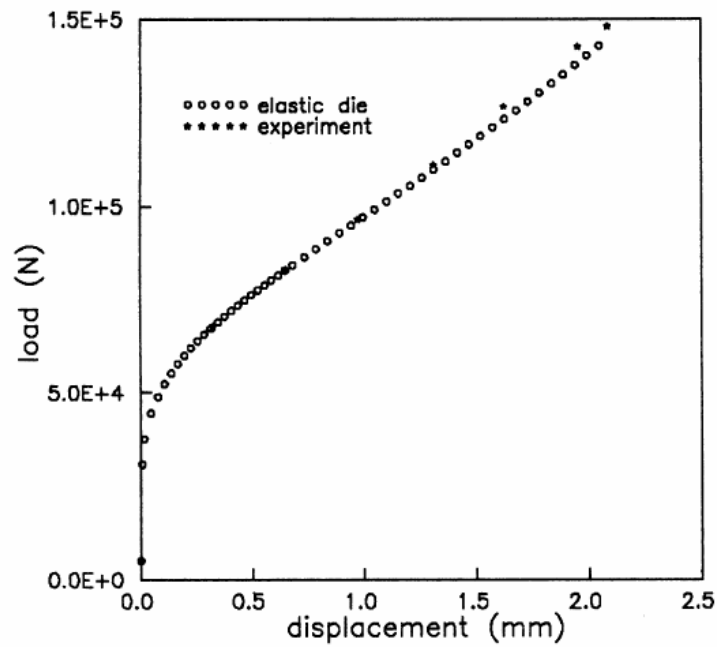
Figure 2.17. Comparison of the relationship of load-displacement curves at each 5% height reduction between prediction and experiment [29]
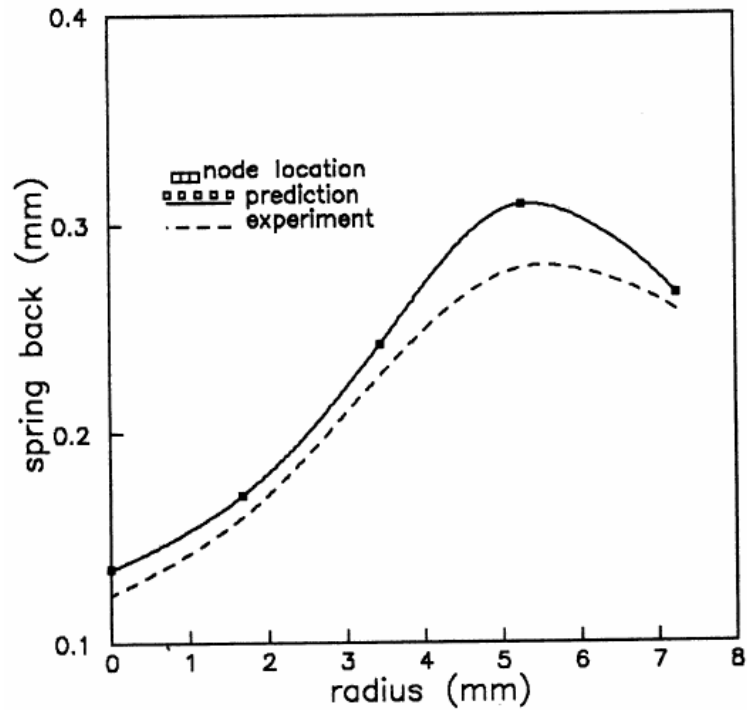
Figure 2.18. Comparison of the levels of spring back of the end of billet along r-axis [29]

More complex forging processes are studied by Lee et al. [30] – [33] to compare the forged part dimensions and die deflections obtained from the finite element analyses with the experimental data. In the forging analyses, both rigid and deformable tool models are used. Results showed that deformable model could more precisely predict the deformations on the tool obtained from the strain gage measurements than the rigid model. Figure 2.19 shows the verification for the experiment where measured deformations are compared with the values calculated for different model types which are listed in Table 2.3.
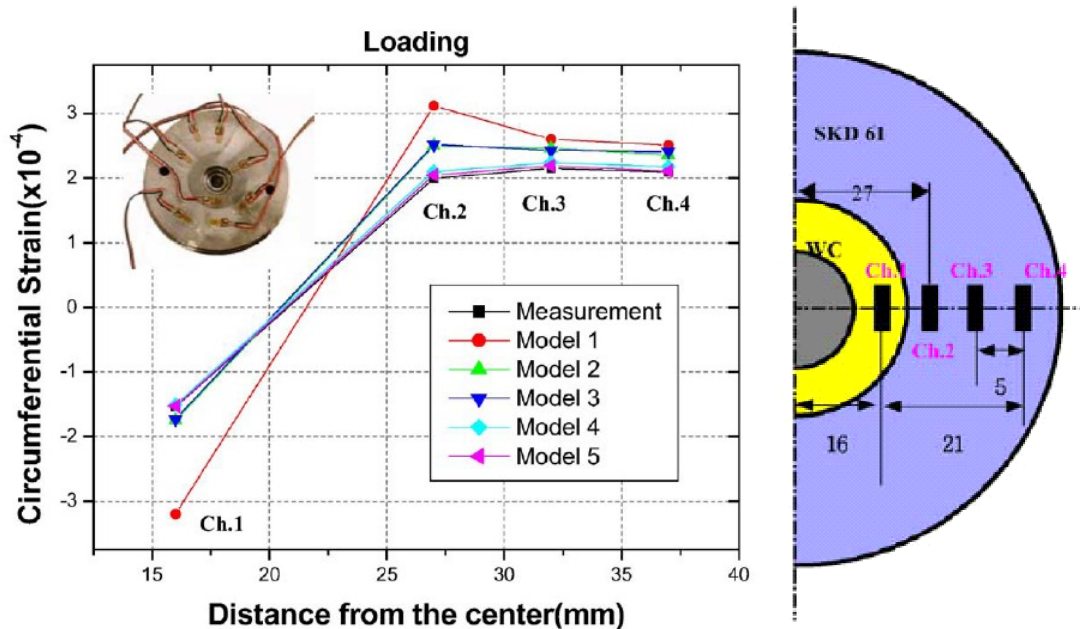
Figure 2.19. Circumferential strain measured on top surface and estimated values in loading stage [30]

Table 2.3 Model approaches used for the present FEA

No	Model of objects		
	Die		Workpiece
	Material	**Dimension**	
1	Rigid	Designed Value	Rigid-Plastic
2	Elastic	Designed Value	Rigid-Plastic
3	Elastic	Machined Value	Rigid-Plastic
4	Elastic	Designed Value	Elasto-Plastic
5	Elastic	Machined Value	Elasto-Plastic

With the increased demand for net shaping, higher dimensional accuracy and better surface quality become crucial features of cold forging technology. Producing within tighter tolerances necessiates the use of die materials with high hardness, high temperature resistance, high compressive strength and low thermal expansion coefficient. Ceramics serve as a better solution when these requirements are considered against conventional tool materials like high speed steel (HSS) and

tungsten carbide (WC). Arbak et al. [34] reported that ceramic dies are providing high dimensional accuracy and better surface quality after performing tests during the production of a bolt forged in 5 stages (Fig. 2.20a).
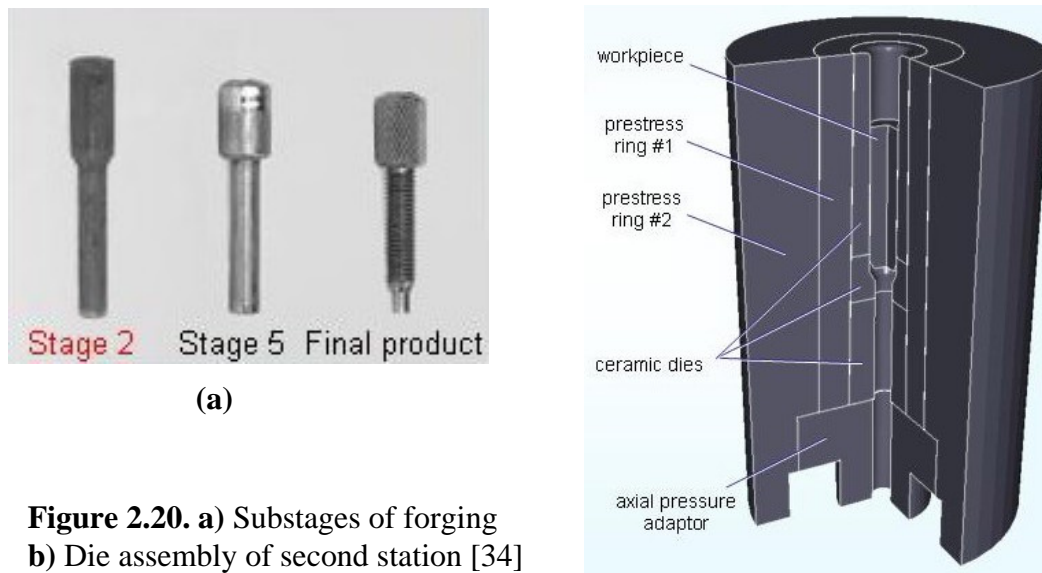
Figure 2.20. a) Substages of forging
b) Die assembly of second station [34]

The tool of the second design stage consists of a radial prestressing ring, a die and an axial compression part at the bottom (Figure 2.20b). The interference amount has an important role on eliminating the tensile stresses on the die insert during forging. Moreover, the unexpected die failure of the ceramic die at the first attempt showed that, although the hoop stresses on the insert are completely on compressive region, there exist circumferential strains remaining in the tensile region (Fig. 2.21). To avoid this problem double stress rings are used.

After forging, measured diameters of the workpiece revealed that the tolerance of the 4.9 mm parts were in IT6 (8 μm) band where the cold forging process lies between IT11 (75 μm) and IT14 (300μm). Also by performing optical measurements by white light confocal microscopy, on the surface of the parts produced by using ceramic tool, average surface roughness is measured as 0.409 μm while ASME B46.1-1995 standard states roughness for similar process between 0.8 μm and 3.2 μm (Fig. 2.22).
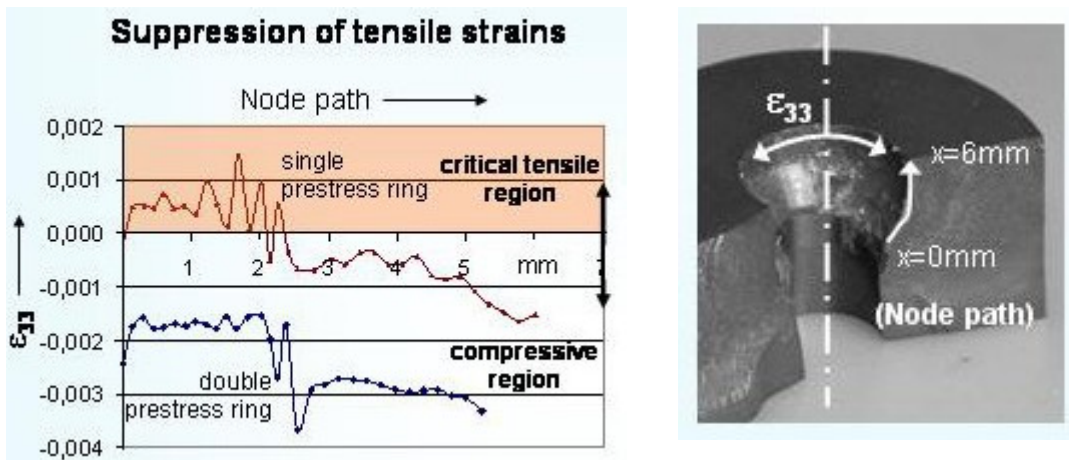
Figure 2.21. Comparison of circumferential strain distribution for different prestressing conditions *(left)*, Path of the critical region of ceramic die *(right)* [34]
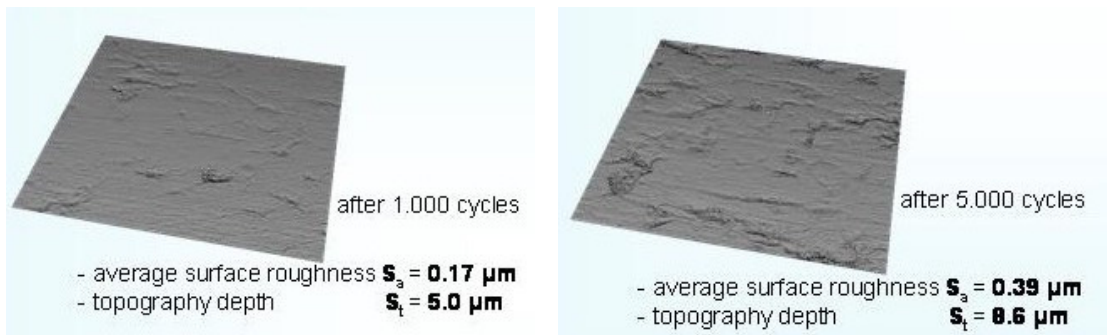
Figure 2.22. Surface roughness measurements [34]

The geometrical accuracy of cold formed parts especially during mass production depends on many parameters as incoming material, the machine, the tool and the process itself [35]. For instance, in forward rod extrusion process, forged part dimensions can be different for two successive blows due to variation in cut off billet length, billet diameter, friction, elastic and thermal die deflection [36] (Fig. 2.23).

34
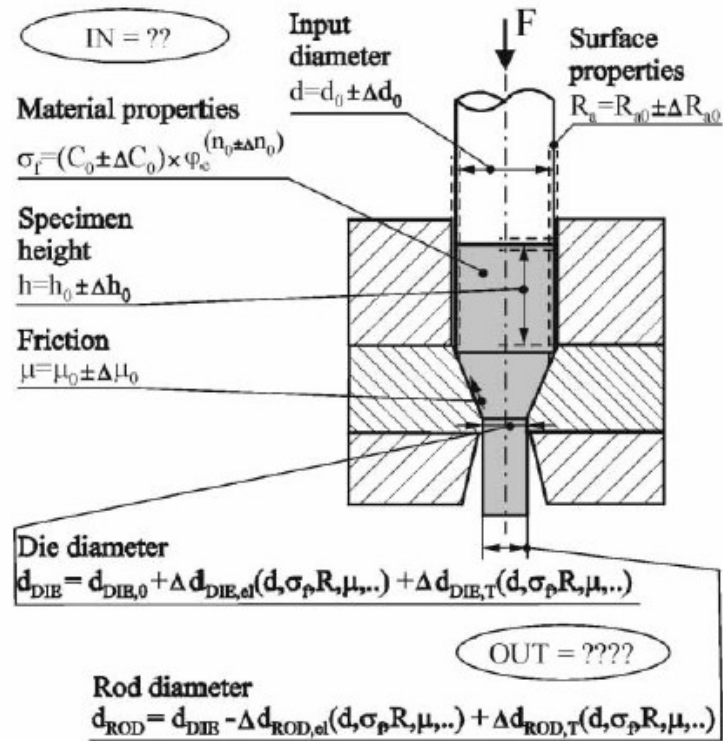
Figure 2.23. Process parameters cause fluctuation in forward rod extrusion [36]

Since die deflection is one of the major factors which cause dimensions of the part going beyond the tolerances, new techniques are being developed to maintain the stability of the process and keep the part within desired tolerances by means of adapting the dies. Osakada et al. [37] presented an idea to control rod extrusion by using a ring shaped die supported by a conical die holder. As the friction between the insert and the holder is kept very low, it is possible to perform the axial movement of the die and correct the outgoing diameter of the part (Fig 2.24a). A similar idea is presented by Jütte [38] where an active inner die diameter is controlled by additional hydraulic pressure (Fig. 2.24b).

There exist two more types of adaptive dies used to adjust inner die diameter which are developed by Strecon named VARI-FIT and DYNA-FIT. In the VARI-FIT system spacer rings are used to determine the axial position of die insert (Fig. 2.25)

and diameter is manually changed up to 100 microns due to the conic inner bore of the container. However in DYNA-FIT system, die adjustment is performed in the press during production by using a hydraulic system.
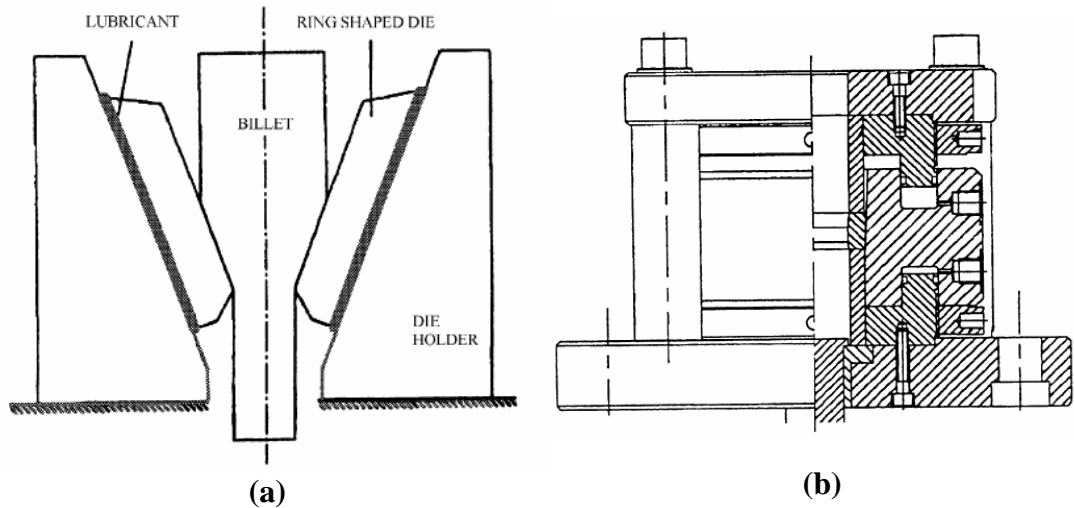
Figure 2.24. Examples of adaptive tooling systems **a)** Cold extrusion tool [37] **b)** Tool with active die [38]
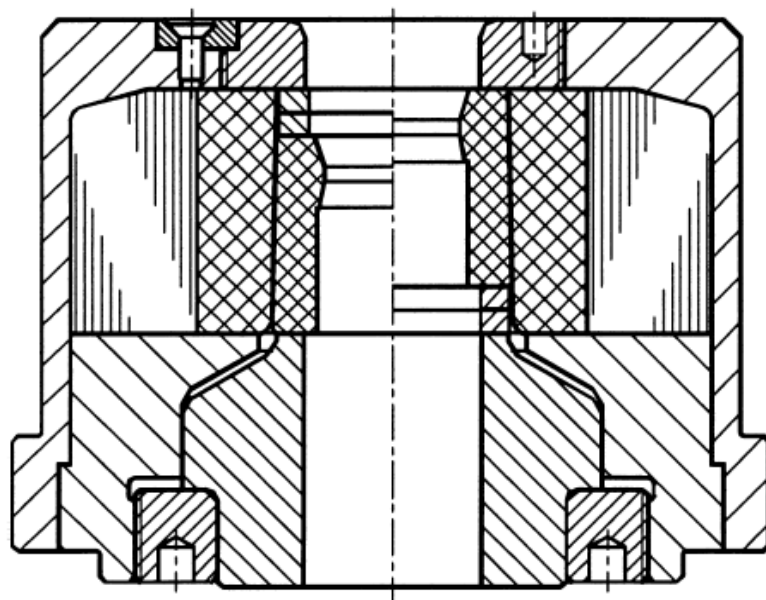
Figure 2.25. Strecon VARI-FIT prestressed container [39]

2.2.4 Optimization of Prestressing

Determination of the interference between the shrink fitted components of a tool assembly has a direct influence on the tool life. Brittle damage evolution analysis performed for extrusion die set of a ball stud (Fig. 2.26) shows that, fracture location on the parts is changing for different interferences [40]. Integrated analyses start with finding the initial stress distribution due to shrink fit of stress rings by considering thick walled multi-layer cylinders under constant internal/external pressures. After conducting FEM analyses, traction boundary conditions at the die surface obtained and transferred to carry out elastic analyses of the die set to predict nonlinear brittle damage evolution.
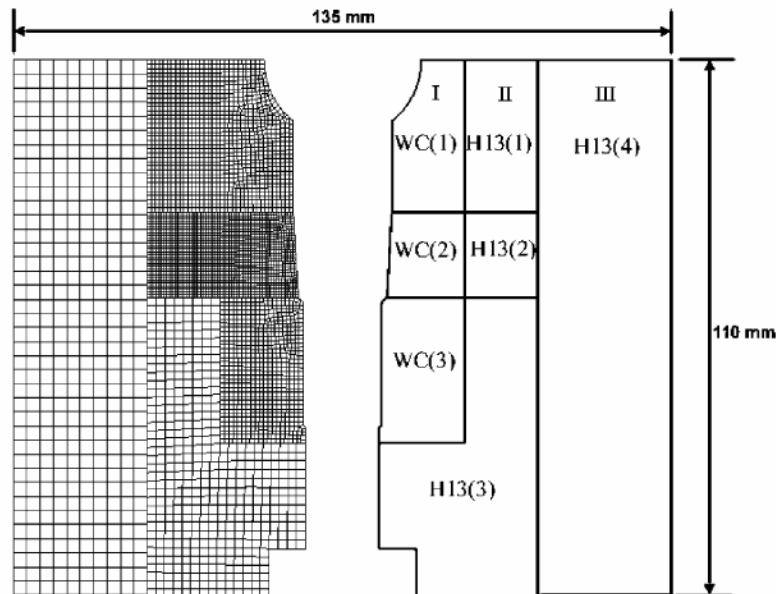
Figure 2.26. Schematic view of extrusion die: **I**, insert die; **II**, first stress-ring; **III**, second stress-ring [40]

Figure 2.27 is showing the two types of fractures for different interferences. In case of large shrink fit, damage is minute since the dies have initially at the compressive stress state along circumference. This is the case where stress ring fails first (Fig. 2.27a). On the other hand, die insert fractures when shrink fit is relatively less as shown in Figure. 2.27b.
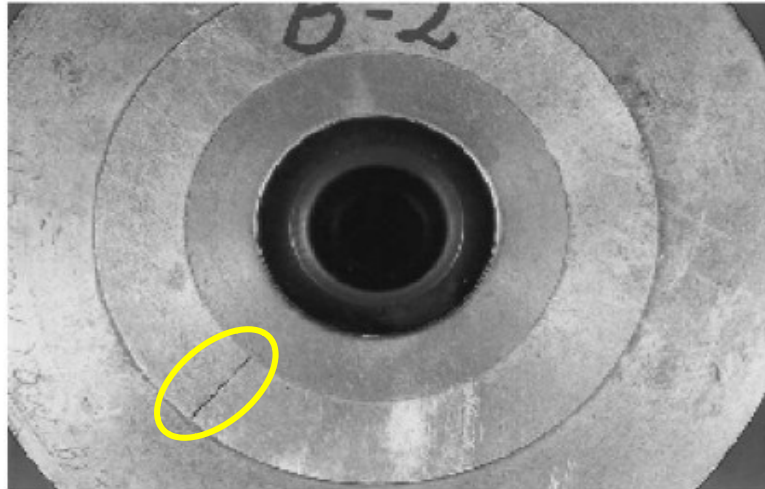
(a)
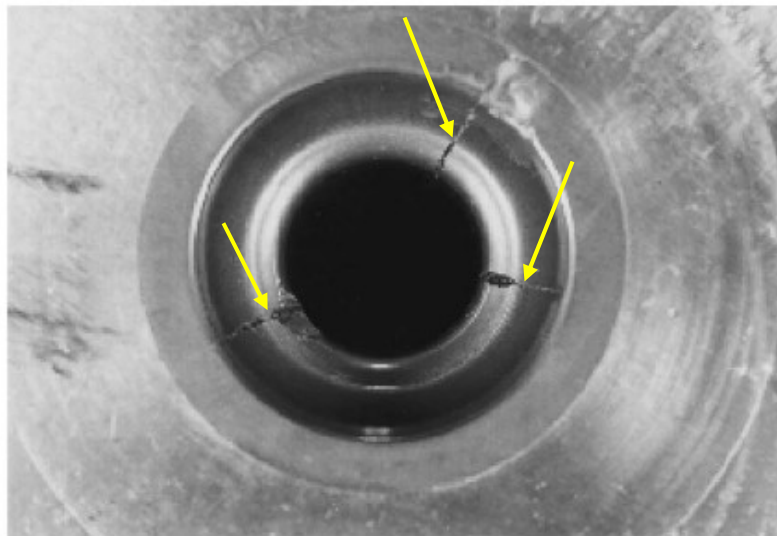
(b)

Figure 2.27. Failure of extrusion dies by damage **a)** Large interference **b)** Small interference [40]

Researchers who performed studies on improving the tool life for prestressed dies, reported that die stress distribution completely changes with the change of interference and has a direct effect on number of load cycle which causes fracture [41 - 46]. It is important to find out correct interference which is high enough to

overcome tensile stress without exceeding the yield limits of prestressing system material (over-prestressing) (Fig. 2.28).

Too Low	Non-Satisfying	Optimum	Too High
High Tensile Stresses	Still Considerable Tensile Stress	Minimized or No Tensile Stress	Risk of Over Prestressing

Figure 2.28. Interference – Prestress Level

There exist some analytical methods proposed to define optimum interference and permissible internal die pressure for one and two stress rings stressed up to yield point or tensile stress formation on the insert. However for the dies with complex geometry and loading, analytical methods of solution supply only approximate solutions.

These methods are based on certain simplifying assumptions by regarding the prestressed die as prestressed thick walled cylinder of infinite length at a constant internal pressure impacting along the height. The most advanced approximation method for the elastic layout is based on Lame's Equations and the theory presented with the optimization equations in detail [47].

2.3 Friction

A very important variable that enters into almost all phases of metal forming but which is not fully coped with yet is the phenomenon of friction. Friction, in a simple manner, can be described as "surface resistance to the relative sliding or rolling motion" while in metal forming operations this term converts to "workpiece-die surface resistance to metal flow". Since in metal forming relative motion between workpiece and tools is present, friction is an inherit part of the process [48].

There are major effects of friction in metal forming operations. Friction results in an increase in the force, affects the surface finish, causes wear on tools and yields heat generation affecting the flow characteristics of the material.

To reduce the friction effect, different types of lubricants are applied on the components depending on the type of the process. There are three basic types of lubrication that govern the frictional conditions [49]. First type is the dry condition where no lubricant is present and oxide layers are present on the die and workpiece materials acting as a separating layer. In this case friction is high and desirable in only a few forming operations such as non lubricated forging of aluminum alloys. For the second type of lubrication, hydrodynamic conditions exist when a thick layer of lubricant is present. For this type, friction conditions are governed by viscosity of the lubricant and relative sliding velocity between the die and the workpiece. The last type of lubrication, named as boundary lubrication, which is the most widely encountered situation in metal forming. Increase in the temperature and the relatively high forming pressures do not allow the presence of hydrodynamic lubrication regime.

The modification of lubrication does not only changes the contact interference between the tool and the workpiece, but also causes a change in the friction conditions such as;

- The velocity field
- The normal and tangential stresses
- The contact velocity
- Temperature conditions on the surface
- The forming pressure

2.3.1 Friction Models

Based on experimental observations, a number of investigations have been carried out to model friction as a function of deformation zone distance. A summary of frictional stress distribution in simple upsetting of a circular cylinder is shown in Table 2.4 [50].

Table 2.4 Various friction models used in bulk metal forming [50]

Friction model	Friction stress distributions	Main assumptions and applications	Authors, (year)
$\tau = \mu \cdot p$		Friction model Friction stress τ is directly proportional to local normal pressure p. It is mainly used for cold metal forming due to its simplicity.	Von Karman, 1925 Kunogi, 1924 Kudo, 1960
$\tau = m \cdot k$		Dry slipping occurs over the whole tool/workpiece interface. k=σ0/√3 is the shear flow stress, and σ0 is the yield stress.	Orowan, 1946
$\tau = \dfrac{K}{2}$		Sticking occurs over the whole interface between tools and workpiece K=1.15σ0.	Sims, 1954 Nadai, 1939
$\tau = \eta \dfrac{dv_x}{dy}$		Viscous slipping friction proportional to relative velocity of slip, occurs over the whole interface between tools and workpiece.	Nadai, 1939
Area I: $\tau = \dfrac{K}{2}$ Area II: $\tau = \mu \cdot p$		The interface is divided into two zones: (I) sticking occurs at the central zone whose centre is the neutral point; (II) dry slipping occurs at the edge zone when frictional stress is less than yield stress in shear.	Orowan, 1943
Area I: $\tau = \tau_{II} \dfrac{r}{OA}$ Area II: $\tau_{II} = \dfrac{K}{2}$ Area III: $\tau = \mu \cdot p$		A zone of restricted plastic deformation exists in the middle of the sticking zone. The tool/workpiece interface is divided into three zones: (I) the stick zone, (II) the drag zone, and (III) the slip zone.	Tselikov, 1958 Unksov, 1961
Area I: $\tau = \tau_A \dfrac{r}{OA}$ Area II: $\tau = f\alpha k$ Area III: $\tau = \mu \cdot p$		Three zones are similar to the model of Tselikov and Unksov: (I) the central sticking zone; (II) the sliding zone and (III) the homogeneous deformation zone.	Bay and Gerved, 1984
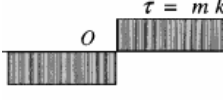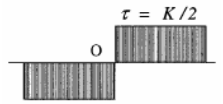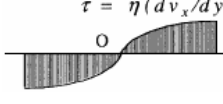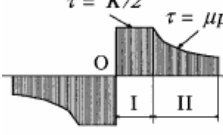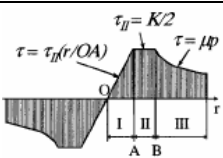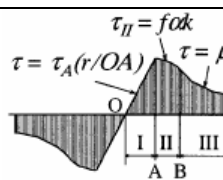
2.3.1.1 Amontons – Coulomb Model

If the normal forces P acting on two components as shown in Figure 2.29 and a lateral force F is applied slide one body over another for given conditions, then the Coulomb coefficient of friction μ is defined as;

$$\mu = \frac{F}{P} = \frac{F/A}{P/A} = \frac{\tau_{friction}}{\sigma_{normal}} \tag{2.8}$$

Even though the surface contact is often limited to only a few asperities on the surface, the area *A* is usually taken as the total area of apparent contact.
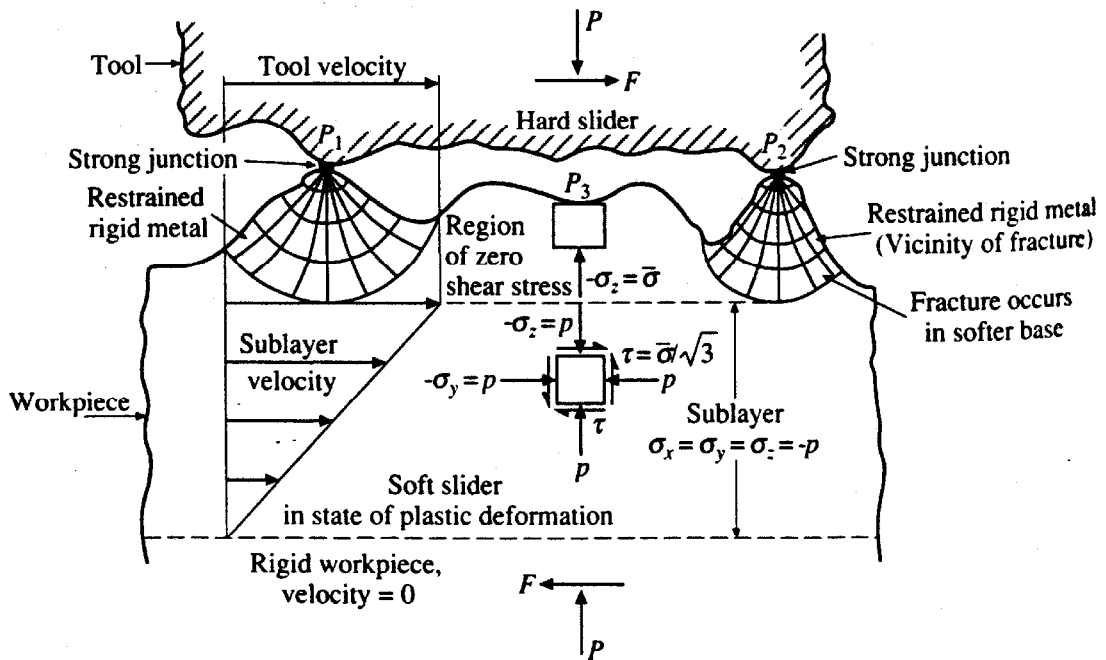
Figure 2.29. Microscopic model of sliding friction of two sliders [51]

42

2.3.1.2 Constant (Shear) Friction Model

According to the Coulomb friction model friction stress $\tau_{friction}$ is directly proportional to normal stress applied on the material. However under high normal stresses, friction stress will be equal to the flow strength in shear of the material. At this critical normal stress value shearing begins instead of sliding. Due to this transition a new friction model has been proposed by Orowan assuming that friction stress is proportional to the yield stress of the material in pure shear k where normal stresses are higher than critical value.

$$\tau_{friction} = m \cdot k \tag{2.9}$$

where m is the shear friction factor.

2.3.1.3 General Friction Model

Wanheim [52] stated that it is necessary to consider the frictional stress as a function of normal pressure, surface topography, length of sliding, viscosity, and compressibility of the lubricant. Related to this, aim, Wanheim, Bay and Petersen [53] developed a general friction model upon the slip-line theory.

$$\tau_{friction} = f \cdot \alpha \cdot k \tag{2.10}$$

where f is the friction factor, α the ratio of real and apparent contact area and k the shear flow stress. The model assumes friction to be proportional to the normal stress at low normal pressure ($\sigma_n / \sigma_0 < 1.5$), but going towards a constant value at high normal pressure ($\sigma_n / \sigma_0 > 3$) where σ_n and σ_0 are normal pressure and flow stress respectively. These two ranges are combined by the intermediate transition region as shown in Figure 2.30.

In practice the friction factor f is determined experimentally and α is found according to the analytical expression;

$$(f\alpha =)\frac{\tau_{friction}}{k} = \frac{\sigma_n/\sigma_0}{\sigma_n'/\sigma_0}\frac{\tau'}{k} \quad \text{(for } \sigma_n < \sigma_n') \tag{2.11a}$$

$$(f\alpha =)\frac{\tau_{friction}}{k} = \frac{\tau'}{k} + \left(f - \frac{\tau'}{k}\right)\left(1 - \exp\left[\frac{\tau'/k(\sigma_n'/\sigma_0)}{\sigma_n'/\sigma_0(f - \tau'/k)}\right]\right) \quad \text{(for } \sigma_n > \sigma_n') \tag{2.11b}$$
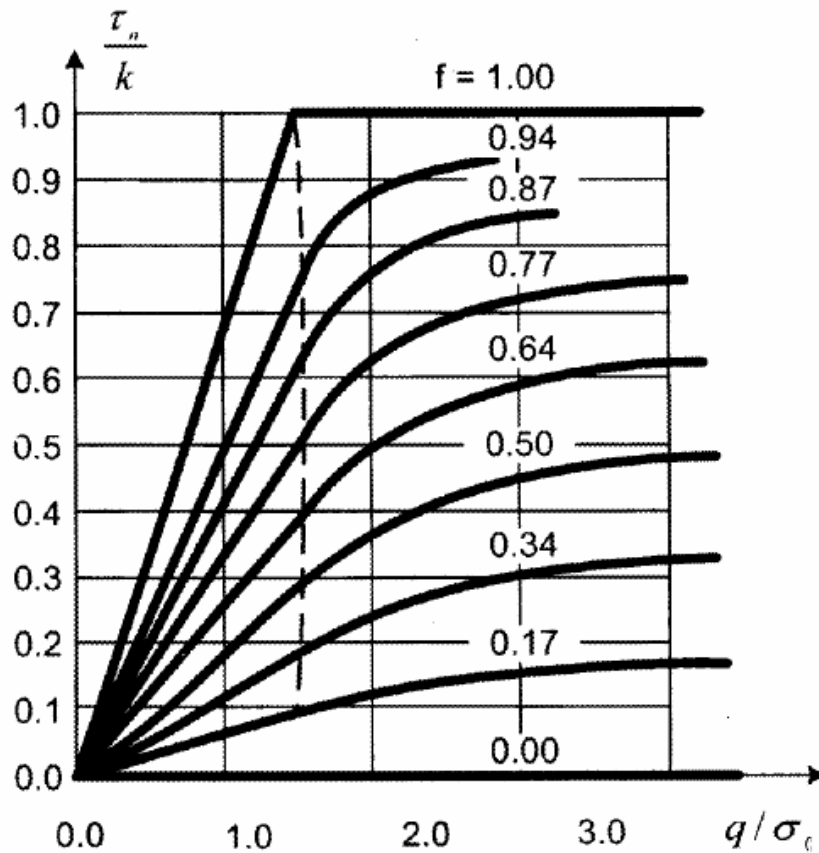
Figure 2.30. Nominal friction stress as a function of normal pressure and friction factor [53]

44

where the limit of proportionality ($\tau'/k, \sigma_n'/\sigma_0$) is given by;

$$\frac{\sigma_n'}{\sigma_0} = \frac{1 + \dfrac{\pi}{2} + \arccos(f) + \sqrt{1-f^2}}{\sqrt{3}\left(1 + \sqrt{1-f}\right)} \tag{2.12a}$$

$$\frac{\tau'}{k} = 1 - \sqrt{1-f} \tag{2.12b}$$

2.3.2 Friction in Finite Element

In finite element analyses, friction model is implemented by specifying the frictional stress at the tool − workpiece interface as a traction boundary condition [54]. Assuming friction to be a traction boundary condition, the power consumption, π_c, due to the friction is expressed by;

$$\pi_c = \int\limits_{S_c}\left(\int\limits_0^{|v_r|} \tau_f \, dv_r\right) dS \tag{2.13}$$

where S_c is the contact interface, v_r is the relative velocity and τ_f is the friction shear stress between workpiece and die. The sense of the friction to the relative sliding velocity, v_r, according to;

$$\tau_f = -\mu\sigma_n \frac{v_r}{|v_r|} \tag{2.14}$$

Quite often in contact problems, neutral lines develop. This means that along a contact surface, the material flows in one direction in part of the surface and in the opposite direction in another part of the surface [55]. For a given normal stress, the friction stress has a step function behavior based upon the value v_r (Fig. 2.31).

45
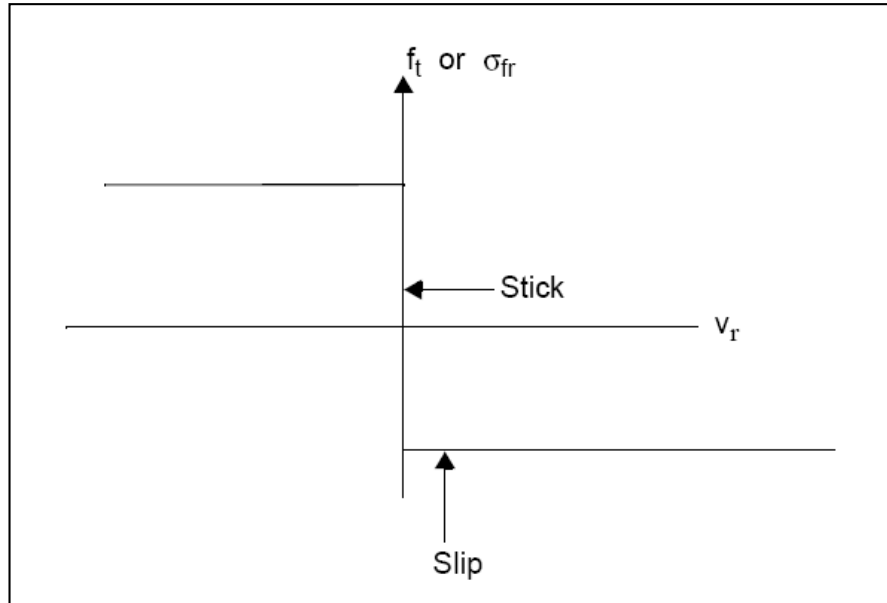
Figure 2.31. Step behaviour of coulomb friction model [55]

In order to avoid numerical problems due to abrupt changes in the friction stress at the neutral point, Chen and Kobayashi [56] proposed an alternative form of Eqn. (2.14), substituting the step function by an arc tangent;

$$\tau_f = -\mu\sigma_n \left\{ \frac{2}{\pi} \arctan\left(\frac{|v_r|}{v_0} \right) \right\} \frac{v_r}{|v_r|} \tag{2.15}$$

where v_0 is an arbitrary constant closer to the relative velocity. Physically, the value of v_0 is the value of the relative velocity when sliding occurs. This value is important in determining how closely the mathematic model represents the step function. A very large value of relative sliding velocity constant results in a reduced value of the effective friction (Fig. 2.32). This reduction is completely hidden in the commercial program. Therefore, for friction sensitive processes this parameter must be checked [57].
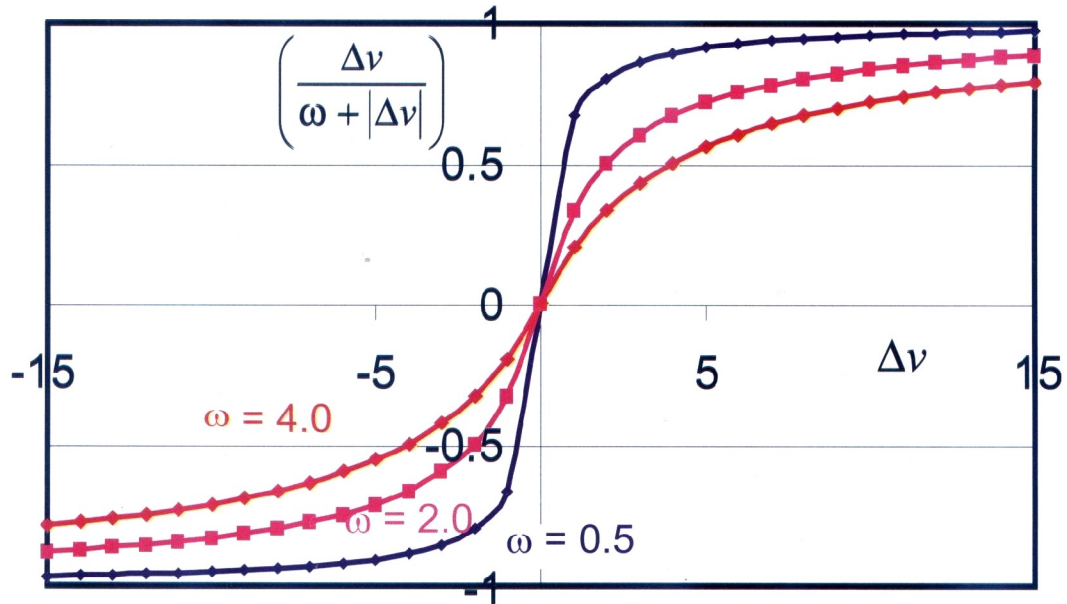
Figure 2.32. Stick slip approximation ($w = v_0$) [57]

2.3.3 Determination of Friction

In analyzing the mechanics of metal forming process a realistic friction condition must be specified in order for a theory to yield a reliable solution. Consequently, considerable effort has been spent to determining satisfactory friction condition in metal forming operations. Different types of testing methods exist to evaluate tribological properties on the contact area. Two major tests are commonly used for this purpose are the ring compression rest and the double cup extrusion test.

2.3.3.1 Ring Compression Test

Ring compression test is frequently used due to its simplicity, sensitivity to friction and unneccessity to measure load. In this test a hollow cylinder is compressed between two flat dies and as the height of the ring decreases, the inner diameter either increases or decreases depending on the friction condition at the interface. Another important parameter is the formation of the neutral point where the velocity of the

deforming material relative to the die velocity becomes zero and the friction stress changes direction (Fig. 2.33). So that for analysing this problem type friction, stress expressions given in chapter 2.3.2 are used.
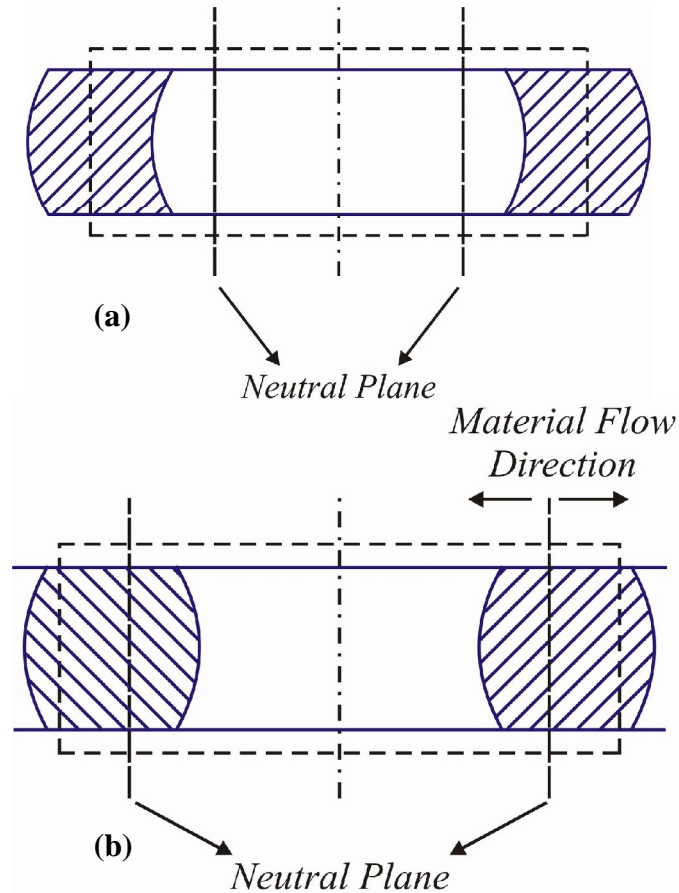
Figure 2.33. Deformation modes in ring compression **a)** Low Friction **b)** High friction

For a given percentage of height reduction, the corresponding measurement of the internal diameter change of the test specimen provides a quantitative knowledge of the magnitude of the prevailing friction coefficient. Generally, the results of theoretical analysis and experimental work are presented in the form of calibration curves, relating the percentage reduction in the internal diameter of the test specimen to its reduction in height for varying degrees of the coefficient of friction as shown in Figure 2.34.
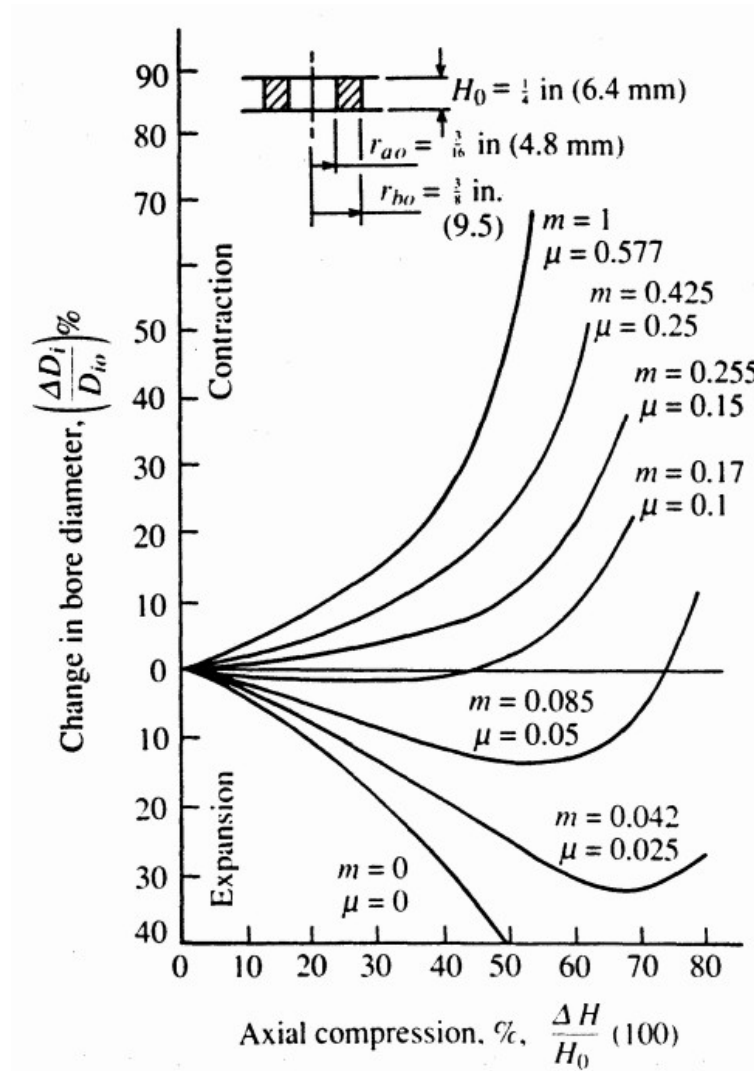
Figure 2.34. Calibration curves for the variation of inner diameter [58]

2.3.3.2 Double Cup Extrusion Test

The double cup extrusion is considered to have some advantages over ring compression test such as emulating severe deformation conditions similar to that occurring in cold forging operations and conducting the test easily and judge on the friction condition according to the differences in cup heights [59]. The ratio of cup heights h_1/h_2 after deformation is the indication of the friction between billet and tool (Fig. 2.35). Friction factor increases as the height ratio increases. If there is no friction, cup heights become equal and the ratio is equal to unity.
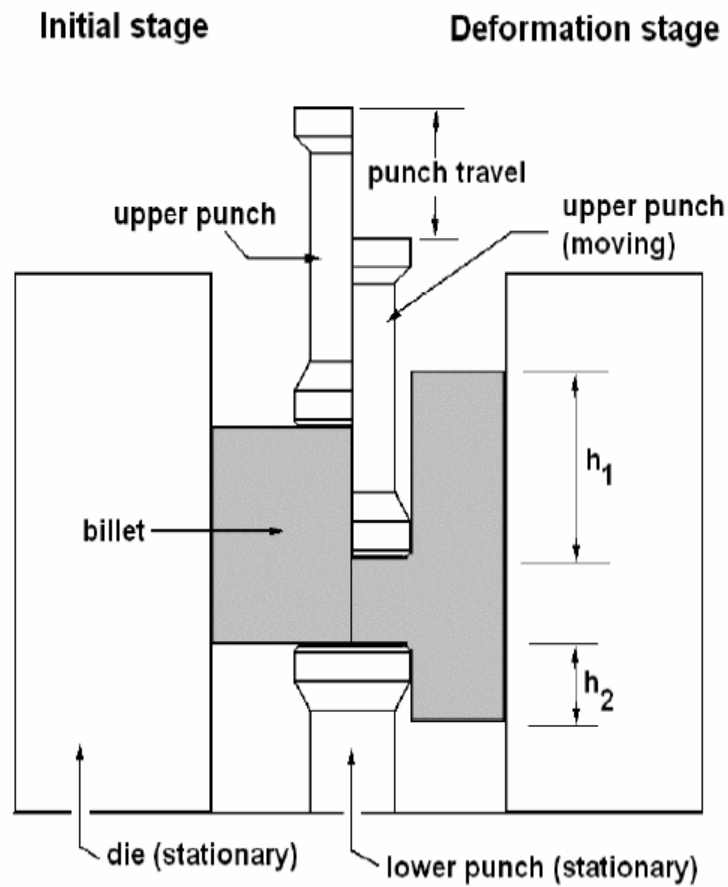
Figure 2.35. Double cup extrusion test set up [59]

2.3.4 Friction in Metal Forming

Since friction has direct influences on many process parameters in cold forging like product geometry, forging load and heat generation, it is required to use an appropriate friction model with correct friction constants in metal forming simulations. In figure 2.36 the head form of a rivet is compared with different FEM simulations in which different friction coefficients are used.
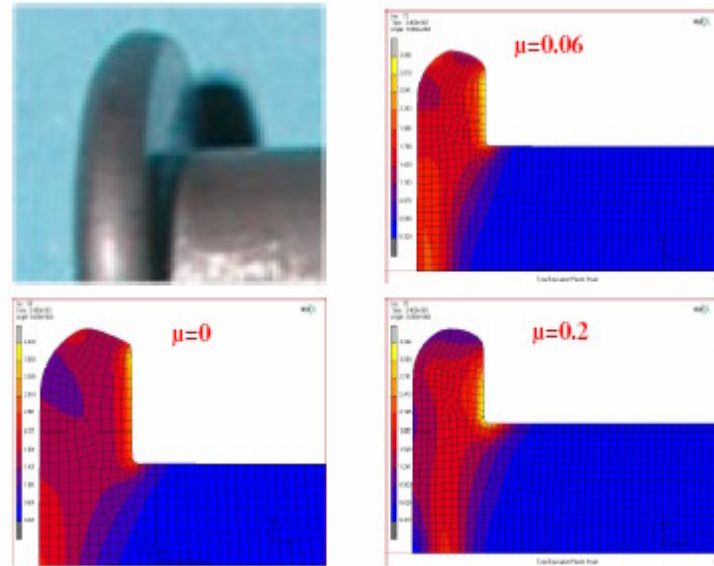
Figure 2.36. Rivet head profile compared with simulation results for different friction coefficients [60]

To obtain the most accurate numerical analysis results, new friction modeling techniques are being developed. Hayhurst et al. [61] performed computational and experimental cylinder and ring upsetting test to determine friction parameters in combined Coulomb and friction factor models (Fig. 2.37). According to the paper, after implementation of the new model in the finite element code, it gives very accurate description for open die forging of solid and hollow cylindrical test pieces. Another method is proposed by Behrens and Schaftstall [62] by included local friction parameters in FEM calculations to create realistic relation between the varying local conditions (contact pressure, sliding velocity, and temperature) and friction coefficient. Data collected from the ring upsetting, combined extrusion process and six stage bolt forming agree well with the simulation results where adaptive friction factor is used. Effect of surface roughness is integrated into the friction model by Becker et al. [63]. Surface texture of the tools is described by using sinusoidal profile and friction coefficient is calculated as a function of amplitude and wave length.

Tests conducted to investigate friction are usually performed by using hydraulic presses where material deforms at low strain rates compared to the mass production of parts in crank presses. Addition to that in real production material sliding velocity and temperature is also different from the test conditions.
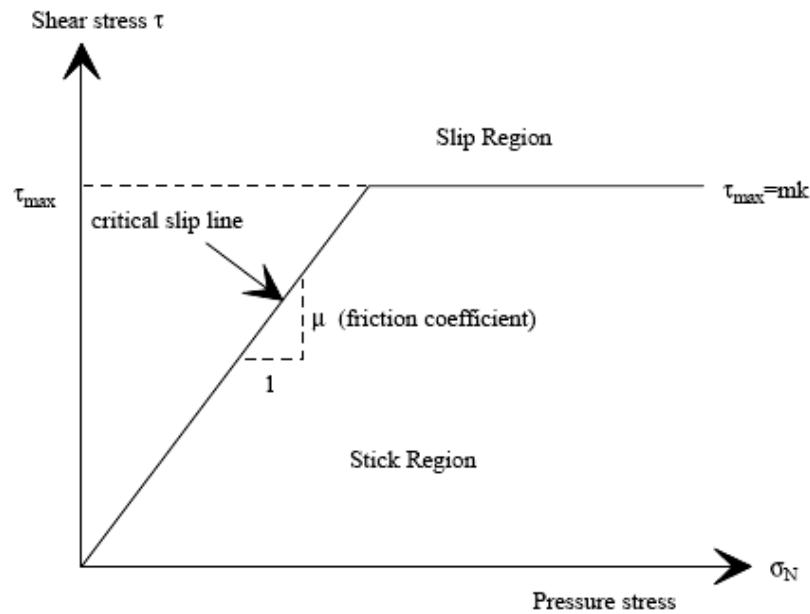
Figure 2.37. Combined friction model [63]

It is found recently that the friction coefficient is highly dependent on temperature. After reaching a certain temperature threshold, the lubricant may break down and result in a drastic increase in the frictional force [64]. To eliminate the usage of lubrication different approaches are under development. Dry forming is one of the methods which is studied by Osakada et al. [65]. To evaluate the effect of different types of coatings, ring upsetting test is performed by using carbon steel, pure aluminum and copper, at room temperature and 1100 $^{\circ}$C. Results of the experiments and computer analyses showed that diamond like carbon coating leads to low friction with aluminum. However, copper and carbon steel exhibits lower friction with uncoated tungsten carbide tool. Friction coefficient for all types of material tested by using uncoated die with mirror surface (Ra=0.02 μm) lies in the range from

0.064 − 0.102. At high temperatures where oxide layer forms on the surface of steel causes significant increase in the friction.

Another recent technique used to reduce friction is ion implantation method. In this method atoms of an element are flung on the material at very high speeds and inject 0.1 − 3 μm under the surface causing dislocation of the atoms near the surface. Yu et al. [66] claim that implantation of carbon ions on tungsten carbide significantly reduces friction in comparison with the other ion species implantation as nitrogen, oxygen and boron. In figure 2.38, pin on disk tribology test results are showing the change of friction with the dose of implanted carbon ions.
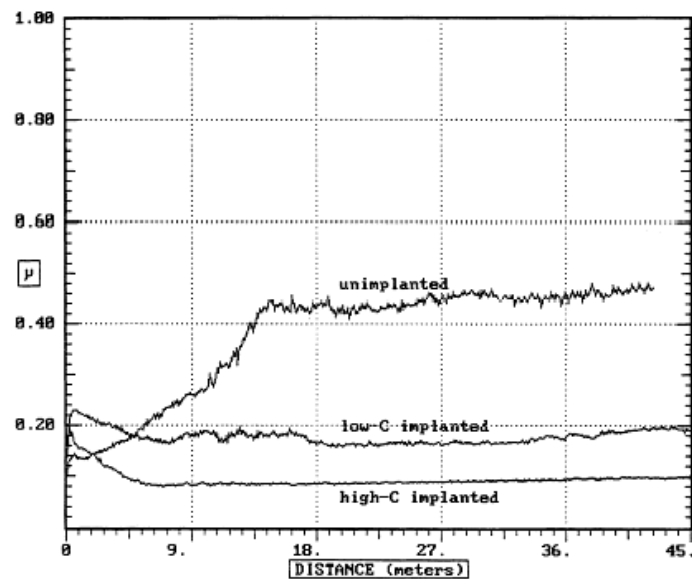
Figure 2.38. Friction coefficient as a function of sliding distance (C implanted) [66]

2.4. Conclusion of Literature Survey

According to the performed literature survey, following topics are utilized which orientate this thesis.

All bolt forming dies are prestressed and modeling of shrink fitting of dies is a prerequisite to perform die stress analyses. Role of shrink fitting is to create a

compressive circumferential stress distribution to prevent tensile stress formation under loading. Though, the amount of prestressing is not directly proportional with the interference and there is an optimum value to achieve maximum prestressing condition.

Dies mostly fail due to two different reasons; overload and fatigue. Failure due to overloading can be predicted by comparing the stress distribution with the material strength values for tension and compression. However, fatigue failure analyses and tool life prediction is more complicated due to process parameters which can not be included into numerical analyses like effect of lubrication.

By using deformable die models, stress distributions and dimensional variations can be calculated more accurately which can not be investigated by using rigid die models.

Even though there is a great number of studies about die stress analyses, most of them are limited to numerical analyses conducted for virtual cases. The ones including real failure conditions are usually not presenting the verification of the design improvements which are done to prevent failure.

Many studies are still performed to determine the most appropriate friction model for cold forging by comparing experimental data with numerical analysis results. There are many different test methods which are widely used in this field like ring compression, forward rod extrusion and backward can extrusion.

While performing numerical analyses, mostly rigid models are used to represent dies. Since the stresses are affected by the elastic properties of dies, there might be errors in the friction stress and force calculations while determining the friction value. So the effects of rigid and deformable die models on the friction analyses must be clearly defined.

CHAPTER 3

PRODUCTION OF BOLT FORMING DIES

3.1 Introduction

Bolts are manufactured in multistage-part-formers by deforming the workpiece in consecutive stations. Depending on the type of press, numbers of stations vary between two and seven. These machines are driven by an electric motor which is connected to main shaft by using clutches. Included crank-rod mechanism is connected to the slide and converts the rotational motion into linear motion. For
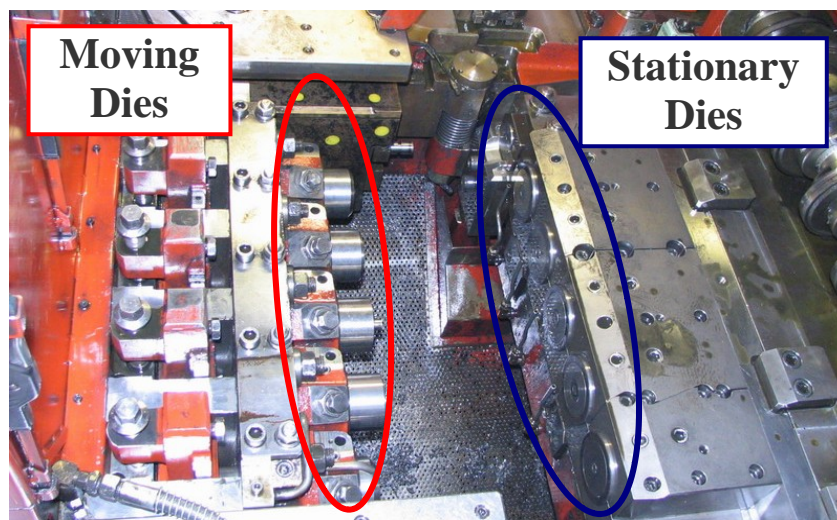
Figure 3.1. Tool layout of five station bolt former

each forming station there is a pair of dies mounted on stationary and moving block (slide) respectively. In Figure 3.1, the tool layout of a five station bolt forming press is shown.

Generally on the moving block, trimming dies, preform, open-close die extrusion or heading punches are mounted and on the stationary block, split prestressed carbide dies are mounted by using steel cases.

3.2 Properties of Bolt Forming Dies

Instead of producing the dies as a single piece, split dies are preferred in bolt production. This method has three important advantages. One of them is the ease of manufacturing of the split dies. The extrusion dies for long parts can be taken as an example for this situation. For instance, to extrude a cylindrical workpiece which is 10 mm in diameter and 60 mm in length, die length should be at least 70 mm in order to allow entrance of punch into the die before starting deformation. The tool which is to be used for machining this die must be longer than the distance between die surface and die shoulder. For the case given above required tool length is approximately 80 mm to be able to machine the die shoulder. Tool deflection during cutting is one of the reasons causing dimensional variation. For such a long grinding tool, deflection due to exerted cutting forces is inevitable. Thus, splitting long dies into shorter parts and machining separately will facilitate production of dies more precisely.

Secondly, stress concentration locations can be removed by splitting the dies at the sharp corners. Longer tool life can be achieved when this manufacturing method is applied. Benefit of this method is frequently confronted during the production of bolts with stepped shaft geometry. If the die is produced as one piece, failures will be observed at the locations shown in Figure 3.2a with circles. To avoid this problem the die should be split as shown in Figure 3.2b.

Another advantage arises when the replacement of a die is required in case of a failure. If it is produced as one piece, whole die will be scraped even the failure occurs at a local area. However, for the split dies, only the renewal of the broken part is sufficient whilst the other parts can be used for further operations. This leads to both saving material and cost.
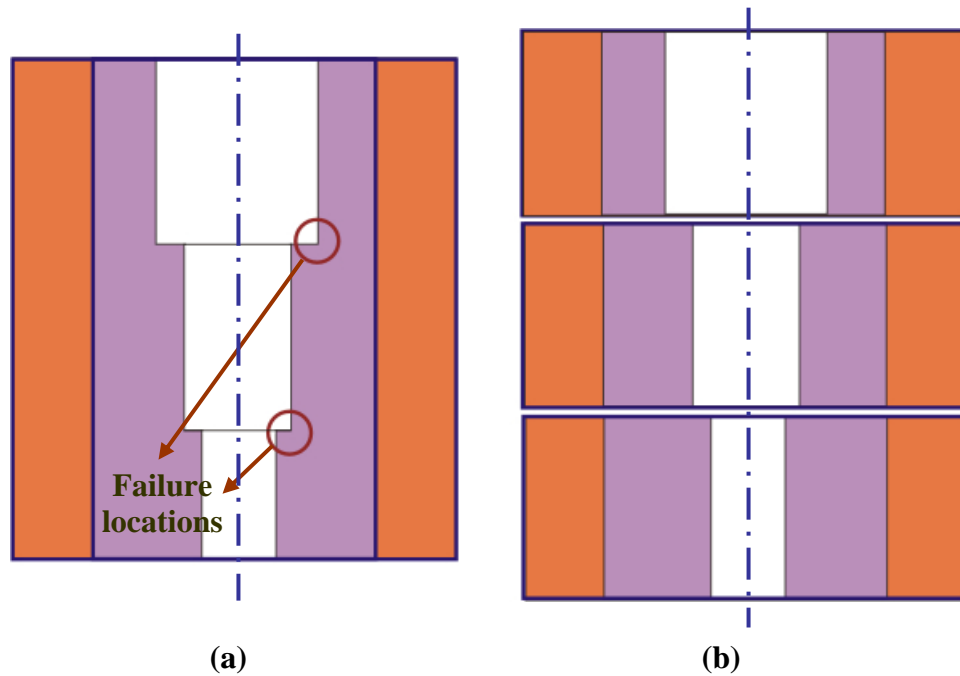
Figure 3.2. Stepped shaft die **a)** Single piece die **b)** Split die

Finally, adaptation of split dies are easier for the parts having similar dimensions; i.e. same metric size hexagonal bolt in different lengths. This type of bolt is generally forged in three steps; forging head preform, heading with pointing and trimming. In the second stage, according to the length of the bolt, two or three split dies can be used to form the shaft where the bottom die performs the pointing. When a shorter bolt is desired to be produced, one of the dies above the pointing die can be replaced by another die with proper length. Such an approach decreases the number of dies used for producing different parts and also reduce the adjustment time during production.

Despite the advantages of using the dies as split, manufacturing them requires being fastidiousness. Especially the dimensional consistency of the bore diameter has great importance. If the dimensional difference between the bore diameters of the consecutive dies exceed a precise amount, material flow will be effected in an undesired way. One of the problems that may arise is scratches on the surface of the shaft during forging or ejection because of the notch formed at the interference of adjacent dies. Another problem caused due to presence of the notch is chip breaking from the workpiece. These chips will start to accumulate between the dies and cause them move apart from each other. After a number of cycles, this situation will yield to totally damaged products.

The separation of dies can also happen due to forces acting on dies. Especially during the extrusion, workpiece exerts axial forces on the die shoulder which may lead to move the die apart from the adjacent die. In such a case same problems will be faced as described above. To eliminate this problem axial compression is needed to apply on the split dies. Screwed cases are being used for this purpose where the back side of the case is closed tightly by using a nut. This creates an axial prestressing on the dies and keeps them in contact under axial loading.

3.3 Tungsten Carbide Inserts

Die inserts are made of tungsten carbide (WC) which are produced by using powder metallurgy techniques. It has a number of unique and impressive characteristics where the most significant ability is to resist abrasion. When its mechanical properties are compared with steel, its compressive strength is also greater than any other metal or alloy. Abrasion resistance is up to 100 times higher and thermal expansion is less than one-half that of steel. Moreover, tungsten carbide resists thermal shock and oxidation up to 650°C. Also carbide compositions have exceptional resistance to galling and welding at the surface. Since carbides are nearly chemically inert, they ideally suit for wear applications in corrosive environments.

Since the bolt production is made at high speeds like one part per second, impact acting on dies makes role of toughness of the carbide insert an important factor. Although carbide materials present a brittle behavior, toughness can be increased by increasing the cobalt binder content [67]. On the other hand, the wear resistance of WC-Co is proportional to its hardness and, hence, inversely proportional to the fracture toughness (Fig. 3.3).
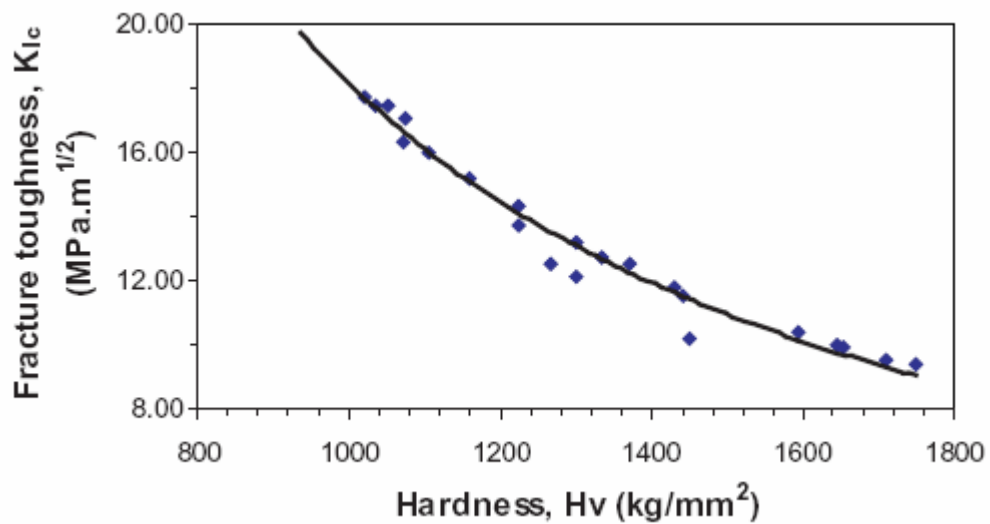
Figure 3.3. Relationship between the hardness and fracture toughness of WC [67]

In some metal forming operations like heading high impact loading is induced on the tools and material is expected to have adequate toughness to prevent fracture. For the backward and forwards extrusion processes, tools are desired to be hard enough to resist wear as the material slides over. Tungsten carbide including less cobalt is preferred for these operations but die material should also have high level of toughness since it will be exposed to impact loading under high forming speeds. In the applications where there exist almost no impact loading and high material flow rates as it is the case in wire drawing, dies with very high hardness is demanded. Thus, carbide inserts with low cobalt content are used for those operations. Production techniques and details of mechanical properties of cemented carbides are explained in Appendix A in detail.

Carbide inserts are supplied from the manufacturer as semi-finished parts in different outer – bore diameters and lengths as shown in Figure 3.4. This semi-finish form prevents time waste during machining the part to the desired dimensions.

Figure 3.4. Tungsten carbide inserts

In the manufacture of high-precision carbide tools, the required precision is obtained by subsequent finishing processes which are grinding, spark erosion and polishing. For grinding, diamond or Cubic Boron Nitride (CBN) grinding stones are used.

Machining must be performed at high speeds and low feed rates to obtain low surface roughness and provide dimensional precision. Chips formed during grinding must be removed from the machining area immediately. Otherwise they will continuously pass between the rotating tool tip and die which leads to damage on surface. Also these carbide chips are harmful to the operator since the sizes are in the range of a few microns and can be transfered to the lungs during inhale. Vacuum units placed near the grinding machines will provide adequate protection.

Grinding tools in different tip forms are being used during machining the carbide dies. Cylindrical tools are preferred for straight holes whereas spherical or conical tools are used to cut die shoulder profiles of extrusion and drawing dies. In some special cases where machining the outer surface of the die is required, tools with wide flat faces are used.

Carbide insert should be mounted on the chuck of the grinding machine coaxially. If the adjustment is not performed correctly, dimensional variations will occur on the forged part. To prevent such situations, axis comparators are used to mount the part which is to be machined.

Machining methods and tools explained above are used to produce dies which are generally being used to forge axisymmetrical parts. However there are many types of bolts in three dimensional shapes like square shaft, hexagonal or non uniform head shapes. For these types of products, manufacturing the punches and dies by only using grinding machines will take excessive time. These processes can be speeded up by using wire electric discharge machining (Wire EDM).

Wire EDM uses an electrically charged thin brass wire, which is moved by a computer control system, close, but not touching the part which is to be cut. This gives wire EDM the ability to be programmed to cut very intricate shapes delicately. Wire and the workpiece are either fully submerged or exposed to vigorously flushed dielectric liquid. The small gap between the wire and part $(0.1 - 0.5$ mm) creates a spark, which vaporizes small particles from the workpiece as the wire advances. The
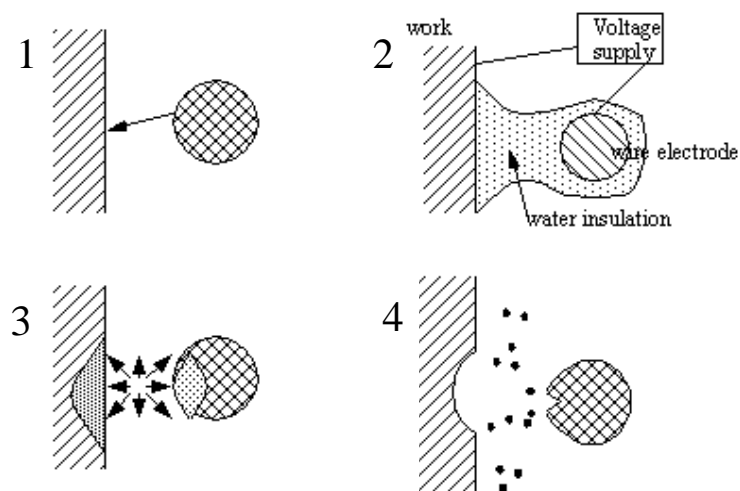
Figure 3.5. Mechanism of Wire EDM

disintegrated particles are flushed away by dielectric fluid and the wire is able to advance further. The wire itself is traveling from a large spool to a spent wire bin after used as an electrode. Mechanism of machining by using wire EDM is represented schematically in Figure 3.5.

Surface quality of the parts cut by wire EDM is not satisfactory. Thus secondary machining processes in the grinding machines are required before using in the production.

Some sorts of bolts are having knurls formed under the head. Operational advantage of these knurls is preventing loosening of the bolts after assembly. To create knurls on the part, opposite geometry must be formed on the heading dies and this is performed by using die sinking electrical discharge machining (Die sinking EDM). The mechanism of die sinking EDM is similar to wire EDM in means of removal of

Figure 3.6. EDM of forming die

material by creating sparks. However, in the die sinking EDM, a graphite, copper or tungsten electrode is machined into the desired shape and fed into the workpiece at the end of a vertical ram. Adjacent strokes of the electrode, shapes the die till the geometry of the electrode form on it (Fig. 3.6).

During both EDM operations, each spark produces a temperature between 8000 and 12000 °C. Even though the dielectric fluid flowing over the machined part acts as a coolant and prevents temperature rise in the part, especially for steel tools, a thin layer below the surface is affected from the spark temperature and is locally heat treated.

This is a kind of quenching process and material shows a brittle behaviour on the surface. Also micro cracks propagate faster under forming loads and cause early tool failure. Tempering the steel parts reduces the effect of quenching on the surface and improves the toughness. For carbide tools, such a predicament is not in question on the account of retaining same crystal structure at elevated temperatures. Thus, any heat treatment effect is not observed on electro discharge machined tungsten carbide die inserts.

3.4 Tool Steels

Die inserts made from tungsten carbide are only one part of the whole assembly of split dies. To perform cold forming and plastically form the workpiece, several components are required according to the operation that will be performed. These parts are mainly manufactured by using tool steels and selection of suitable material is done by analysing the function of the part in the process, exposed thermal and mechanical loads. Tool steels have been classified into several types as illustrated in Table 3.1. Various types are further subdivided according to a letter code followed by a number, as shown in the second column of this table.

Table 3.1. Classification of some tool steels showing weight % composition [68]

Type	AISI	DIN	C	Mn	Si	Cr	V	W	Mo
Carbon (Water Hardening)	W1	1.1545	1.0	0.25	0.25	-	-	-	
Low Alloy	L6	1.2713	0.7	0.5	0.25	0.9	-	-	0.3
Shock Resisting	S2	1.2550	0.47	0.40	1.05	-	0.22	-	0.45
Die Steels for Cold Working	O2	1.2842	0.9	1.6	0.25	0.22	1.8	-	0.3
	A2	1.2363	1	0.62	0.25	5.1	0.32	-	1.2
	D2	1.2379	1.5	0.3	0.25	12	0.6	-	0.95
Die Steels for Hot Working	H13	1.2344	0.39	0.35	1	5.1	1	-	1.4
	H21	1.2581	0.35	0.30	0.3	3.5	0.5	9	-
High Speed Steels	M2	1.3343	0.83	0.27	0.32	4.1	2	6.1	5
	T1	1.3355	0.78	0.25	0.30	4.1	1.1	18.2	0.7
	T15	1.3202	1.55	0.27	0.27	4.4	4.9	12.4	0.5

Carbides present in tool steels play a dominant role in the control of the mechanical properties desired in a tool steel. Major properties of the steels are considered to be wear resistance, toughness and hot hardness. In general, one may rationalize the main reason for high values of these properties as follows:

High wear resistance: More carbide
High toughness: Low %C in the steel
High hot hardness: More alloy carbides

AISI designations for the steel grades are summarized as follows [69];

W Steels: The W stands for water hardening. These steels are similar to the plain carbon 1095 steel and have very low hardenability. The toughness of the steel is improved significantly if the steel is shallow hardened which refers to steels having low hardenability, and requiring faster quench speeds.

L Steels: The L stands for low alloy, and these steels have compositions similar to the AISI alloy steels.

S Steels: The S stands for shock resisting. The high toughness needed for shock load resistance is obtained by reducing the %C in these steel to low levels, which also results in the low wear resistance and hot hardness.

O Steels: The O stand for oil hardening. The key alloying elements for the various for the O steels Mn and V are mainly responsible for its improved hardenability over the W steels allowing them to generally be oil quenched.

A Steels: The A stands for air hardening. Hardenability of these steels is improved to the point that they may be air hardened. The key element additions allowing hardenability improvement are Cr and Mo.

D Steels: These steels are called high carbon, high chromium steels and the D symbol is usually correlated with the term direct hardening. The steels may be air hardened. Combination of high carbon and high alloy content results in excellent wear resistance, moderately good hot hardness, but poor toughness.

H Steels: The H stands for hot hardness. These are usually the steels of choice for the die steels of extrusion operations that are done hot. Here, the combination of low carbon and moderate to high alloy content gives good toughness and hot hardness but only fair wear resistance.

M and T Steels: The M and T stands for the molybdenum and tungsten additions in these high speed tool steels. The carbides of these two elements are stable to quite high temperatures. Therefore, the high level of these alloying elements produces large carbide volume fractions which give good wear resistance and hot hardness, but poor toughness.

Raw materials used for the production of steel are iron ore lumps, sinters, coke (made from cooking coal) and fluxes such as limestone.

The main steps in steel manufacturing process are as follows;

Melting: Raw materials are charged in a blast furnace where hot air is pumped to melt iron and fluxes at 1600°C. The molten metal when cooled and solidified is called pig iron.

Refining: Molten metal from the blast furnace is taken to steel melting shop where further reduction of impurities is done in oxygen furnace. The crude steel in liquid form is taken in a ladle for further refining/ addition of ferro alloys, silicon, manganese, chromium, molybdenum etc.

Casting: The liquid steel is cast into semi-finished products such as billets, blooms, slabs called continuous casting

Rolling: These semi products are heated at 1200°C to make metal malleable and then rolled into finished products. There are different rolling mills for different products. Wire rods can be drawn to make wires.

Steels used for tool production are generally received in form of rolled rods in different lengths and diameters (Fig. 3.7).
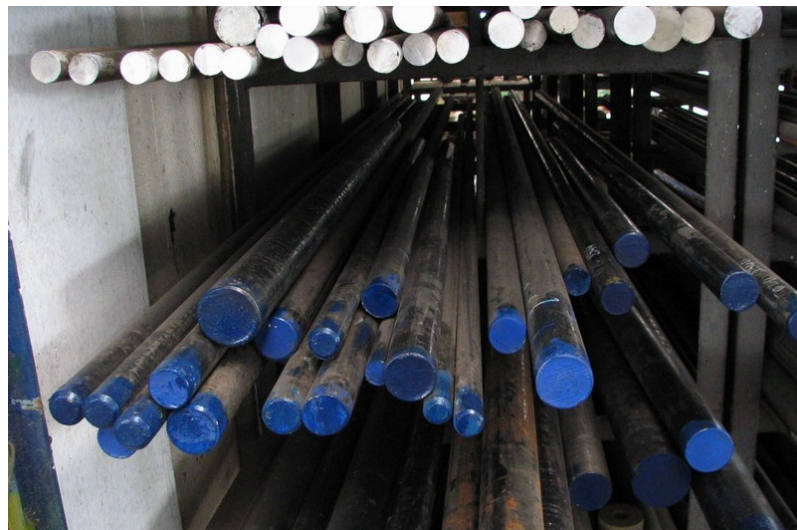
Figure 3.7. Rolled steel rods

According to the length of produced tool component, billets are cut off by using saws, water jets or plasma cutters. Machining of steel parts is generally performed by using lathes and milling machines. For precise machining, computer numerical control (CNC) machines must be preferred. In addition, selections of cutting tool and machining parameters have a significant role to obtain good surface quality and achieve dimensional accuracy.

Initially, parts are subject to rough machining till part dimensions get close to design dimensions (Fig. 3.8). Final machining is performed after heat treatment owing to the dimensional change occurred during the heating and cooling.

Some steel parts, as it is the case for carbide inserts having non uniform profiles, can not be manufactured by using cutting tools. Similar to production of knurl dies, EDM methods are essential to shape these parts. Main usage area of this method is writing the bolt strength grade and manufacturers trademark symbol on the heading punches. First, the letters are embossed on the copper electrodes by
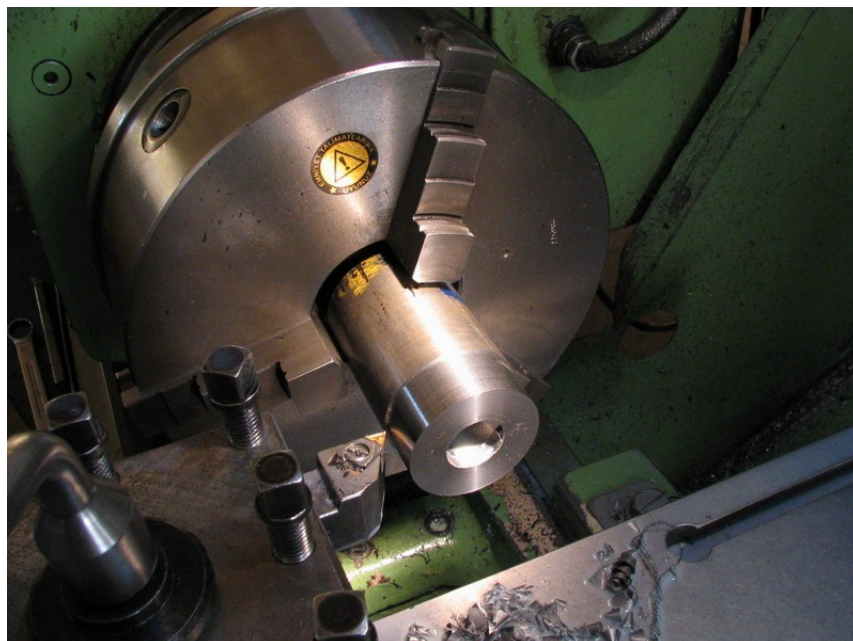
Figure 3.8. Rough machining of steel rods

hammering the letters and then by using EDM, letters are formed on the heading punch (Fig. 3.9). During the cold forming process these letters deforms the material and marking is done on the head of the bolt.

Figure 3.9. Copper marking electrodes *(Left),* Heading punches *(right)*

Different from the carbide inserts, electric discharge machined steel parts have to be tempered. Otherwise, die cracking will be observed around the letters which will cause distortions on the forged product.

3.5 Heat Treatment of Steels

Heat treatment is combination of heating and cooling operations applied to a metal or alloy in the solid state to obtain desired mechanical properties. The crystal structure of steels at room temperature is consisting of ferrite and perlite where perlite is a combined structure of ferrite and cementide. When the steel alloy heated up a certain temperature, at least 727 ^{o}C, depending on the carbon content, crystal structure shifts to a new phase called austenite which is a body centered cubic structure. If the material cooled down to room temperature at high rates, for instance by using oil or water, distorted atoms forms a new crystal type called martensite,

which provides high hardness but very low toughness which may lead material become so brittle that even it can fractures at small deformations. To improve the toughness and ductility of the steel, a secondary heating operation is required called tempering. The object of tempering is to reduce the brittleness in hardened steel and to remove the internal strains caused by the sudden cooling in the quenching bath. The tempering process consists in heating the steel between $300 - 750$ $^{\circ}$C and then cooling it. Figure 3.10 is showing how material mechanical properties are influenced by these heat treatment operations.
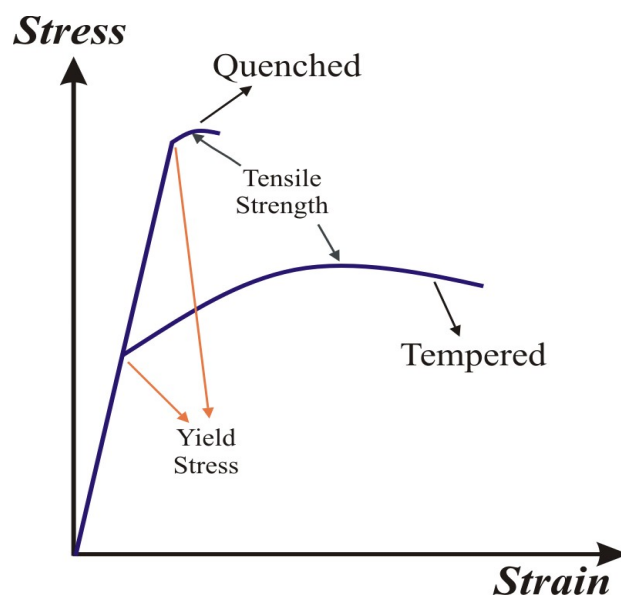
Figure 3.10. Effect of quenching and tempering on stress - strain relationship

The heat treatment of tool steels involves many subtle effects that are not present in heat treating low alloy and plain carbon steels. As the alloying content of the tool steel increases, a well developed secondary hardening peak is formed, which has its maximum hardness for the high speed tool steels. It is possible to characterize the different types of tool steels by the shapes of their hardness versus tempering temperature curves. Figure 3.11 presents the generalized curves for the tool steel types listed in Table 3.1. Also in Table 3.2 secondary peak temperatures and maximum hardness values are shown for major tool steels.
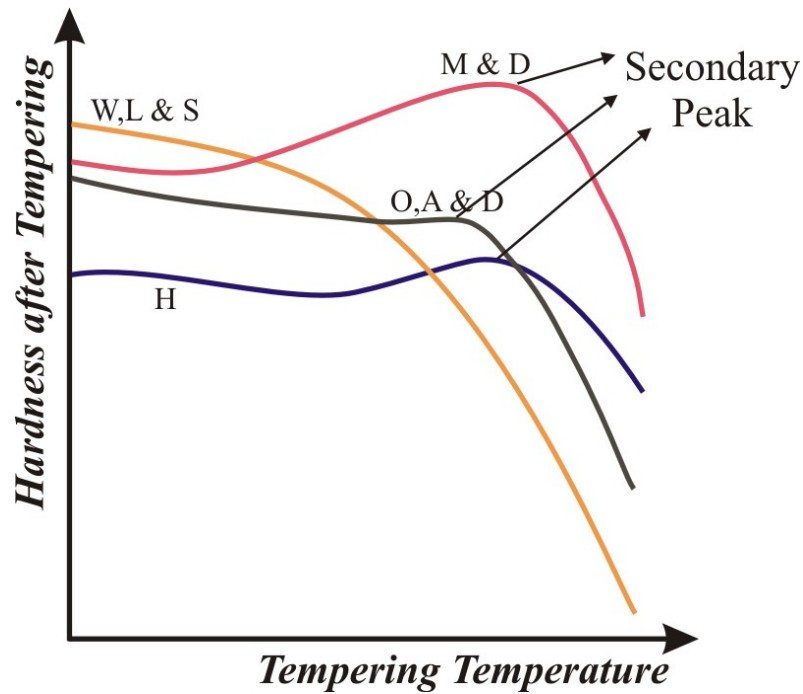
Figure 3.11. Hardness vs. tempering temperature of the various types of tool steels [69]

Table 3.2. Secondary hardness peak temperatures during tempering [69]

Type	AISI	DIN	Secondary Peak	
			Max. Hardness (HRC)	**Temp. of max. Hardness (^{o}C)**
Carbon (Water Hardening)	W1	1.1545	none	none
Low Alloy	L6	1.2713	none	none
Shock Resisting	S2	1.2550	none	none
Die Steels for Cold Working	O2	1.2842	57	260
	A2	1.2363	57	454
	D2	1.2379	58-59	482
Die Steels for Hot Working	H13	1.2344	52-54	524
	H21	1.2581	52-56	532
High Speed Steels	M2	1.3343	64-66	543
	T1	1.3355	65-67	527
	T15	1.3202	67	543

One of the most cardinal steel components in the tool assembly is the prestressing ring which is shrink fit on the carbide insert. Heat treatment of these rings has a key role on the tool life, since the yield stress determines the maximum applicable prestressing on carbide insert. H13 which is a hot working steel whic is widely preferred for prestressing application of carbide inserts. In Figure 3.12 tempering curve is shown for this material which is taken from the steel supplier Uddeholm Tooling AB. As it can be seen from the graph, retain austenite formation occurs between the temperatures 425 – 550 $^{\circ}$C which reduces the toughness of the material. To overcome this problem double or triple tempering must be done.

If the heat treatment is performed by using standard furnaces without any sensitive temperature control, a variable hardness distribution on the steel ring will be unavoidable.
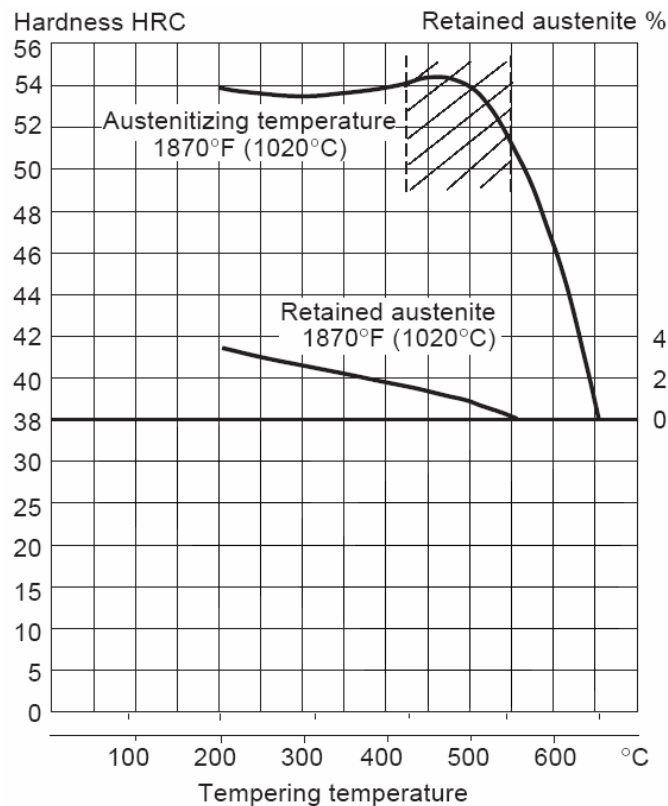
Figure 3.12. Tempering diagram of H13 hot work steel

However by using the new generation furnaces having atmosphere control called vacuum furnaces, possibility of decarburizing and oxidation on the steel is prevented and also uniform temperature distribution is achieved on the part during heating and cooling. In Figure 3.13 oxidation on the steel ring after heat treatment made in a conventional furnace is shown.
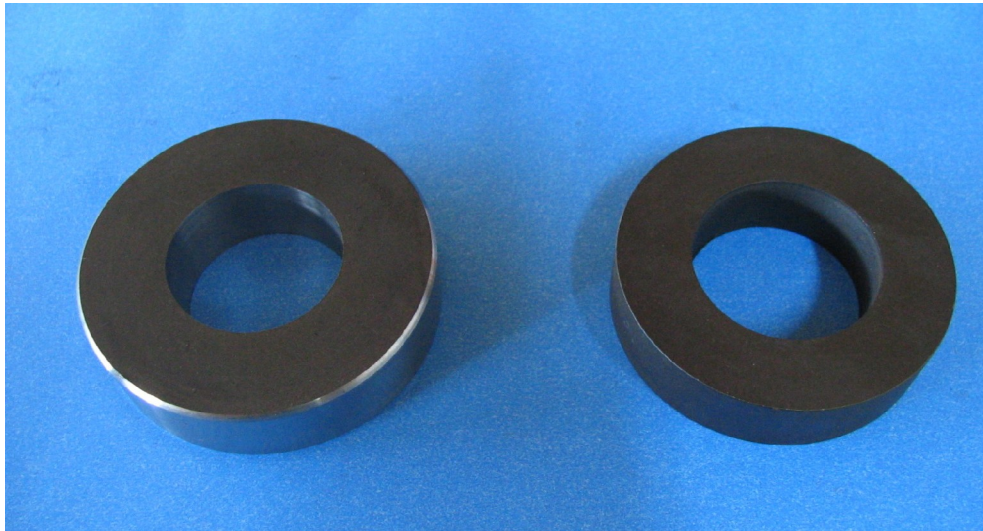
Figure 3.13. H13 Steel rings: raw *(left),* Heat treated *(right)*

3.6 Insert – Ring Assembly

Since prestressing is desired on the carbide insert, there exist dimensional difference between the outer diameter of the insert and inner diameter of the ring prior to the assembly. Two conventional methods are used to assemble these two interfering components. First method is using external pressure on the insert to slide into the ring at room temperature. To perform this operation, insert has to be conical with an angle of approximately 0.5^{o} or chamfered to provide uniform contact while press fitting. To prevent galling due to high contact stresses and friction, solid lubricants are used.

Another method is heating the ring and making it expand enough to place on the insert. This method is generally used when the insert outer dimensions are uniform. As the ring cools down, it shrinks and applies circumferential compression on the insert. By using this method, possibility of damage on the surface of the parts has also been prevented.

There exist two important points while performing the shrink fitting of two parts by using heating – cooling method. Firstly, the maximum heating temperature of the steel ring should not exceed recrystalization or tempering temperature. Otherwise, hardness of the steel will reduce and will result in decrease in the yield stress of the ring. This situation will yield to unexpected plastification of the ring during assembly and early tool failure. To eliminate this problem, temperature controlled furnaces should be used as shown in Figure 3.14. In these devices, according to the prestressed temperature, a closed loop control system continuously measures the inside temperature by using thermo couples and stabilize the temperature by using thermostat mechanism.

Figure 3.14. Temperature controlled furnace

Second important point is the determination of interference by considering the expansion of the inner diameter at the heating temperature. In case of presence of excess interference, heated ring will not be able to be placed on the die insert and damage the parts because of improper contact during cooling. Therefore, design parameters should be checked properly for assembly. The allowable interference can be calculated by using the formula given in Eqn. 3.1 where ΔL, L_0, α and ΔT represents, change in length, initial length, coefficient of thermal expansion and temperature change respectively.

$$\frac{\Delta L}{L_0} = \alpha \cdot \Delta T \tag{3.1}$$

The term on the left side of the Eqn. 3.1 is equal to the total strain in all directions of a part after heating. Expansion of the bore diameter of a cylinder can be found by calculating change of the circumference after heating. Initial circumference can be calculated as;

$$L_0 = 2 \cdot \pi \cdot r \tag{3.2}$$

If the radial expansion is taken as u then circumference of the bore after heating can be calculated as follows;

$$L_f = 2 \cdot \pi \cdot (r + u) \tag{3.3}$$

Change in the circumference of the bore becomes;

$$\Delta L = L_f - L_0 = 2 \cdot \pi \cdot u \tag{3.4}$$

Radial expansion is calculated by putting Eqn. 3.2 and 3.4 into Eqn. 3.1.

$$u = r \cdot \alpha \cdot \Delta T \tag{3.5}$$

Although coefficient of thermal expansion varies with the temperature, this formula gives adequate results to calculate bore diameter expansion. An sample assembled die is shown in Figure 3.15.

Figure 3.15. Assembled bolt forming die

3.7 Final Machining

After the assembly of insert and ring either by using press fitting or heating – cooling method, internal diameter of the insert and outer diameter of ring shrinks and expands respectively due to interference pressure exerted on the parts. Amount of shrinkage on the insert can lead dimensions to go beyond the design tolerances. To overcome this problem, assembled dies are final machined.

3.8 Honing and Polishing

Honing is a finishing operation conducted on a surface, typically inside of an cylinder, as the dies used in bolt forming. However it is a surface finish operation instead of being a gross geometry modifying operation. Hones can be in different

types like pedal or brush. Either type applies a slight, uniform pressure to a light abrasive that wipes over the entire surface. However there are some geometry limitations for honing. Blind or stepped holes like extrusion dies are not suitable and there will be always an unhoned portion at the bottom of the die. For this purpose pats having through hole are always more effective to hone.

However, even machining operation is performed at very high speeds and low feed rates, there will still be a texture on the machined surface inside the die which increases friction, heat generation and surface roughness of the forged part. To improve surface texture, polishing is applied on the die bores by using special brushes and pastes. This operation regarded as the most important step of whole die production system which has a direct influence on the tool performance and life. In many tool making companies, the most experienced workers are dedicated to this operation. In some cases, depending on the size and geometry of the die, polishing can take even one work day.

3.9 Tool Coatings

To improve wear resistance of the forming dies, different types of hard coatings are applied. Physical vapor deposition (PVD) and chemical vapor deposition (CVD) are two most common types of thin-film hard coating methods. Based on their high hardness, the most effective coating systems are nitrides, borides and carbides of elements like Ti, Cr, W, Zr.

PVD, is a term used to describe a thin-film coating processes which are applied under vacuum conditions. These processes involve the generation of positively charged ions of various metals. The parts to be coated are given a negative charge in order to attract the positively charged ions. The result is a very strong mechanical bond between the coating and the tool. PVD coatings such as titanium nitride (TiN), titanium carbonitride (TiCN), chromium nitride (CrN), and aluminum titanium nitride (AlTiN) work well for many applications.

CVD is a thin-film coating with a diffusion type bond that results from the reaction between various gaseous phases and the heated surface of a part. The final product is a hard, wear-resistant coating with an extremely strong bond. CVD is sometimes referred to as a "hot coating" because the process approaches temperatures around 1000°C. For this reason, for bolt forming dies, this type of coating is mostly not preferred.

The micrographs given in Figure 3.16 provide a clear illustration of the thickness ratio of the different coatings. The PVD coating lies between 3 and 5 microns, while the CVD coating is in the range of $5 - 20$ microns. While the individual layers are still clearly visible in the CVD coating, the up to 2,000 individual wafer-thin layers of the PVD coating cannot be optically resolved.
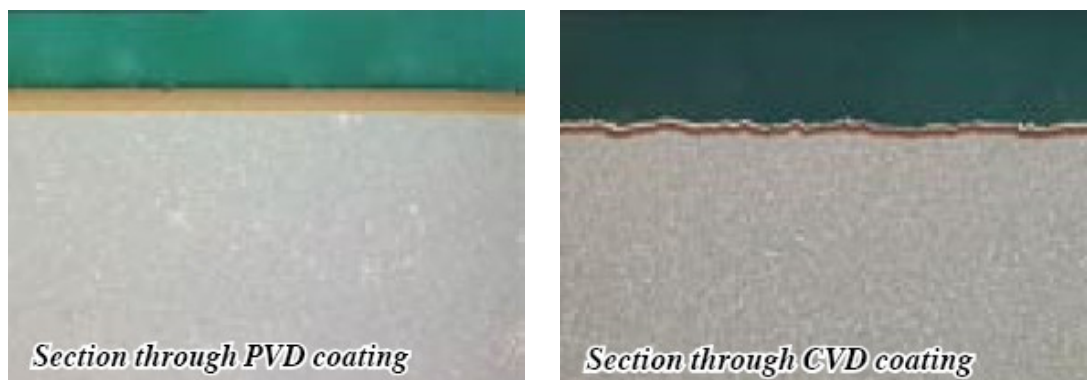
Figure 3.16. PVD and CVD coated sections [70]

CHAPTER 4

MODELLING AND STRESS ANALYSIS OF PRESTRESSED FORMING DIES

4.1 Introduction

In all bolt forming operations like wire drawing, open and close die extrusion, upsetting, heading, etc. prestressed carbide tools are used (Fig. 4.1). Therefore, modeling of prestressing is a prior task for all analysis that will be performed to investigate die stress distribution before and during forging.
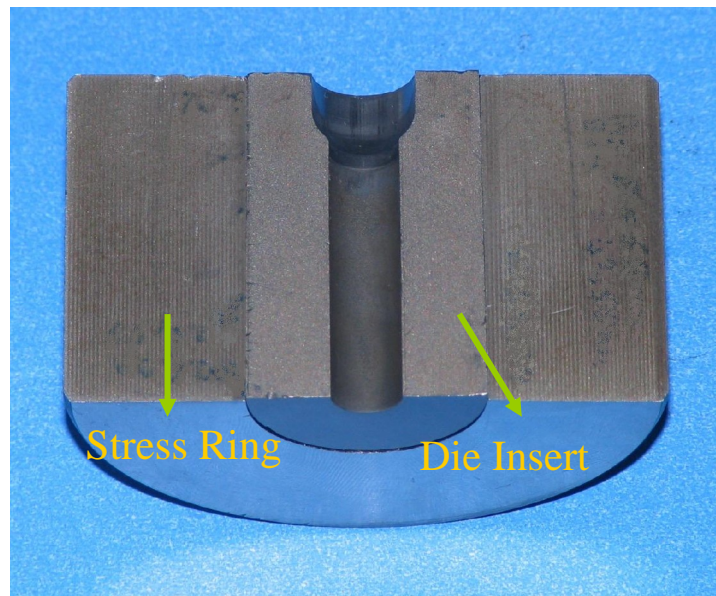
Figure 4.1. Prestressed extrusion die

As it is described in Chapter 3, two different methods are present to assembly die insert and stress ring, which are heating – cooling of ring and press fitting of die insert into the ring. To model prestressing, first heating – cooling method is considered. Secondly, this operation is investigated by using the special contact algorithm of the commercial finite element software program MSC.Superform to solve initial interference between the insert and ring which represents the shrink fit.

Before starting to model prestressing, first, material properties of stress ring is determined by conducting tensile tests. Next, to create correct heating and cooling condition, tests are performed to determine the convection coefficient between the part and environment. After that by using two different methods, shrink fitting process is modeled, analysed and results are examined. Afterwards, these results are compared with results of analytical formulas and experiments.

In the following step, optimization of prestressing is investigated to determine the most appropriate insert diameter and interference for a specific die bore and outer diameters. After completion the modeling of radial prestressing, effects of axial prestressing is examined by dealing a sample split die assembly.

After implementation of deformable dies into the cold forging simulations, differences between the result of analyses performed by rigid and deformable dies are evaluated.

Finally, four case studies are presented in which die stresses are analysed and design modifications are performed to prevent die failure.

4.2 Stress ring material properties

As the assembly of the bolt forming die is explained in Section 3.6, stress ring is heated up to a certain temperature to make it expand and place the die insert inside it. To model this assembly process, all the material and process parameters must be defined correctly for die components which are;

79

- ➢ Young's Modulus
- ➢ Poison's Ratio
- ➢ Yield Stress
- ➢ Mass Density
- ➢ Conductivity
- ➢ Specific Heat
- ➢ Coefficient of Convection (Heating and cooling)
- ➢ Environment Temperature (Heating and cooling)

All the material properties except the yield stress of stress ring are obtained directly from the material suppliers. Since the rings are heat treated before assembly, different yield stresses are obtained for different heat treatment conditions. Although approximate yield stresses can be found in the literature, it is compulsory to perform tests for different hardness values to obtain reliable data.

Initiation of plastic deformation on the ring has a significant effect on prestressing and this is related with the yield stress of the material. So that, tensile tests have been performed to determine this material property in order to predict plastification in the analyses correctly. Test specimens are produced with the dimensions given in Figure 4.2 from the raw material H13 (1.2344).
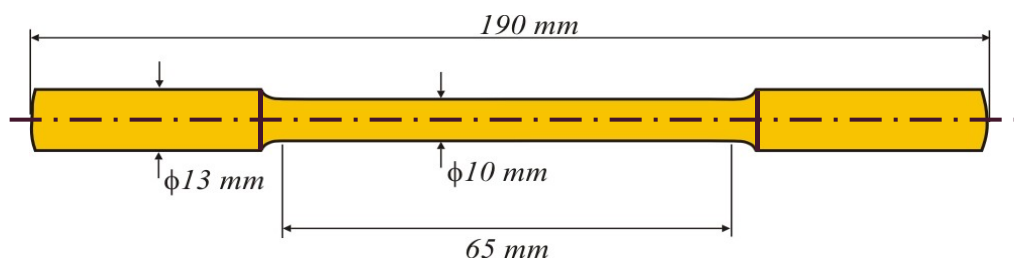
Figure 4.2. Dimensions of tensile test specimens

One of the specimens is heat treated with the same method explained in Section 3.5 as the other one kept as raw (Figure 4.3). Specimens are tested by using a 40 tons

hydraulic tensile test machine. Since the displacement sensor is mounted on top of the machine, Young's Modulus values could not be measured accurately and compared with the supplier data (Fig. 4.4).

(a)

(b)

Figure 4.3. Test specimens **a)** Specimen 1 (As supplied) **b)** Specimen 2 (Heat Treated)

Figure 4.4. 40 tons tensile test machine *(left)*, Displacement sensor *(right)*

Data acquisition system of the test machine collects the data and plot on the computer screen. Embedded software program is used to calculate force-displacement data, yield stress, rupture stress and total elongation. Test results show that, when hardness of the stress ring is around 42 HRc, yield stress is measured approximately 1200 MPa. In Table 4.1 results are given for both raw and heat treatment specimens.

Table 4.1. H13 (1.2344) steel tensile test results

	Hardness (HRC)	Yield Stress (MPa)	Ultimate Tensile Stress (MPa)	% Elongation
Specimen 1 (Raw)	20.6	542	742	17.4
Specimen 2 (Heat Treated)	42.4	1226	1378	9.7

The rest of the material properties are obtained from the data sheet of the material supplier Böhler Steel and are listed in Table 4.2.

Table 4.2. Material Properties of H13 (1.2344) steel

Chemical composition (%)	C: 0.39, Si: 1.10, Mn: 0.40, Cr: 5.20, Mo: 1.40, V:0.95							
Mechanical Properties	**Temperature (^{o}C)**							
	20	100	200	300	400	500	600	700
Density (g/cm^3)	7.80	-	-	-	-	7.64	7.60	-
Young's Modulus (GPa)	215	-	-	-	-	176	165	-
Poisson's Ratio	0.3	-	-	-	-	-	-	-
Specific Heat (J/kg)	460	-	-	-	-	550	590	-
Thermal Expansion Coefficient (10^{-6} 1/K)	-	11.5	12	12.2	12.5	12.9	13	13.2
Thermal Conductivity (W/mK)	-	24.3	26.10	27.3	27.8	27.7	27.5	27.3

4.3 Determination of convection coefficient

To determine the convection coefficient during heating and cooling, a steel ring which is initially at room temperature with inner, outer diameter and length of 21.6 mm, 50.3 mm and 30mm respectively is first heated for 10 minutes in the furnace which is at 450°C and surface temperature is measured by using a Raytek infrared thermometer. After that, heated part is hanged outside of the furnace and cooled at the room temperature 25 ^{o}C while measuring the surface temperature every 8 seconds. After 408 seconds, temperature decreases down to 239 ^{o}C and measurement is terminated.

Collected data is plotted by using MS. Excel as shown in Figure 4.5 and Figure 4.6 for heating and cooling respectively.

To determine the convection coefficient, axisymmetric coupled analyses are performed for different convection coefficients. In the heating analyses convection coefficients is taken as 0.05, 0.07 and 0.09 N/s/^{o}C/mm and in the cooling analyses addition to these values, cooling simulation with 0.03 N/s/^{o}C/mm is performed. After heating the part for 10 minutes, temperature difference between the surface and core is between 1-2 ^{o}C for all convection values. In Figure 4.7, temperature distribution is shown for the convection coefficient of 0.05.
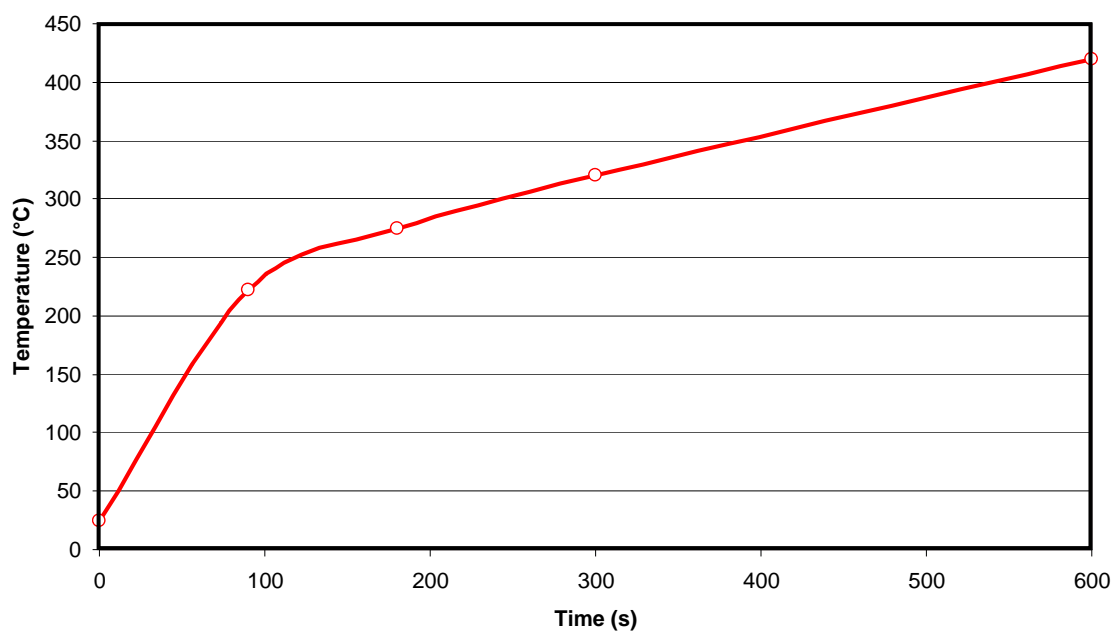
Figure 4.5. Experiment temperature vs. time graph during heating
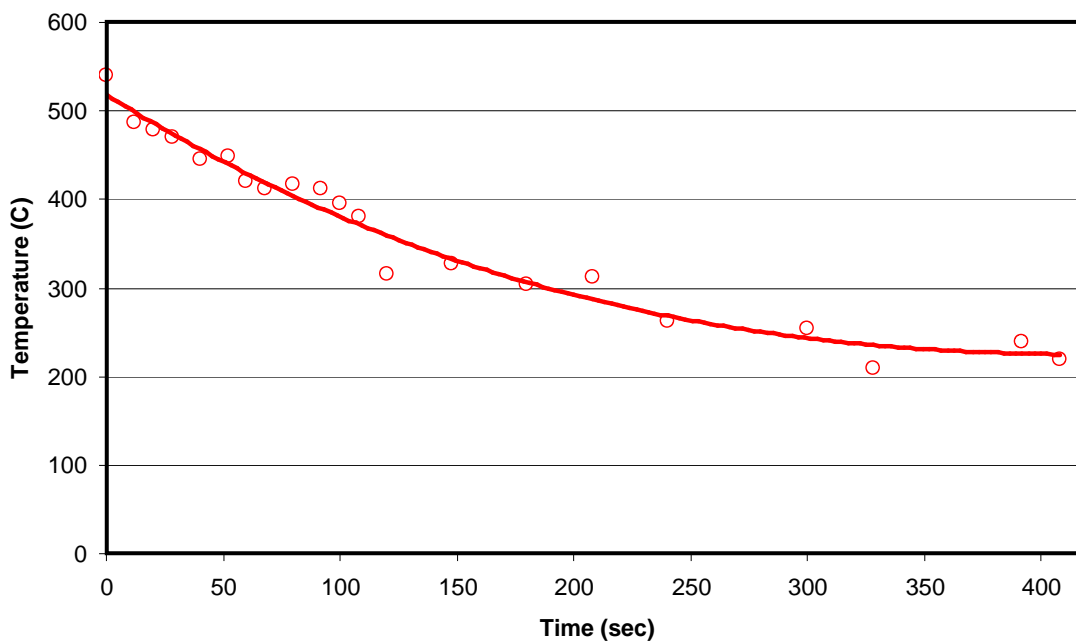
Figure 4.6. Experiment temperature vs. time graph during cooling

Figure 4.7. Temperature distribution on the ring after 10 minutes (h=0.05 N/s/^{o}C/mm)

When the simulation results are compared with the experimental data, it is seen that, the convection coefficient is different between these thermal operations. For heating, convection coefficient is determined as 0.07 N/s/^{o}C/mm. For cooling the experiment data is scattering around 0.05 N/s/^{o}C/mm due to unstable air flow compared to the inside of the furnace. Convection coefficient is expected to be larger for cooling than heating since the airflow outside the furnace is more than inside the furnace. In the finite element analyses, heat transfer only due to convection is considered. However, in the furnace there exists also heat transfer by radiation between the steel part and heating coils. Since this effect is neglected in the analyses, heating coefficient of convection is calculated larger than cooling convection coefficient. In the Figures 4.8 and 4.9 simulation results are compared with the experimental data.

Figure 4.8. Experiment – FEA comparison for heating
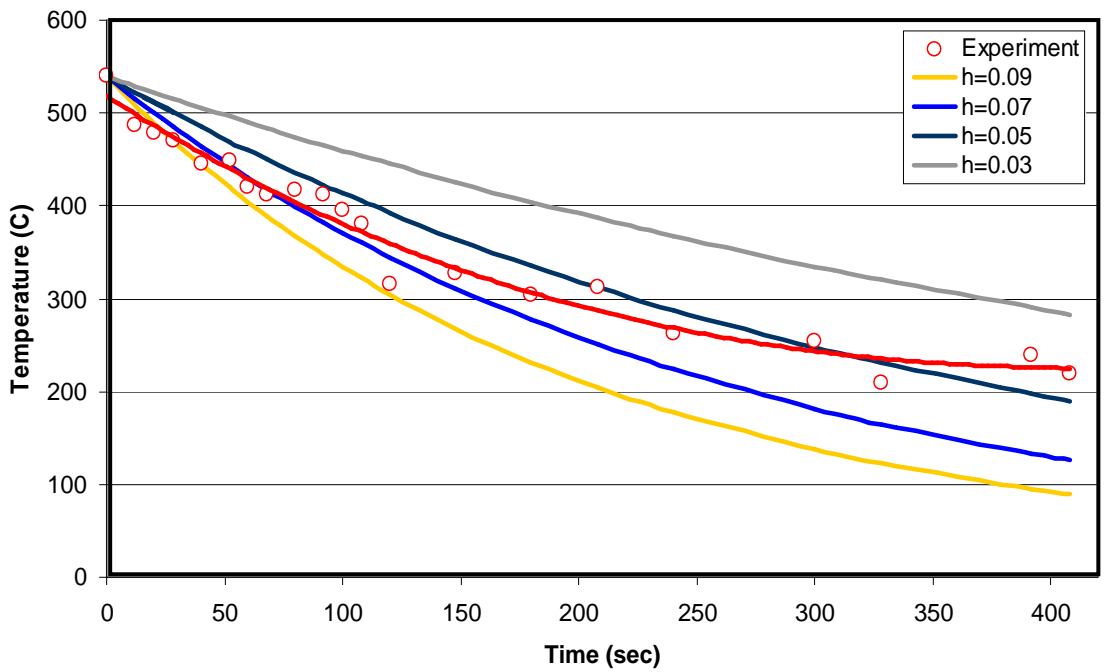
Figure 4.9. Experiment – FEA comparison for cooling

86

4.4 Prestressing by Heating - Cooling

To investigate the die assembly by heating and cooling, axisymmetric coupled analyses have been conducted. The selected insert dimensions for this process are, 10 mm and 28 mm which are representing bore and outer diameter respectively. Outer diameter of the ring is selected as 50 mm. To determine allowable interference to assemble parts by heating, Eqn. (3.5) is used. Thermal expansion coefficient of the ring is taken constant as 11.5×10^{-6} $1/^{\circ}K$ whereas initial temperature and heating temperature is taken as 25 $^{\circ}$C and 450°C. Under these conditions, expansion of the diameter is calculated as 0.128 mm:

$$u = 28(mm) \cdot 11.5 \cdot 10^{-6}(1/^{o} K) \cdot (450 - 25)^{o} K \qquad (4.1a)$$

$$u = 0.128 \, mm \qquad (4.1b)$$

FEM solution of diameter expansion due to heating gives 0.142 mm which is higher than analytical calculation owing to varying thermal expansion coefficient depending on the temperature. Diameter expansion of inner bore versus temperature is shown in Figure 4.10.
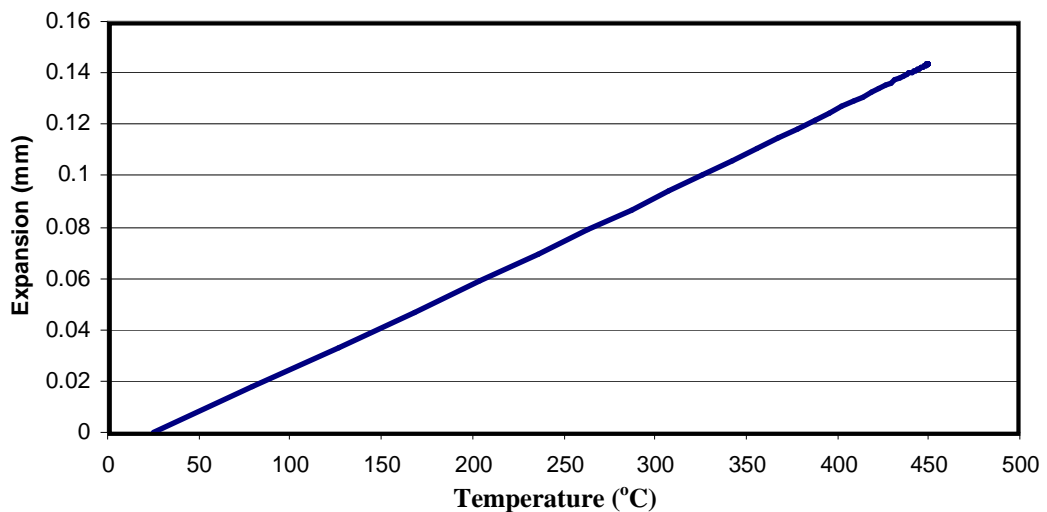
Figure 4.10. Bore diameter expansion versus temperature

Generally, the relative interference is defined as the ratio of absolute interference between two parts to outer diameter of insert. For prestressed cold forming dies, this value is between 4-8 ‰. For this case, relative interference is chosen as 5‰ which corresponds to 0.14 mm absolute interference. This interference is generated by machining the outer diameter of insert as 28.14 mm. Initial gap after combining parts before cooling is 2 microns in the FEA model (Fig. 4.11).
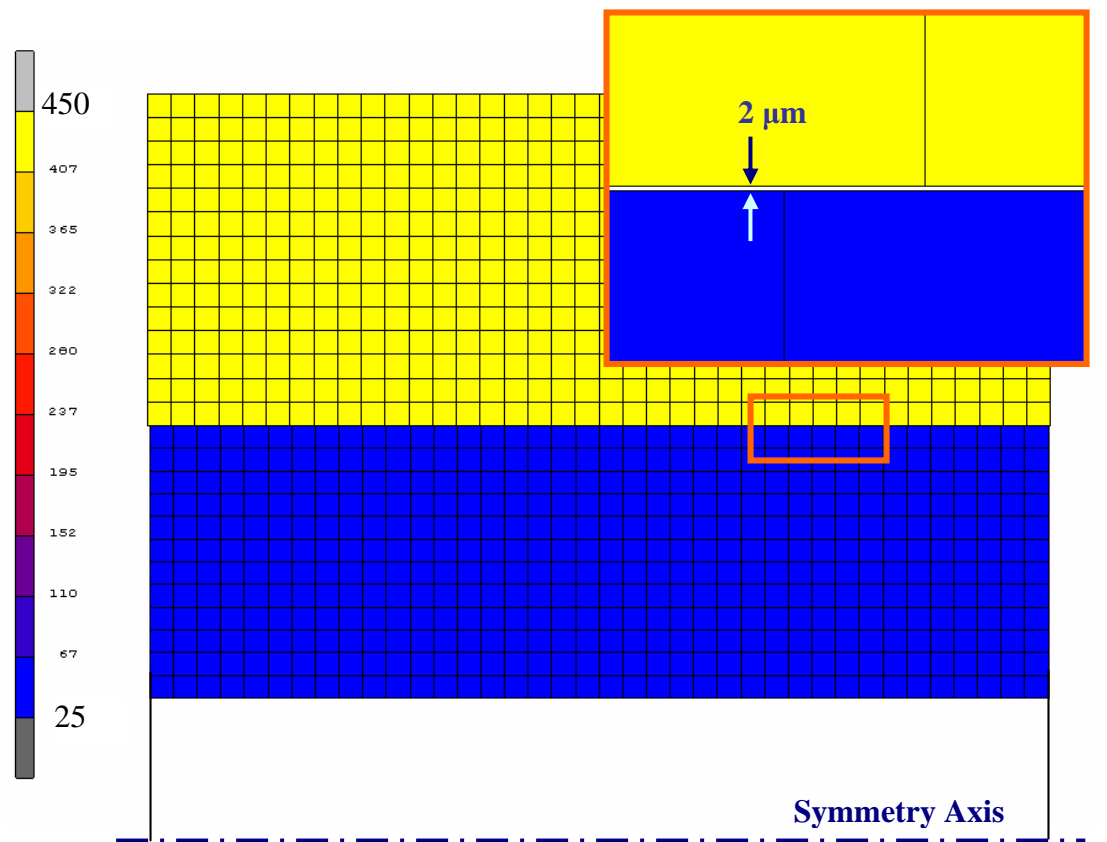
Figure 4.11. Temperature distribution before cooling

Assembly of two parts is completed by combining heated ring taken by prestate option of MSC.Superform and importing insert model at room temperature. The ambient temperature is defined as 25 ^{o}C and process time is chosen as 25 minutes to establish equilibrium condition.

When the parts reach to thermal equilibrium, compressive hoop stresses on the bore surface of the insert reaches up to 841 MPa. Radial normal pressure between two mating surfaces is 357 MPa. Also after prestressing, bore diameter of insert shrinks by 0.019 mm. In Figure 4.12 radial and hoop stress distribution and in Figures 4.13, radial displacement of two parts are shown along the radius from inner surface of insert to outer surface of ring.

Another important parameter is the equivalent stress distribution on the tool components in order to determine plastification which might lead to loss of prestressing.
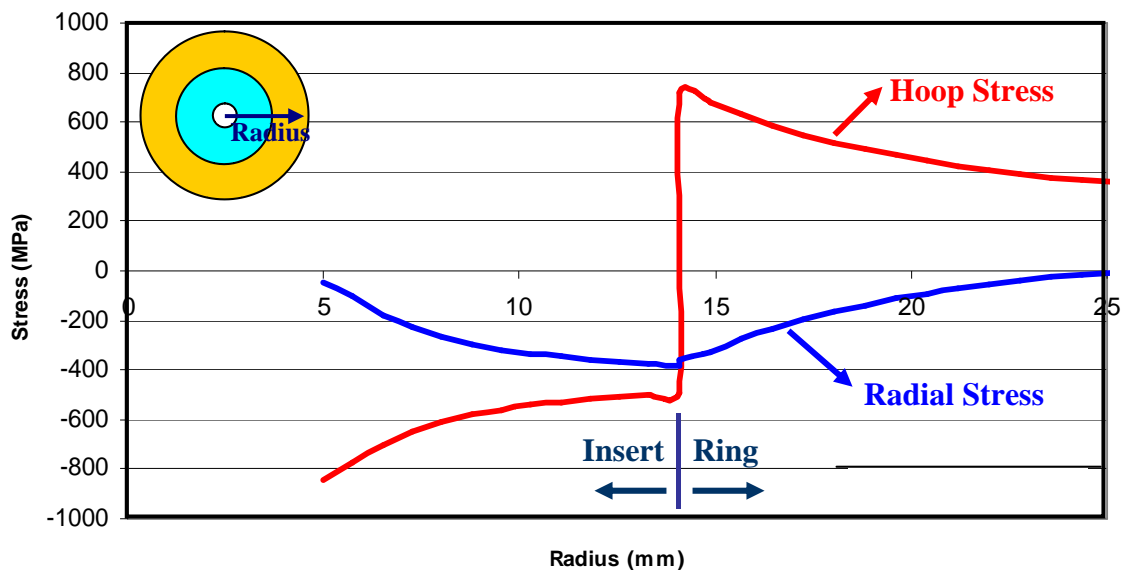
Figure 4.12. Hoop and radial stress distribution after prestressing
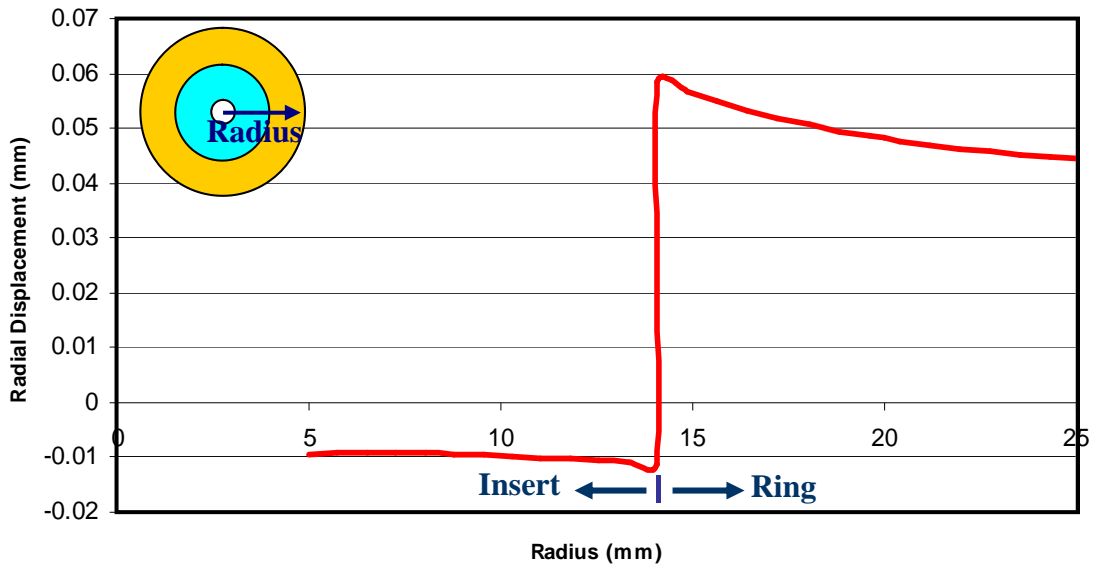
Figure 4.13. Radial displacement distribution after prestressing

The yield stress of ring material H13 is taken from the results of tension tests. For the carbide insert, yield stress is assumed equal to the maximum compressive strength, considering occurrence of brittle fracture after initiation of plastic deformation. Figure 4.14 shows the equivalent stress distribution calculated according to von Misses criterion with the yield stress of insert and ring materials. The maximum equivalent stress on the insert is located on the bore surface with value of 849 MPa which is much lower than the yield stress. For the ring, the most critical location is the interference surface and the equivalent stress is reaching up to 961 MPa. If the interference is increased by an amount, the part which will plastify firstly is to be the stress ring.
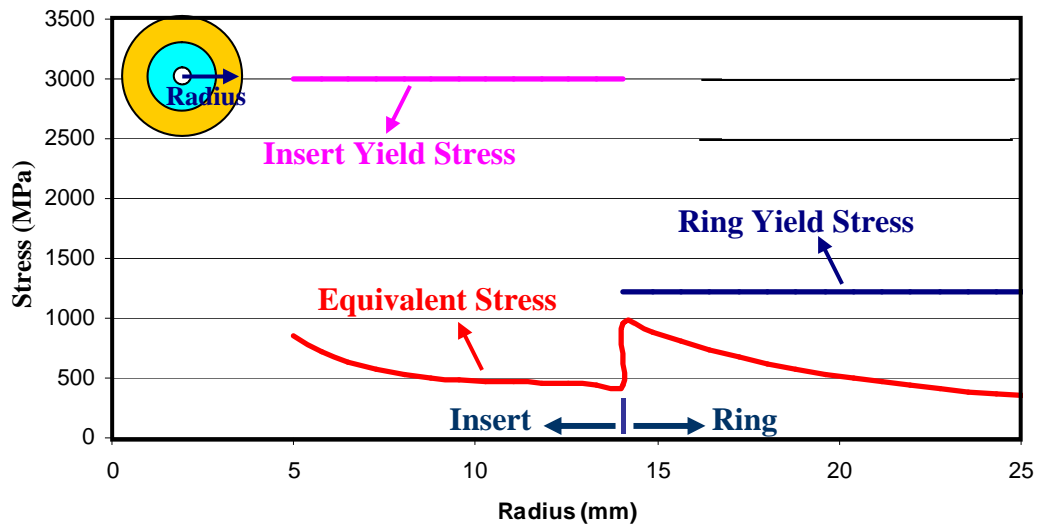
4.14. Equivalent stress distribution with yield limits

For some die geometries, for instance if there exist small fillets which are frequently present in bolt forming dies, meshing by using quadrilateral elements may lead problems at these locations. In these situations, using triangular elements gives better mesh quality in representing those small curvatures. To compare the stresses
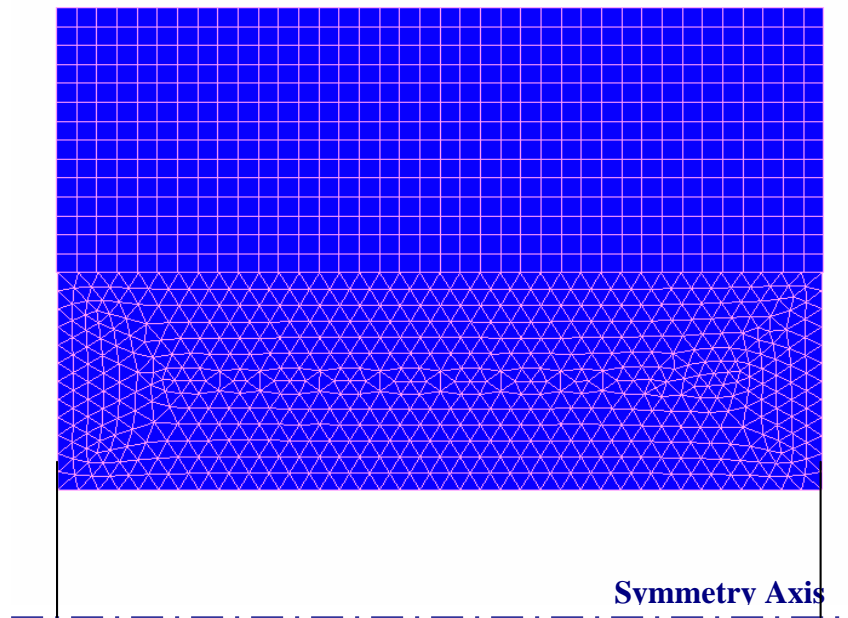
Figure 4.15. Triangular mesh structure on die

91

formed under the elastic deformations during shrink fit, hoop stress distributions are compared for both types of elements. The new die model and mesh structure used in this analysis is shown in Figure 4.15.

The plot in Figure 4.16 is showing that stress distribution for prestressing simulation made by using quadrilateral and triangular elements are in well agreement. Even though, triangular elements are not suitable for plastic deformation analyses, they can be used for elastic deformation analyses on dies.

Before going further in analysing prestressing by using different modeling methods, a convergence test is performed to determine optimum element size for accurate results.
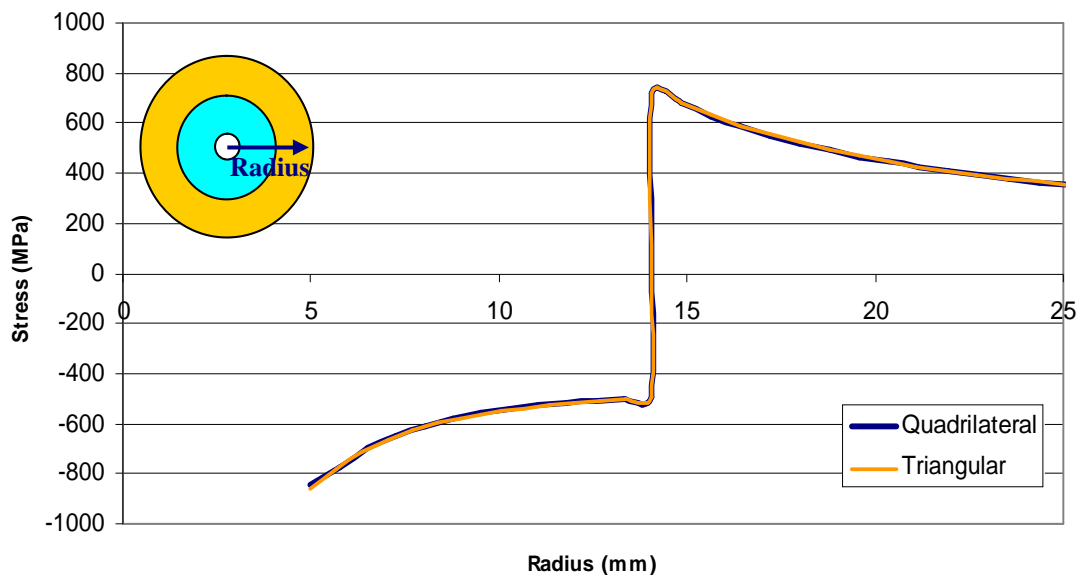
Figure 4.16. Hoop stress distribution for different element types

The effect of mesh quality on the stress distribution is investigated for element sizes of 2, 1.5, 1.0, and 0.5 mm. Results are showing that, stress distribution is not affected by element size except the areas close to contact region where the highest

stresses are present and vary 3% between the largest and smallest element size (Fig. 4.17).

Previous heating and cooling analyses are performed by using element size of 0.8 mm which are giving satisfactory results according to this convergence study. To maintain the consistency, subsequent simulations are made by using the same mesh density.

4.5 Prestressing by Defining Initial Contact

For simple die assemblies with few numbers of dies, applying prestressing with heating – cooling method is applicable. However, for more complex die assemblies with large number of components, this method will not be practical. In such cases, a simpler way of modeling prestressing is required. The commercial FEM software MSC.Superform has an option to define the interference as an initial contact condition.
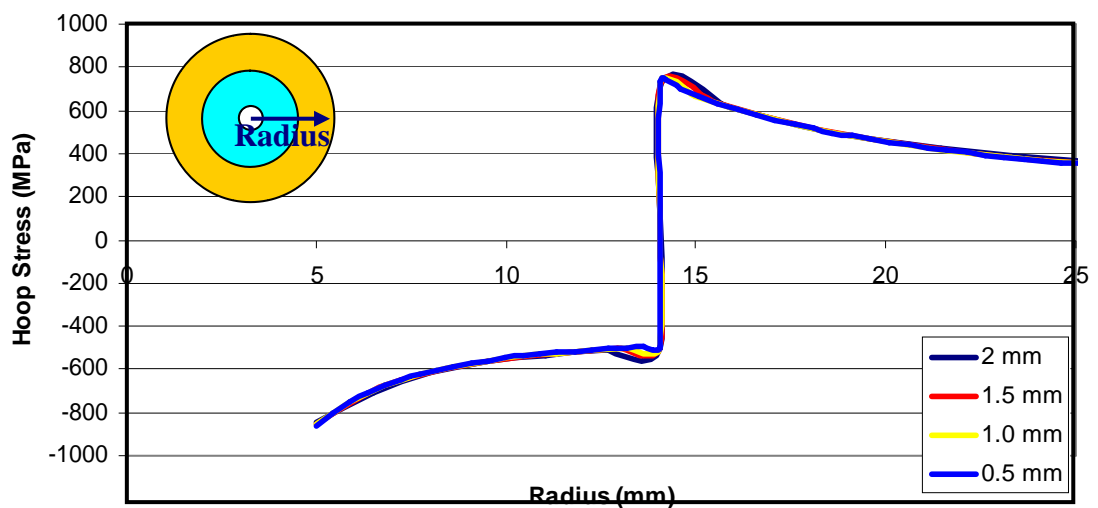
Figure 4.17. Hoop stress distribution for different element sizes

93
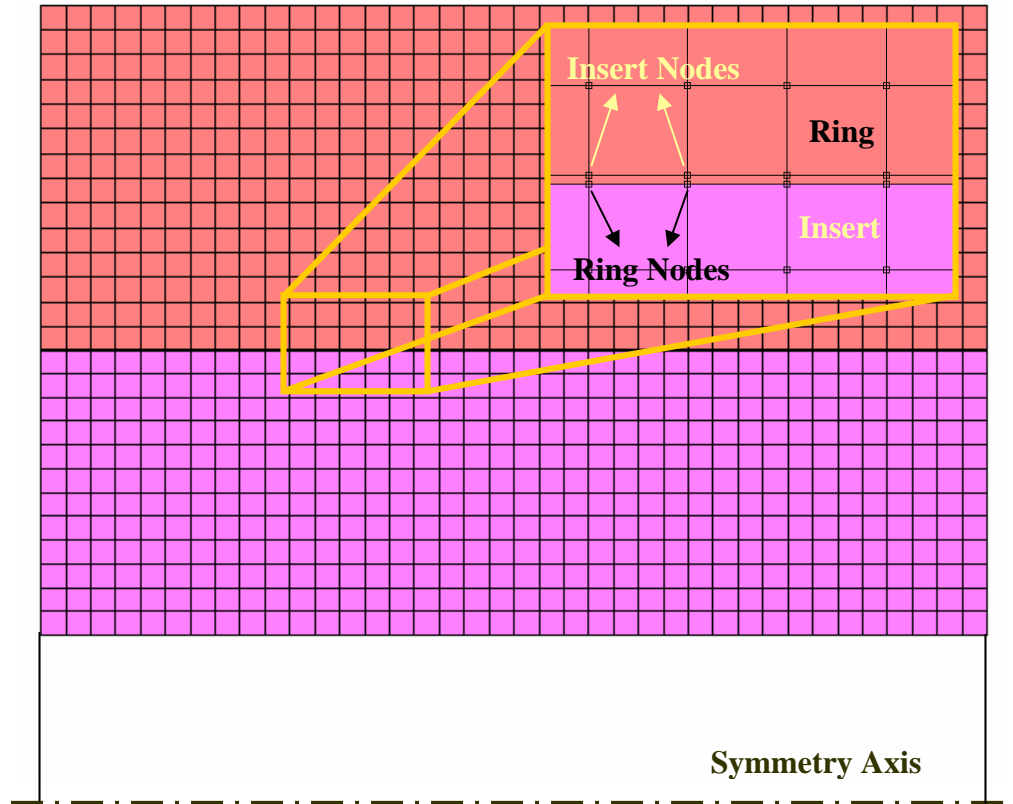
Figure 4.18. Overlapping nodes representing interference

Without considering the thermal conditions, finite element mesh is generated by overlapping the nodes at the contact region according to the amount of interference. For the axisymmetric models, the distance between the overlapping nodes is equal to the radial interference. The parts having same dimension with the ones analysed in previous section is prestressed by using overlapping method. In Figure 4.18, mesh quality of two parts which are modeled together is shown with the overlapped nodes.

After the calculation of the non-linear contact problem, the hoop, radial and equivalent stress distributions and radial displacement on the bodies are the major process parameters that are being analysed. Since there exist reference data gathered from the thermal assembly of the parts, results of this analyse are compared with the previous one. In Figure 4.19, hoop and radial stresses are plotted on the same graph and the results are almost identical.
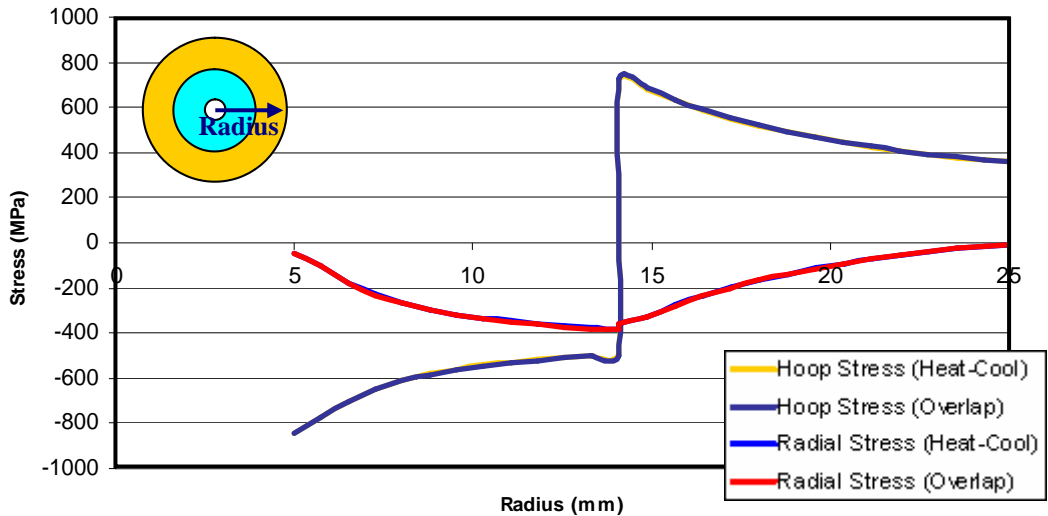
Figure 4.19. Stress distribution comparison for two shrink fit methods

As the hoop and radial stresses, equivalent stress distribution is also the same for two proposed methods (Fig. 4.20). Finally, the plot of radial displacements of both methods is showing that these methods are suitable for modeling shrink fitting of tool components (Fig. 4.21). When the simplicity and calculation time is concerned, use of node overlapping provides ease of modeling for especially complex die assemblies.
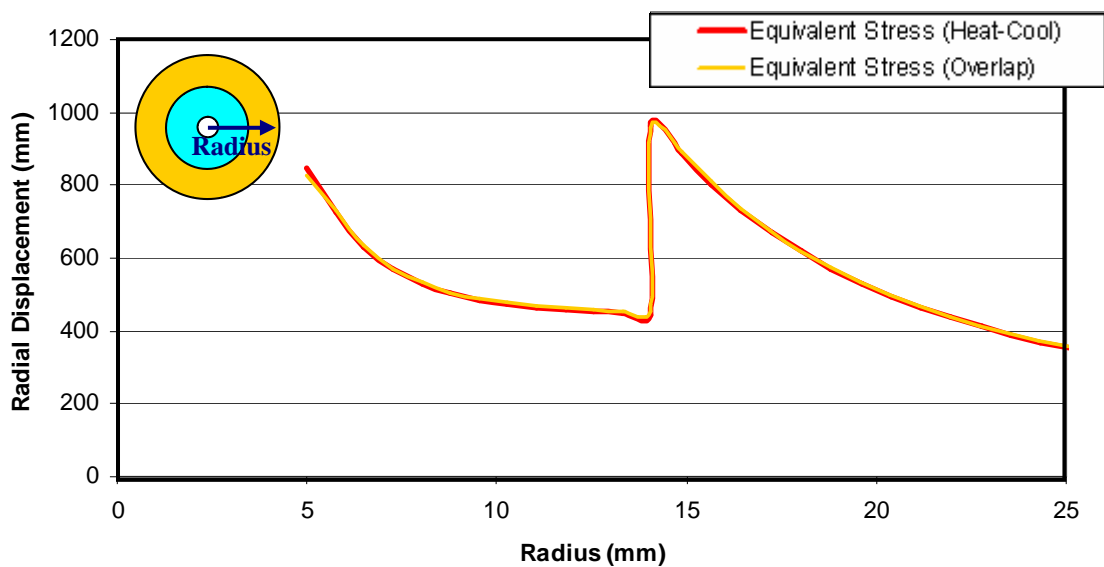
Figure 4.20. Equivalent stress distribution comparison for two shrink fit methods
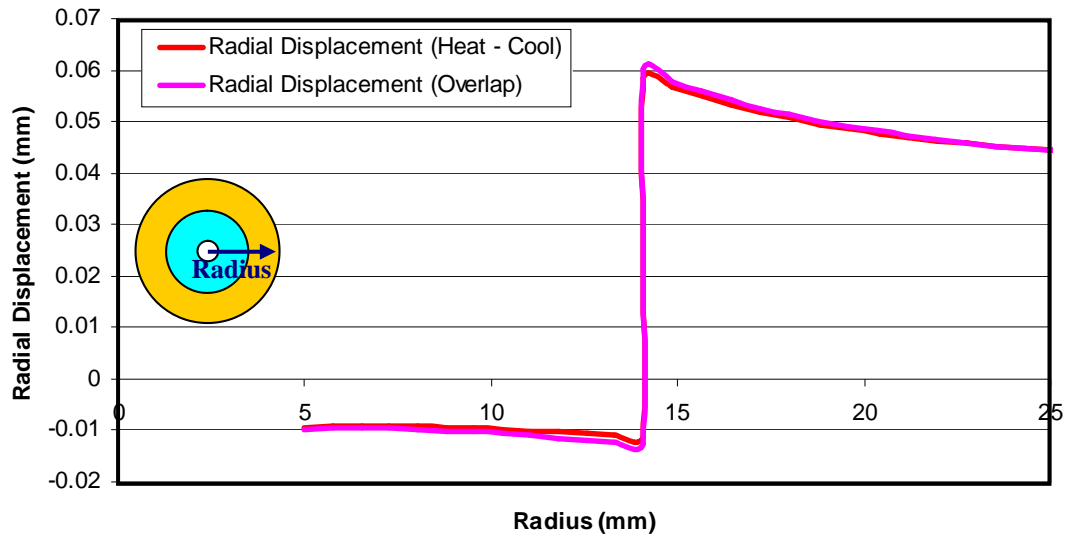
Figure 4.21. Radial displacement distribution comparison for two shrink fit methods

4.6 Verification of FEM Analyses

Up to this point shrink fitting of stress ring and die insert is only analysed by using finite element method. Even though the results of both modeling methods are in good agreement, it is necessary to verify the results of these FEM analyses for correctness.

Shrink fitting of two thick cylinders is a general axisymmetric problem which can be solved analytically by using theory of elasticity. In the next section, solution of this problem is explained in detail where stress and displacement equations are defined.

4.6.1 Analytic Formulation of Shrink Fit

In the general three dimensional elasticity problem there are 15 unknown quantities which must be determined at every point in the body, namely, the 6 cartesian components of stress, the 6 cartesian components of strain and the 3 components of displacement. Attempts can be made to obtain a solution to a given problem after following quantities have been defined.

96

- The geometry of body

- The boundary conditions

- The body-force field as a function of position

- The elastic constants

In order to solve these 15 unknown quantities, 15 independent equations are required. Three of them provided by the equations of equilibrium (eqs. 4.2), six are provided by strain-displacement relations (eqs. 4.3) and the remaining six can be obtained from the stress - strain expressions (eqs. 4.4).

$$\frac{\partial \sigma_{xx}}{\partial x} + \frac{\partial \sigma_{xy}}{\partial y} + \frac{\partial \sigma_{xz}}{\partial z} + F_x = 0 \qquad (4.2a)$$

$$\frac{\partial \sigma_{yx}}{\partial x} + \frac{\partial \sigma_{yy}}{\partial y} + \frac{\partial \sigma_{yz}}{\partial z} + F_y = 0 \qquad (4.2b)$$

$$\frac{\partial \sigma_{zx}}{\partial x} + \frac{\partial \sigma_{zy}}{\partial y} + \frac{\partial \sigma_{zz}}{\partial z} + F_z = 0 \qquad (4.2c)$$

$$\varepsilon_{xx} = \frac{\partial u}{\partial x} \qquad (4.3a)$$

$$\varepsilon_{yy} = \frac{\partial v}{\partial y} \qquad (4.3b)$$

$$\varepsilon_{zz} = \frac{\partial w}{\partial z} \qquad (4.3c)$$

$$\varepsilon_{xy} = \frac{1}{2}\left(\frac{\partial u}{\partial y} + \frac{\partial v}{\partial x}\right) \qquad (4.3d)$$

$$\varepsilon_{xz} = \frac{1}{2}\left(\frac{\partial u}{\partial z} + \frac{\partial w}{\partial x}\right) \qquad (4.3e)$$

$$\varepsilon_{yz} = \frac{1}{2}\left(\frac{\partial v}{\partial z} + \frac{\partial w}{\partial y}\right) \qquad (4.3f)$$

$$\varepsilon_{xx} = \frac{1}{E}\left[\sigma_{xx} - \nu\left(\sigma_{yy} + \sigma_{zz}\right)\right] \qquad (4.4a)$$

$$\varepsilon_{yy} = \frac{1}{E}\left[\sigma_{yy} - \nu\left(\sigma_{xx} + \sigma_{zz}\right)\right] \qquad (4.4b)$$

$$\varepsilon_{zz} = \frac{1}{E}\left[\sigma_{zz} - \nu\left(\sigma_{xx} + \sigma_{yy}\right)\right] \qquad (4.4c)$$

$$\varepsilon_{xy} = \frac{\left(1+\nu\right)}{E}\sigma_{xy} \qquad (4.4d)$$

$$\varepsilon_{xz} = \frac{\left(1+\nu\right)}{E}\sigma_{xz} \qquad (4.4e)$$

$$\varepsilon_{yz} = \frac{\left(1+\nu\right)}{E}\sigma_{yz} \qquad (4.4f)$$

A solution to an elasticity problem, in addition to satisfying these 15 equations, must also satisfy the boundary conditions. Boundary conditions are often classified to define four different types of boundary-values listed below [71];

Type 1: If the displacements are prescribed over the entire boundary, the problem is classified as type 1 boundary value problem.

Type 2: The most frequently encountered boundary value problem is the type where normal and shearing forces are given over the entire surface.

Type 3: This type of boundary-value problem where the normal and shearing forces are given over a portion of the boundary and the displacements are given over the remainder of the body. Shrink fitting of the parts can be given as an example for this type of problem. In the shrinking process, a radial displacement is given to the parts at the interference section. On all other surfaces, both normal and shearing components of stress are zero.

Type 4: This type of boundary problem is the most general of the considered types. Over a portion of the surface displacements are prescribed. Over a second portion, normal and shearing stresses are prescribed. Over a third portion, normal component of displacement and the shearing component of the stress are prescribed and over the fourth portion, the shearing component of displacement and the normal component

of stress are prescribed. The first three types of problem can be regarded as special cases of this general fourth type.

As in the case of shrink fitting of two thick cylinders, there exist a special class of problems known as plane problems, which can be solved more readily than the general three-dimensional problem since certain simplifying assumptions can be made in their treatment. The geometry of body and the nature of the loading on the boundaries which permit a problem to be classified as a plane problem given in Figure 4.22 where the region having uniform thickness, bounded by two parallel planes and by any closed lateral surface is defined as B_L.
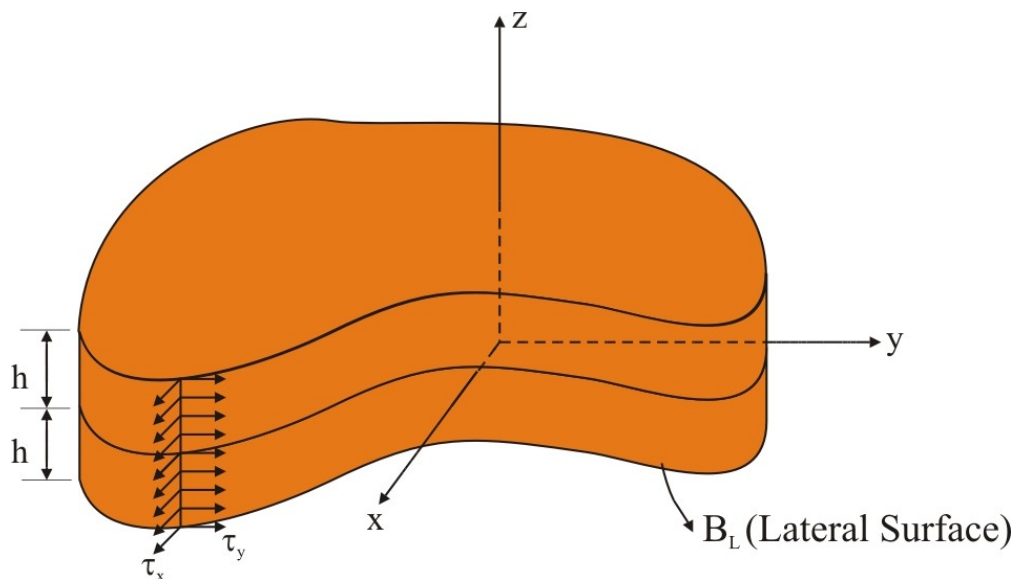
Figure 4.22. Body considered for the plane elasticity approach

Additions to the restrictions on the geometry of the body, following restrictions are imposed on the load applied to the planes of the body.

➤ If there exist any body forces, they can not vary through the thickness, that is, $F_x = F_x(x,y)$ and $F_y = F_y (x,y)$ and body force in z direction must equal to zero.

➢ The surface tractions or loads on the lateral boundary B_L must be in the plane of the model and must be uniformly distributed across the thickness. $T_x = T_x(x,y)$, $T_y = T_y(x,y)$ and $T_z = 0$.

➢ No loads can be applied to the parallel planes bounding the top and bottom surfaces; that is $T_n = 0$ on $z = \pm h$.

Once the geometry and loading have been defined, stresses can be determined by using either plane strain or plane stress approach. Usually plane strain approach is used when the body is very thick relative to its lateral dimensions. The plane stress approach is employed when the body is relatively thin in relation to its lateral dimensions.

In plane problems, three unknowns, σ_{xx}, σ_{yy} and τ_{xy} must be determined which will satisfy the required field equations and boundary conditions. The most convenient sets of field equations to use in this determination are the two equations of equilibrium and one stress compatibility.

The equilibrium equations in two dimensions are;

$$\frac{\partial \sigma_{xx}}{\partial x} + \frac{\partial \sigma_{xy}}{\partial y} + F_x = 0 \qquad (4.5a)$$

$$\frac{\partial \sigma_{yx}}{\partial x} + \frac{\partial \sigma_{yy}}{\partial y} + F_y = 0 \qquad (4.5b)$$

The stress compatibility equation for the case of plane strain is;

$$\nabla^2 \left(\sigma_{xx} + \sigma_{yy} \right) = -\frac{2(\lambda + \mu)}{\lambda + 2\mu} \left(\frac{\partial F_x}{\partial x} + \frac{\partial F_y}{\partial y} \right) \qquad (4.5c)$$

Supposing body force field is defined by $\Omega(x,y)$ so that the body force intensities are given by;

$$F_x = -\frac{\partial \Omega}{\partial x} \qquad (4.6a)$$

$$F_y = -\frac{\partial \Omega}{\partial y} \qquad (4.6b)$$

Substituting Eqs. (4.6) into Eqs. (4.5) and noting that $2(\lambda+\mu)/(\lambda+2\mu)=1/(1-\upsilon)$,it gives;

$$\frac{\partial \sigma_{xx}}{\partial x} + \frac{\partial \tau_{xy}}{\partial y} = \frac{\partial \Omega}{\partial x} \qquad (4.7a)$$

$$\frac{\partial \tau_{xy}}{\partial x} + \frac{\partial \sigma_{yy}}{\partial y} = \frac{\partial \Omega}{\partial y} \qquad (4.7b)$$

$$\nabla^2 \left(\sigma_{xx} + \sigma_{yy} - \frac{\Omega}{1-v} \right) = 0 \qquad (4.7c)$$

Assuming stresses represented by a function ϕ such that;

$$\sigma_{xx} = \frac{\partial^2 \phi}{\partial y^2} + \Omega \qquad (4.8a)$$

$$\sigma_{yy} = \frac{\partial^2 \phi}{\partial x^2} + \Omega \qquad (4.8b)$$

$$\tau_{xy} = -\frac{\partial^2 \phi}{\partial x \partial y} \qquad (4.8c)$$

The expression ϕ is known as Airy stress function. If Eqs. (4.8) are substituted into Eqs. (4.7), two equilibrium equations are exactly satisfied and Eqn. (4.7c) gives;

$$\nabla^4 \phi = -\frac{1-2v}{1-v} \nabla^4 \Omega \qquad (4.9)$$

101

If body force intensities are zero or constant such as in a gravitational field, then;

$$\nabla^4 \Omega = 0$$

(4.10)

and Eqn. (4.9) become;

$$\nabla^4 \phi = 0$$

(4.11)

This is a biharmonic equation and can be written as;

$$\frac{\partial^4 \phi}{\partial x^4} + 2\frac{\partial^4 \phi}{\partial x^2 \partial y^2} + \frac{\partial^4 \phi}{\partial y^4} = 0$$

(4.12)

When Eqn. (4.11) is solved for ϕ, expressions containing x,y and a number of constants will be obtained. This equation also shows that σ_{xx}, σ_{yy} and τ_{xy} are independent of elastic constants.

Shrink fitting of two rings can be solved by employing polar coordinate system. In order to solve this two dimensional elasticity problem by a polar coordinate reference frame, the equations of equilibrium, the definition of Airy's stress function and one compatibility equation must be established in term of polar coordinates.

The stress equations of equilibrium in polar coordinates can be derived from the free body diagram of the polar element shown in Figure 4.23.

The average values of the normal and shearing stresses which act on surface 1 are denoted by σ_{rr} and $\tau_{r\theta}$, respectively. Since the stresses vary as a function of r, values of the normal and shearing stresses on the surface of the normal and shearing stresses acting on surface 3 are given by $\sigma_{rr} + (\partial \sigma_{rr}/\partial r)dr$ and $\tau_{r\theta} + (\partial \tau_{r\theta}/\partial r)dr$.

Similarly the average values of normal and shearing stresses on surface 2 are given by $\sigma_{\theta\theta}$ and $\tau_{r\theta}$. Since the stresses also vary as a function of θ, values of the normal and shearing stresses on surface 4 are $\sigma_{\theta\theta} + (\partial\sigma_{\theta\theta}/\partial\theta)d\theta$ and $\tau_{r\theta} + (\partial\tau_{r\theta}/\partial\theta)d\theta$.
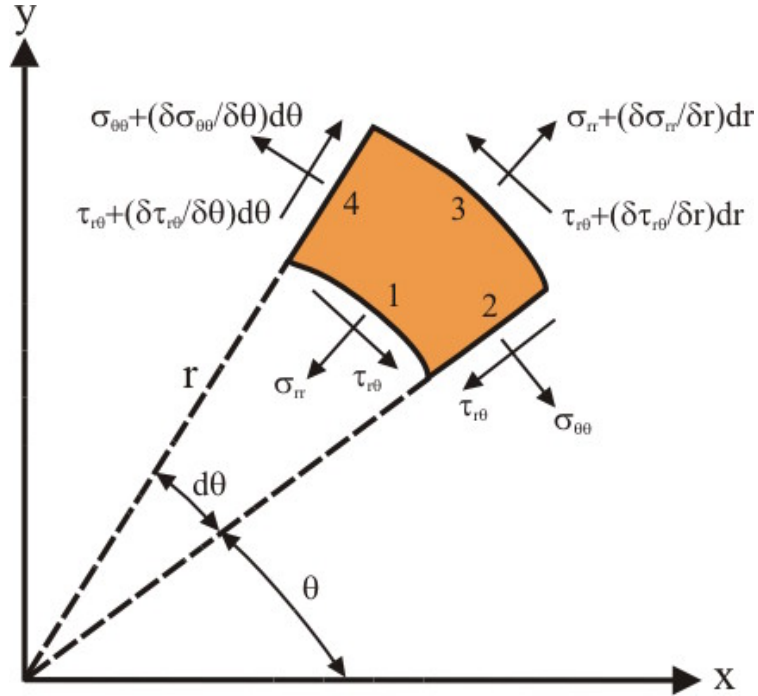
Figure 4.23. Polar element

For this polar element with unit thickness, sum of all forces in radial and tangential directions must be equal to zero. By summing the forces in these directions by neglecting body force intensity, gives the equations of equilibrium in polar coordinates.

$$\frac{\partial\sigma_{rr}}{\partial r} + \frac{1}{r}\frac{\partial\tau_{r\theta}}{\partial\theta} + \frac{1}{r}(\sigma_{rr} - \sigma_{\theta\theta}) = 0 \qquad (4.13a)$$

$$\frac{1}{r}\frac{\partial\sigma_{\theta\theta}}{\partial\theta} + \frac{\partial\tau_{r\theta}}{\partial r} + \frac{2\tau_{r\theta}}{r} = 0 \qquad (4.13b)$$

103

As mentioned before, stress function ϕ has to satisfy $\nabla^4\phi = 0$ however the definition of ∇^4 operator defined in Eqn. (4.12) must suit polar coordinate system. By using following expressions;

$$r^2 = x^2 + y^2 \qquad (4.14a)$$

$$\theta = \arctan\frac{y}{x} \qquad (4.14b)$$

and differentiating Eqs. (4.14) gives;

$$\frac{\partial r}{\partial x} = \frac{x}{r} = \cos\theta \qquad (4.15a)$$

$$\frac{\partial r}{\partial y} = \frac{y}{r} = \sin\theta \qquad (4.15b)$$

$$\frac{\partial\theta}{\partial x} = -\frac{y}{r^2} = -\frac{\sin\theta}{r} \qquad (4.15c)$$

$$\frac{\partial\theta}{\partial y} = \frac{x}{r^2} = \frac{\cos\theta}{r} \qquad (4.15d)$$

Substituting Eqs (4.15) in (4.12) gives;

$$\nabla^4\phi = \left(\frac{\partial^2}{\partial r^2} + \frac{1}{r}\frac{\partial}{\partial r} + \frac{1}{r^2}\frac{\partial^2}{\partial\theta^2}\right)\left(\frac{\partial^2\phi}{\partial r^2} + \frac{1}{r}\frac{\partial\phi}{\partial r} + \frac{1}{r^2}\frac{\partial^2\phi}{\partial\theta^2}\right) = 0 \qquad (4.16)$$

The polar stress components σ_{rr}, $\sigma_{\theta\theta}$ and $\tau_{r\theta}$ are described in terms of the cartesian components σ_{xx}, σ_{yy} and τ_{xy} as follows;

$$\sigma_{rr} = \sigma_{xx}\cos^2\theta + \sigma_{yy}\sin^2\theta + \tau_{xy}\sin 2\theta \qquad (4.17a)$$

$$\sigma_{\theta\theta} = \sigma_{yy}\cos^2\theta + \sigma_{xx}\sin^2\theta - \tau_{xy}\sin 2\theta \qquad (4.17b)$$

$$\tau_{r\theta} = \left(\sigma_{yy} - \sigma_{xx}\right)\sin\theta\cos\theta + \tau_{xy}\cos 2\theta \qquad (4.17c)$$

By substituting Eqs. (4.8) into Eqs. (4.17) polar components of Airy's stress function are obtained;

$$\sigma_{rr} = \frac{1}{r}\frac{\partial \phi}{\partial r} + \frac{1}{r^2}\frac{\partial^2 \phi}{\partial \theta^2} \tag{4.18a}$$

$$\sigma_{\theta\theta} = \frac{\partial^2 \phi}{\partial r^2} \tag{4.18b}$$

$$\tau_{r\theta} = \frac{1}{r^2}\frac{\partial \phi}{\partial \theta} - \frac{1}{r}\frac{\partial^2 \phi}{\partial r \partial \theta} \tag{4.18c}$$

Since the equation $\nabla^4 \phi = 0$ is a fourth order biharmonic partial differential equation which can be reduced to an ordinary fourth order differential equation by using separation of variables where;

$$\phi^{(n)} = R_n(r)\begin{Bmatrix} \cos n\theta \\ \sin n\theta \end{Bmatrix} \tag{4.19}$$

The resulting differential equation is an Euler type which yields different stress functions. One of the stress functions can be expressed in the following form;

$$\phi_{(r)} = a + b\ln r + cr^2 + dr^2 \ln r \tag{4.20}$$

By using Eqs. (4.18), stresses can be expressed as;

$$\sigma_{rr} = \frac{b}{r^2} + 2c + d(1 + 2\ln r) \tag{4.21a}$$

$$\sigma_{\theta\theta} = -\frac{b}{r^2} + 2c + d(3 + 2\ln r) \tag{4.21b}$$

$$\tau_{r\theta} = 0 \tag{4.21c}$$

The displacements in radial and circumferential directions associated with this function can be determined by integrating the stress displacement relations, giving;

$$u_r = \frac{1}{E}\left[-(1+v)\frac{b}{r} + 2(1-v)cr + 2(1-v)dr\ln r - (1+v)dr\right] \quad (4.22a)$$
$$+ \alpha_2\cos\theta + \alpha_3\sin\theta$$

$$u_\theta = \frac{1}{E}(4dr\theta) - \alpha_1 r - \alpha_2\sin\theta + \alpha_3\cos\theta \quad (4.22b)$$

The terms containing α_1, α_2 and α_3 are associated with rigid body motions. Since the stress solution is independent of θ, this stress function ϕ can be used to solve problems having rotational symmetry as in the case of shrink fitting of cylinders.

According to symmetry conditions u_r and u_θ must be independent of θ. This condition can be satisfied only when $d = 0$. Therefore, for cases where rotational symmetry is present stresses and displacements are defined in following form;

$$\sigma_{rr} = \frac{b}{r^2} + 2c \quad (4.23a)$$

$$\sigma_{\theta\theta} = -\frac{b}{r^2} + 2c \quad (4.23b)$$

$$\tau_{r\theta} = 0 \quad (4.23c)$$

$$u_r = \frac{1}{E}\left(-(1+v)\frac{b}{r} + 2(1-v)cr\right) \quad (4.23d)$$

$$u_\theta = 0 \quad (4.23e)$$

4.6.1.1 Stress and Displacement Distributions on a Single Ring

Firstly, a long hollow cylinder is considered as shown in Figure 4.24, which is subjected to an internal pressure P_i and an external pressure P_o. The inside and outside radius of the cylinder is denoted as r_i and r_o respectively.
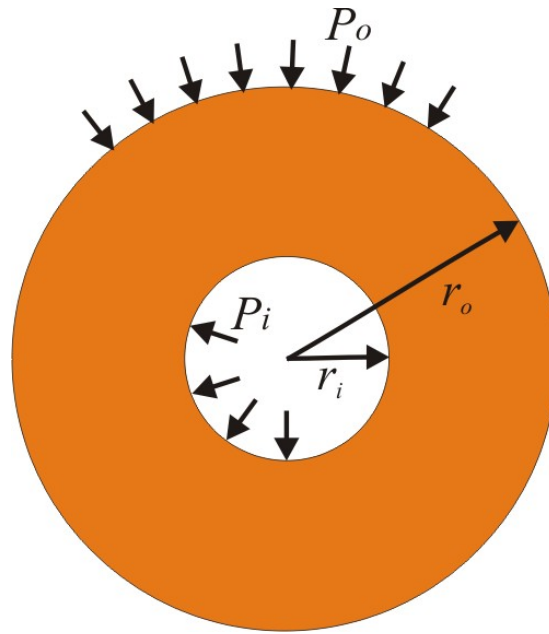
Figure 4.24. Cylinder subjected to internal and external pressure

For this problem, the boundary conditions are defined as follows;

$$\sigma_{rr} = -P_i \qquad \tau_{r\theta} = 0 \qquad \text{at } r = r_i \qquad (4.24a)$$

$$\sigma_{rr} = -P_o \qquad \tau_{r\theta} = 0 \qquad \text{at } r = r_o \qquad (4.24b)$$

When solving Eqn. (4.23a) and (4.23b), constants b and c are found as;

$$b = \frac{r_i^2 r_o^2 (P_o - P_i)}{r_o^2 - r_i^2} \qquad (4.25a)$$

$$c = \frac{r_i^2 P_i - r_o^2 P_o}{2(r_o^2 - r_i^2)} \qquad (4.25b)$$

These values are substituted into Eqns. (4.23) to provide required solution.

$$\sigma_{rr} = \frac{r_i^2 r_o^2 (P_o - P_i)}{(r_o^2 - r_i^2) r^2} + \frac{r_i^2 P_i - r_o^2 P_o}{2(r_o^2 - r_i^2)} \tag{4.26a}$$

$$\sigma_{\theta\theta} = -\frac{r_i^2 r_o^2 (P_o - P_i)}{(r_o^2 - r_i^2) r^2} + \frac{r_i^2 P_i - r_o^2 P_o}{2(r_o^2 - r_i^2)} \tag{4.26b}$$

$$\tau_{r\theta} = 0 \tag{4.26c}$$

$$u_r = \frac{1}{E}\left(-(1+v)\frac{r_i^2 r_o^2 (P_o - P_i)}{(r_o^2 - r_i^2) r} + (1-v)\frac{r_i^2 P_i - r_o^2 P_o}{(r_o^2 - r_i^2)} r\right) \tag{4.26d}$$

$$u_\theta = 0 \tag{4.26e}$$

Stress and displacement distributions for two special cases of this problem are give as follows;

Case 1: External Pressure Equals Zero ($P_o = 0$)

$$\sigma_{rr} = \frac{r_i^2 P_i}{r_o^2 - r_i^2}\left(1 - \frac{r_o^2}{r^2}\right) \tag{4.27a}$$

$$\sigma_{\theta\theta} = \frac{r_i^2 P_i}{r_o^2 - r_i^2}\left(1 + \frac{r_o^2}{r^2}\right) \tag{4.27b}$$

$$\tau_{r\theta} = 0 \tag{4.27c}$$

$$u_r = \frac{r_i^2 P_i}{Er(r_o^2 - r_i^2)}\left((1+v)r_o^2 + (1-v)r^2\right) \tag{4.27d}$$

$$u_\theta = 0 \tag{4.27e}$$

$$\sigma_{rr} = \frac{r_o^2 P_o}{r_o^2 - r_i^2}\left(\frac{r_i^2}{r^2} - 1\right)$$

(4.28a)

$$\sigma_{rr} = \frac{r_o^2 P_o}{r_o^2 - r_i^2}\left(\frac{r_i^2}{r^2} + 1\right)$$

(4.28b)

(4.28c)

$$\tau_{r\theta} = 0$$

$$u_r = -\frac{r_o^2 P_o}{Er\left(r_o^2 - r_i^2\right)}\left((1+v)r_i^2 + (1-v)r^2\right)$$

(4.28d)

$$u_\theta = 0$$

(4.28e)

4.6.1.2 Stress and Displacement Distributions on Two Shrink Fitted Rings

In Figure 4.25 two hollow shrink fitted cylinders with different material properties are shown without any internal or external pressure. The inner, interference, outer diameter of the cylinders and interference are denoted as r_i, r_f, r_o and δ
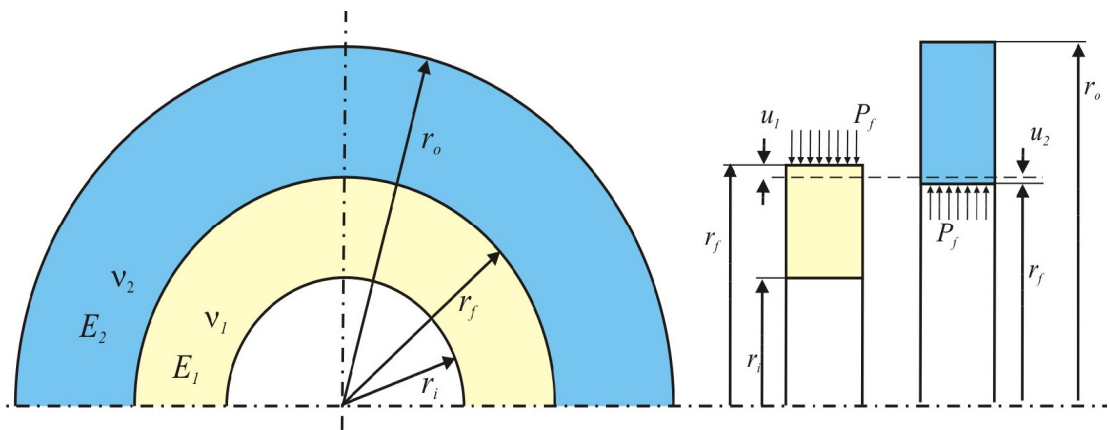
Figure 4.25. Shrink fitted cylinders [72]

respectively. Also radial displacements on the outer surface of inner ring and inner surface of outer ring after shrink fitting are denoted by u_1 and u_2.

To determine the stress and displacement distributions on the cylinders, firstly boundary conditions are defined as the following;

$$\sigma_{rr} = 0 \qquad \tau_{r\theta} = 0 \qquad \text{at } r = r_i \qquad (4.29\text{a})$$

$$\sigma_{rr} = P_f \qquad \text{at } r = r_f \qquad (4.29\text{b})$$

$$\sigma_{rr} = 0 \qquad \tau_{r\theta} = 0 \qquad \text{at } r = r_o \qquad (4.29\text{c})$$

$$\delta = |u_1| + |u_2| \qquad \text{at } r = r_f \qquad (4.29\text{d})$$

By solving Eqs. (4.23) using these boundary conditions, constants for inner and outer rings are obtained. For the inner ring stresses and displacements are expressed in following form;

$$\sigma_{rr} = \frac{r_i^2 r_f^2 P_f}{\left(r_f^2 - r_i^2\right) r^2} - \frac{P_f r_f^2}{\left(r_f^2 - r_i^2\right)} \qquad (4.30\text{a})$$

$$\sigma_{\theta\theta} = \frac{r_i^2 r_f^2 P_f}{\left(r_f^2 - r_i^2\right) r^2} + \frac{P_f r_f^2}{\left(r_f^2 - r_i^2\right)} \qquad (4.30\text{b})$$

$$\tau_{r\theta} = 0 \qquad (4.30\text{c})$$

$$u_r = \frac{1}{E}\left(-(1+v)\frac{r_i^2 r_f^2 P_f}{\left(r_f^2 - r_i^2\right) r} - (1-v)\frac{P_f r_f^2}{\left(r_f^2 - r_i^2\right)} r\right) \qquad (4.30\text{d})$$

$$u_\theta = 0 \qquad (4.30\text{e})$$

and for the outer ring;

$$\sigma_{rr} = -\frac{r_f^2 r_o^2 P_f}{\left(r_o^2 - r_f^2\right) r^2} + \frac{P_f r_f^2}{\left(r_o^2 - r_f^2\right)} \quad (4.31a)$$

$$\sigma_{\theta\theta} = -\frac{r_f^2 r_o^2 P_f}{\left(r_o^2 - r_f^2\right) r^2} - \frac{P_f r_f^2}{\left(r_o^2 - r_f^2\right)} \quad (4.31b)$$

$$\tau_{r\theta} = 0 \quad (4.31c)$$

$$u_r = \frac{1}{E}\left((1+v)\frac{r_f^2 r_o^2 P_f}{\left(r_o^2 - r_f^2\right) r} + (1-v)\frac{P_f r_f^2}{\left(r_o^2 - r_f^2\right)} r\right) \quad (4.31d)$$

$$u_\theta = 0 \quad (4.31e)$$

In these expressions P_f refers to pressure on the interference surface and it is expressed as in the following form;

$$P_f = \frac{\delta}{r_f\left(\frac{v_2}{E_2} - \frac{r_o^2 + r_f^2}{E_2\left(r_f^2 - r_o^2\right)}\right) - \left(\frac{v_1}{E_1} + \frac{r_i^2 + r_f^2}{E_1\left(r_i^2 - r_f^2\right)}\right)} \quad (4.32)$$

For the case of two shrink fitted rings with internal pressure, Eqn. (4.29a) replaced with following boundary condition where P_i represents the pressure applied to the inner surface.

$$\sigma_{rr} = P_i \qquad \tau_{r\theta} = 0 \qquad \text{at } r = r_i \quad (4.33)$$

By using the boundary conditions in Eqs (4.29 b,c,d) and (4.33), stress and displacement expressions are obtained. For inner ring;

$$\sigma_{rr} = \frac{r_i^2 P_i - r_f^2 P_f}{r_f^2 - r_i^2} - \frac{\left(P_i - P_f\right)r_i^2 r_f^2}{\left(r_f^2 - r_i^2\right)r^2} \tag{4.34a}$$

$$\sigma_{\theta\theta} = \frac{r_i^2 P_i - r_f^2 P_f}{r_f^2 - r_i^2} + \frac{\left(P_i - P_f\right)r_i^2 r_f^2}{\left(r_f^2 - r_i^2\right)r^2} \tag{4.34b}$$

$$\tau_{r\theta} = 0 \tag{4.34c}$$

$$u_r = \frac{1 - \nu_1}{E_1} \cdot \frac{r_i^2 P_i - r_f^2 P_f}{r_f^2 - r_i^2} + \frac{1 + \nu_1}{E_1} \cdot \frac{\left(P_i - P_f\right)r_i^2 r_f^2}{\left(r_f^2 - r_i^2\right)r} \tag{4.34d}$$

$$u_\theta = 0 \tag{4.34e}$$

and for the outer ring;

$$\sigma_{rr} = \frac{P_f r_f^2 \left(1 - \dfrac{r_o^2}{r^2}\right)}{r_o^2 - r_f^2} \tag{4.35a}$$

$$\sigma_{\theta\theta} = \frac{P_f r_f^2 \left(1 + \dfrac{r_o^2}{r^2}\right)}{r_o^2 - r_f^2} \tag{4.35b}$$

$$\tau_{r\theta} = 0 \tag{4.35c}$$

$$u_r = \frac{r_f^2 P_f r}{E_2 \left(r_o^2 - r_f^2\right)}\left[\left(1 - \nu_2\right) + \left(1 + \nu_2\right)\frac{r_o^2}{r^2}\right] \tag{4.35d}$$

$$u_\theta = 0 \tag{4.35e}$$

where P_f is the interference pressure and defined as;

$$P_f = \left(\frac{2r_i^2 r_f P_i}{r_f^2 - r_i^2} + \delta \cdot E_1 \right) \frac{1}{r_f \frac{E_1}{E_2} \left(\frac{r_f^2 + r_o^2}{r_o^2 - r_f^2} + \nu_2 \right) + \frac{r_f \left(r_f^2 + r_i^2 \right)}{r_f^2 - r_i^2} - \nu_1 r_f} \qquad (4.36)$$

4.6.1.3 Stress and Displacement Distributions on Three Shrink Fitted Rings
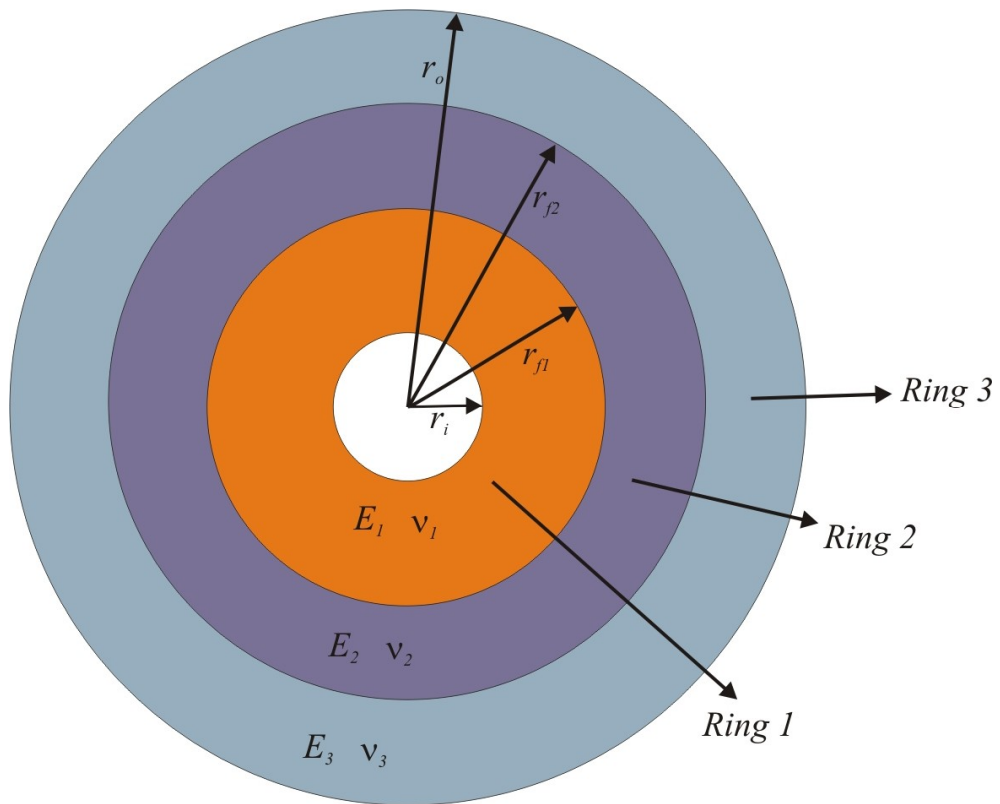
Figure 4.26. Three ring assembly by shrink fitting

For a three-ring assembly stress and displacement distributions can be obtained by using following radial displacement, radial and hoop stress equations [73].

$$u_r = c_1^i r + \frac{c_2^i}{r}, i = 1, 2, 3 \tag{4.37a}$$

$$\sigma_{rr}^i = \frac{E_i}{1 - v_i^2}\left[c_1^i\left(1 + v_i\right) - c_2^i\left(\frac{1 - v_i}{r^2}\right)\right], i = 1, 2, 3 \tag{4.37b}$$

$$\sigma_{\theta\theta}^i = \frac{E_i}{1 - v_i^2}\left[c_1^i\left(1 + v_i\right) + c_2^i\left(\frac{1 - v_i}{r^2}\right)\right], i = 1, 2, 3 \tag{4.37c}$$

In these equations superscript i refers the ring numbers respectively as shown is Figure 4.26. To solve six unknowns, six boundary conditions are defined.

$$\sigma_{rr}^1 = 0 \qquad \text{at } r = r_i \tag{4.38a}$$

$$\sigma_{rr}^1 = \sigma_{rr}^2 \qquad \text{at } r = r_{f1} \tag{4.38b}$$

$$\sigma_{rr}^2 = \sigma_{rr}^3 \qquad \text{at } r = r_{f2} \tag{4.38c}$$

$$\sigma_{rr}^3 = 0 \qquad \text{at } r = r_o \tag{4.38d}$$

$$\delta_1 = \left|u_r^1\right| + \left|u_r^2\right| \qquad \text{at } r = r_{f1} \tag{4.38e}$$

$$\delta_2 = \left|u_r^2\right| + \left|u_r^3\right| \qquad \text{at } r = r_{f2} \tag{4.38f}$$

By aid of a mathematics software like MathCad, Mathematica or MathLab, stress and displacement distributions on the rings can be calculated after solving six unknowns c_1^1, c_2^1, c_1^2, c_2^2, c_1^3 and c_2^3 and substituting into Eqns (4.37).

4.6.2 Comparison of FEA with Analytic Formulations

Three different cases are analysed to compare FE analysis results with the analytical solutions. First one is prestressing a die insert by single ring and second one is performing prestressing same insert by using two rings. In the first case, part dimensions are chosen the same as the ones used in previous FEM analyses. However, for two ring assembly, whilst bore and outer diameter is taken same with the first case, middle ring outer and inner diameters are re-defined with appropriate interferences. These two cases are analysed for load free condition. In the third case, uniform internal pressure is applied on the die insert in FE model. The analytical formulas used in this case are derived by using the new boundary conditions.

To solve the stress and displacement distribution equations and calculate stress and displacement values along the radius, MathCad is used which is a mathematics software. This software supplies not only a user interface to input material properties and part dimensions but also provides a graphical representation of the results. Another advantage of using this software is exporting stress and displacement data to MS Excel to plot together with the data gathered from simulation software. All developed program codes used in this section are presented in Appendix B.

To perform the calculations of shrink fit assembly of one ring over the die insert with no internal pressure, Eqns. 4.30, 4.31 and 4.32 are used. Bore and outer diameters of the insert and ring are taken same as given in Section 4.4. Since no thermal effects are included in elasticity solution, only Young's Modulus and Poison's Ratio are defined. The process parameters are entered to program as shown in Figure 4.27. First ring refers to die insert whereas second is stress ring.

Figure 4.27. Data input region for MathCad

Similar to comparison procedure done before when comparing the result of two different shrink fit modeling types, stress and displacement distributions along the radius is calculated by using two different methods. When the hoop, radial, equivalent stress and radial displacement distributions obtained from FE analyse performed with overlapping method is plot with the analytical solutions, the results are almost coincide with an error less than 1%. In Figure 4.28, 4.29 and 4.30, comparison of results obtained from these two methods are presented.
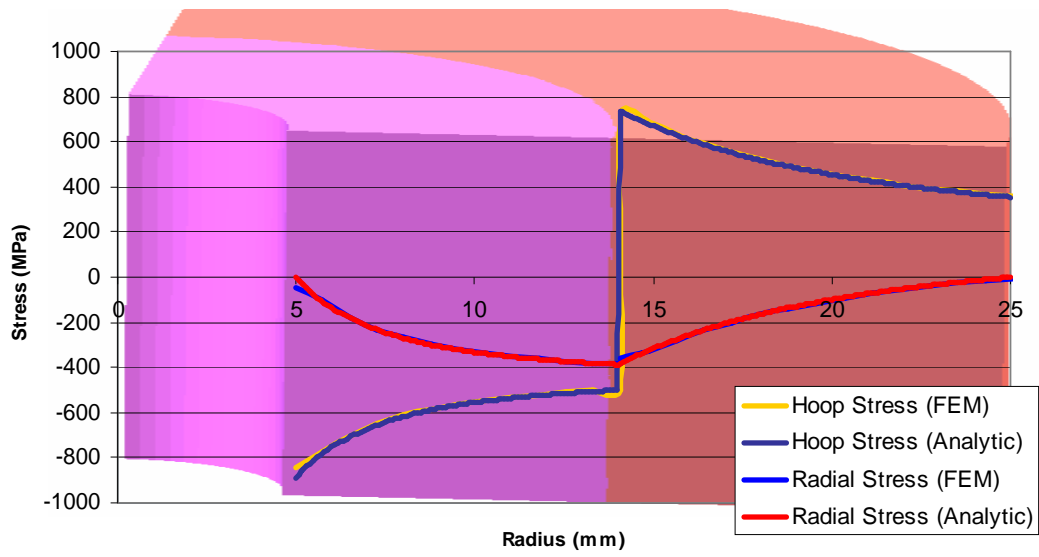
Figure 4.28. Radial and hoop stress distribution solution of analytic formulas and FEA
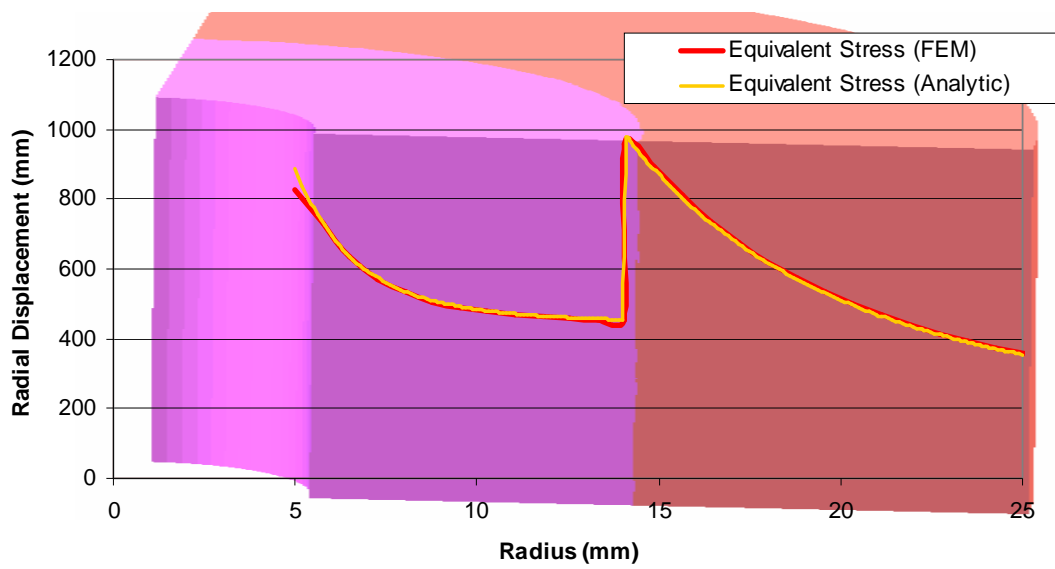
Figure 4.29. Equivalent stress distribution solution of analytic formulas and FEA
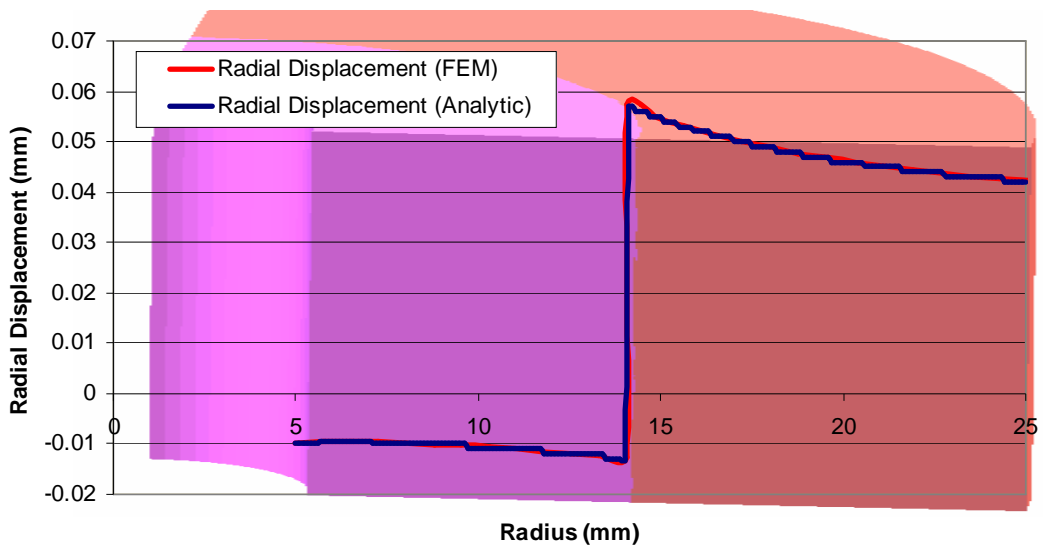
Figure 4.30. Radial displacement distribution solution of analytic formulas and FEA

In the two ring case, a middle insert is defined with a bore and outer diameters of 28mm and 40mm respectively. Initial relative interference between the insert - middle ring is 5.7 ‰ (0.16mm) and middle ring – outer ring is 4.3 ‰ (0.12 mm). However, after assembling the insert and middle ring, interference between two steel rings will increase due to the expansion of middle ring.

The FE analysis of this assembly is done in two consecutive steps by only overlapping nodes according to initial interferences as shown in Figure 4.31.

The analytical solution of this process is more complicated compared to one ring case. To obtain the individual stress and displacement distribution equations for the components, it is required to solve six unknowns present in Eqns. 4.37 by using the boundary conditions given in Eqns. 4.38. In the MathCad software, this calculation is made by using an iterative solver where an initial guess is defined for each unknown constant.
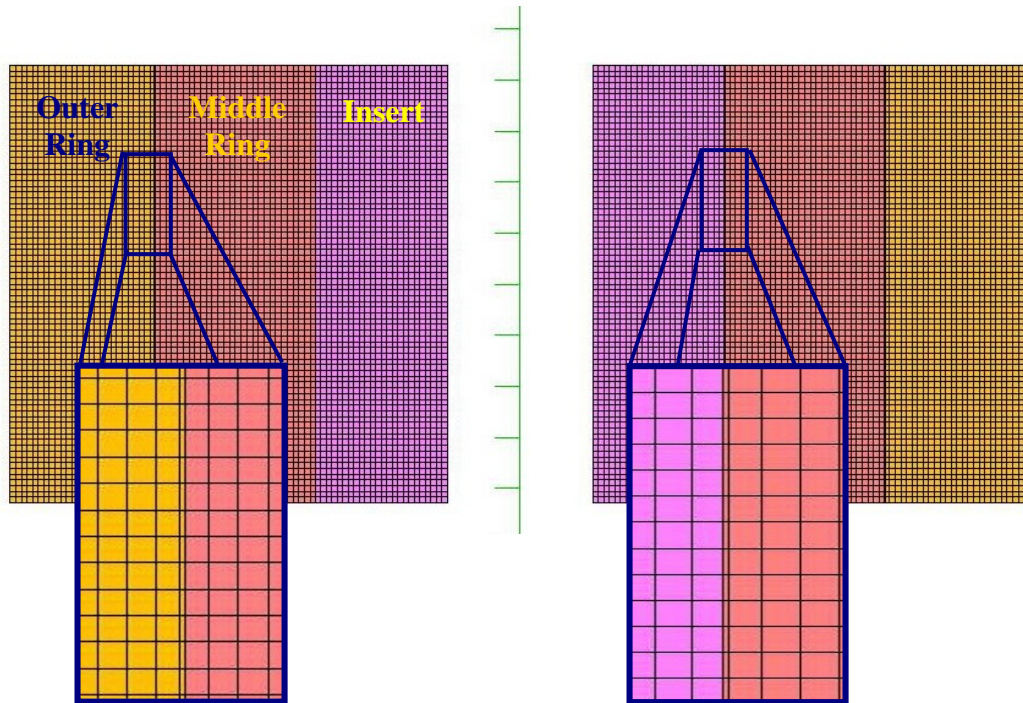
Figure 4.31. Mesh structure of three ring assembly

Similar to one ring system, stress and displacement distributions are ploted on the same graph to evaluate solution accuracy of FE analyses (Fig. 4.32, 4.33 and 4.34). The results are again in good agreement and give almost same distribution for both calculation methods. Approximately 2% difference is possibly has occurred due to the initial guess of the constants but not yielding to a significantly different results from FE analyses.

This analysis also shows the effectiveness of using two prestressing rings instead of one ring when the hoop stresses generated on the insert are taken into account. When one stress ring is used, maximum compressive circumferential stress obtained on the die insert is 840 MPa. However, for the same tool dimensions, compressive hoop stresses increased up to 1250 MPa when two stress rings are used. In other words by only changing the stress ring numbers, circumferential stresses are improved by 49% in this case.
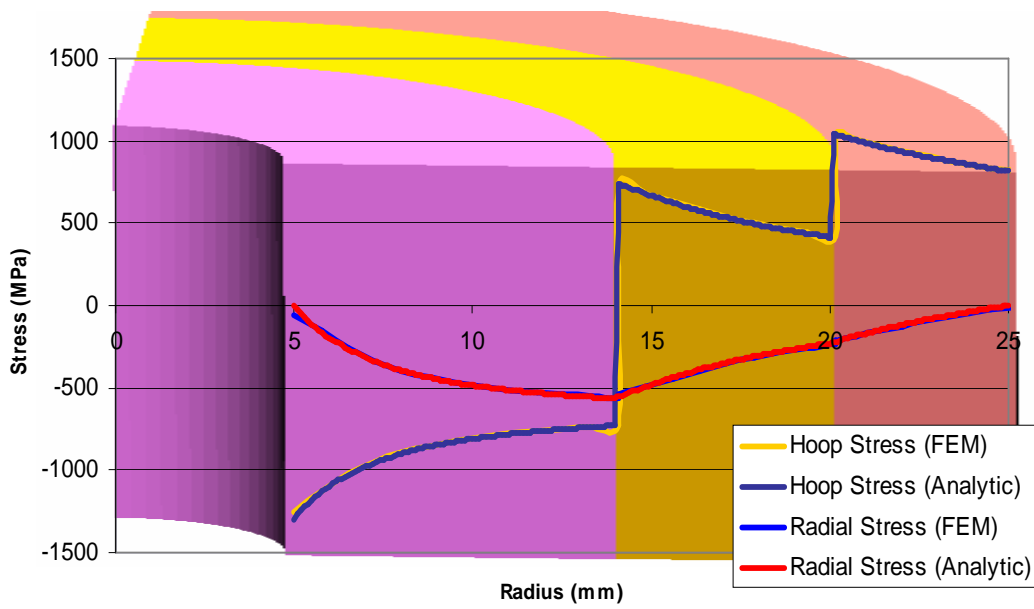
Figure 4.32. Radial and hoop stress distribution solution of analytic formulas and FEA (Two ring system)
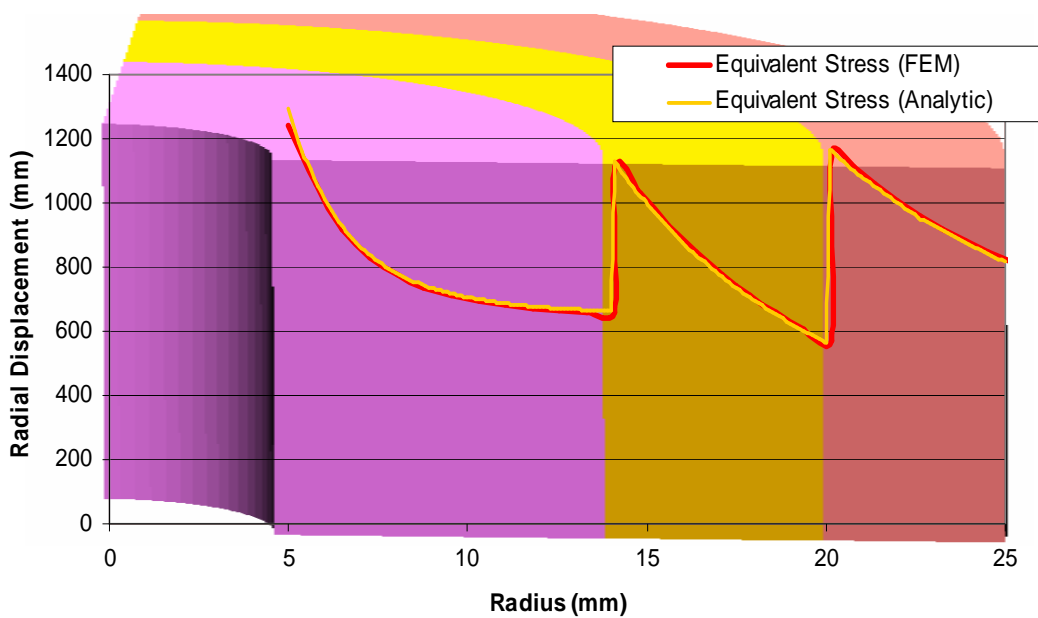
Figure 4.33. Equivalent stress distribution solution of analytic formulas and FEA (Two ring system)
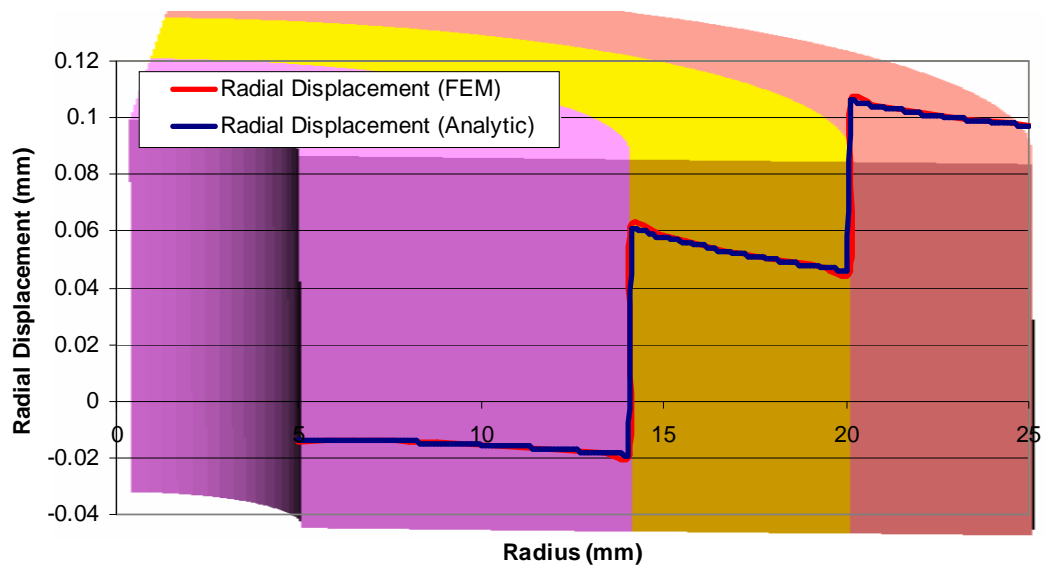
Figure 4.34. Radial displacement distribution solution of analytic formulas and FEA (Two ring system)

The final step of comparing the FE results with analytic formulas is analysing the dies by applying an internal pressure of 1000 MPa which represents the forming load on the die insert. The analyses performed for load free shrink fit assembly is repeated for these two cases where the uniform pressure is taken as the new boundary condition applied on the bore surface of die insert. In the FE analyses, only a new loadcase is defined for the applied pressure. In addition, for analytical calculations, the unknown constants are derived again by modifying the stress boundary condition on the inner surface. Program code written by using MathCad for one ring and two ring systems with internal pressure are given in Appendix B.3 and B.4. The results of the both calculation methods which are compared only for the radial and hoop stress distributions, are providing equivalent results (Fig. 4.35 and 4.36).
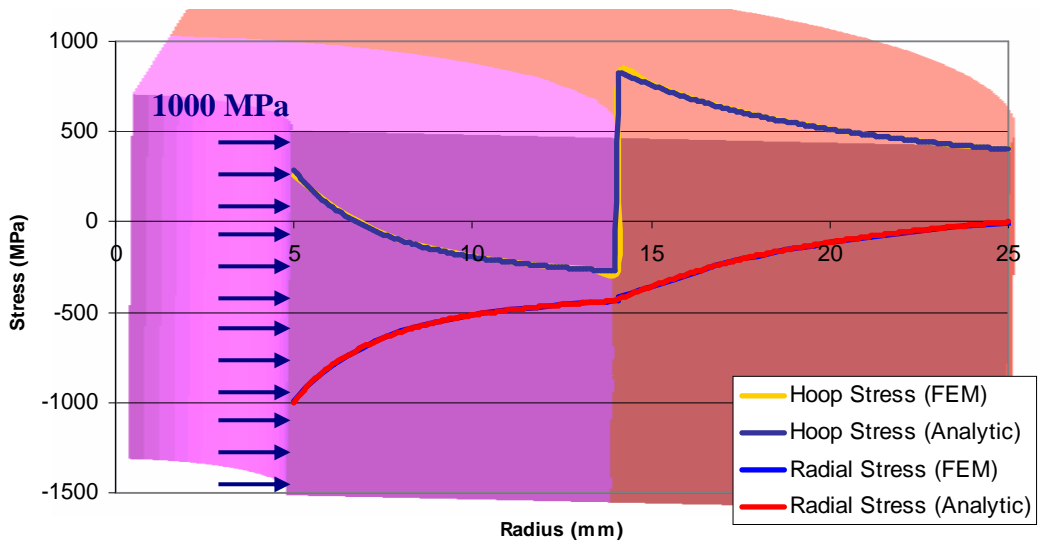
Figure 4.35. Radial and hoop stress distribution solution of analytic formulas and FEA with internal pressure (One ring system)
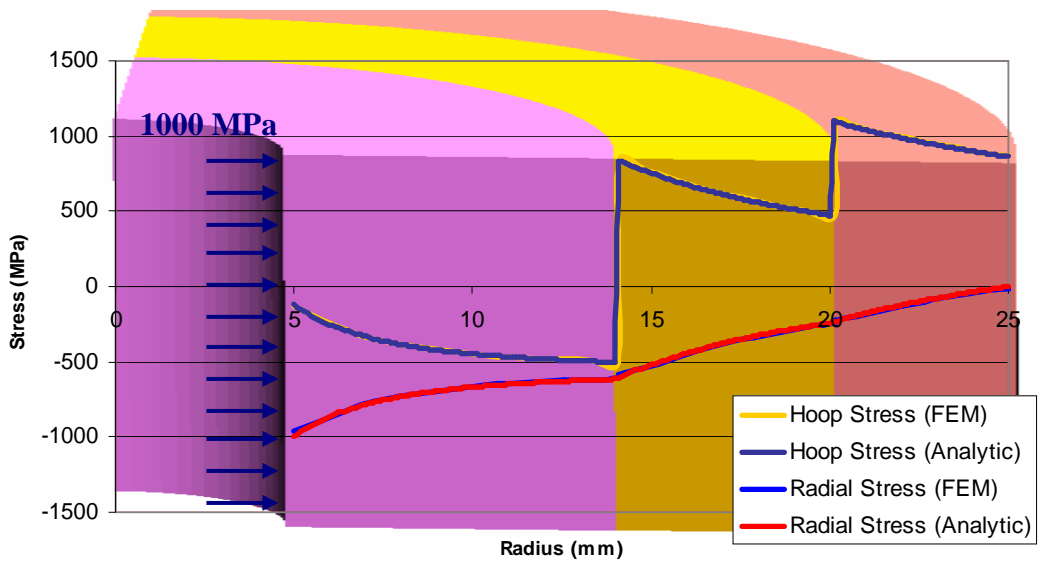
Figure 4.36. Radial and hoop stress distribution solution of analytic formulas and FEA with internal pressure (Two ring system)

Carbide inserts are frail to the tensile stresses which may lead to fatigue or brutal failure depending on the amount of generated stress. The analyses above are again showing how prestressing condition improves the stress distribution on the tool. Under the loading of 1000 MPa, tensile circumferential stresses formed on the die insert when only one stress ring is used are around 290 MPa. On the other hand, if the insert is prestressed by using two rings, circumferential stresses are preserved in the compressive region. For the same dimensions of forming tool, the tool life could be prolonged by using stress rings more than one with the optimum interferences.

4.6.3 Shrink Fit Assembly Experiment

In the previous section, the results of FE analyses of the assembly of die insert with uniform bore cross section along the length with one and two stress rings are in good agreement with the analytic solutions obtained by using theory of elasticity. To verify the results of computer simulations, a simple shrink fit test is performed by assembling one carbide die insert and two stress rings made from H13 hot work steel. The dimensions of the inner and outer diameters of parts after assembly is compared with the FE simulation results.

The insert inner and outer diameters are selected as 10 mm and 28 mm which are same with the ones used in previous calculations. The middle ring outer diameter is 50 mm whereas the second ring's is 70 mm. Before the production of stress rings, interferences are determined by using the MathCad program of two and three ring assembly where the equivalent stress will not exceed yield stress. First the insert and middle ring are assembled so the applicable interference between these two parts that will not yield the ring material is found as 5‰ (0.14 mm). The initial interference between middle and outer ring is defined as 1.4‰ (0.04 mm). However, this interference will increase after assembling the insert and middle ring so according to the analytical formulas actual interference will become 4.2‰ (0.12 mm).

The insert and rings are machined by using grinding machines and rings are heat treated to increase hardness between 40 - 45 HRC. In addition, the insert hardness must be around 62 HRC to be able to use material properties obtained from supplier.

After the production of parts are completed, three hardness measurements are performed for per part to check raw carbide appropriateness and heat treatment quality of the rings. Measured insert hardness is around 64 HRC and ring harnesses are between 42 – 47 HRC. The measurement locations on the parts are shown in Figure 4.37 and the measured values are listed in Table 4.3.
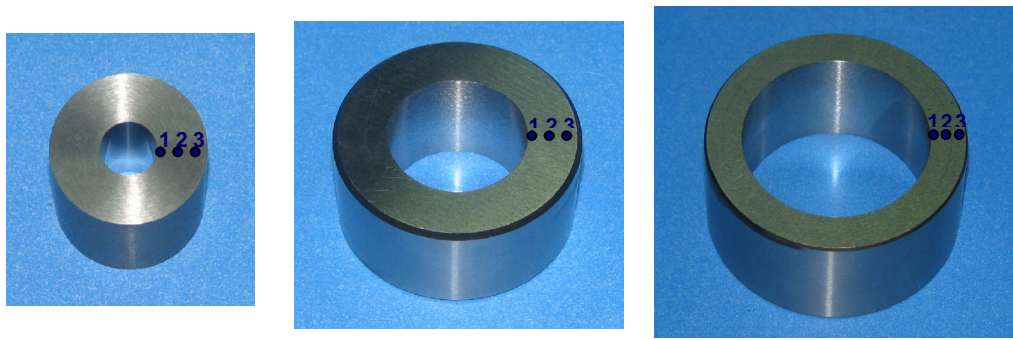
Figure 4.37. Hardness measurement locations on die insert *(left),* middle ring *(middle)*, outer ring *(right)*

Table 4.3. Hardness values on the shrink fit experiment components

	Hardness (HRC)		
	Die Insert	**Middle Ring**	**Outer Ring**
1	64.9	42.5	47
2	64.2	43.2	47.8
3	63.3	44.7	46.7

After each step of assembly, the inner and outer diameters are measured by using dial bore gage and calipers with resolution of 10 microns. To measure interference diameters precisely, surface of the tools are scanned by using perthometer and measured by aid of the computer software of the device.

The FE model is generated similar to the previous two ring assembly configuration shown in Figure 4.31. After each fitting operation, radial coordinates are taken from the nodes on inner, interference and outer surfaces.

In Figure 4.38 whole tool assembly after two shrink fitting is shown. According to the measured values given in Tables 4.4 and 4.5 before and after assembly is showing that, the maximum dimensional difference between experiment and FE analyses is 10 microns which is also equal to the measurement resolution. It is probable that the difference could be smaller than 10 microns, however devices with higher resolution is required to measure these values.

Figure 4.38. Tool after assembly of insert and two rings

Table 4.4. Diameters after assembly of insert and middle ring

	Die Insert Inner Diameter (mm)	**Die Insert Outer Diameter (mm)**	**Middle Ring Outer Diameter (mm)**
Initial	9.99	28.14	50.04
Test	9.97	28.11	50.12
FEA	9.97	28.12	50.13

Table 4.5. Diameters after assembly of insert and two rings

	Die Insert Inner Diameter (mm)	Die Insert Outer Diameter (mm)	Middle Ring Outer Diameter (mm)
Initial	9.99	28.14	70.00
Test	9.96	28.10	70.07
FEA	9.95	28.11	70.08

According to the test results given in this chapter the reliability of the FE analyses for shrink fit operation of bolt forming dies are proven. In the analyses presented later in this thesis, tool prestressing is performed by defining initial contact between the tool bodies.

4.7 Effect of Taper Angle on Circumferential Stresses

To perform the assembly of the insert and ring by press fitting, the requirement of a fillet or tapered conical surface on the insert has been explained before in Section 3.6. In addition to providing ease in assembly, another function of this conical geometry is to prevent the die insert move out of the stress ring during the ejection of the part after forming. This situation mostly occurs when the insert is assembled with no angle and the friction stress between the insert and workpiece is high enough to overcome friction between insert and ring.

Heading operation is a good example for this case. During the deformation of the head of the bolt, shaft exerts pressure on the die and makes it expand. After the punch releases the die shrinks and compresses the shaft of the bolt as the ejector starts moving the part out of die. Due to the friction stress on the insert, it starts to slide out of the ring (Fig. 4.39). After the part, with die insert stuck over its shaft, is transferred to the next station, the dies and other components of the press will be damaged as the punch hits the workpiece.

126

The insert taper half angle α can take a value between 0.2^o to 1.5^o depending on the die assembly. For assembling thick inserts into the rings, this angle is kept small close to $0.2 – 0.3^o$. Higher values are preferred to be used mostly for the assembling front conical dies into the case. An example of this process is presented in Section 4.11.1 where the optimum interference of a front conical die is investigated.
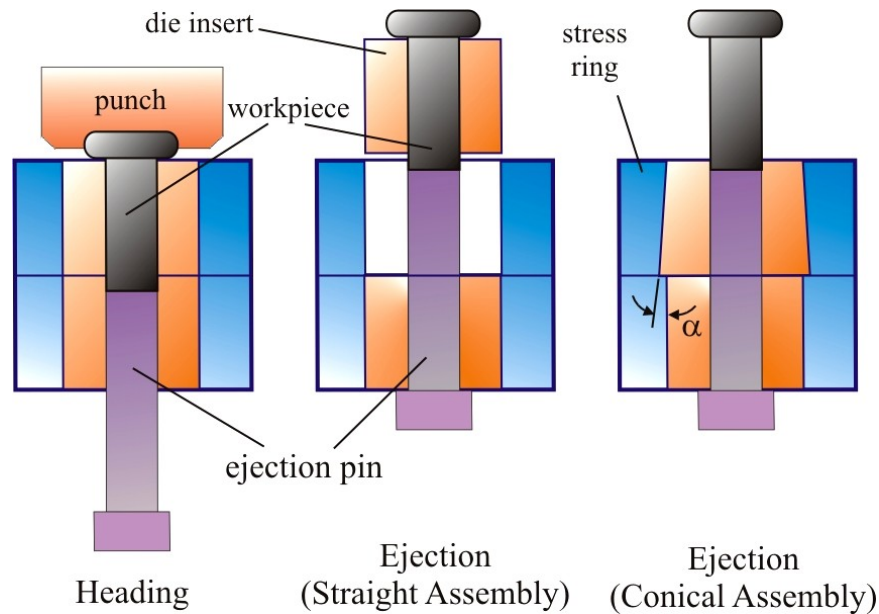
Figure 4.39. Stuck of die insert on the workpiece during ejection

To determine the necessity of modeling the conical angle for the shrink fit assembly, its effect on the generated hoop stresses is investigated. For this purpose, dies are shrink fitted with half angle of 0, 0.2, 0.4, 0.6, 0.8, 1 and 1.5 degrees and the hoop stress distribution is plotted along the inner surface. The die component diameters are taken as shown in Figure 4.40. The interference is specified as 5 ‰ (0.14 mm) and same for all angles.

The analysis results which are given in Figure 4.41 show that, the difference of hoop stress values between the two ends of the die is less than 5 % for the angles below 1°. However, the effect of the assembly angle becomes more significant for the
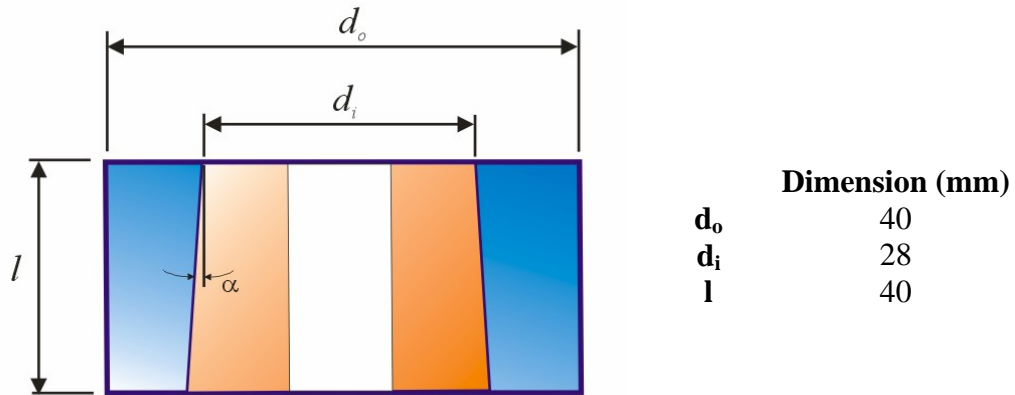
Figure 4.40. Tool assembly parameters with conical die insert

	Dimension (mm)
d_o	40
d_i	28
l	40

angles above 1°. According to these results, shrink fitting of dies which are performed with an angle larger than 1° should be modeled with the conical die insert for more accurate stress analyses. Another result gathered from these analyses is the reduction of compressive circumferential stress with increasing cone angle. Since the ring thickness at the bottom side of die gets less, effect of prestressing reduces.
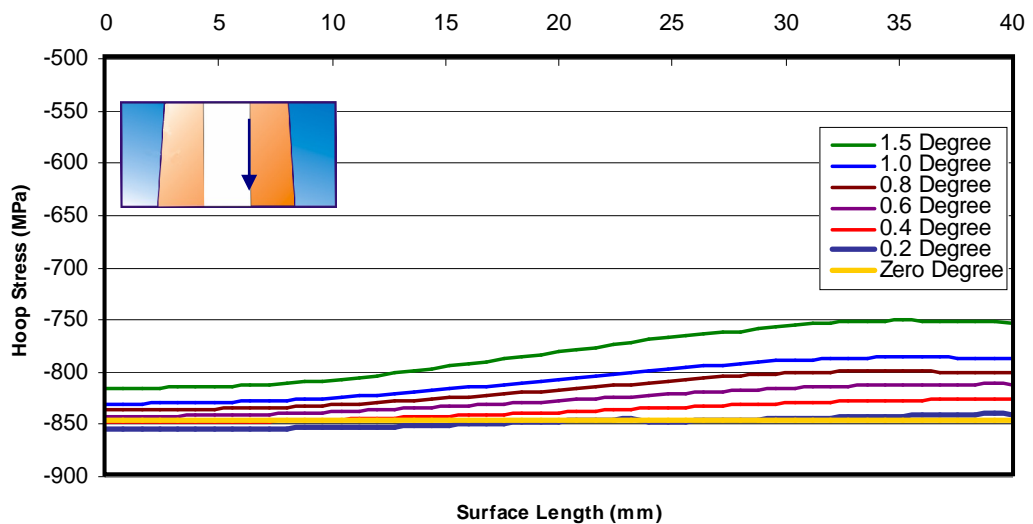
Figure 4.41. Hoop stress distribution for different shrink fit assembly angles

4.8 Optimization of Prestressing

The amount of prestressing can be set by performing assembly with different interference values. Although the amount of interference is the most important factor in prestressing, the dimensions of die components have also effect on the generated stress distribution. To obtain the best prestressing condition, the optimum values must be defined for diameters and interference. However, in bolt forming, the inner diameter of the insert and the outer diameter of stress ring is constrained by workpiece and case housing diameter on the press where the dies are assembled. The only parameters left for optimization are the insert outer diameter and interference.

While determining these values, two parameters must be taken into account. One of them is the value of circumferential stress on the die insert and the other one is the equivalent stress values on the die components. When the previous shrink fit analyses are examined, it can be seen that the minimum circumferential stress occurs on the bore surface of die insert. To prevent any sudden or fatigue failure, this stress value should be kept as low as possible. While performing this task the equivalent stress values on die components must be kept lower than yield stress of the materials to prevent plastic deformation. The most critical location where the plastic deformation occurs first is the inner surface of the stress ring. So the optimum interference and insert outer diameter must be selected by regarding these parameters.

A program is written by using MathCad, which is based on the analytical calculations of the shrink fitting, to determine optimum prestressing conditions. This program performs iterative calculations to compute circumferential and equivalent stresses on the critical locations for different insert diameter and interference values.

The range of the insert outer diameter is set between bore diameter and stress ring outer diameter. In each iteration, the circumferential stresses are calculated for the interference starting from 0.02 to 0.4mm for fix insert outer diameter. Then the

insert diameter is increased by 1% of the difference between the bore and ring outer diameter and calculations are repeated.

In each iteration, calculated circumferential stress is compared with the lowest value which is computed up to that iteration. If the last computed value is lower than the stored one and the equivalent stress is lower than yield stress on the inner surface of ring, the insert outer diameter and interference values used in this iteration are stored. If not, the stored values are not changed and next iteration starts. The program algorithm is shown schematically in Figure 4.42 and the code is given in Appendix C.
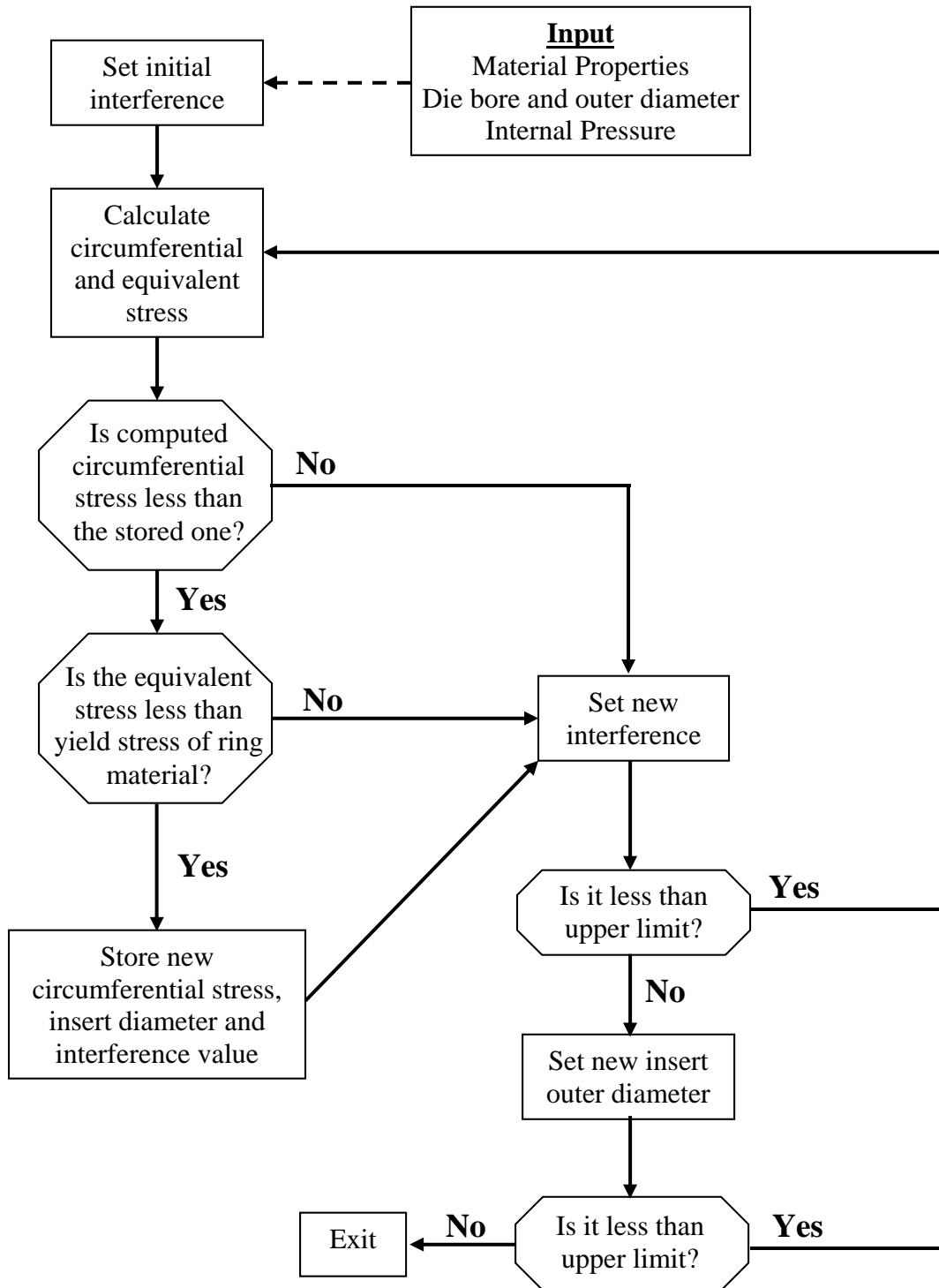
Figure 4.42. Flow chart of the optimization process

131

For the die geometry showed in Figure 4.28 where 1000 MPa pressure is applied, optimum insert outer diameter and interference is calculated by using the program is 21.5 mm and 5.1 ‰ (0.11) respectively. If the tool is assembled by using these dimensions and interference, the tensile circumferential stress will be reduced from 290 MPa to 125 MPa, in other words 57% improvement will achieved. Despite the optimum prestressing condition for one stress ring, the circumferential stresses are in tensile region. To keep them in compressive region two or more stress rings should be used.

4.9 Axial Prestressing

In addition to the radial prestressing, there is a second type of prestressing which is applied on axial direction to keep the split dies in contact under loading. This type of prestressing is mostly used in processes like extrusion or stepped bolt forming processes where dies are subjected to high axial loads. This is achieved by using special type of casing with internal threads. Other part of the casing is a matching nut which is screwed at the backside.

Figure 4.43. Axial prestressed extrusion die set

To see the effect of this type of prestressing an extrusion die set is analysed which is shown in Figure 4.43. This set is composed of 7 parts which are two shrink fitted dies, three blocks, case and nut.

The first step of this analysis is to measure the part dimensions to create the FE model. Secondly the dies and blocks are placed in the case and the nut is screwed by hand till it can not be tighten by hand anymore and the total length of the case is measured as 90.25 mm. As the next step, the nut is tighten by using a wrench and the total length is measured again. It has been determined that the total length is reduced to 90.05 mm which means that the nut is screwed additional 0.2 mm which provides axial prestressing.

According to the collected data, an axisymmetric FE analyse is performed where die components are compressed 0.2 mm by using a rigid tool representing nut. In this analysis, deformations on the threads of case and nut is neglected (Figure 4.44).
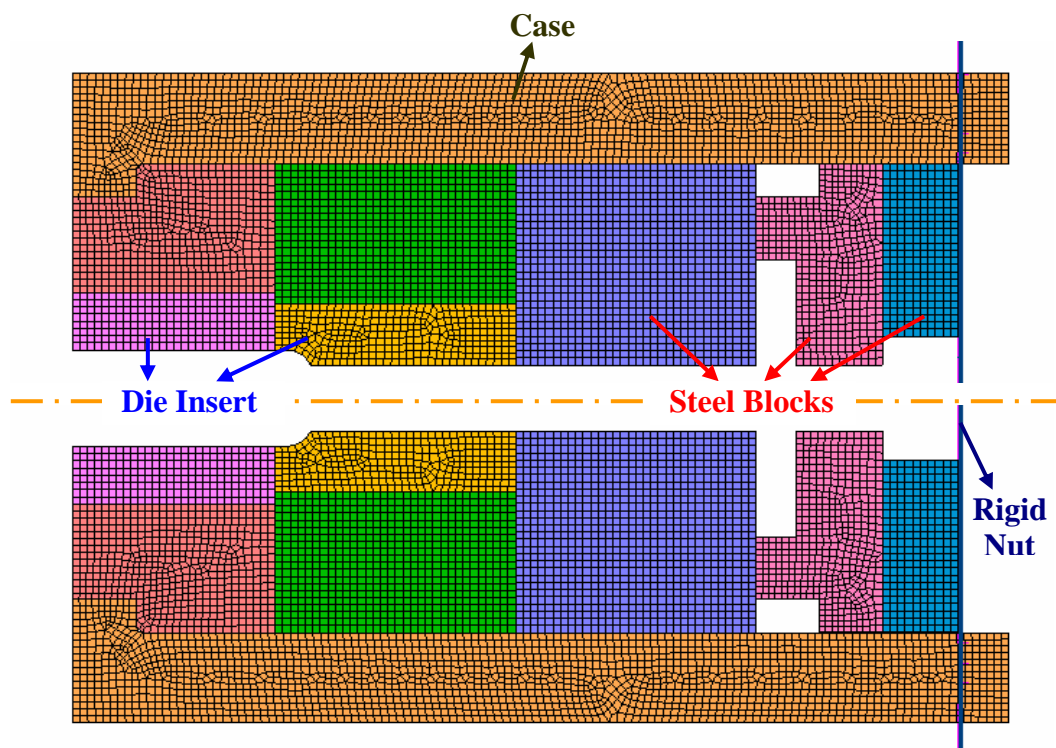
Figure 4.44. FE model of extrusion die set

133

At the end of the compression, total load acting on the rigid nut is calculated as 215 kN. This means that to break the contact between the shrink fitted dies, the extrusion force must exceed 215 kN. To check this situation, approximate extrusion force is calculated by using analytical formulation proposed by Siebel [74] given in Eqn. 4.39.

$$F_{total} = A_0 \sigma_{fm} \left(\varphi + \frac{2}{3} \tan \alpha + \frac{2 \mu \varphi}{\sin 2\alpha} \right) + \pi d_0 h \mu \sigma_{f0}$$ (4.39)

The equivalent plastic strain φ is defined as:

$$\varphi = 2 \ln \left(\frac{d_0}{d_1} \right)$$ (4.40)

and the mean flow stress is found from:

$$\sigma_{fm} = \frac{1}{\varphi} \int_{\varphi} \sigma_f \, d\varphi$$ (4.41)

The inlet diameter d_0 is 8 mm and outlet diameter d_1 is 5.5 mm. Material is assumed as a low carbon steel QST32-3 whose flow curve is available in MSC.Superform database. In order to calculate the integral given in Eqn. 4.36, the flow curve must be expressed in terms of $\sigma_f = C \varepsilon^n$. By fitting an exponential curve to the flow curve at room temperature and strain rate of 1.6 1/s, the material constant C and n is found as 650 and 0.13 respectively (Fig. 4.45). Moreover, the initial flow stress σ_{f0} of the material is equal to 340 MPa.

Although the die shoulder is in spherical form, to perform the calculations, cone angle 2α is assumed to be 90°. The extruded workpiece height h is taken as 15 mm and finally the coulomb friction coefficient μ is chosen as 0.07.

Total force to extrude this part is calculated as 51 kN which is much lower than the prestressing force. Since during this process the adjacent dies will be kept in contact and the undesired material flow between dies will be prevented.
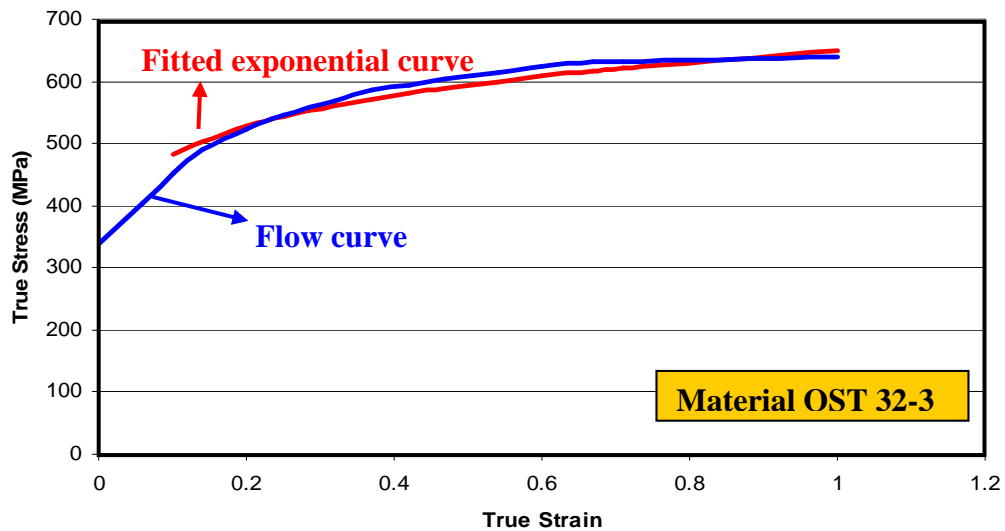
Figure 4.45. Determination of material constants

4.10 Comparison of Rigid and Deformable Die Model

Two different methods exist to perform die stress analyses. First of them is performing the forming process by using rigid die models and transfer the normal and shear stress distributions on the deformable die assembly as boundary conditions. By using this type of analyses, die stress distribution can be determined for only one forming step. For every stage of process, stress transfer procedure must be repeated.

The second method of stress analyses is modeling the dies as deformable bodies instead of using rigid dies. This will add the effect of tool deflections under loading during the deformation of workpiece. In Figure 4.46a, normal and shear stress distributions on a rigid extrusion die is shown. These stresses are applied as boundary conditions on the shrink fitted dies as in Figure 4.46b. Combined model of deformable dies with workpiece for same extrusion process is shown in Figure 4.47.

Normal Stress   **Shear Stress**

(a)

(b)
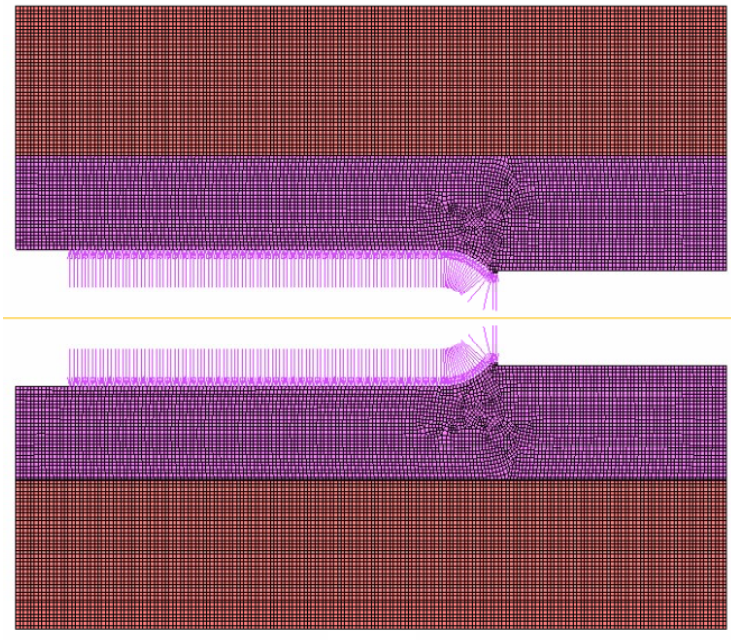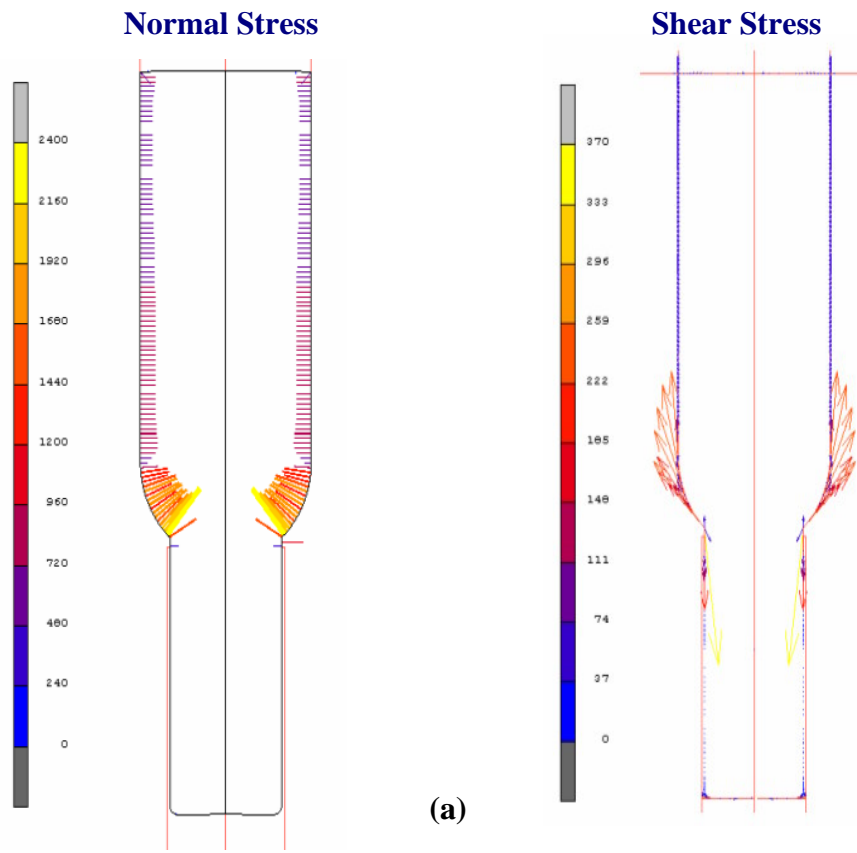
Figure 4.46. a) Normal and shear stresses on rigid die **b)** Transferred normal stresses on shrink fitted deformable die

136
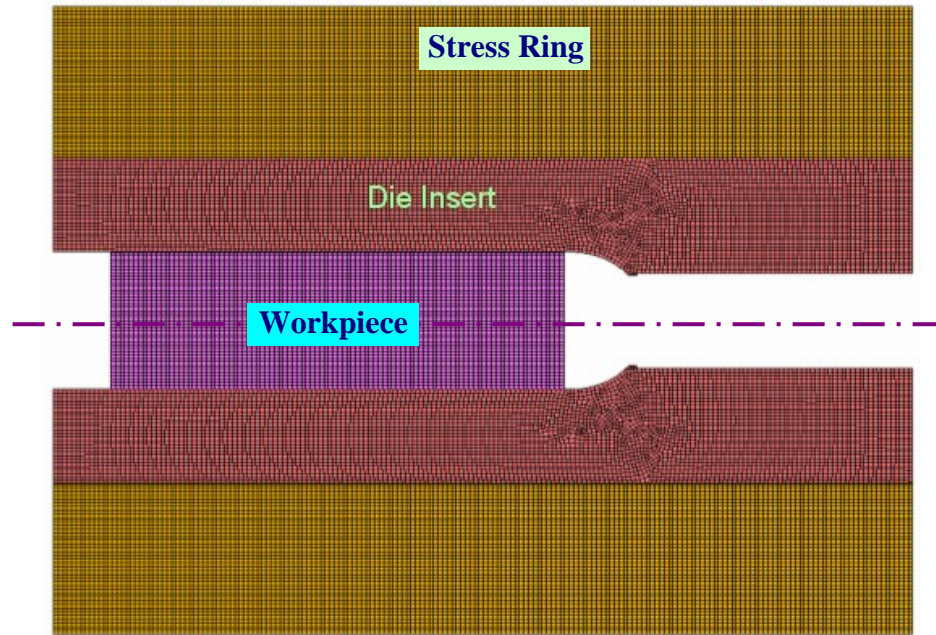
Figure 4.47. Complete model of workpiece and deformable

To see the effect of die model, on the stresses acting on tools and forming load, extrusion processes for different equivalent plastic strains (0.85, 1.2 and 1.6) are analysed. In these analyses three different materials are used, QST 36-3, 20MnB4 and C25B, which are commonly used in bolt production. The mechanical properties and flow curves of these materials are taken from the literature [60]. Die geometry and workpiece dimensions with process parameters are given in Figure 4.48.

Die inlet diameter D_i is 11 mm whereas due to the clearance between die insert and workpiece, billet diameter D_{wp} is smaller than inlet diameter and equal to 10.9 mm. The length of the billet L_{wp} is 30 mm. The insert and ring outer diameters D_1, D_2 are 26 mm and 50 mm respectively. At the exit side there is a relief hole to reduce frictional work on the extrudate, whose diameter, is about 0.05 mm larger than the extrusion exit diameter D_o. The exit length L_d is also kept small and taken as 0.5 mm to reduce effect of friction. Finally, the die shoulder is in spherical form with a radius R_d of 5 mm.

137
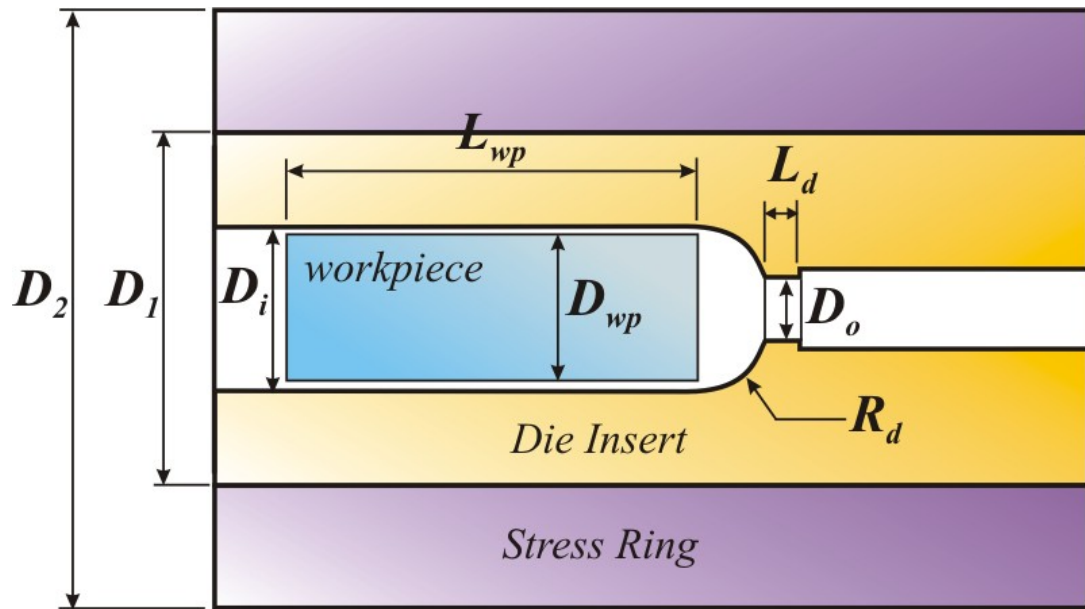
Figure 4.48. Extrusion die and workpiece dimensions

In the analyses performed by using rigid dies, the inner profile of the die is kept the same with the deformable case and represented by only using curves.

The results of analyses performed by taking Coulomb friction coefficient μ=0.1 showed that the forming force and normal stress distributions are different in all analyses conducted for different die models. The maximum extrusion force is always calculated 6-12% lower in the presence of deformable dies for all materials and equivalent strain values. The force and stroke curves obtained from the analyses by using rigid and deformable dies are given in Figure 4.49, 4.50 and 4.51 for workpiece material of C25B at three different equivalent plastic strains. For equivalent strain of 0.85, maximum force is computed as 136.2kN whereas it is calculated as 128.4 kN when deformable dies are used and force reduction corresponds to 6 %. For the equivalent strain 1.6, the extrusion forces are 272.5 kN and 244.1 kN for analyses including rigid and deformable dies respectively in which the difference is 11 %. Hence, the difference between the forming forces for two different die models increases as the equivalent strain value and forming load increases. This result can be verified by the results of analyses conducted by using other materials which are given in Appendix D.
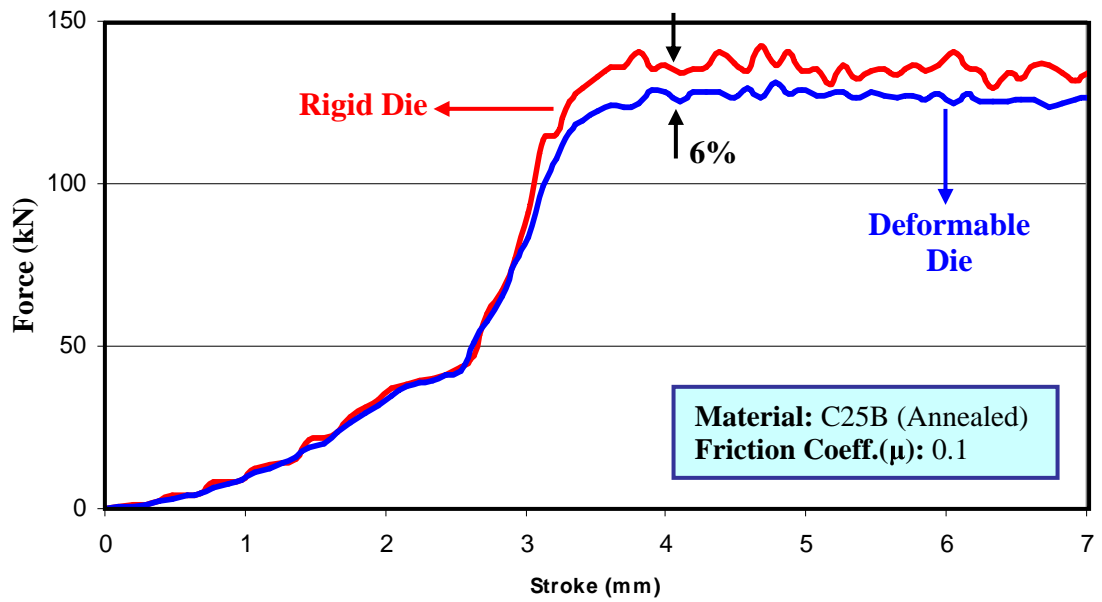
Figure 4.49. Force vs. stroke curve for $\bar{\varepsilon} = 0.86$
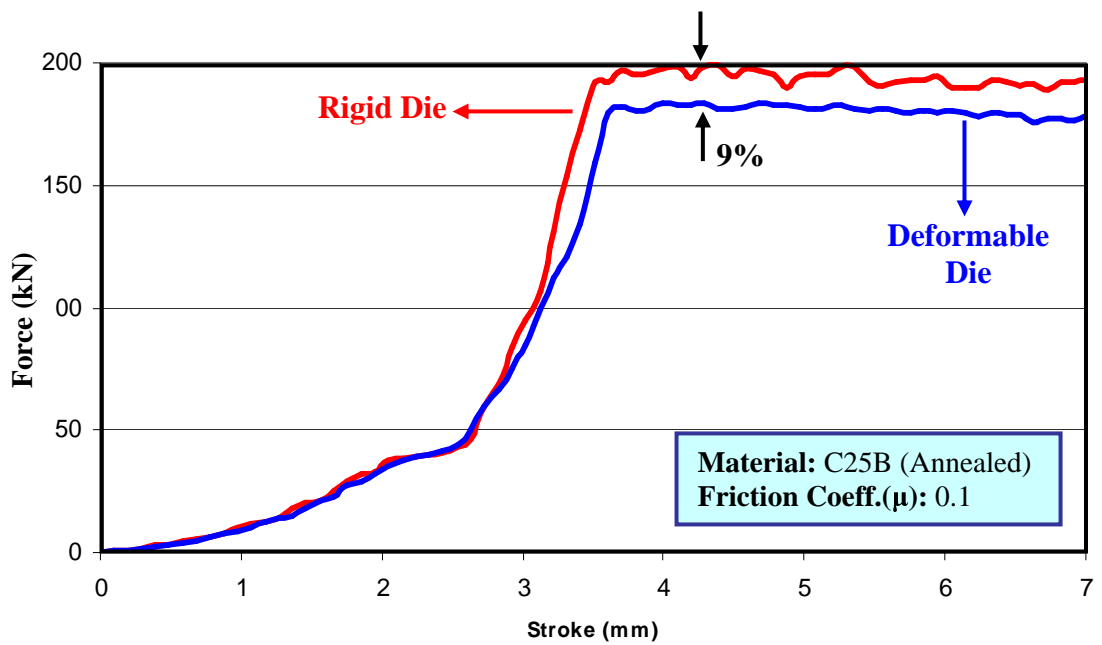
Figure 4.50. Force vs. stroke curve for $\bar{\varepsilon} = 1.2$
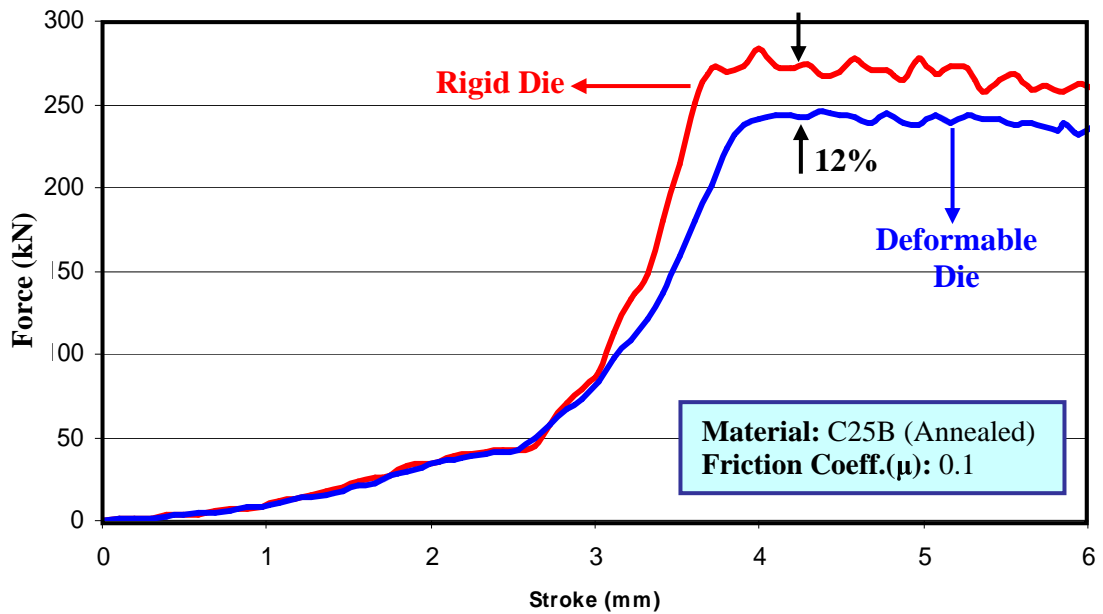
Figure 4.51. Force vs. stroke curve for $\bar{\varepsilon} = 1.6$

When the normal stress distribution is investigated, the reason for the difference in the extrusion forces between two die models is clarified. Calculated normal stresses acting on deformable tools are lower than the stresses acting on rigid dies. Also, alternating stresses are formed on the radius and fillet locations when the rigid tools are used which are extinguishing in the presence of deformable tools. All these excessive normal stress values lead to increase in calculated forming force due to the increased friction forces. Moreover, as it is observed in the force versus stoke curves, difference in the normal stress values are increasing as the forming load increases. In Figure 4.52, 4.53 and 4.54 normal stress distributions along the die surface are shown for workpiece material of C25B at three different equivalent strains. Normal stress distribution obtained for other materials are presented in Appendix D.
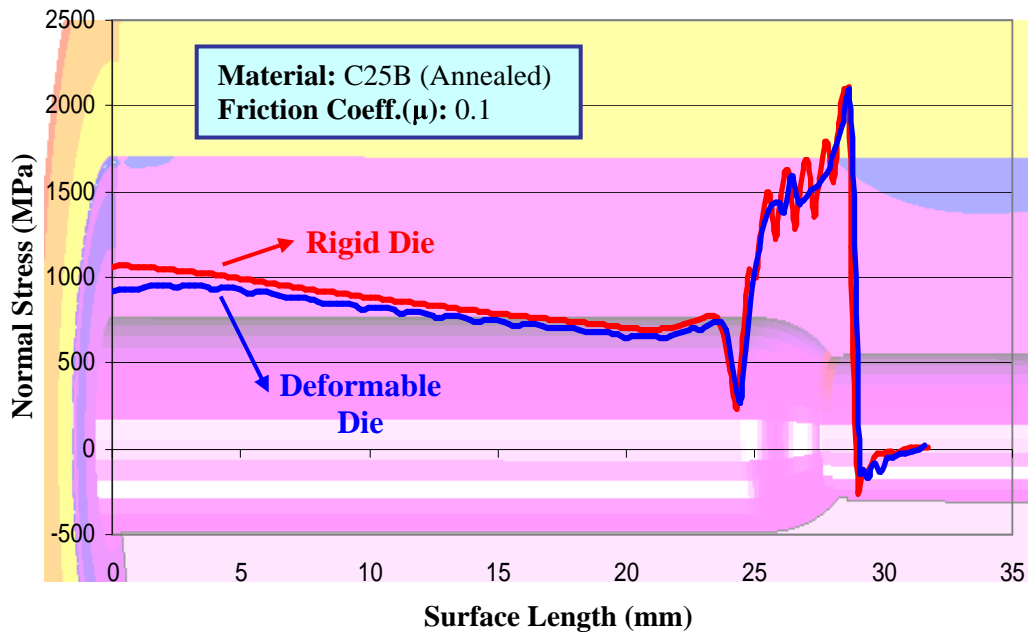
Figure 4.52. Normal stress distribution along die surface for $\varepsilon = 0.85$
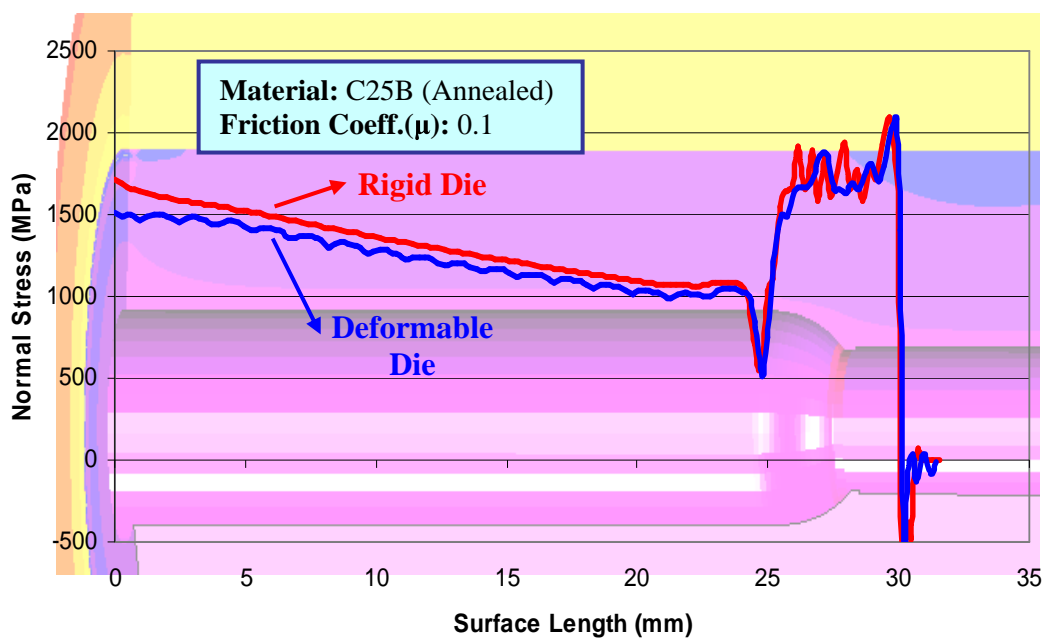
Figure 4.53. Normal stress distribution along die surface for $\varepsilon = 1.2$
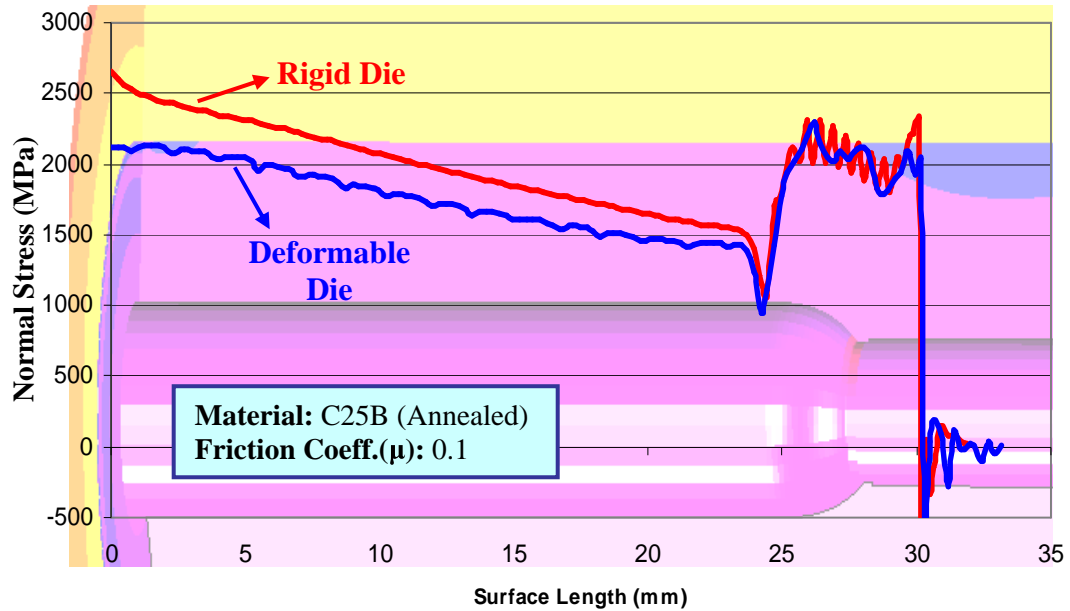
Figure 4.54. Normal stress distribution along die surface for $\varepsilon = 1.6$

Another difference between the forming analyses with different die models is the solution time. In these analyses when deformable tools are implemented in the models, solution time increases up to 10 times even there exist only one ring and insert. For more complex die assemblies this time increase may reach much higher values. Since this looks like a big disadvantage of using deformable dies, there can be some cases in which the die stress analyses cannot be performed accurately by using rigid dies and transfer the load on deformable tools. An example of such a case is given in Section 4.11.4 where a die failure occurs at a middle stage of forming.

The forged part dimensions are also different between these two analysis types. Since the deformable dies are deforming under the loading the forged part will expand. This effect cannot be observed if rigid dies are used. The difference in the dimensions of the extruded parts analysed in this section can be given as an example for this claim. The parts are ejected out of the dies by using a rigid curve

representing kickout pin. Due to the elastic spring back, extruded part diameter expands as it is pushed out. After kickout is completed the diameters of extruded and unextruded sections, D_e and D_u, are measured (Fig. 4.55). The diameters of these two sections of the part which is forged by using rigid dies are measured as 11.006 mm and 5.002 mm. For the part which is extruded by using deformable dies, the diameter of unextruded part D_u is 11.016 mm and the diameter of unextruded part D_e is 5.003 mm. Since both of the parts are released and expanded due to spring back, difference of 10 microns is caused by the deformation of die under high internal pressures.
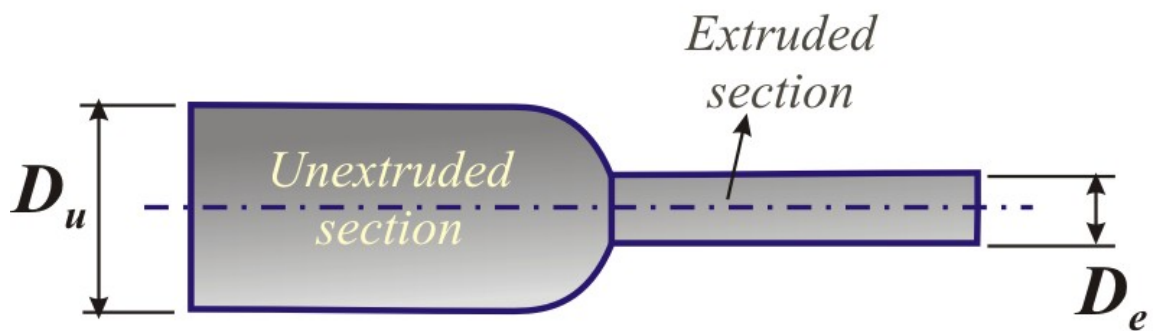
Figure 4.55. Extruded and unextruded section diameters

The results presented above show that both die modeling methods give different results. The presence of high normal stresses leads to increase in the calculated force. In addition to that, stress analyses performed by stress transfer from rigid to deformable dies, the overall stress distribution will include errors. Moreover when die geometries becomes more complex and stresses acting on tool surfaces vary, transferring the all stress data will be a difficult task and time consuming. In addition, it is required to repeat the same procedure for every solution increment which is not a feasible thing to do.

On the other hand, calculation of normal stress and forming force higher than it should be provides a safety condition for both die and press. If die stress analysis is to be performed for a single die with uniform cross section, stress data taken from the analyses with rigid tool can be used to obtain safer conditions. An example of this case is shown in Section 4.11.1 where the optimum prestressing is investigated.

To sum up, advantages and disadvantages of two different ways of modeling bolt-forming dies are given in Table 4.6.

Table 4.6. Advantages and disadvantages of different die modeling methods

Stress transfer method	Using deformable die models
Advantages	**Advantages**
Short modeling time	More accurate stress analyses
Short solution time for forming and die stress analyses	Elimination of alternating stresses
	More accurate product dimensions
Disadvantages	**Disadvantages**
Loose of accuracy during stress transfer	Long modeling time
Presence of peak stresses	Long solution time
Obtaining die stress distribution for only one increment in each time	Contact problems in complex die assemblies
Dimensional inaccuracy due to ignoring die expansion	

4.11 Case Studies

In this section industrial bolt production cases are analysed in which possible die failures are determined and modifications are performed to improve tool life by using FE analyses. Results of these modifications are also presented wherever it is

144

possible. All cases here are studied in *Norm Fasteners Co.* Material properties like flow curve at different strain rates, Young's modulus and Poison's ratio used in the analyses are acquired from [60].

4.11.1 Prestressing Optimization of Conical Die

In this case, optimization of prestressing is studied of a conical die used for head preforming in the third station. Analysed part is a M10 stepped bolt which is forged in 5 stations (Fig. 4.56). Since the part is heat treated after forging and this requires element boron, 20MnB4 medium carbon steel is used. To reduce its hardness and increase formability, raw material is annealed prior to production.
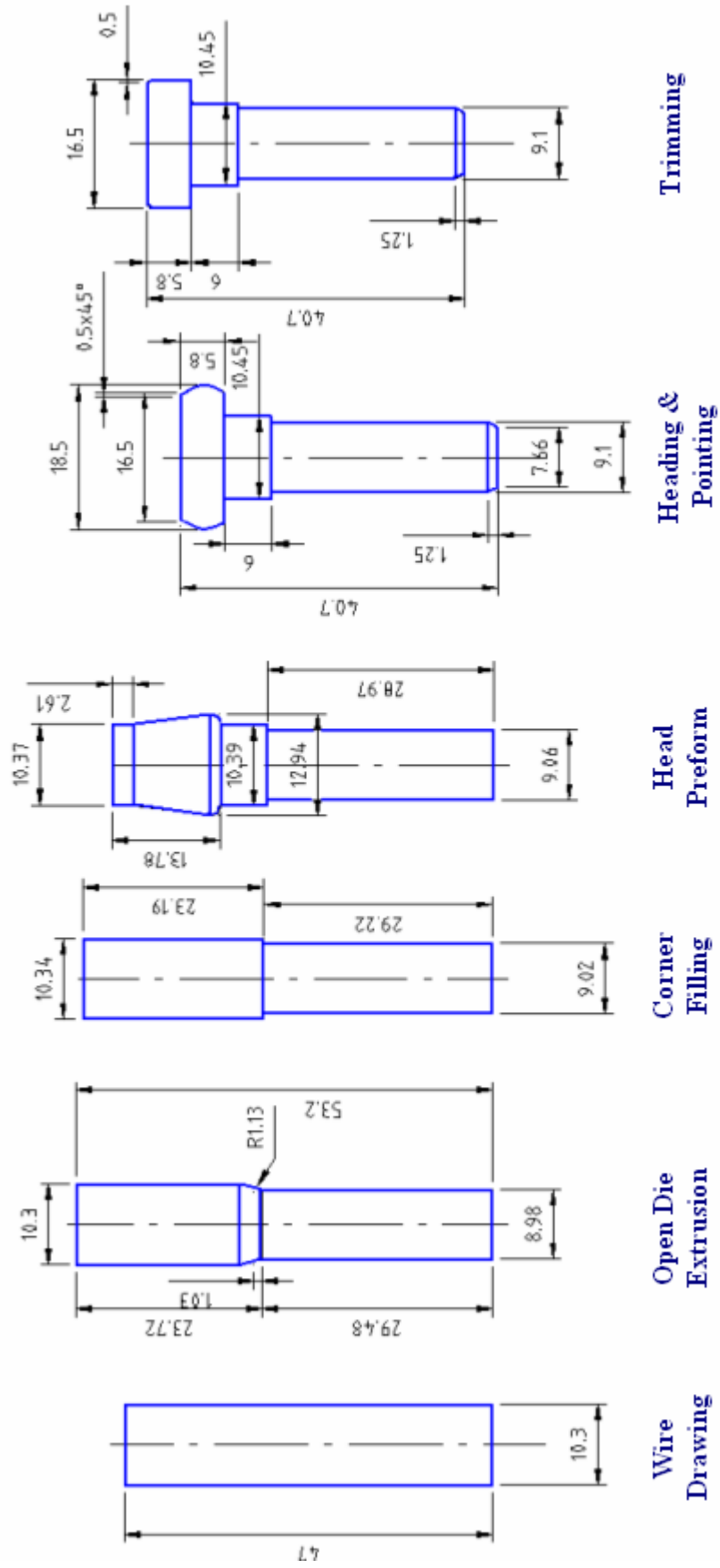
Figure 4.56. Forging steps of M10 step bolt

Figure 4.57. M10 Cylinder head stepped bolt

Before starting to forge the material, the wire is drawn from 11 mm to 10.30 mm. After the drawing, wire is cut off into billets with length of 47 mm. In the first station, the diameter of billet is reduced to 8.98 mm ($\bar{\varepsilon} = 0.27$ and 24 % area reduction) by performing open die extrusion with a cone angle of 26°. Since a sharp edge is required at the step region, in the second station a close die forging process takes place which is named as corner filling. Before creating the head form of the bolt, a preform shape is required due to the prevent buckling during heading. So that in the third and fourth stations two stage heading process is performed where the slenderness ratio is 2.24. Also in the fourth station pointing operation takes place which is performed to form the tapered tip section of the bolt. Finally in the fifth station the cylinder head is formed having diameter of 18.5mm by trimming the bolt head with a cylindric trimming tool (Fig. 4.57).

In the third station, during the head preform, a thin die which placed at the front side of stationary die case is needed to form the step part. Since these dies are assembled into casings with taper angles greater than 2° they are named as conical dies. Generally this type of dies mostly fail due to high internal pressures at low cycles.

All forming operations starting from the wire drawing are modeled and analysed by using rigid tools. Although for accurate results it is necessary to use deformable die models, in order to include safety condition by calculating internal pressure higher, rigid tools are used in third station analyses (Fig. 4.58).
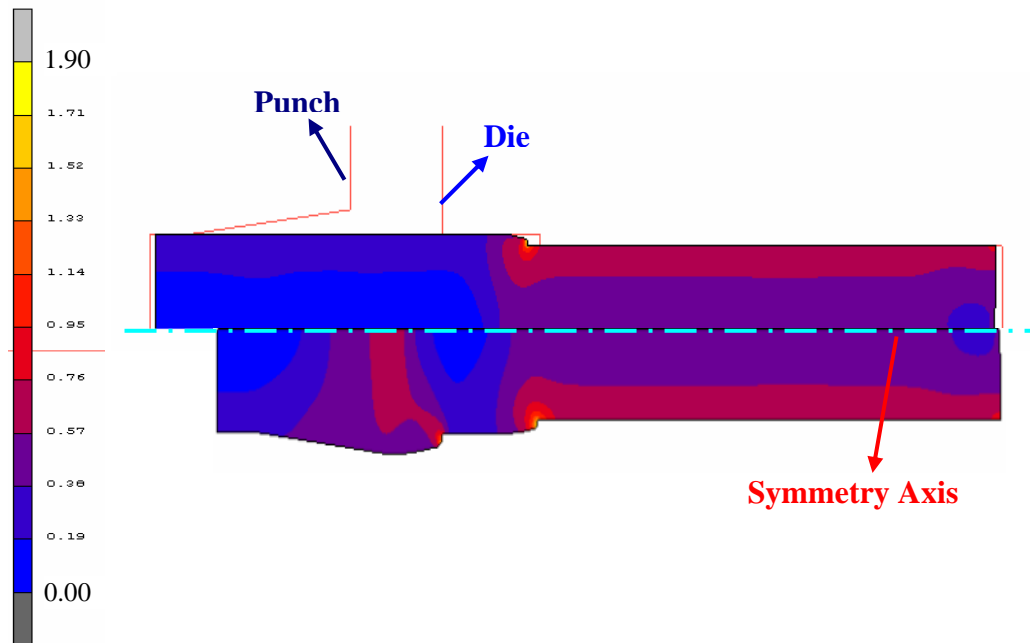
Figure 4.58. Plastic strain distribution at the beginning and end of deformation

Highest normal stress distribution occurs at the final phase of deformation. Along the step surface, normal stress values are calculated between $1200 - 2100$ MPa (Fig. 4.59). Shear stresses on the surface which are around 100 MPa are not included in the stress analyses since their effect is negligible compared to normal stresses.

Figure 4.59. Normal stress distribution on the step surface
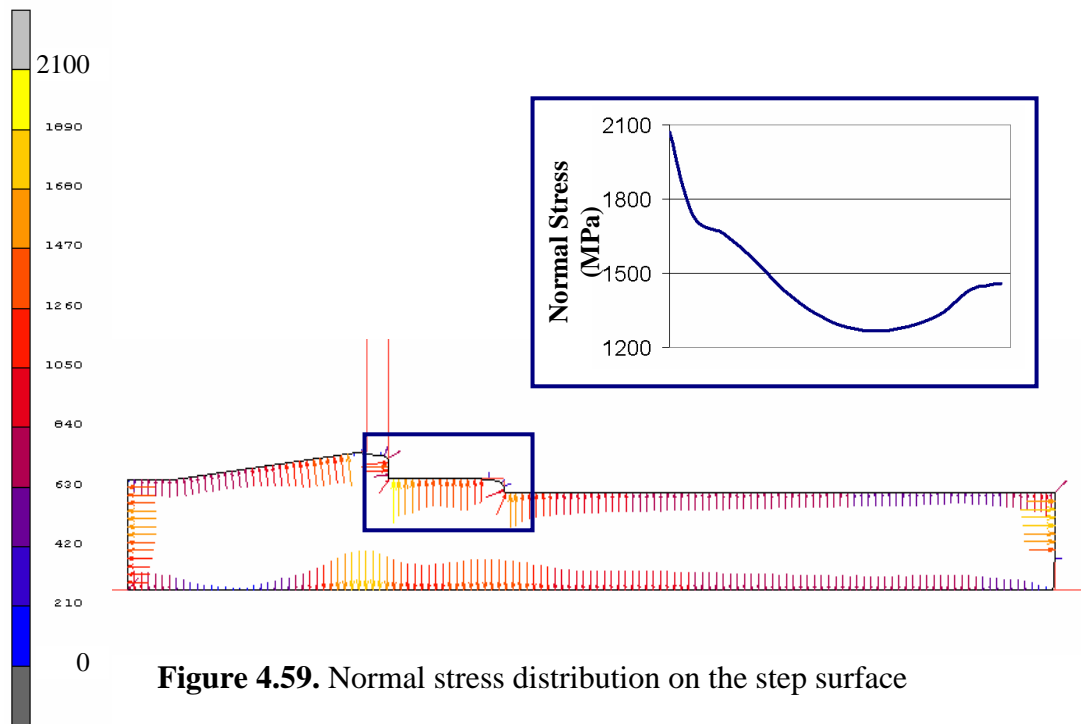
Before starting die stress analyses initially, the die insert diameter is selected as 26 mm with the ring outer diameter of 59.21 mm. Bore diameter of the insert is a design constraint as 10.39 mm. Also the outer diameter of ring varies due to cone angle of 5°.

To specify a maximum interference value where stress ring does not yield after the assembly, MathCad program is used. Figure 4.60 shows the equivalent stress distribution on die components for 6.1 ‰ (0.16 mm). Since the equivalent stress value on the ring inner surface is about to exceed the yield stress, at higher interferences, ring material will yield during assembly.
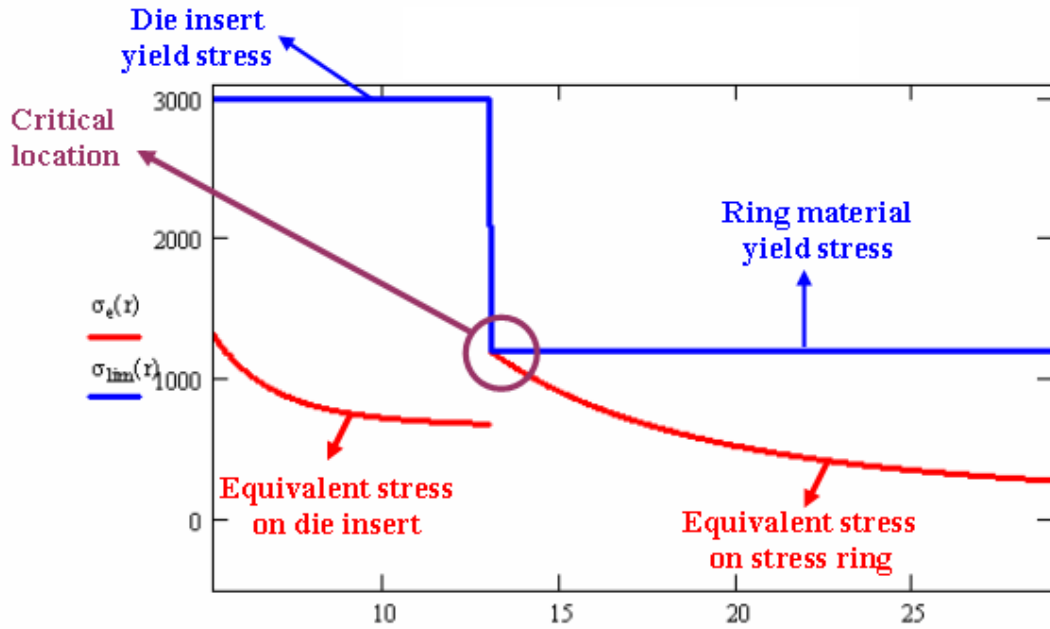
Figure 4.60. Equivalent stress distribution along radius

After applying the normal stress distribution on the bore surface as boundary conditions for 6.1 ‰ interference, the ring is plastically deformed at the inner surface. By reducing the interference down to 4.6 ‰ (0.12 mm), plastification on the ring is eliminated.

Another important parameter is the generated circumferential stresses on the bore surface of the die insert. When one ring is used for prestressing with 4.6 ‰ interference, hoop stresses increase up to 1000 MPa close to front surface. This will yield to fatigue failure of the die at low cycle numbers. To reduce the tensile hoop stresses, two ring prestressing system is analysed. Interferences are first defined by analytical formulas then applied to FE analyses for more accurate calculations due to varying pressure and ring outer diameter. After using a middle ring by preserving the dimensions of insert and defining interferences of 4.6 ‰ and 3 ‰ between insert – middle ring and middle – outer ring respectively, tensile circumferential stresses reduced to 360 MPa (Fig. 4.61).

150
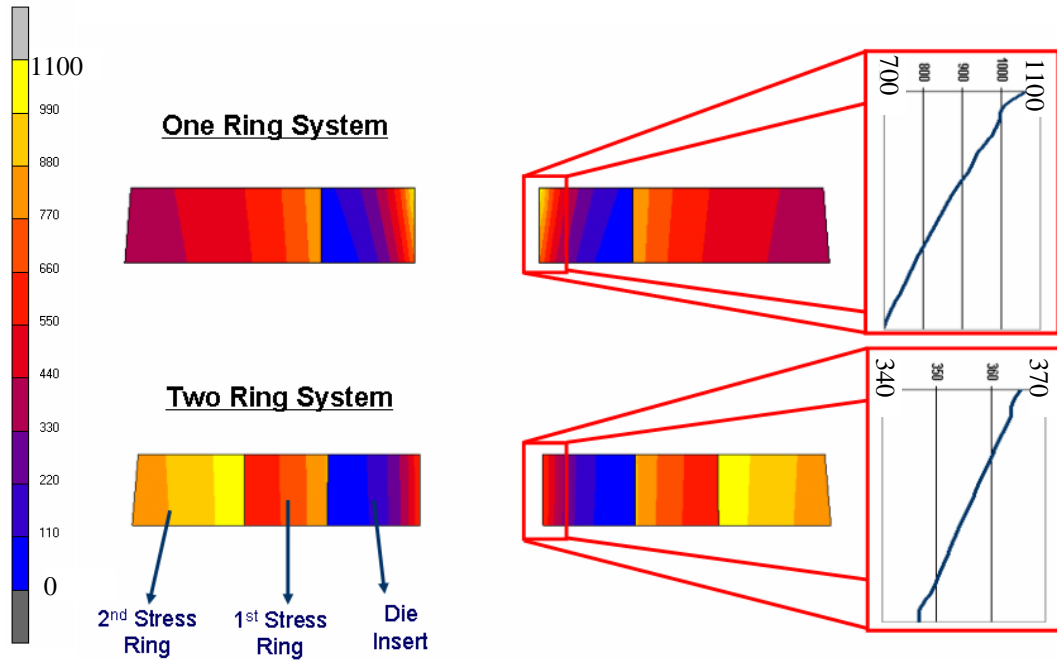
Figure 4.61. Circumferential stress distribution for one and two ring systems

4.11.2 Protrude Failure on a Rivet Die

Second die stress analysis is focused on the failure of a die protrude which forms the groove under the head of 4.80 mm rivet. At every $20,000 - 30,000$ pieces, fracture occurs on this region (Fig. 4.62).

This part is produced by using a low carbon steel QST 36-3, in two stations following the wire drawing. In the first station a preform is given to the head of part and in the second station, final heading is performed with forming the groove under the head (Fig. 4.62).

Firstly, the factors cause die failure is investigated by analysing current design. As the first step, wire drawing operation is simulated by reducing the diameter of the raw material from 5.50mm to 4.75mm. After cutting of the billet in 25.13 mm, the head preform is formed by using rigid tools.
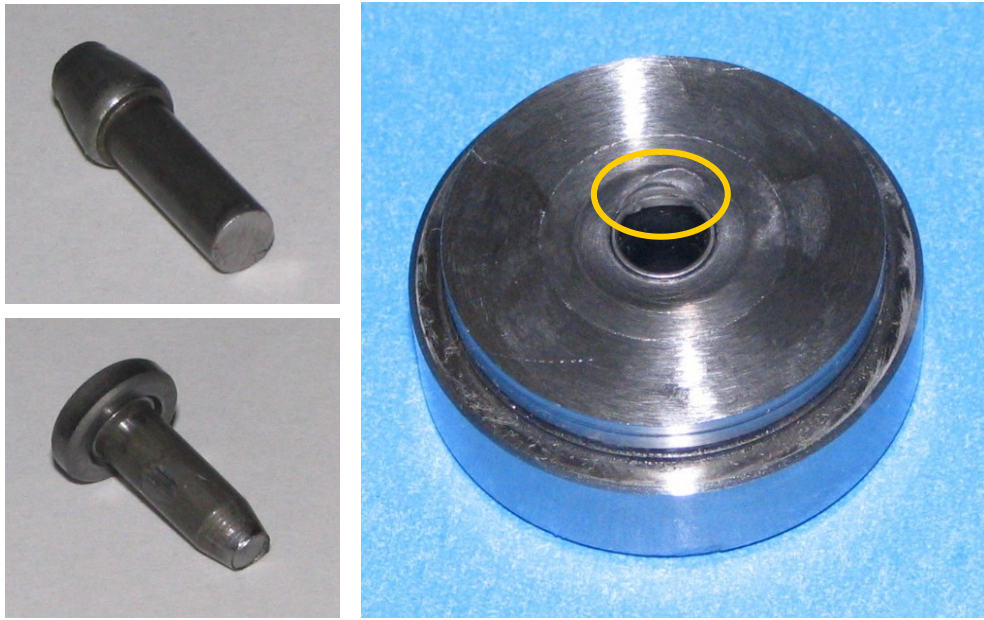
Figure 4.62. Forged parts at each station *(left)*, Fractured die

To analyse the stress distributions on the die insert in the second station, stationary dies are modeled as deformable bodies where the punch is assumed rigid. The stationary die consists two components. First one is a front conical die with thickness of 4.5mm and the second one is main die where shaft and groove is formed. There also exist steel support dies which do not have a direct role on forging. So that they are omitted in the analyses. For the assembling of the dies while prestressing, node overlapping method is used. The conical die is shrink fitted into the case is with 6 ‰ (0.16mm) interference and the interference between main die insert and stress ring is 5 ‰ (0.06mm). Initially 1250 MPa compressive circumferential stresses are generated on the die insert (Fig. 4.63).

At the last stage of heading process where maximum forging load is present, the minimum compressive stresses calculated as 3200 MPa where the compressive strength of the die insert is exceeded (Fig. 4.64).
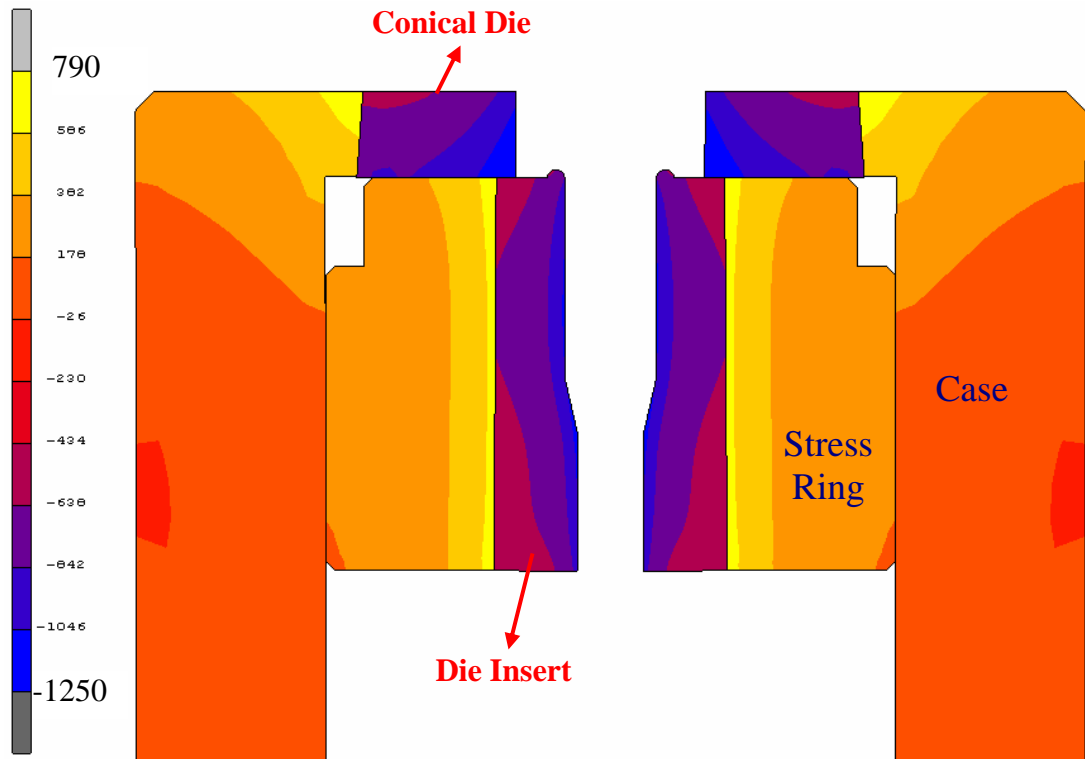
Figure 4.63. Circumferential stress distribution after prestressing of tool components

To reduce the stresses on the protrude, two parameters can be modified. One of them is increasing the interference above 5 ‰. Analytical calculations showed that when the interference is set above 5 ‰ and the internal pressure exceeds 650 MPa, stress ring plastically deforms. According to the results of FE analyse, the internal pressure on the die insert reach up to 800 MPa. So that the other parameter which is the head preform must be modified to eliminate die failure.

Before starting stress analyses on dies for new preform geometries, initially the material flow is analysed to check die filling by using rigid tools.

Some of the preform shapes result in improper die filling and lap formation. Two examples of these cases are shown in Figure 4.65.
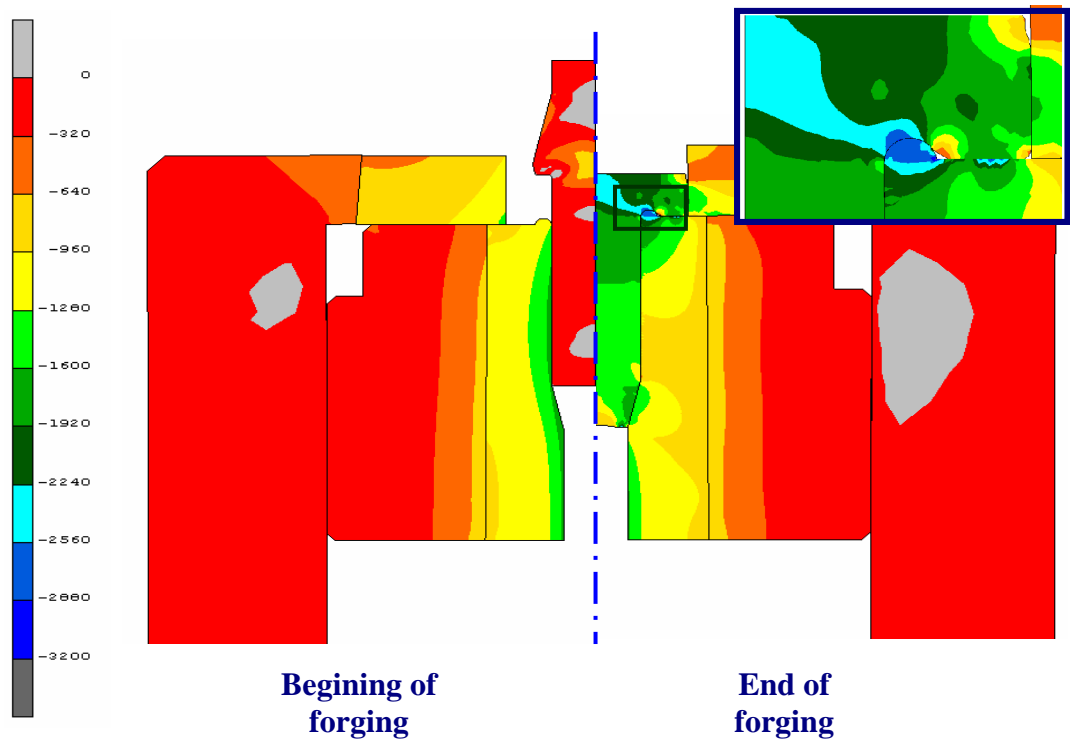
Figure 4.64. Minimum principal stress distribution at the beginning and end of forging
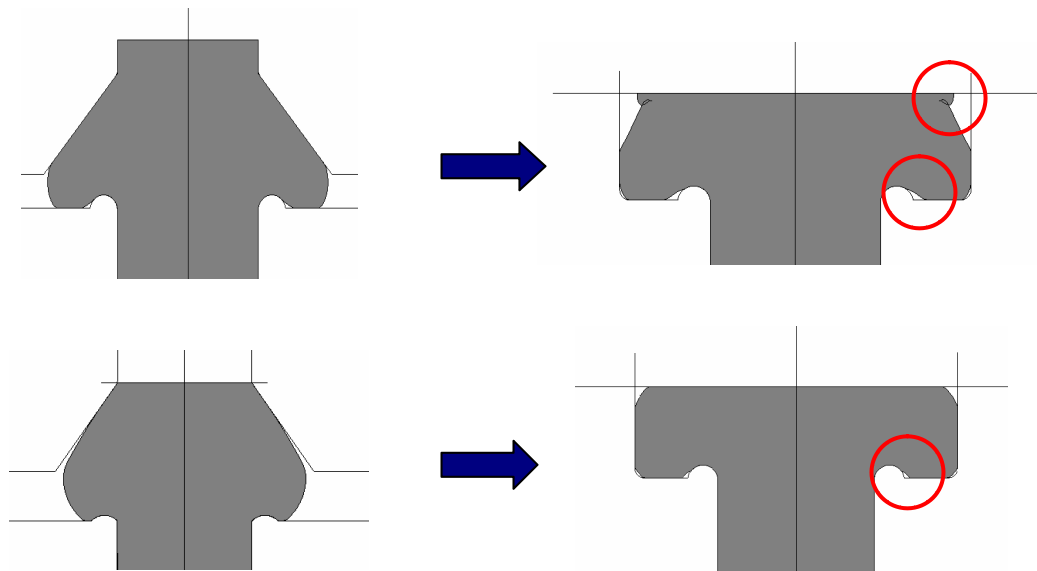
Figure 4.65. Improper material flow for two different preform geometries

154

Among the several preforms tried to obtain proper head shape, two of them establish the best material flow. By using the same deformable die model, these two parts are forged and the principal stress values on the protrude are compared with the previous results. By using the first preform, compressive principal stresses are reduced to 2500 MPa, where as the second one reduces to 2000 MPa. The preform geometries with resultant stress distribituon around the protrude is shown in Figure 4.66.
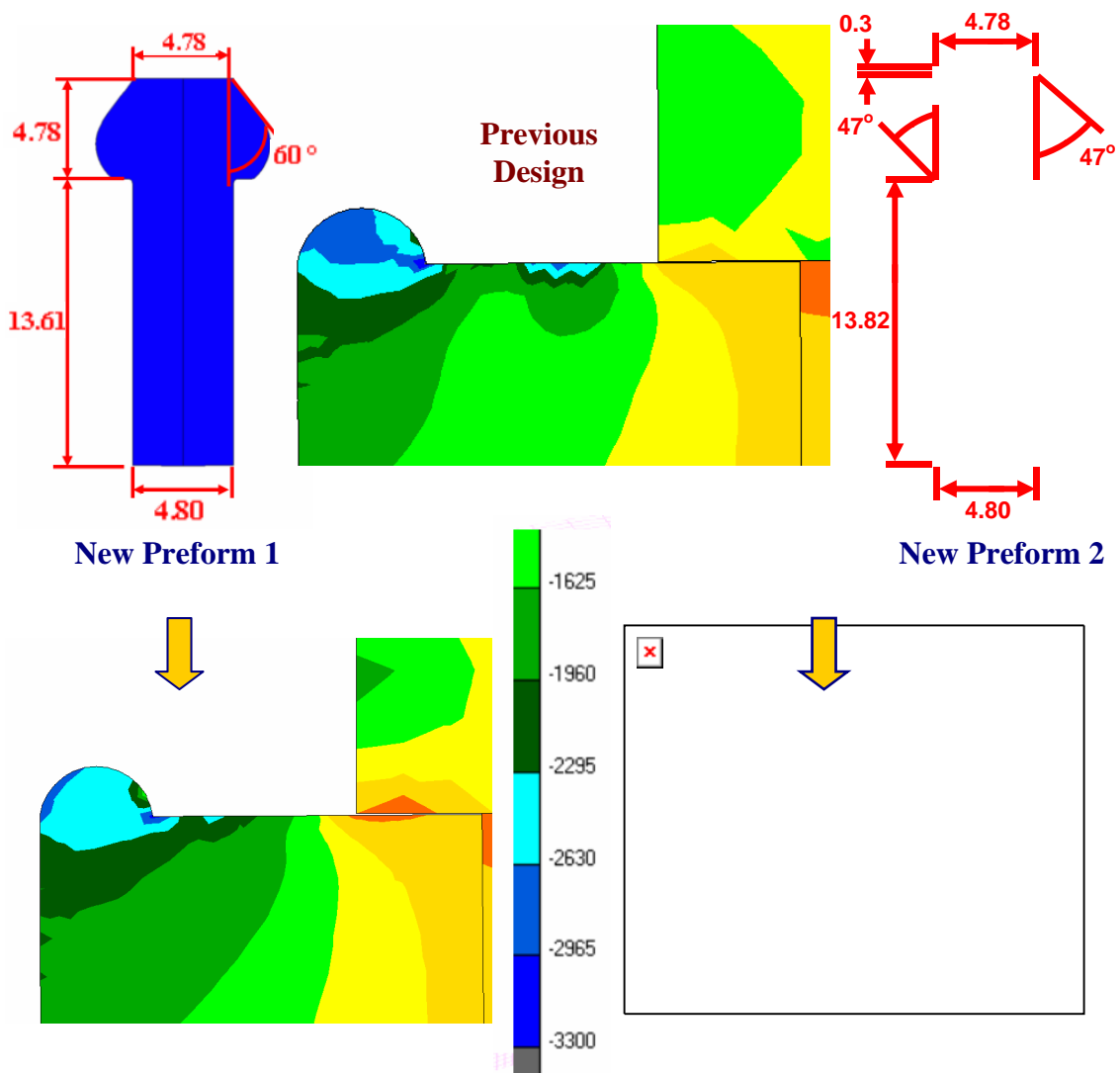
Figure 4.66. Comparison of principal stress distribution between two new preform shapes and previous design

After producing the new dies for first station and using in the forging operation, tool life increase is recorded up to 100,000 cycles. The old and new head preform of real part is shown in Figure 4.67.
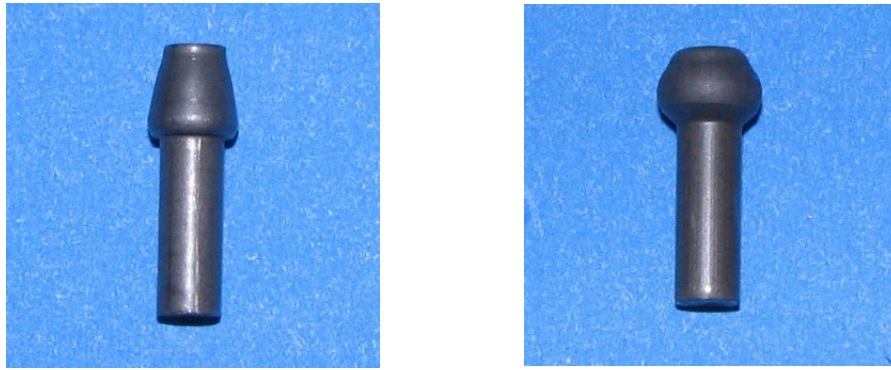
Figure 4.67. Head preform; Old design *(left),* New design *(right)*

4.11.3 Die Stress Analyses of a Cylinder Head Pin

In this third case, elimination of the tensile stresses on a die insert is studied. The pin that is shown in Figure 4.68 is designed to be forged in three stations. As in the all bolt forming processes, the production is starting with the wire drawing process. After the diameter of the wire is reduced to 9.7mm from 10mm, to flatten the shear surfaces which are formed during cropping the billet, a corner filling operation is performed.
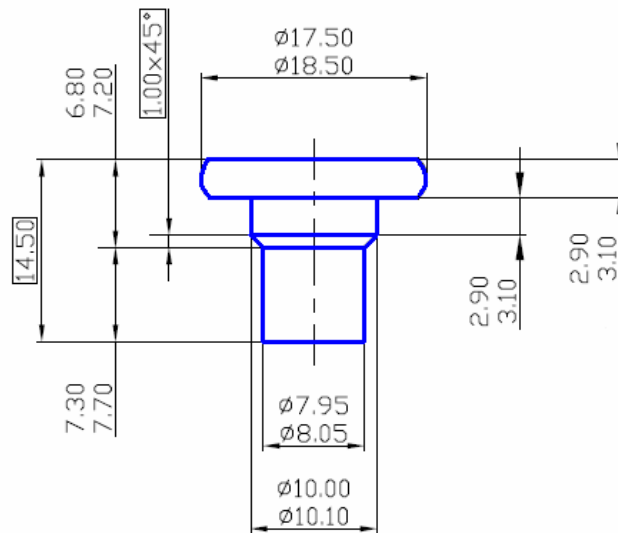
Figure 4.68. Cylinder head pin dimensions

In the second station, the diameter of the billet is reduced to 7.95 mm by extrusion. Finally, in the third station, heading is performed and part is completely formed.

First, the material flow behavior and forming forces are analysed by performing forging simulations with rigid tools. Again, to reduce deformation forces, used medium carbon steel is annealed before production (20MnB4). The analyse results show that in all forming steps, the material flow is as desired and part is formed without any defects (Fig. 4.69)

The forging forces are calculated as 79 kN, 77kN and 235 kN in each station respectively. Therefore, the total force acting on the ram of the press will be 391 kN which is close but lower than the selected press capacity which is 400 kN.
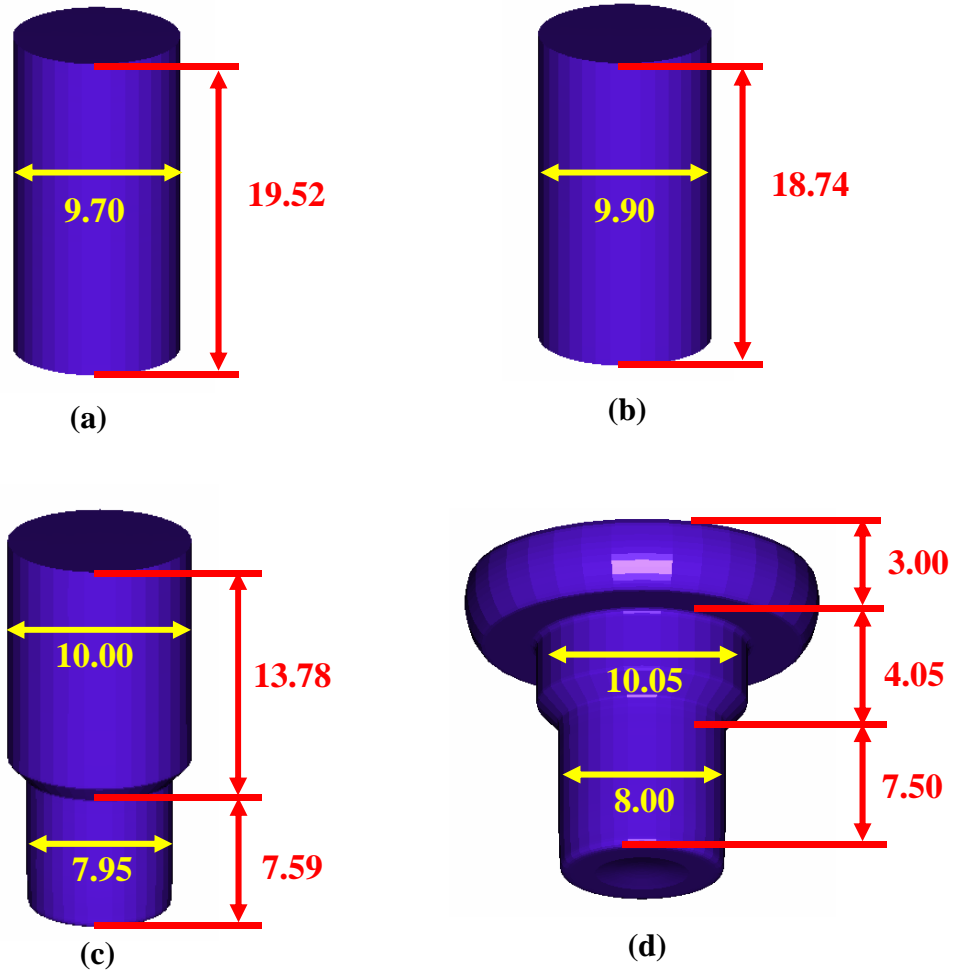
Figure 4.69. Forging steps; **a)** Wire drawing **b)** Corner filling **c)** Extrusion **d)** Heading

When the stresses acting on the die in the third station is considered, possible bending effect is noticed on the conical face of the insert. The stress values are around 2000MPa which may lead to formation of tensile stresses at the beginning of the conical surface (Fig. 4.70).
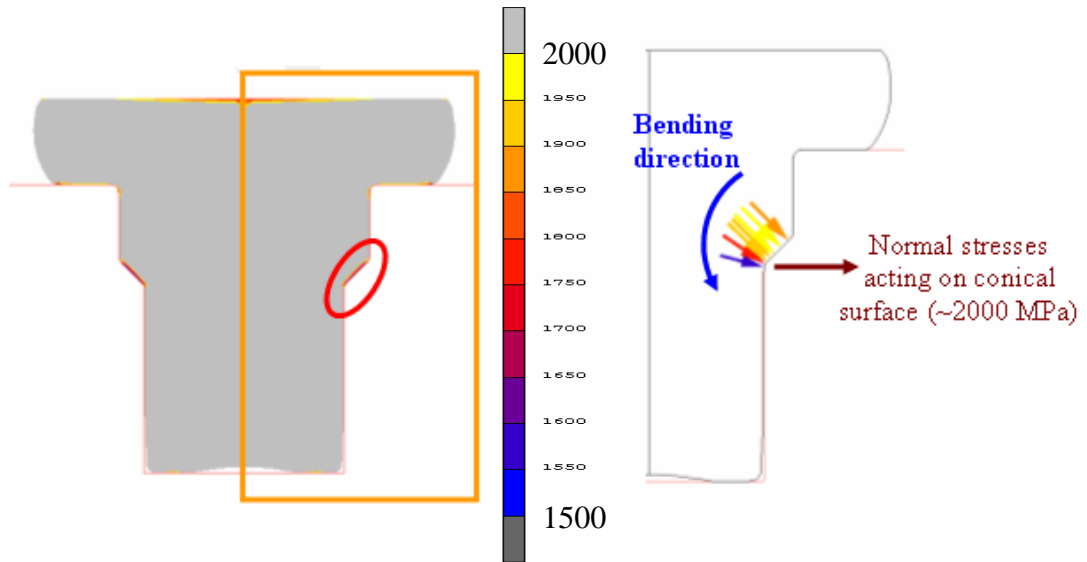
Figure 4.70. Normal stresses acting on the conical face

To investigate the stresses on the critical region in detail, third station stationary dies are modeled with deformable tools as shown in Figure 4.71. Die insert and ring materials are selected as G55 and H13 (1.2344) respectively. The interference between insert and ring is set as 5 ‰ (0.12 mm) and performed by using node overlapping method. The kickout pin and the punch is modeled as rigid tools. The friction coefficient is taken as 0.08 on insert and 0.1 on the punch and kickout pin since their surface is rougher than the bore surface of the insert.

It is expected to see maximum tensile stresses at the end of the stroke. However, no tensile stresses are determined on the insert at the final stage of forming. When the forging process is monitored from beginning to end, formation of tensile stresses are seemed to start at the 11 % of the stroke and have a maximum value of 700MPa at the 26 % of stroke (Fig. 4.72). After this stage, stress values diminish towards the end of stroke. This implies that if the analyse was performed by stress transfer method, it would be a time consuming procedure to define formation of tensile principle stresses.
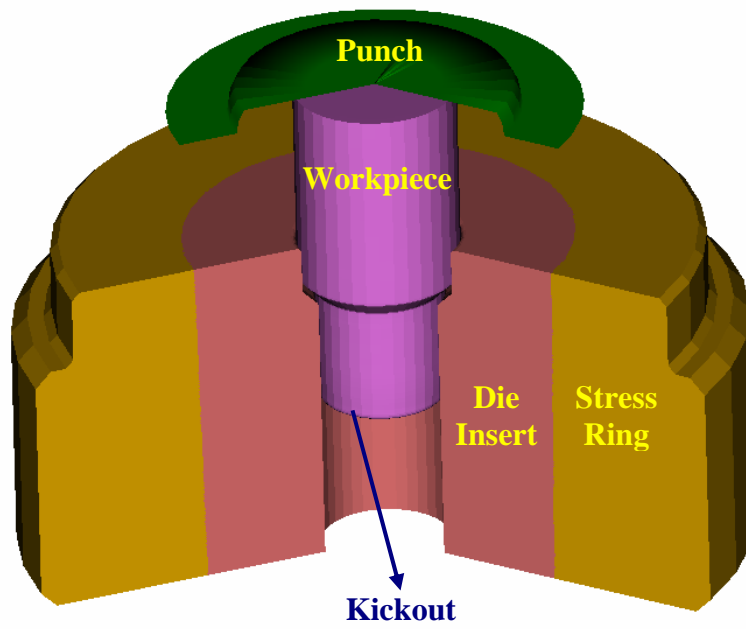
Figure 4.71. Deformable die model of the third station
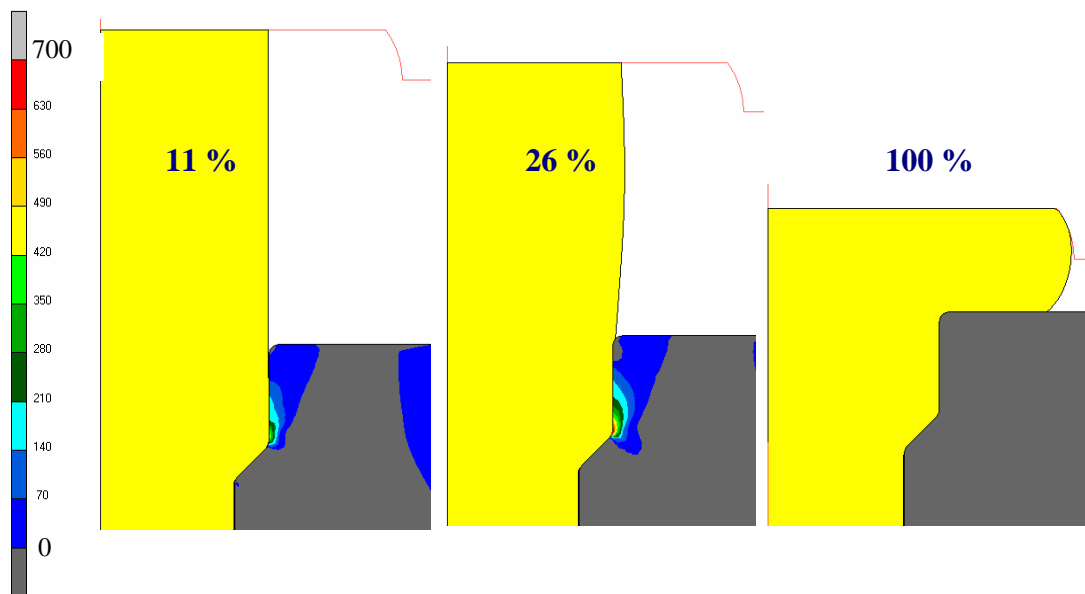
Figure 4.72. Principle tensile stress distributions at different stoke stages

By splitting the insert from the location where tensile stresses are formed, probable failure can be eliminated. New die design of this product is made according to this approach and the die insert is split into two pieces as shown in Figure 4.73.
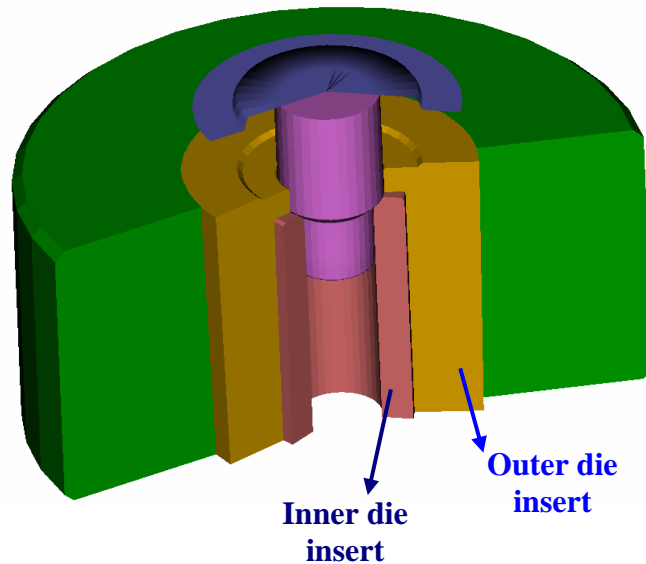
Figure 4.73. New third station die design with two die

The interferences between the components are defined by using MathCad program for the two ring system. To find the interference between the carbide inserts, the outer insert is considered as middle ring. Calculated values for the optimum prestressing are 1.4 ‰ (0.02 mm) between the two carbide inserts and 5.2 ‰ (0.14 mm) between outer insert and stress ring.

At the stroke stage where maximum tensile stresses occur, use of split die insert reduces the principal stresses down to 70 MPa which results in 90 % improvement. Figure 4.74 is showing the improved stress distribution at 26 % of stroke.

According to the simulation results, third station dies are produced according to the new design. 105,000 parts are produced with these dies without any tool failure and specimens taken from the each forging station is shown in Figure 4.75.
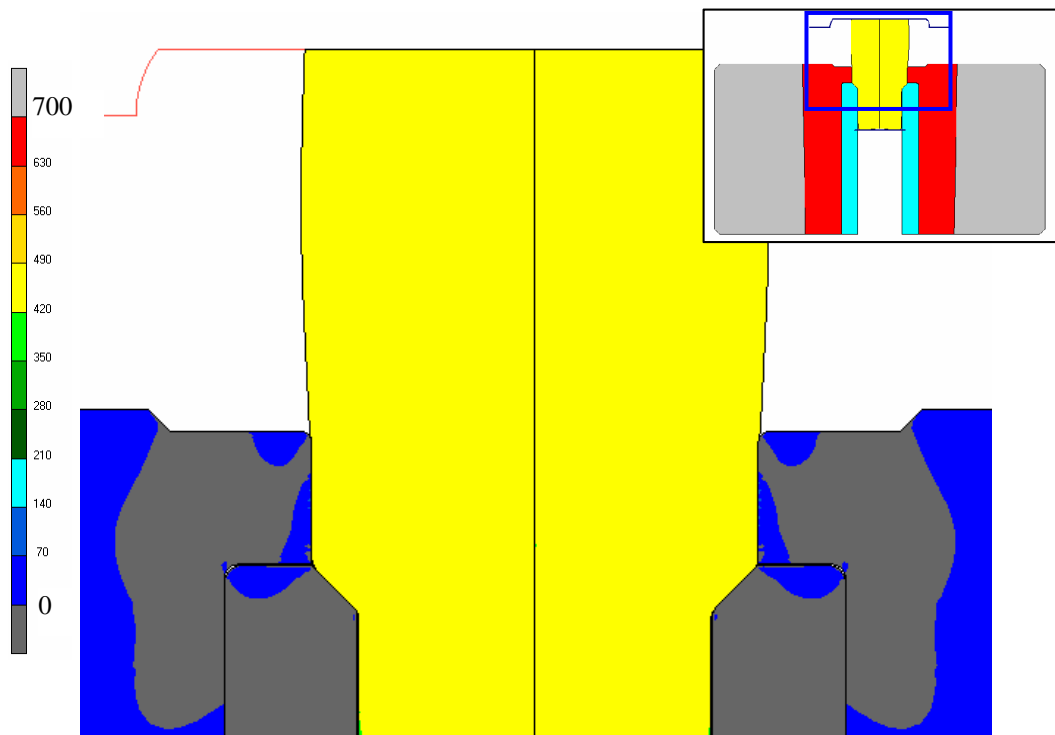
Figure 4.74. Principle stress distribution on the split die insert

Figure 4.75. Forged parts in each station

4.11.4 Elimination of Tool Failure on a Heading Die

In this last case study, the factors lead to fracture on the heading die of a M16 hexagonal bolt is investigated (Fig. 4.76). The problem occurs in the second station of a five step forging process.
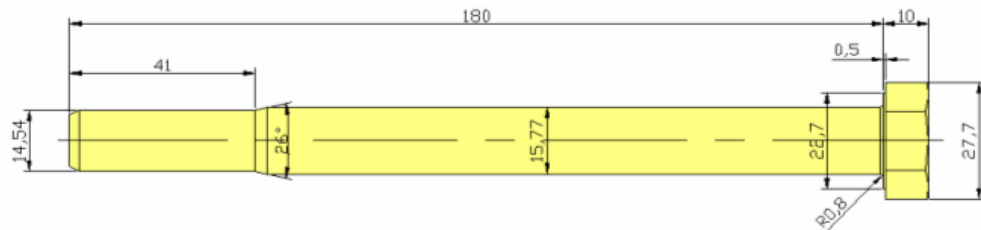
Figure 4.76. M16 x 180 DIN 931 Hexagonal

The material used for this is named as C25B which is another medium carbon steel type. Raw material is first drawn from 16mm to 15.63 mm and cut off into 213.22mm billets. The height of the material that will be formed into head is 38.74mm. For the diameter of 15.63mm the height / diameter ratio is calculated as 2.48 and since there exist risk of buckling, preform heading is performed in the first
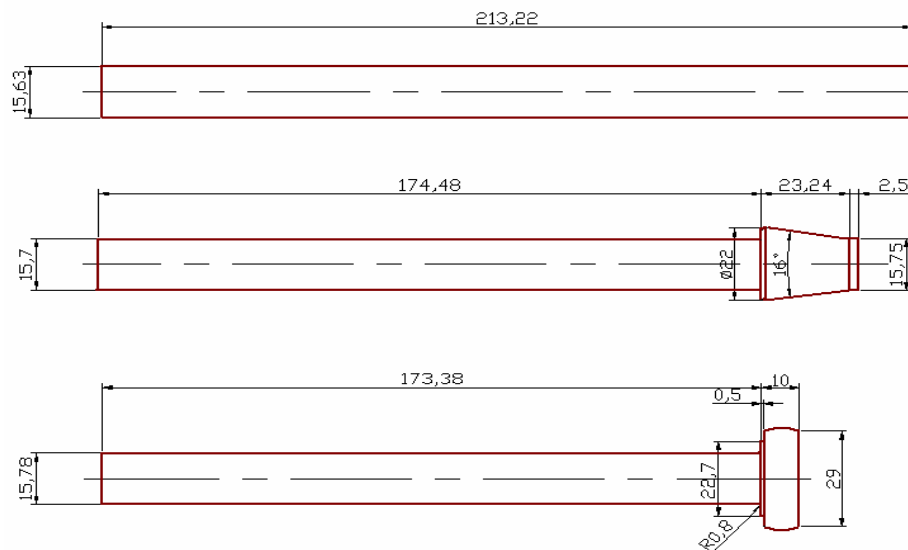
Figure 4.77. Part dimensions after wire drawing, preform heading and heading operations

station. In the second station where die failure is present, heading operation takes place. The dimensions of the parts for wire drawing and first two stations are given in Figure 4.77.

Before analysing the die failure wire drawing and preform heading processes are simulated by using rigid tools and forged part is transferred to the second station model where all the die components except cases are included.

The failure occurs on the region, where washer under the head is formed, after 2000 – 3000 cycles. An unused and failed die photos are shown in Figure 4.78.

Figure 4.78. Unused *(left)* and failed *(right)* second

All the inserts used in this production are made from tungsten carbide grade G55 and rings are made from H13 steel. The interference between the components are taken as 5 ‰ as an average value.

The main dimensions like height and diameters are measured by using caliper and dial gauges. However to measure the profile around the washer area, a surface scanner device called perthometer is used (Fig. 4.79).
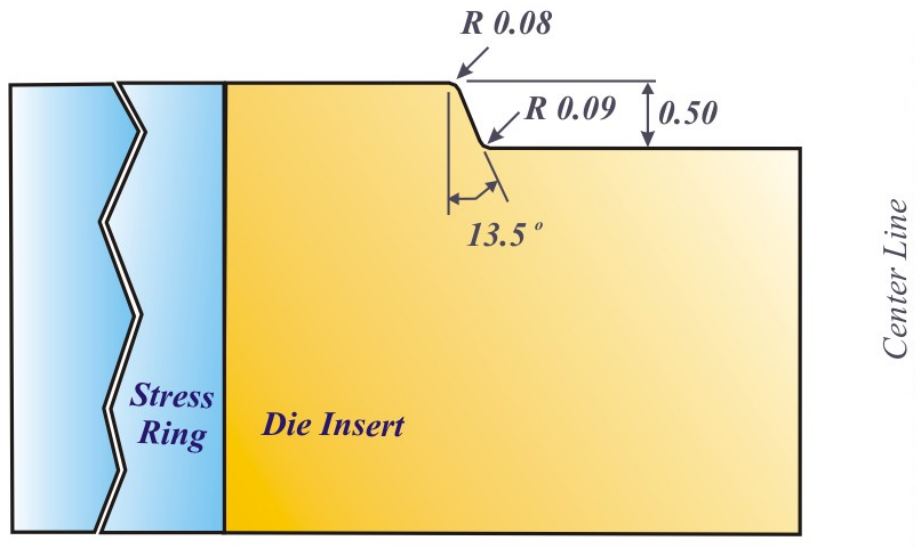
Figure 4.79. Second station die dimensions around washer region
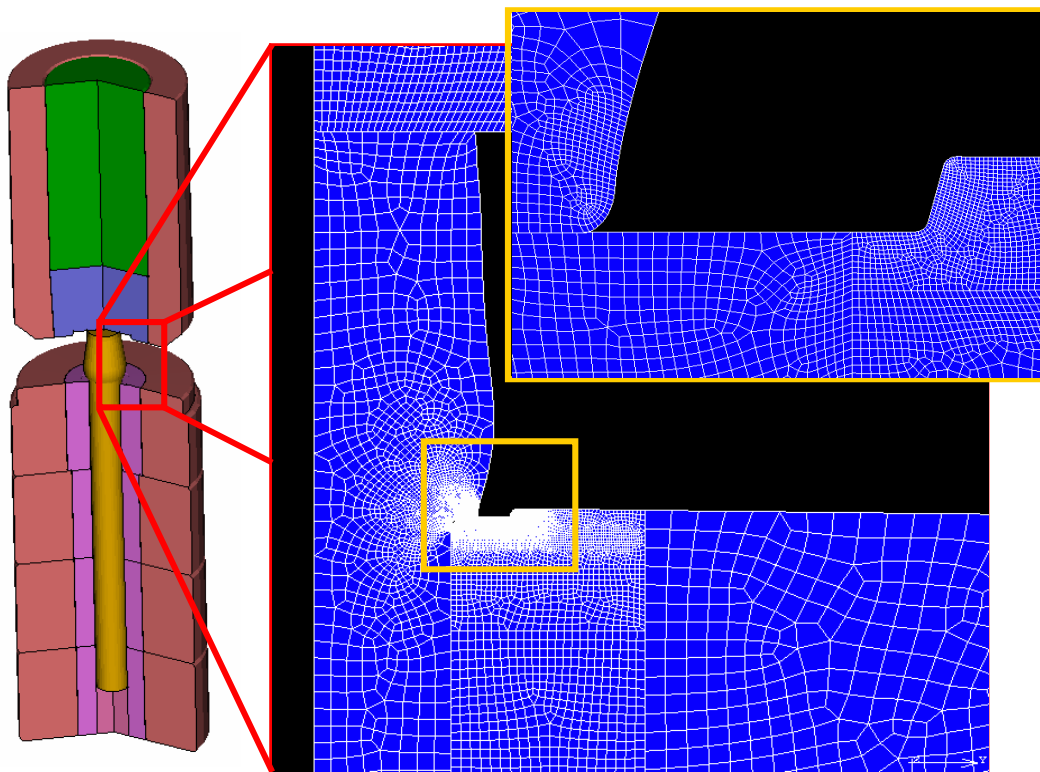
Figure 4.80. Mesh structure of the failed die

165

Since the radii on the critical region have small values, elements having edge length of 0.02mm is required to have a fine mesh structure. Also to keep the total number of elements as low as possible, fine mesh is applied locally around the failure location while element sizes set 0.80mm on the rest of the model by applying transition (Fig. 4.80). Also, to obtain same element sizes on the contact are between workpiece and die, local remeshing subroutine is runned in the analyses which is given in Appendix E.

(a)   **(b)**
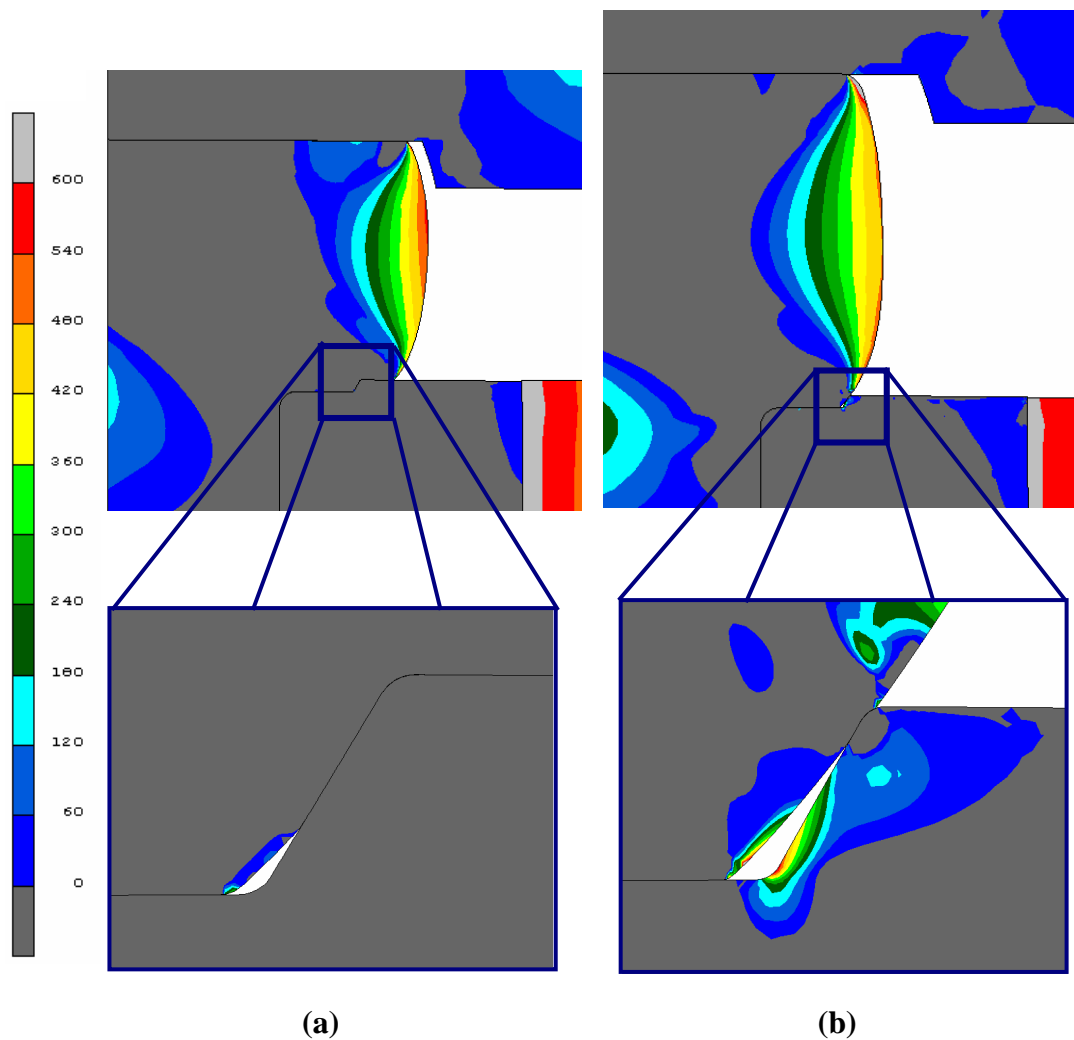
Figure 4.81. Principal stress distributions **a)** Final stage of heading **b)** 84 % of Stroke

Firstly, the principal stresses around the fillet are investigated at the end of the heading process and no tensile stresses are determined (Fig. 4.81a). However when the whole process is monitored it has been noticed that, principle stress values increase up to 620 MPa while material flows over the conical surface as shown in Figure 4.81b.

Since the tensile stresses are generated because of the bending of the the conical surface, the radius at the tip of the surface is increased by grinding. In this case tools are modified before performing analyses. So that analyses have done to verify the stress improvement on the washer location. The new fillet radius is measured as 0.40mm after repeating the perthometer scan (Fig. 4.82).
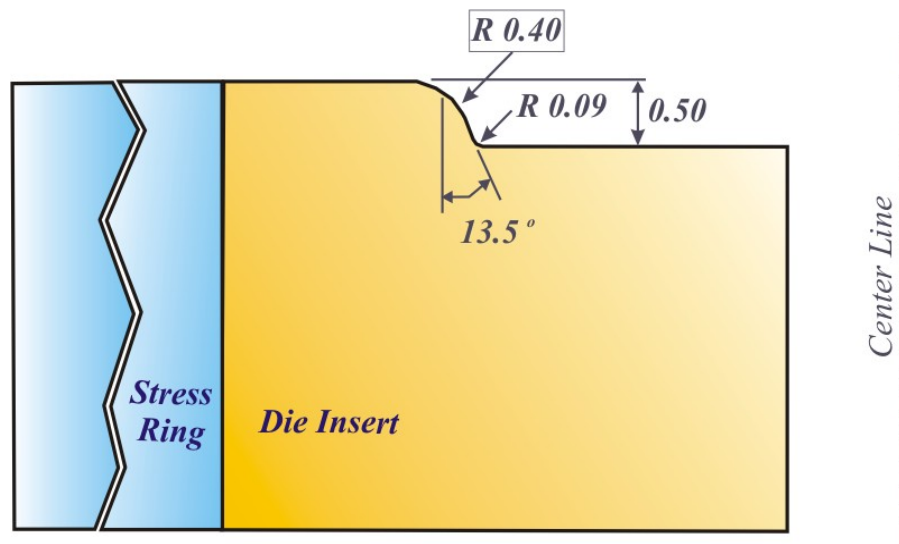
Figure 4.82. Second station die dimensions around washer region after modification

Although the radius is increased, tensile principle stresses are still formed on the bottom part of conical surface. However, after the modification maximum stress value is reduced to 335 MPa which corresponds to 46 % improvement on the fracture location. The principle stress distribution on the modified tooling is shown in Figure 4.83.

Tool life is followed in the mass production of this part and approximately 50,000 forging cycles are recorded before the failure of the die. This analyse shows that by making a slight geometrical change on the die, tool life can be increased significantly.
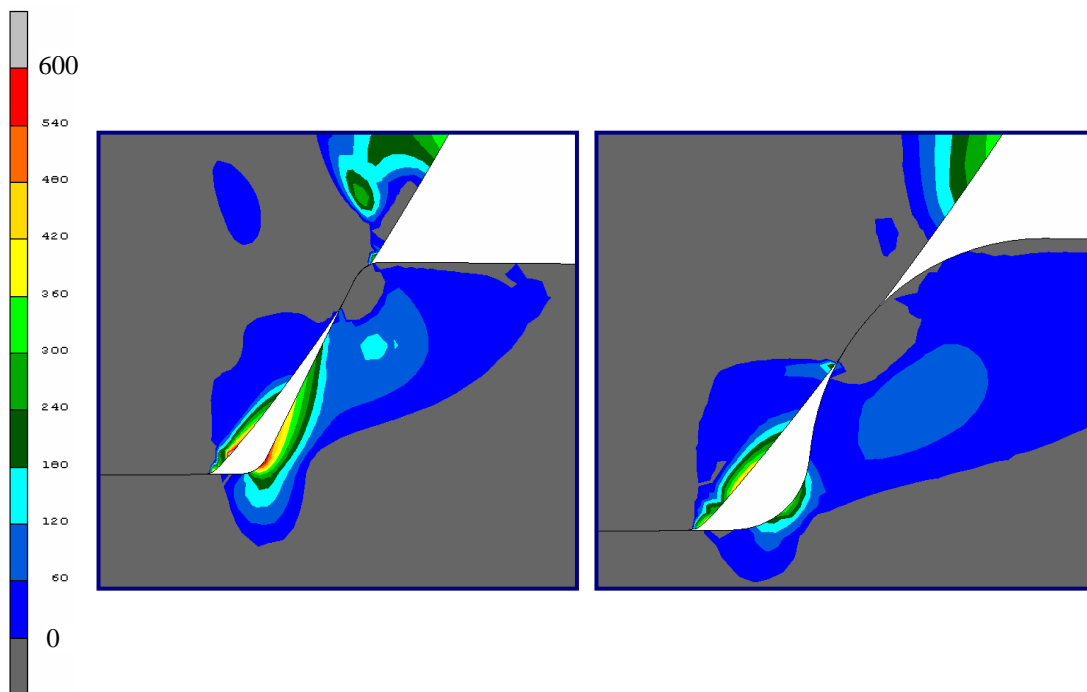
Figure 4.83. Comparison of principal stress distribution for old *(left)* and new *(right)* die geometries

CHAPTER 5

FRICTION ANALYSES IN COLD FORGING PROCESSES

One of the most important parameter in the cold forging simulations is the implementation of tribological conditions on the contact areas between workpiece and die. In this section, analyses are based on two main friction models; Coulomb and Shear. By performing ring upsetting and forwards rod extrusion tests, the most appropriate friction model for the cold forming simulations is investigated.

5.1 Ring Upsetting Tests

To generate the conditions similar to the forging process, test equipment and specimens are produced by using the same materials used in bolt forming. Firstly, two flat upsetting dies are produced from tungsten carbide which is shrink fitted into blind stress ring made of H13 (Fig. 5.1)
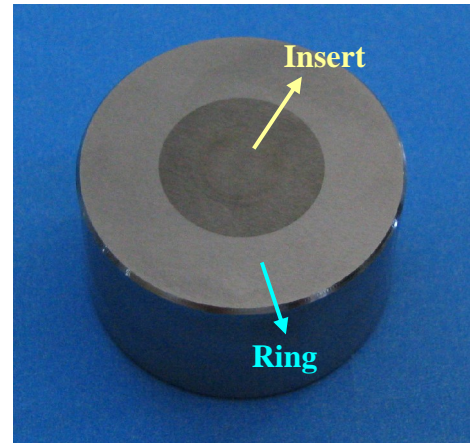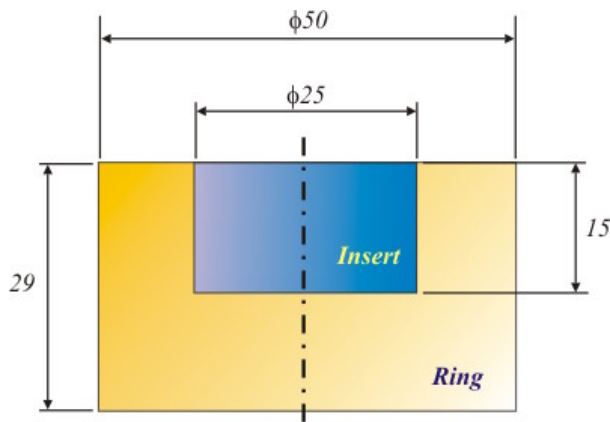
Figure 5.1. Ring upsetting test die

It was required to polish flat surface of the die but polishing tools were only applicable to holes. So that final machining of the surfaces of the dies are performed in the surface grinding machine. Hence, a slightly rougher surface is obtained when compared to bolt forming dies.

Specimens are produced by using four different materials, which are QST 36-3, raw 20MnB4, annealed 20MnB4 and annealed C25B. The outer diameter of the rings defined as 11 mm because the raw material diameter for QST 36-3 and 20MnB4 was restricted to 12 mm. To prevent buckling, the height of the specimens is set as 6mm. Since the specimens are machined in the CNC turning machine and the smallest cutting tool diameter is approximately 5mm, the smallest hole diameter, which can be machined on these speciements, is 5.20 mm. So that the final outer diameter:height:inner diameter ratio of the rings becomes 11:6:5.2.

The ring upsetting tests are performed for three different conditions. Firstly, rings are upsetted without using any coating and lubricant (Fig. 5.2a). Secondly, rings are coated with phosphate and soap which is a common application in bolt forming (Fig. 5.2b). Again, no lubricant is used during the upsetting of these coated specimens. In

the final test, forming oil is applied on the phosphate and soap coated specimens. The aim of performing these three different tests is to determine friction coefficients for different forming conditions and also to determine effect of phosphate – soap coating and lubricant on the reduction of friction.

Upsetting test are performed on the same tensile test machine which is used for tension test of the stress ring materials and shown in Figure 4.3. Rings are upsetted down to 2.4 mm that corresponds to 60% height reduction in seven steps at a speed of 0.1 mm/sec. At each step, height and inner diameter of the ring is measured and recorded. For these measurements a digital caliper and a dial bore gage is used. For each condition and material type, upsetting test is performed twice. When three different conditions and four different materials are considered, totally 24 tests are performed.

(a) **(b)**
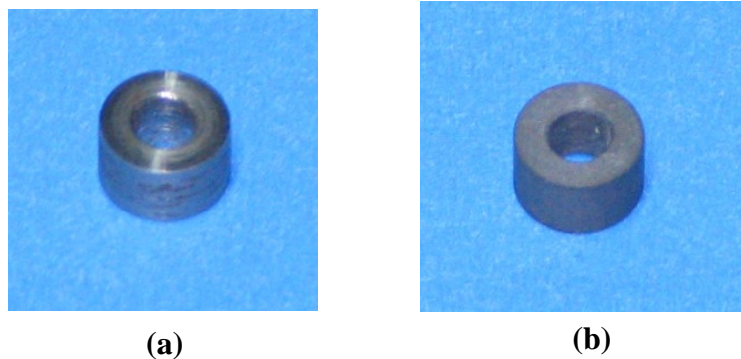
Figure 5.2. Ring upsetting specimens **a)** Uncoated **b)** Phosphate – soap coated

For each test, height reduction versus inner diameter variation is plotted. In the all tests, as a general behavior, hole starts to expand until 10% height reduction and after that according to the friction condition, it may continue to expand or shrink. In Figure 5.3, plot of hole diameter change is given for the material QST 36-3. In addition, the close results of repeated tests show that the consistency and stability is achieved while performing these tests.
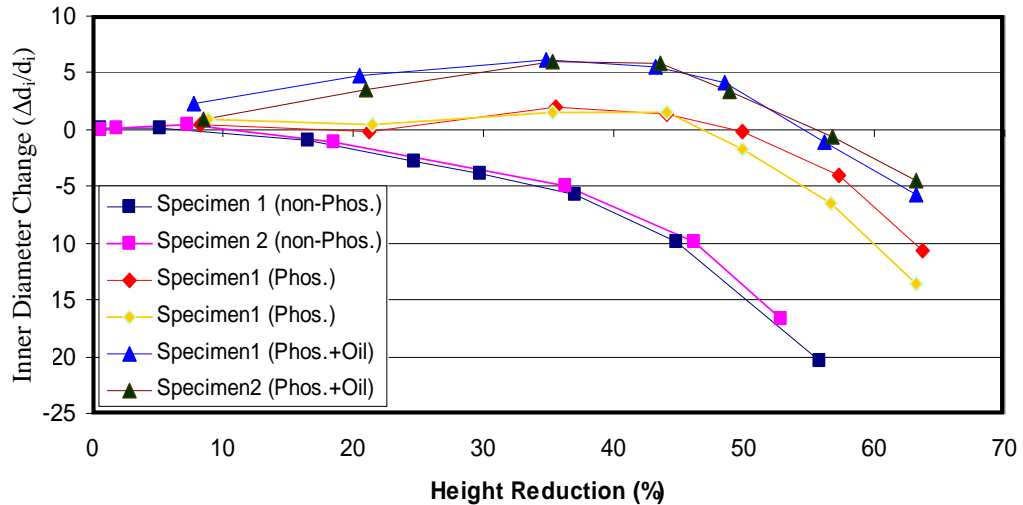
Figure 5.3. Inner diameter variation for each test condition

This plot also gives an idea about the effect of application of coating and lubricant on the friction condition. Since the diameter expansion increases with the decrease in friction, the influence of phosphate-soap coating is more evident than the lubricant.

To find out the friction coefficient and appropriate model according to test data, calibration curves are generated by doing FE analyses. Before performing the simulations, a convergence study has been made to find out the suitable relative sliding velocity constant.

5.2 Determination of Relative Sliding Velocity Constant

An axisymmetric model of 6mm height ring with outer and inner diameters of 11 mm and 5.2 mm respectively, is created as shown in Figure 5.4. Two symmetry axes are defined where one of them is representing the rotational symmetry and the other one divides the ring into two sections along its height.

Height of the ring is reduced by 60 % with a rigid punch, which is moving at a speed of 0.1mm/s (Fig. 5.5). Friction constants are taken 0.1 for Coulomb and 0.2 for

Shear model in all analyses. Height reduction versus inner diameter change is plotted for the relative sliding velocity constants 0.0005, 0.001, 0.005, 0.01, 0.05, 0.1, 0.25 and 0.5. The results given in the Figures 5.6 and 5.7 show that for the deformation speed 0.1mm/s, the diameter change converges when relative sliding velocity constant is taken 0.001.
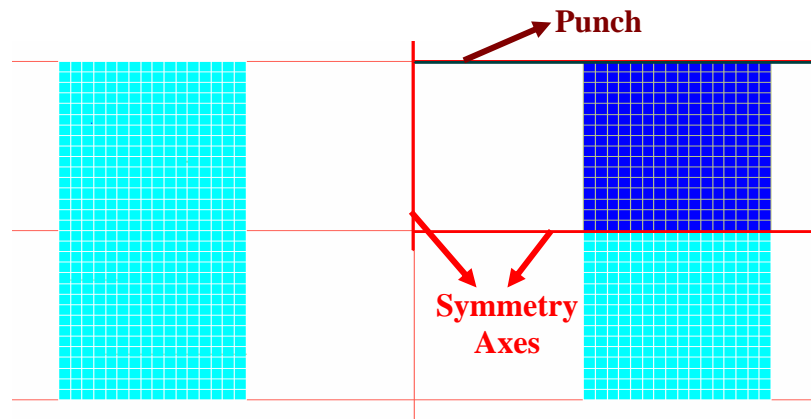
Figure 5.4. FEA model of ring specimen with ¼ symmetry
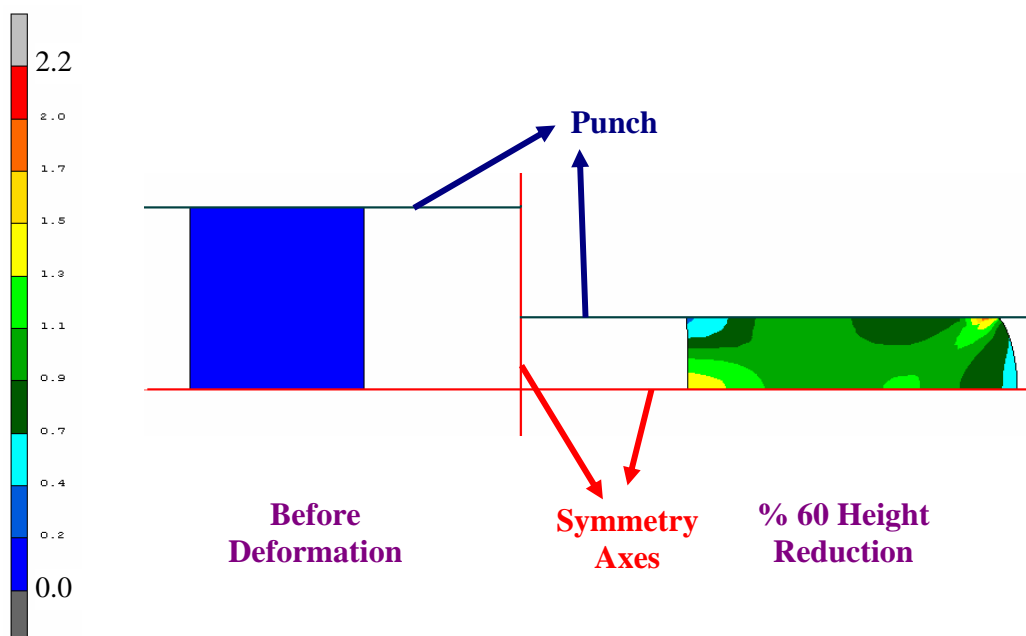
Figure 5.5. Plastic strain distribution on the compressed ring
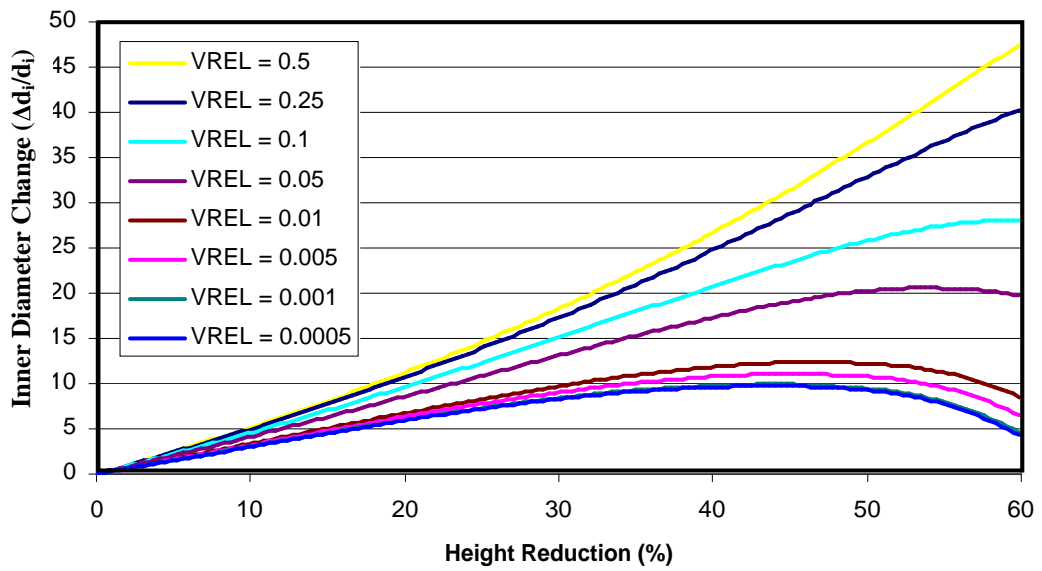
Figure 5.6. Height reduction vs. diameter change for Coulomb friction model
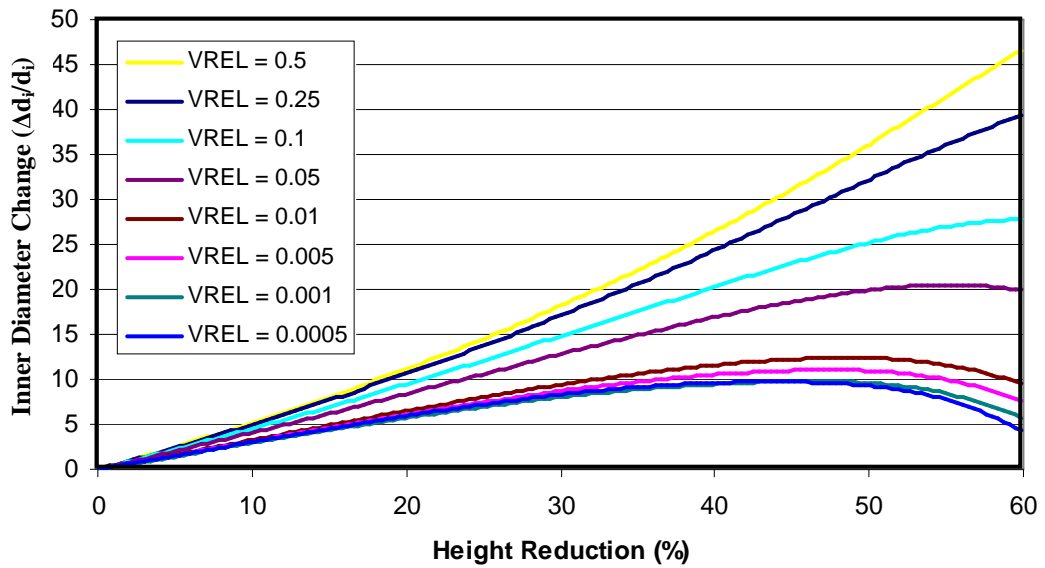
Figure 5.7. Height reduction vs. diameter change for Shear friction model

As a result, in the analyses performed for creating calibration curves, this constant value is taken as 0.001.

5.3 Friction Calibration Curves

Same ¼ symmetric model which is shown in Figure 5.4 is used in the analyses to create calibration curves. To obtain the amount of average internal diameter change during the compression of workpiece, a subroutine is written which records the radial displacement of each node and calculates average diameter dimension change at each increment. The Fortran code of the subroutine is given in Appendix F. This procedure is performed for both Coulomb and Shear friction models for different friction values and obtained calibration curves are presented in Figures 5.8 to 5.15 with the experimental data.
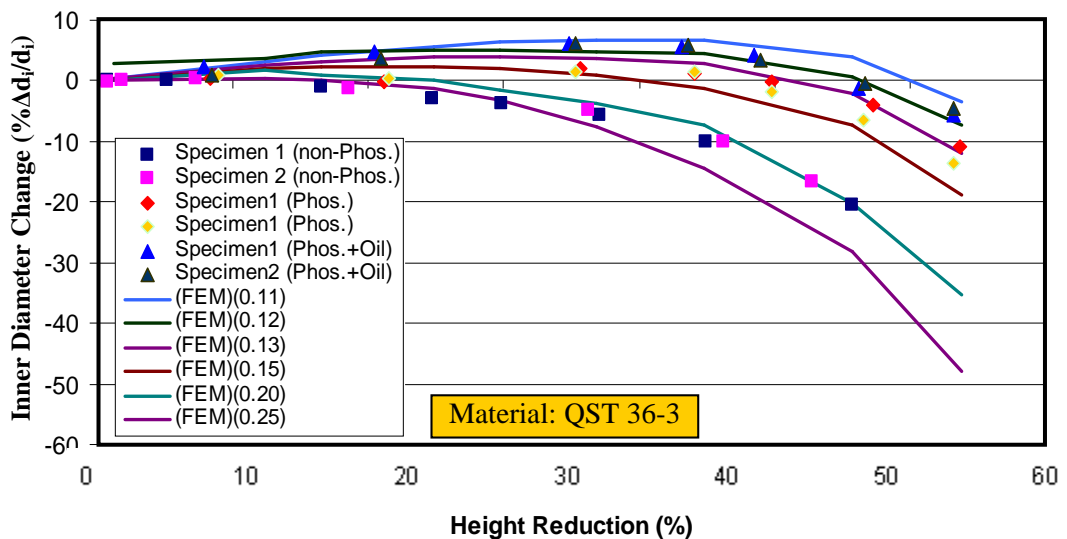
Figure 5.8. Coulomb friction calibrations curves for QST 36-3

175
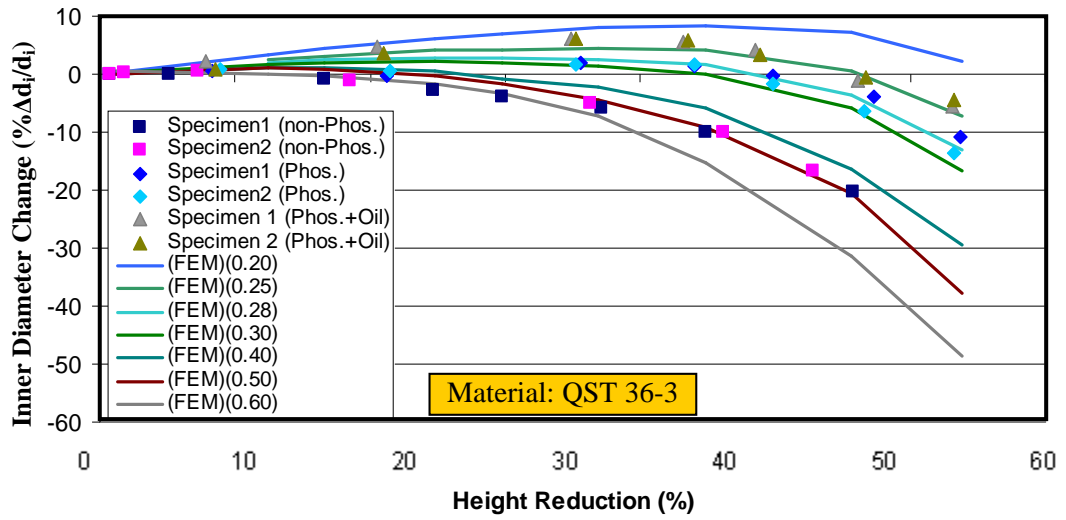
Figure 5.9. Shear friction calibrations curves for QST 36-3
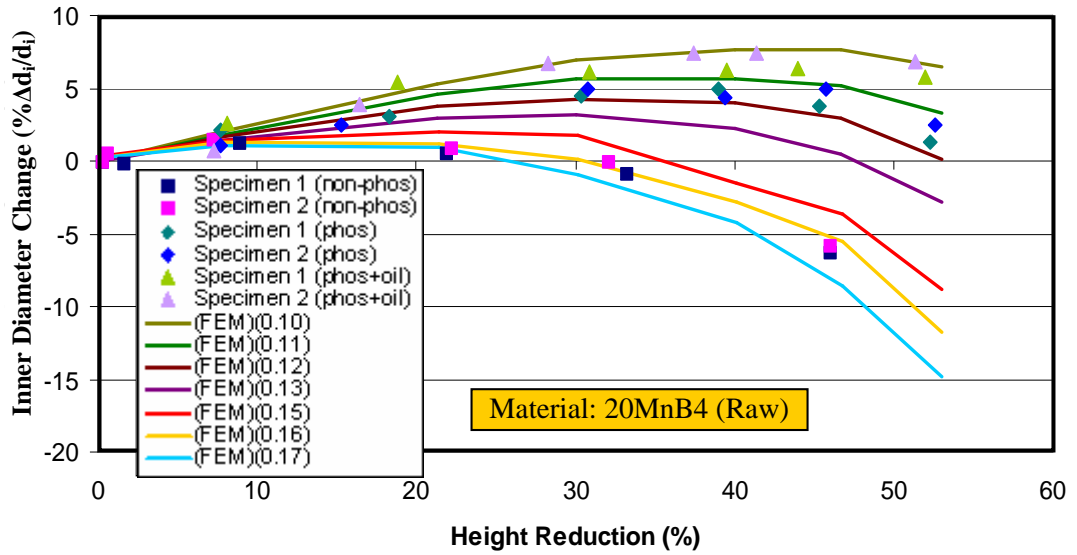
Figure 5.10. Coulomb friction calibrations curves for 20MnB4 (Raw)
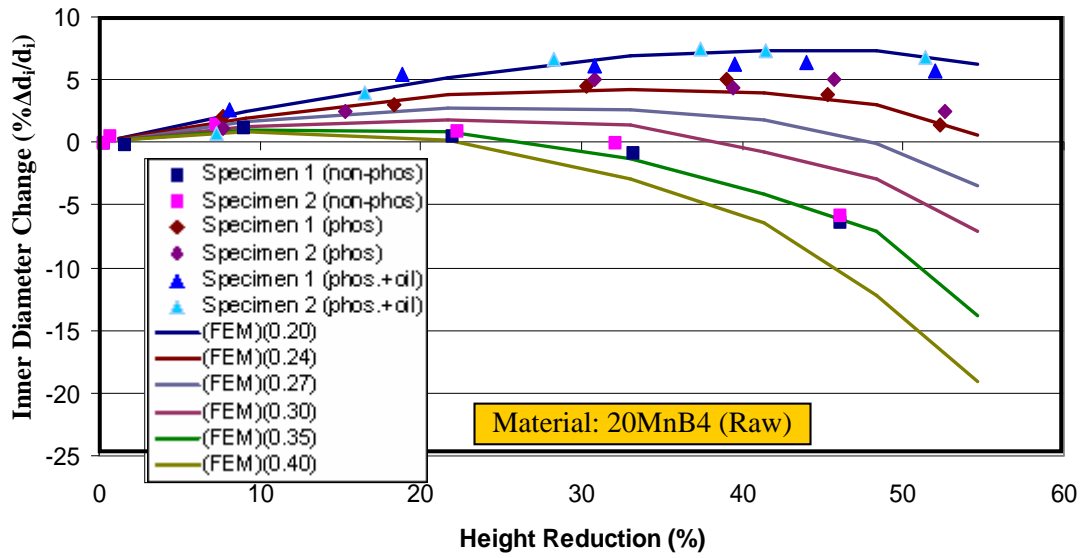
Figure 5.11. Shear friction calibrations curves for 20MnB4 (Raw)
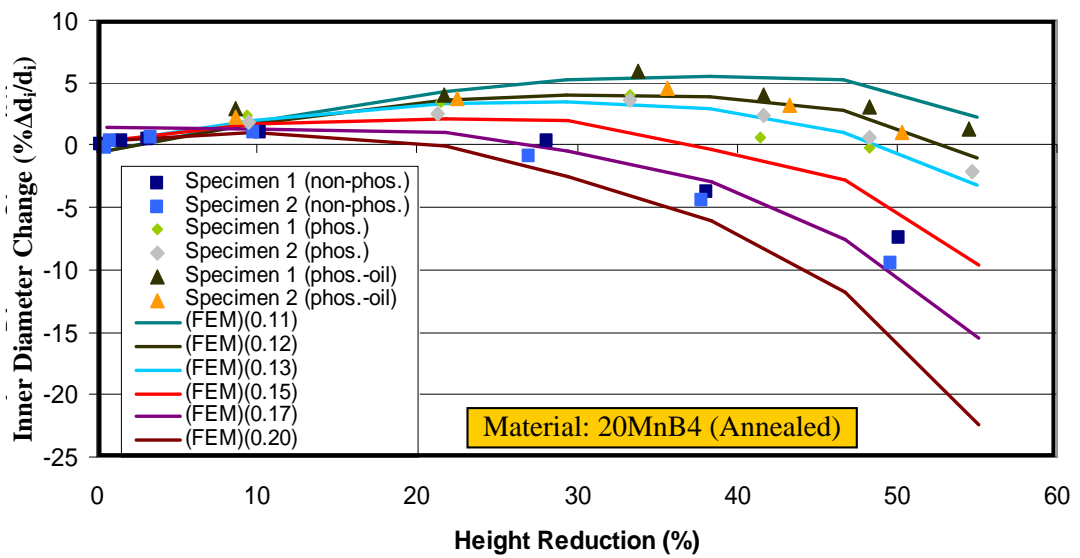
Figure 5.12. Coulomb friction calibrations curves for 20MnB4 (Annealed)

177
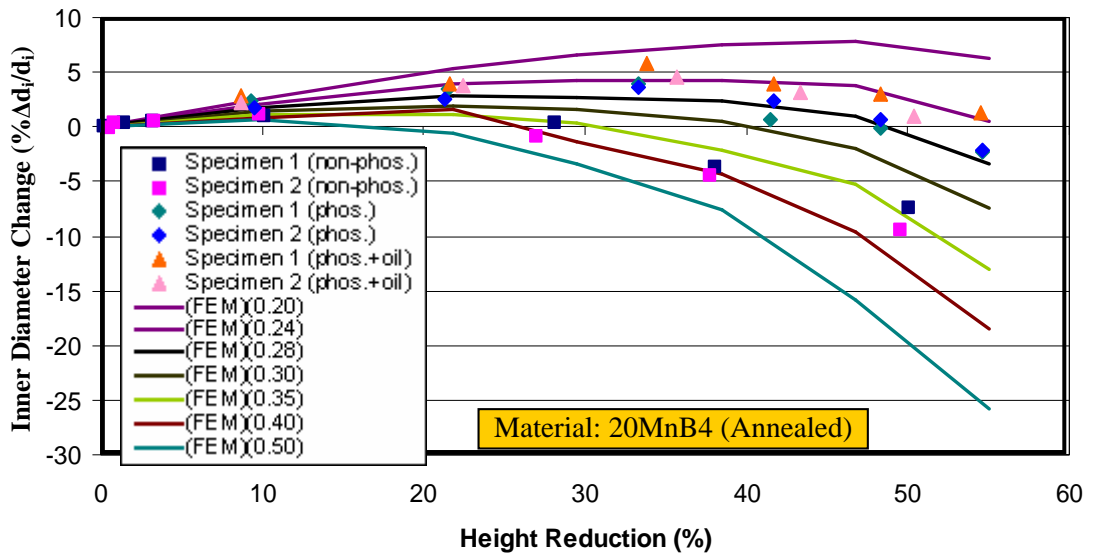
Figure 5.13. Shear friction calibrations curves for 20MnB4 (Annealed)
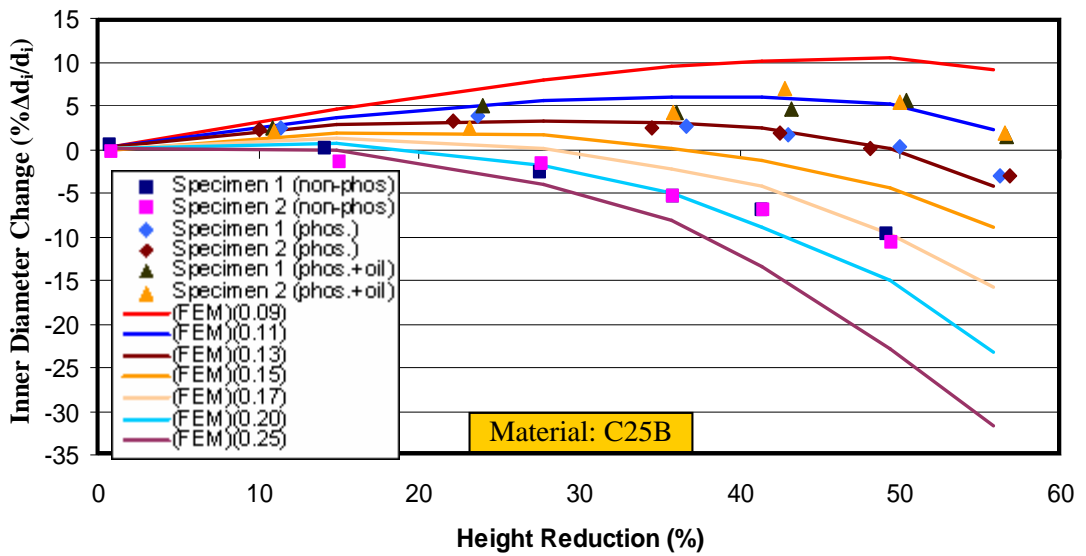
Figure 5.14. Coulomb friction calibrations curves for C25B

178
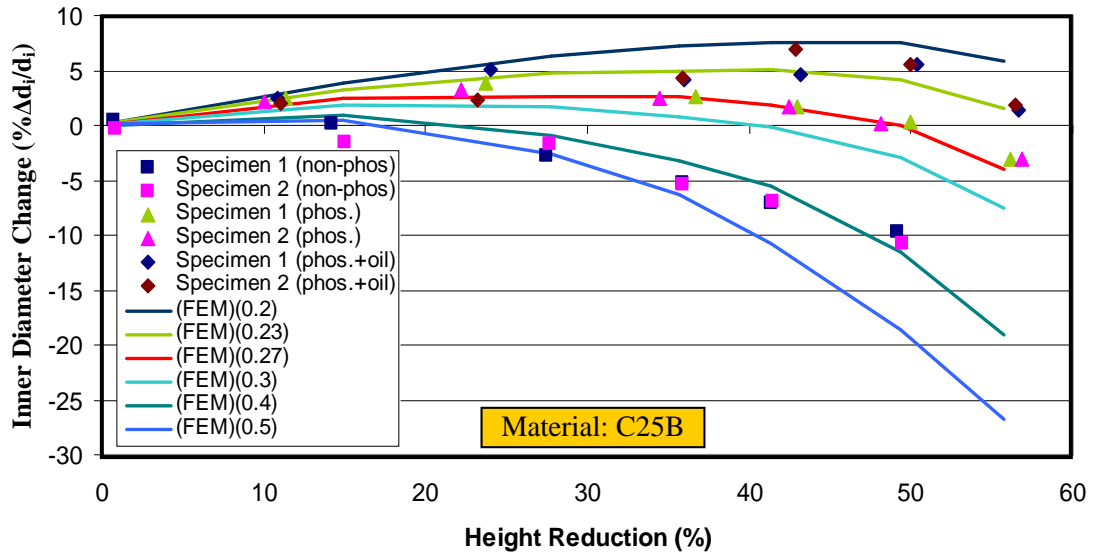
Figure 5.15. Coulomb friction calibrations curves for C25B

When all the calibration curves are examined, it can be seen that experimental data fit on both Coulomb and Shear calibration curves. For the condition where no coating or lubrication is present, the Coulomb friction is approximately 0.20 whereas the Shear friction is found as approximately 0.40. When the phosphate-soap coating is applied on the test specimen, friction values significantly reduce to approximately 0.13 for Coulomb and 0.27 for Shear friction model. When the oil is applied in addition to the coating, there become a slight reduction in the friction coefficients and determined as approximately 0.11 for Coulomb model and 0.24 for Shear model. Determined friction coefficient values by using calibration curves are given in Table 5.1 for each material.

These values slightly vary for each material type. This variation occurs due to the difference in formability characteristics of ring materials. As the normal stresses acting on the tool surfaces different for each material, the tribological conditions (interaction of asperities between two mating surfaces and function of coating and lubricant) will be also different.

179

Table 5.1. Friction coefficient values obtained from ring compression test

	Friction Coefficient							
	QST 36-3		20MnB4 (Annealed)		20MnB4 (Raw)		C25B	
	Coulomb	*Shear*	*Coulomb*	*Shear*	*Coulomb*	*Shear*	*Coulomb*	*Shear*
Uncoated	0.20	0.50	0.17	0.35	0.16	0.35	0.20	0.40
Coated	0.13	0.28	0.13	0.28	0.12	0.24	0.13	0.27
Coating + Oil	0.12	0.25	0.12	0.24	0.11	0.20	0.11	0.23

To determine which friction type calibration curve fits the experimental data better, standard deviations of both models are compared for each material. This is calculated according to the differences between the values of the calibration curves and experimental data (Figure 5.16). By using Eqn. 5.1 the standard deviation $\bar{\sigma}$ is calculated where N is the number of data points and x_i is the value of each data point.
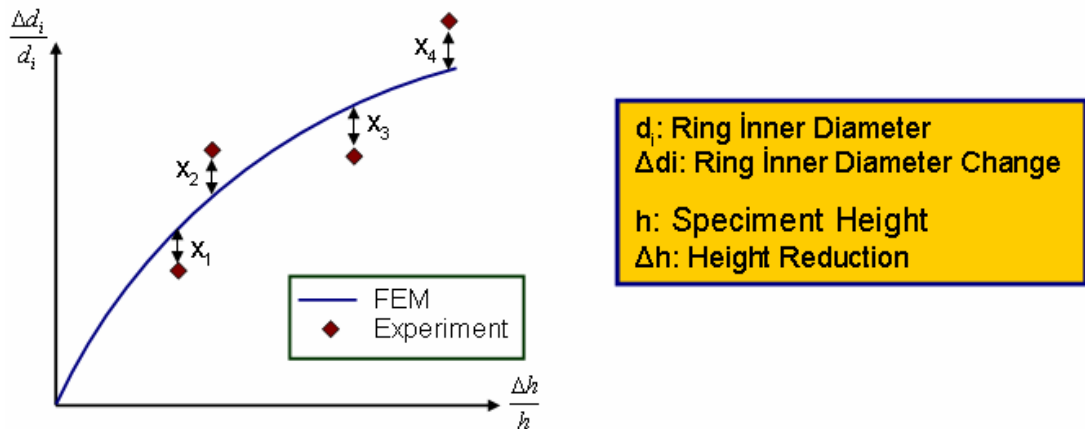
Figure 5.16. Standard deviation of experiment data

$$\bar{\sigma} = \sqrt{\frac{1}{N}\sum_{i=1}^{N}(x_i - \bar{x})^2}$$ (5.1)

The average value of data points $\bar{x}$ is calculated by using Eqn 5.2

$$\bar{x} = \frac{1}{N} \sum_{i=1}^{N} x_i = \frac{x_1 + x_2 + \cdots + x_N}{N}$$
(5.2)

The results given in Table 5.2 show that, data points fit on the Shear calibration curves better than the Coulomb since the standard deviation values calculated are lower for shear model for most of the experiments.

Table 5.2. Standard deviation of friction calibration curves

		QST 36-3		20 MnB4 Annealed		20 MnB4 Rolled		C25 B	
		Cou.	She.	Cou.	She.	Cou.	She.	Cou.	She.
Uncoated	Spc. 1	2.08	**1.77**	**1.28**	2.12	0.59	**0.32**	1.83	**1.44**
	Spc. 2	1.08	**0.93**	1.24	**1.12**	**0.34**	0.48	1.87	**1.37**
Phosphated	Spc. 1	1.80	**1.44**	0.82	**0.69**	0.51	**0.46**	**0.55**	0.62
	Spc. 2	2.45	**1.75**	**0.46**	0.74	1.00	**0.90**	0.60	**0.51**
Phosphated +Oil	Spc. 1	**0.8**	1.22	1.05	**0.80**	1.11	**0.97**	1.10	**0.81**
	Spc. 2	1.60	**1.43**	0.41	**0.37**	0.53	**0.48**	1.34	**1.16**

5.4 Forward Rod Extrusion Test

Although the Shear friction model seems more appropriate according to the results of ring compression tests, in order to determine the consistency of the friction models for different processes, forward rod extrusion tests are performed for two different equivalent plastic strain values; 0.68 and 1.2.

To determine the effect of friction clearly, extrusion process is performed by using specimens at different lengths. Since the container friction is the only parameter different for these specimens, this test will provide measuring the difference in the extrusion force due to friction. Although the billets are coated with phosphate and soap, the faces are remaining uncoated due to final machining. In addition, no lubrication is used during the tests which are performed on the same tensile test machine used in previous experiments.

Two dies are manufactured as single piece to prevent forming problems, which might occur if the dies were split. However, due to the limitations of die insert dimensions, the maximum billet length is set as 35 mm for the extrusion process with equivalent plastic strain 0.68 and 25 mm for equivalent plastic strain 1.2 (Fig 5.17).

Figure 5.17. Extrusion test specimens

The billets are first cut off from the wire drawn from 10mm to 9.7 which is made of annealed 20MnB4. Then billet faces are machined to shorten them to desired lengths; 15, 20, 25, 30 and 35mm. There exist a clearance of 0.1 mm between the workpiece and the dies. The output diameters of the dies are 6.98 mm and 5.35 mm respectively.

For each equivalent strain value and billet length, two extrusion tests have been performed. The amount of difference between two tests for each condition is not exceeding 6%. So that the precision of the experiments can be accepted as very high. In Figure 5.18 and 5.19 force – displacement curves of extrusion process of 25 mm billet for both equivalent plastic strain values are shown while the remaining curves are given in Appendix G.

To verify the correctness of measured force, the average force curves are compared for different billet lengths at the stroke where length of the remaining billet in the container is same. As shown in Figure 5.20, for equivalent plastic strain of 0.68, the extrusion force reduces to approximately 70 kN in all conditions where the billet length reduces to 10mm.
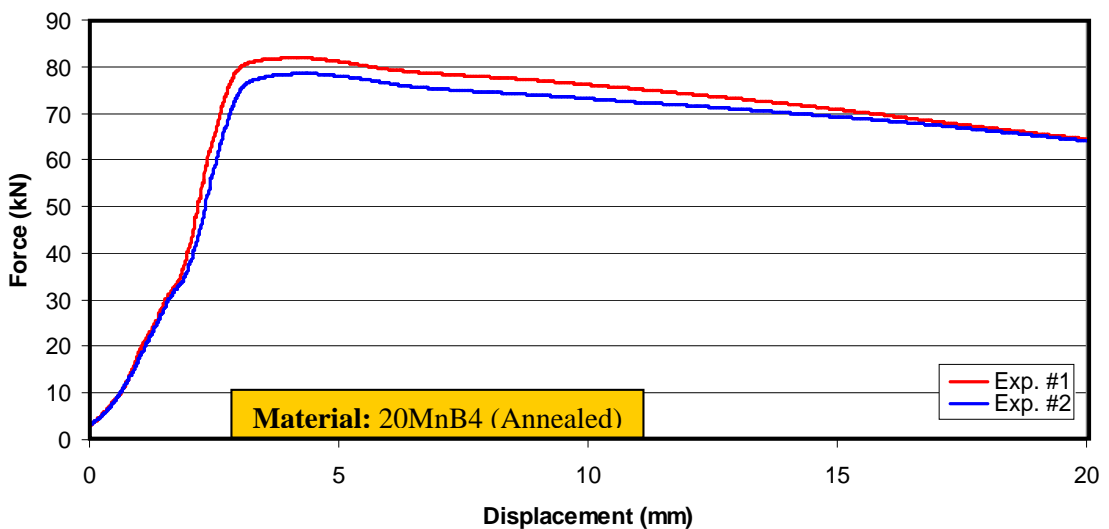
Figure 5.18. Force vs. displacement curve for equivalent plastic strain $\varphi = 0.68$
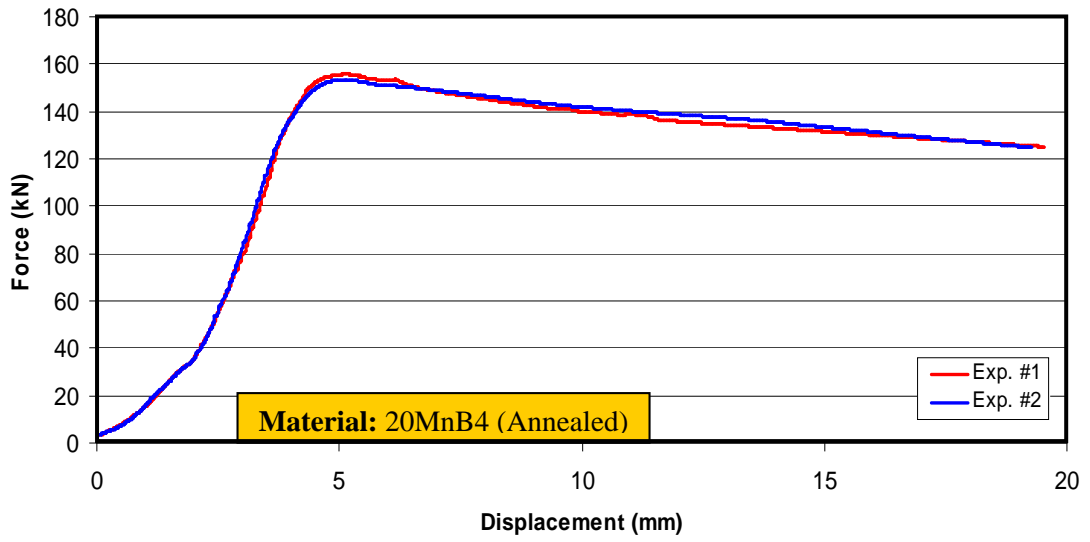
Figure 5.19. Force vs. displacement curve for equivalent plastic strain $\varphi = 1.2$
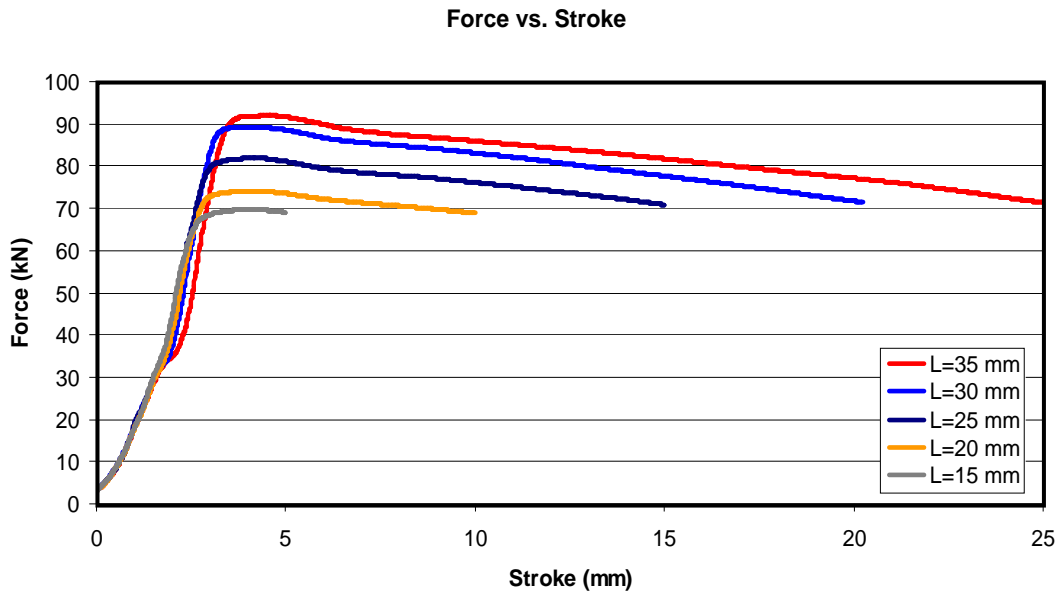
Figure 5.20. Measured force verification for different specimen lengths ($\varphi = 0.68$)

Similarly, in Figure 5.21, force comparison of the extrusion process with equivalent strain of 1.2 is shown. When the billet length reduces to approximately 8 mm, extrusion force is measured as around 120 kN in all conditions. Therefore, these two figures represent the consistency of the force measurements during the tests.
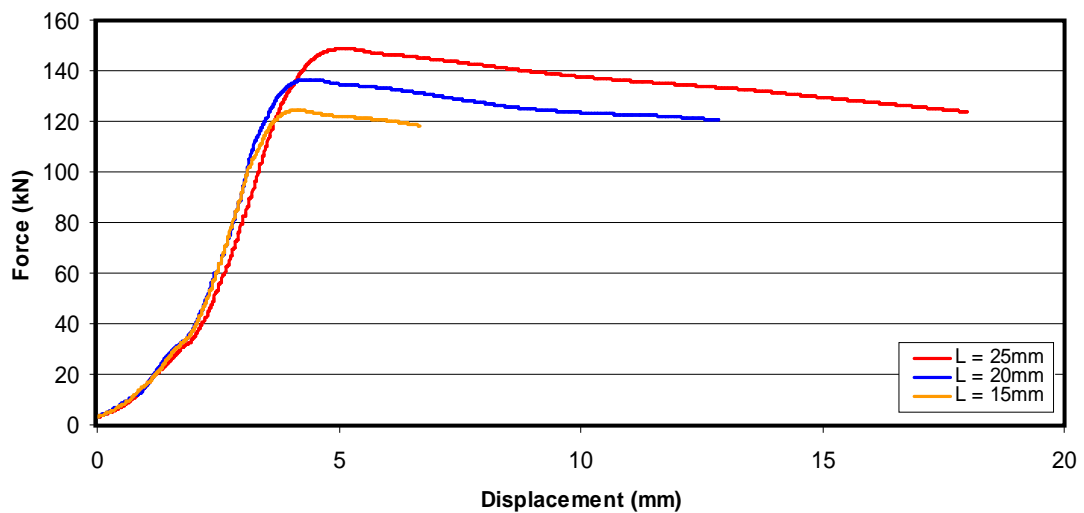
Figure 5.21. Measured force verification for different specimen lengths ($\varphi = 1.2$)

To find out the friction coefficient between the die and workpiece, first an analytical approach is used. Then, for each extrusion condition, several FE simulations have been made for different friction models and constants. Finally, the effects of rigid and deformable tool models on the calculated extrusion forces for different billet length / diameter ratios are investigated.

5.4.1 Calculation of Friction Coefficient Analytically

Since all the process parameters are the same for the extrusion processes except the billet length, the difference in the measured forming force is caused by the variation in the friction force on the container which is proportional to billet lengths. For this purpose, the friction force term, which is present in the basic forward rod extrusion

force calculation methods that are proposed by Siebel and Avitzur is used. These force equations for Siebel's and Avitzur's models are given in Eqns. 4.39 and 5.3 respectively.

$$F_{total} = A_0 \sigma_{fm} \left(f(\alpha)\varphi + \frac{2}{\sqrt{3}} \left(\frac{\alpha}{\sin^2 \alpha} - \cot \alpha \right) + \mu \cot \alpha \left(1 + \frac{\varphi}{2} \right) \varphi \right) + \pi d_0 h \mu \sigma_{f0}$$

(5.3)

with

$$f(\alpha) = \frac{1}{\sin^2 \alpha} \left[1 - \cos \alpha \sqrt{1 - \frac{11}{12} \sin^2 \alpha} + \frac{1}{\sqrt{11 \cdot 12}} \ln \frac{1 + \sqrt{11/12}}{\sqrt{\frac{11}{12}} \cos \alpha + \sqrt{1 - \frac{11}{12} \sin^2 \alpha}} \right]$$

(5.4)

For two billets with different lengths, force difference due to friction can be formulated as in the Eqn. 5.5 where ΔF is total force difference, Δh is difference in length, d_0 is the inlet diameter, σ_{f0} is initial yield stress and μ is the Coulomb friction coefficient.

$$\Delta F = \pi \cdot \Delta h \cdot d_0 \cdot \mu \cdot \sigma_{f0}$$

(5.5)

Since there are differences in measured forces between the two experiments performed for each billet length, average maximum forces are calculated by taking the mean average. For both equivalent strain values, calculated average values are given in Table 5.3 and Table 5.4.

Table 5.3. Average Extrusion Forces for Equivalent Plastic Strain 0.68

	Billet Length (mm)				
	35	*30*	*25*	*20*	*15*
$F_{max,1}$ (kN)	92	89.2	82	74	69.8
$F_{max,2}$ (kN)	94.4	84.4	78.5	75.6	69.5
$F_{max,avg.}$ (kN)	93.2	86.8	80.3	74.8	69.7

Table 5.4. Average Extrusion Forces for Equivalent Plastic Strain 1.2

	Billet Length (mm)		
	25	*20*	*15*
$F_{max,1}$ (kN)	153.9	140.5	124.4
$F_{max,2}$ (kN)	153.2	137.5	125.5
$F_{max,avg.}$ (kN)	153.6	139.0	125.0

Firstly, force differences are calculated for consecutive billet lengths. For the equivalent strain 0.68, ΔF values calculated as in Eqn. 5.6

$$\Delta F_{1,\ \varphi\ =\ 0.68} = F_{avg,35} - F_{avg,30} \qquad \Delta F_{1,\ \varphi\ =\ 0.68} = 6.4 \text{ kN} \qquad (5.6a)$$

$$\Delta F_{2,\ \varphi\ =\ 0.68} = F_{avg,35} - F_{avg,30} \qquad \Delta F_{2,\ \varphi\ =\ 0.68} = 6.5 \text{ kN} \qquad (5.6b)$$

$$\Delta F_{3,\ \varphi\ =\ 0.68} = F_{avg,25} - F_{avg,20} \qquad \Delta F_{3,\ \varphi\ =\ 0.68} = 5.5 \text{ kN} \qquad (5.6c)$$

$$\Delta F_{4,\ \varphi\ =\ 0.68} = F_{avg,15} - F_{avg,10} \qquad \Delta F_{4,\ \varphi\ =\ 0.68} = 5.1 \text{ kN} \qquad (5.6d)$$

When the initial yield stress of annealed 20MnB4 is taken as 390 MPa, by using Eqn. 5.5 friction coefficients are calculated as;

$$\mu_{1,\ \varphi\ =\ 0.68} = 0.10 \qquad (5.7a)$$

$$\mu_{2,\ \varphi\ =\ 0.68} = 0.11 \qquad (5.7b)$$

$$\mu_{3,\ \varphi\ =\ 0.68} = 0.09 \qquad (5.7c)$$

$$\mu_{4,\ \varphi\ =\ 0.68} = 0.08 \qquad (5.7d)$$

Same calculations are performed to find the friction coefficients by using the average forces given in Table 5.2. The ΔF values and friction coefficients are given below.

$$\Delta F_{1,\ \varphi\,=\,1.2} = F_{avg,25} - F_{avg,20} \qquad \Delta F_{1,\ \varphi\,=\,1.2} = 14.6\ kN \qquad (5.8a)$$

$$\Delta F_{2,\ \varphi\,=\,1.2} = F_{avg,15} - F_{avg,10} \qquad \Delta F_{1,\ \varphi\,=\,1.2} = 14.0\ kN \qquad (5.8b)$$

$$\mu_{1,\ \varphi\,=\,1.2} = 0.24 \qquad (5.9a)$$

$$\mu_{2,\ \varphi\,=\,1.2} = 0.23 \qquad (5.9b)$$

There is a significant inconsistency between the friction coefficients for two extrusion processes with different equivalent strains. For the same material coating and die production methods, difference exceeds 100 %. The main reason for this situation is assuming the normal stress equal to initial yield stress. It is expected to have higher normal stresses when the equivalent strain value increases. If the normal stress value taken lower than it should be, calculated friction coefficients will be higher than their real value. To determine the correct friction coefficients, FE analyses provide a more reliable environment.

5.4.2 Determination of Friction Coefficient by FEA

To represent the test parameters closest to real conditions, raw material is first drawn from 8.00 mm to 7.70 mm and trimmed. Also dies used in experiments are modeled by using deformable tools and prestressing is applied by using node overlapping method. Since the punch speed is very low compared to crank presses, thermal effects are neglected and process assumed to be isothermal. Finally, punch is modeled as rigid tool and effects of elastic deformations on the punch are considered as having no influence on the forming force.

As the first step, a convergence study is carried out to determine the suitable workpiece element size by investigating the forming force and normal stress distribution on the die container.

5.4.2.1 Determination of Appropriate Workpiece Element Size

Since the friction stress calculated by using Coulomb model is directly depending on the normal stress distribution, accurately calculated stress distribution has a great importance for the accuracy of the results. For this purpose, a convergence study is performed to determine the appropriate element size of the workpiece. Extrusion process with equivalent strain 0.68 is investigated by using Coulomb friction coefficient equal to 0.13. Normal stress distribution along the container surface and extrusion force is compared for element sizes of 1.5, 1.0, 0.7, 0.5, 0.3 and 0.1mm.

When normal stress distributions are plotted where the extrusion force reaches the highest value, it shows that normal stresses are fluctuating sharply for element sizes above 0.7 mm and reaches a stable distribution for element sizes 0.5mm and smaller (Fig. 5.22).
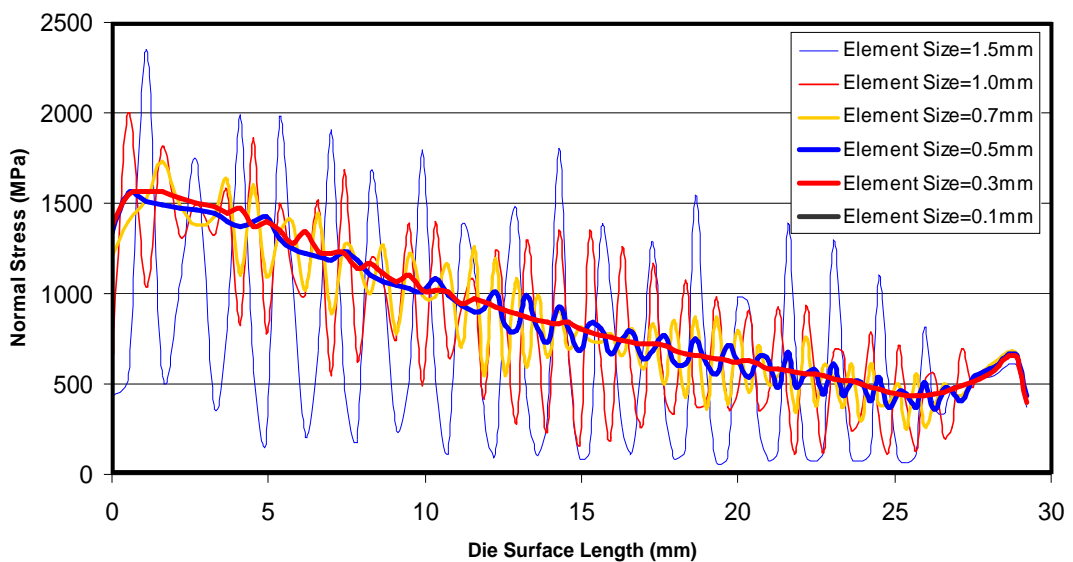
Figure 5.22. Normal stress vs. die surface length for different element sizes

Also forming force deviations are presented in Figure 5.23 for different element sizes. It starts to converge to 160 kN when the element size is set smaller than 0.7 mm. Also solution time is increasing sharply when element size goes below 0.3 mm which are listed in Table 5.5.
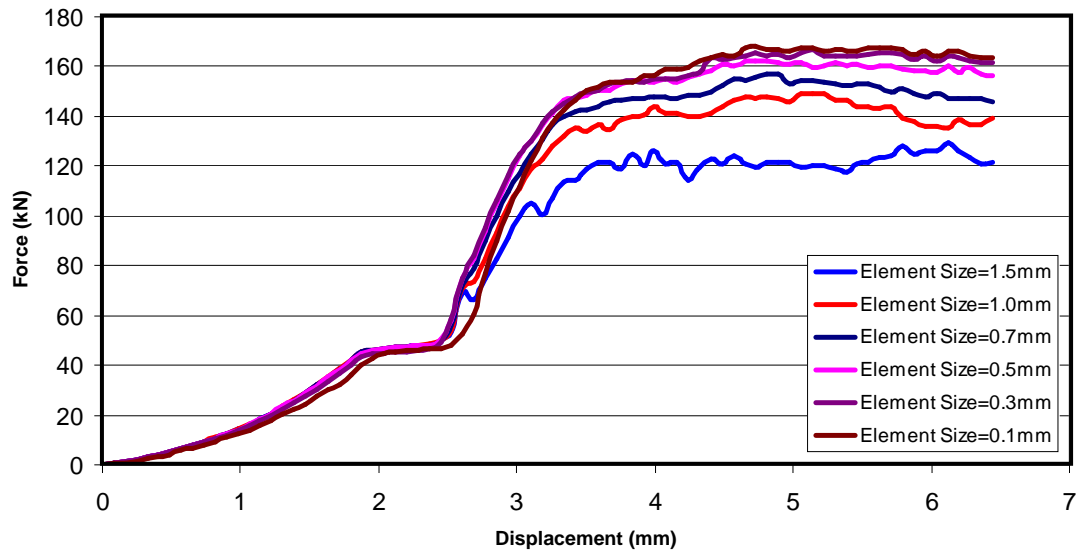
Figure 5.23. Extrusion force vs. displacement for different element sizes

Table 5.5. Solution time for different element sizes

Element Size (mm)	Solution Time (min.)
1.5	96
1.0	98
0.7	104
0.5	115
0.3	155
0.1	843

According to the results given above, element size of 0.5mm provides satisfactory normal stress distribution and force calculation. So that in the FE analyses, element size is taken as 0.5 mm. Another parameter which is investigated before the main extrusion anaylses is determination of effect of punch friction on the forming force.

5.4.2.2 Effect of Punch Friction on Forming Force

The same model of element size convergence study is used in the analyses to resolve how friction on the punch influences the extrusion force for different conditions. For this purpose, two extrusion analyses are performed with two different friction values between punch and workpiece which are 0.01 and 0.20 respectively whilst the friction between die and workpiece is set to 0.13. All the other simulation parameters are kept same. The force displacement curves of two analyses are plotted and shown in Figure 5.24. The calculated force variation throughout the extrusion process is almost the same for two different cases. This is showing that punch friction has not a significant effect on forming force, and it is taken as 0.15 in further analyses.
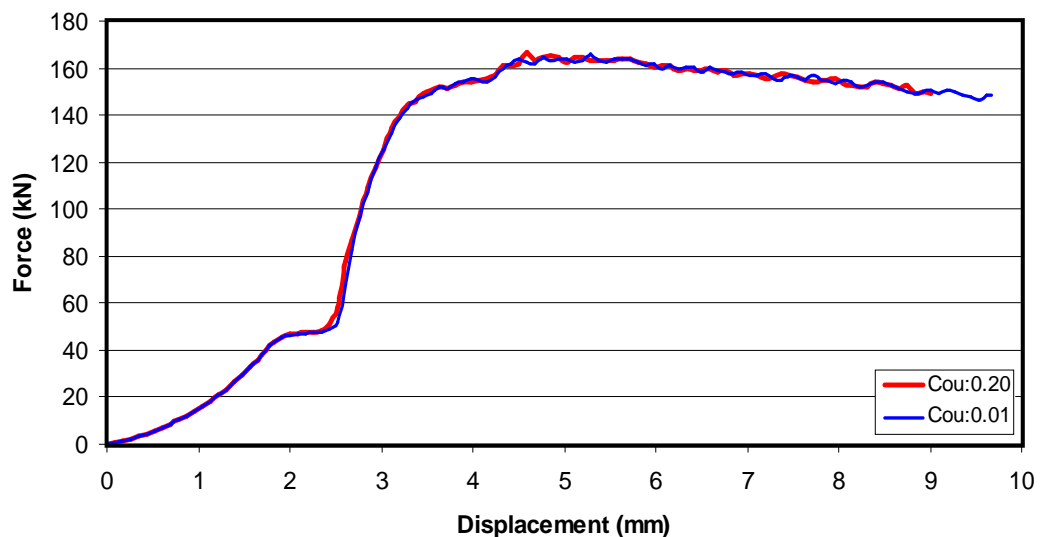
Figure 5.24. Force vs. displacement curves of extrusion process for different punch frictions

5.4.2.3 Comparison of FE Analyses to Experiment Results

To find out the appropriate friction model and friction coefficient for the forward rod extrusion process, finite element analyses are performed for each height/diameter ratio and equivalent plastic strain value. The parameter investigated in these analyses is the closeness of the deformation force versus the punch displacement calculated from computer simulations to experimental data.

Analyses are first performed for the equivalent plastic strain equal to 0.68. After making several simulations the friction constants giving the closest force values to test data are found as 0.09 for Coulomb and 0.13 for shear friction model for all height/diameter ratios. Also the force reduction trend with the stroke is more similar for the Coulomb than shear model. In the Figures 5.25 to 5.34, calculated forming force from FE simulations are plotted with the experiment data. For Coulomb model, the results are plotted for constants 0.08, 0.09 and 0.10 where as for shear model constants are set as 0.12, 0.13 and 0.14.
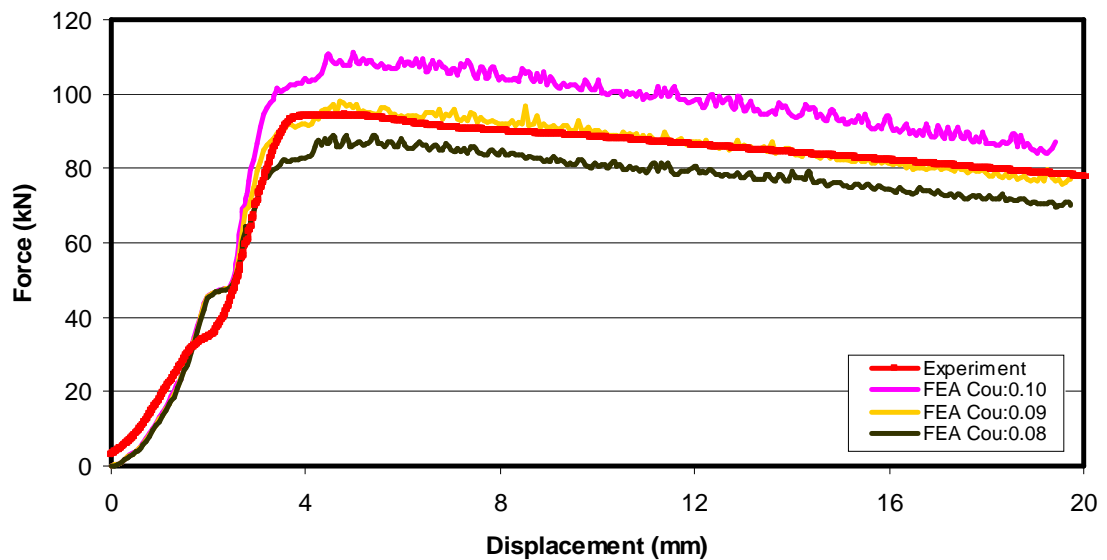
Figure 5.25. Comparison of calculated extrusion force by using Coulomb friction model with experiment data for $h/d = 3.5$ and $\varphi = 0.68$
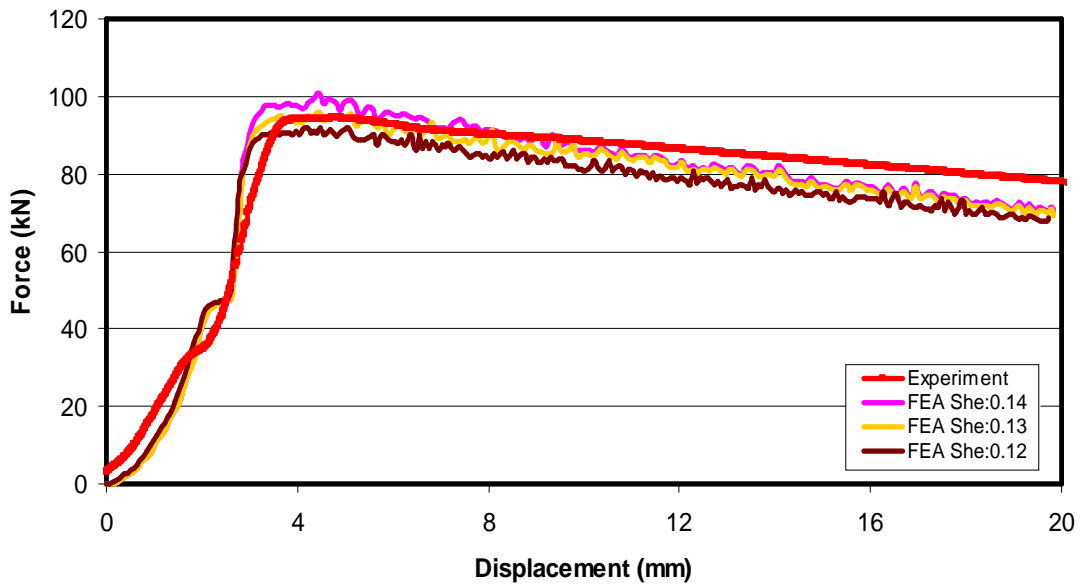
Figure 5.26. Comparison of calculated extrusion force by using shear friction model with experiment data for $h/d = 3.5$ and $\varphi = 0.68$
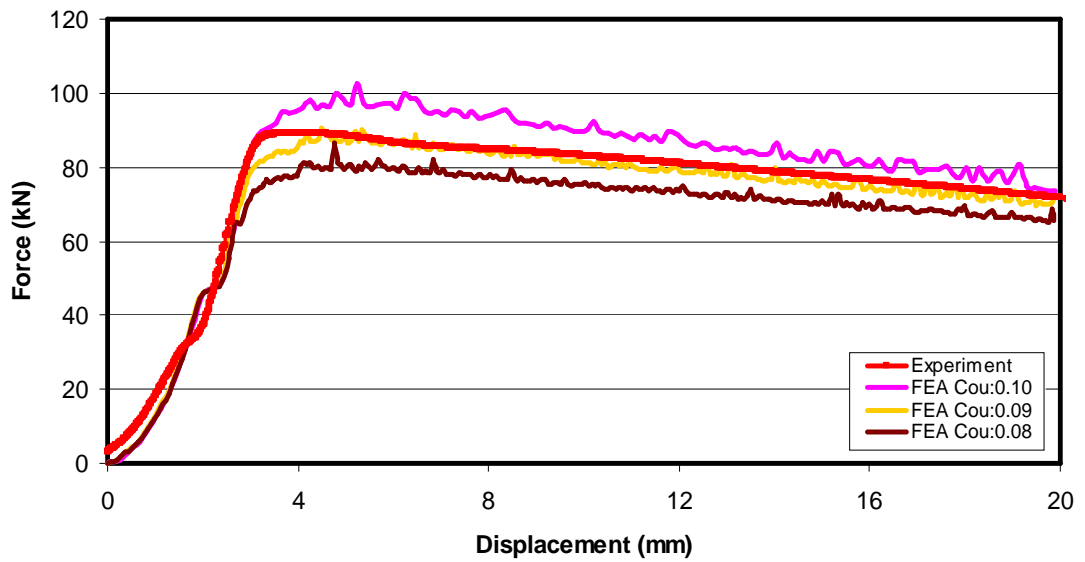
Figure 5.27. Comparison of calculated extrusion force by using Coulomb friction model with experiment data for $h/d = 3.0$ and $\varphi = 0.68$
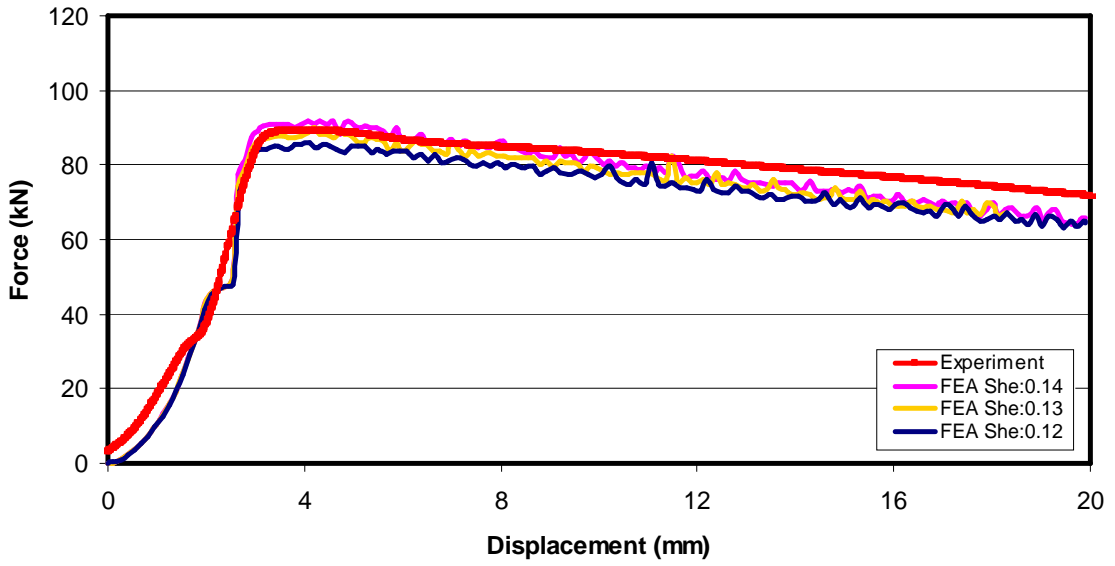
Figure 5.28. Comparison of calculated extrusion force by using shear friction model with experiment data for $h/d = 3.0$ and $\varphi = 0.68$
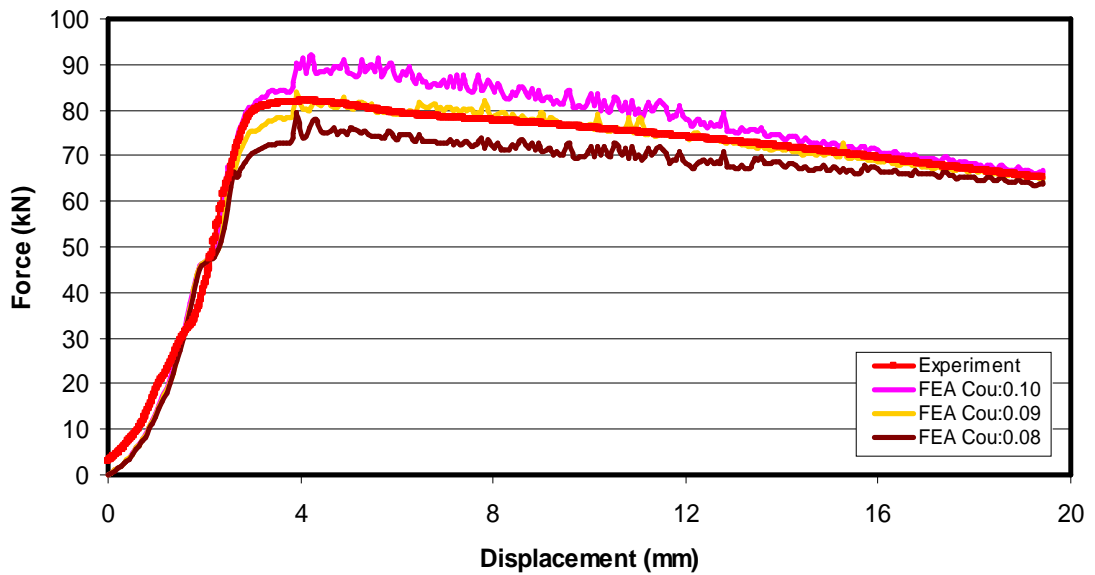
Figure 5.29. Comparison of calculated extrusion force by using Coulomb friction model with experiment data for $h/d = 2.5$ and $\varphi = 0.68$
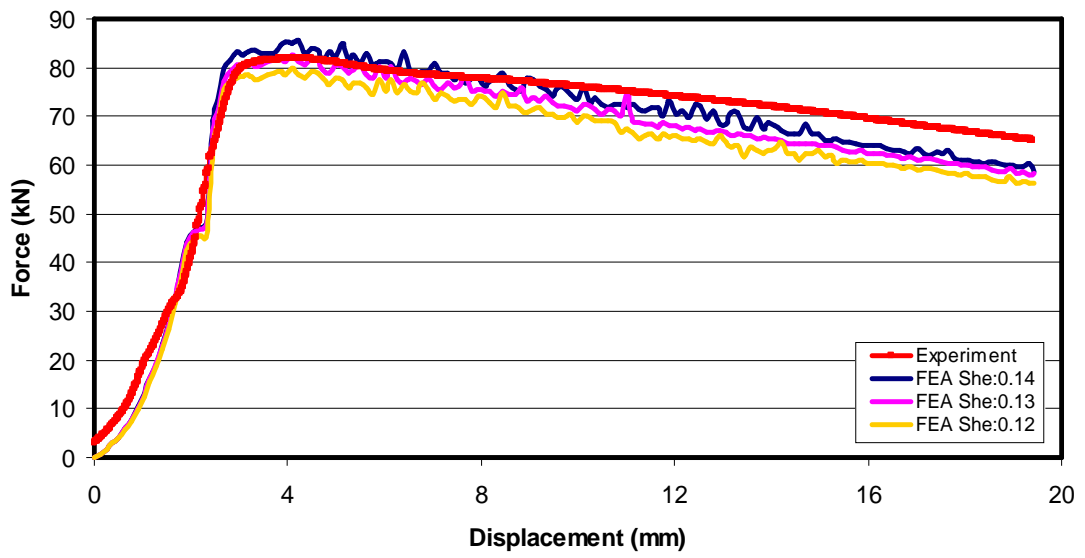
Figure 5.30. Comparison of calculated extrusion force by using shear friction model with experiment data for $h/d = 2.5$ and $\varphi = 0.68$
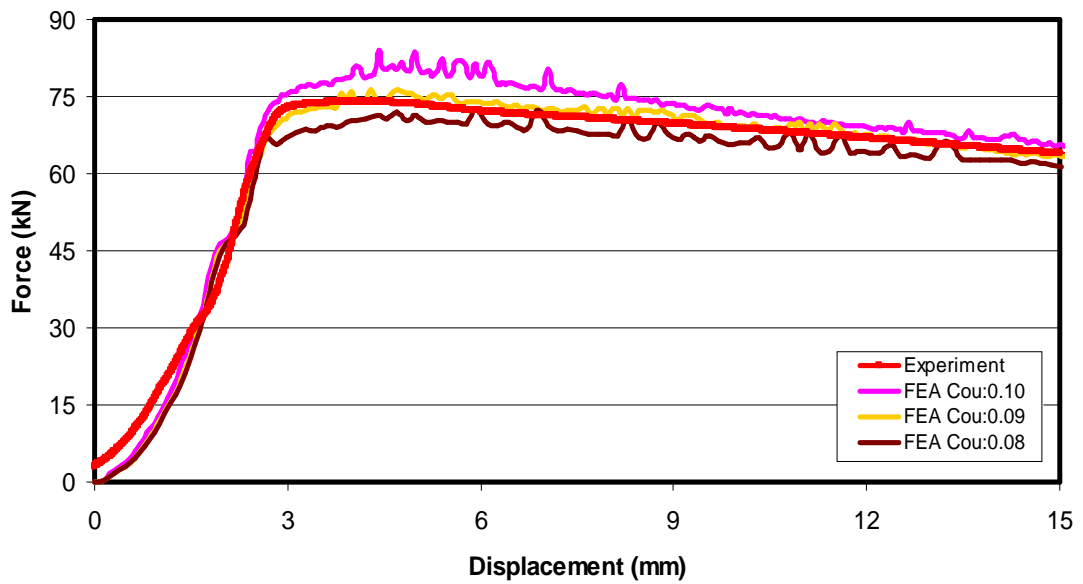
Figure 5.31. Comparison of calculated extrusion force by using Coulomb friction model with experiment data for $h/d = 2.0$ and $\varphi = 0.68$
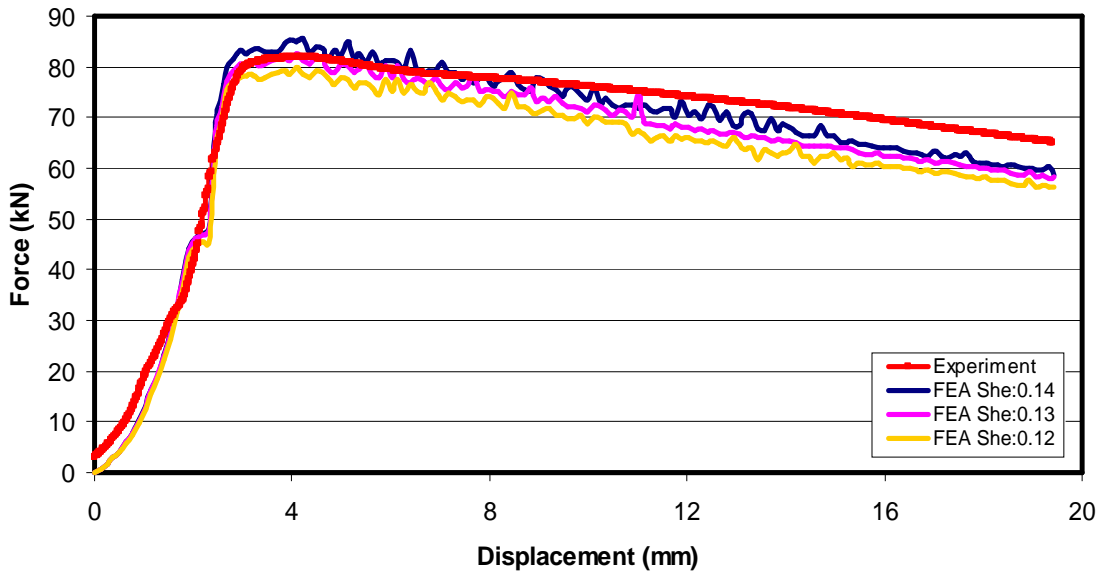
Figure 5.32. Comparison of calculated extrusion force by using shear friction model with experiment data for $h/d = 2.0$ and $\varphi = 0.68$
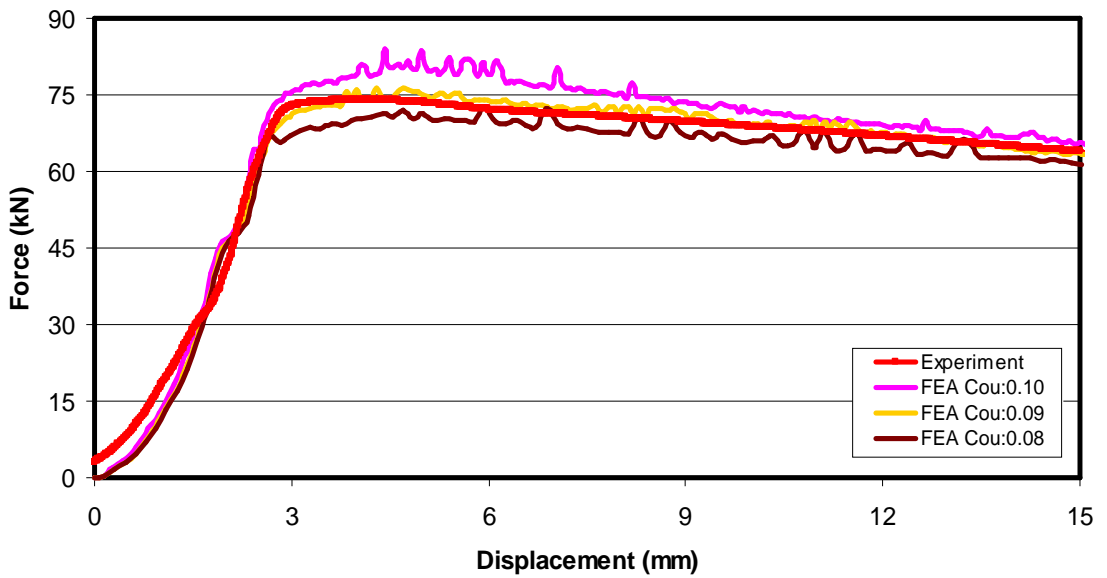
Figure 5.33. Comparison of calculated extrusion force by using Coulomb friction model with experiment data for $h/d = 1.5$ and $\varphi = 0.68$

196
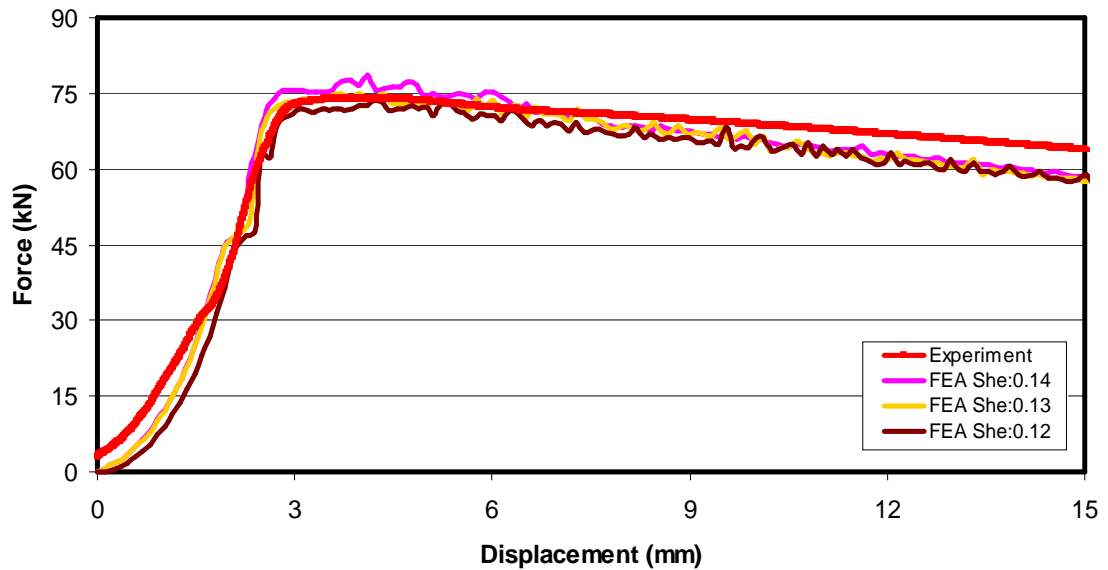
Figure 5.34. Comparison of calculated extrusion force by using shear friction model with experiment data for $h/d = 1.5$ and $\varphi = 0.68$

In the same way, extrusion simulations are repeated for the equivalent strain value 1.2 by using both friction models. The plots given in Figure 5.35 to 5.40 are showing the results of analyses performed with Coloumb friction constant 0.09 fits very close to force – stroke data gathered from experiment. However for the Shear friction model the most appropriate constant is found as 0.30 which is much bigger than the value found in the analyses with equivalent plastic strain 0.68. Since dies and specimens are similar and same conditions are present in the both experiments, it is expected to have similar friction coefficients for both conditions. Therefore, Coulomb friction model seems more appropriate for the cold forming simulations.
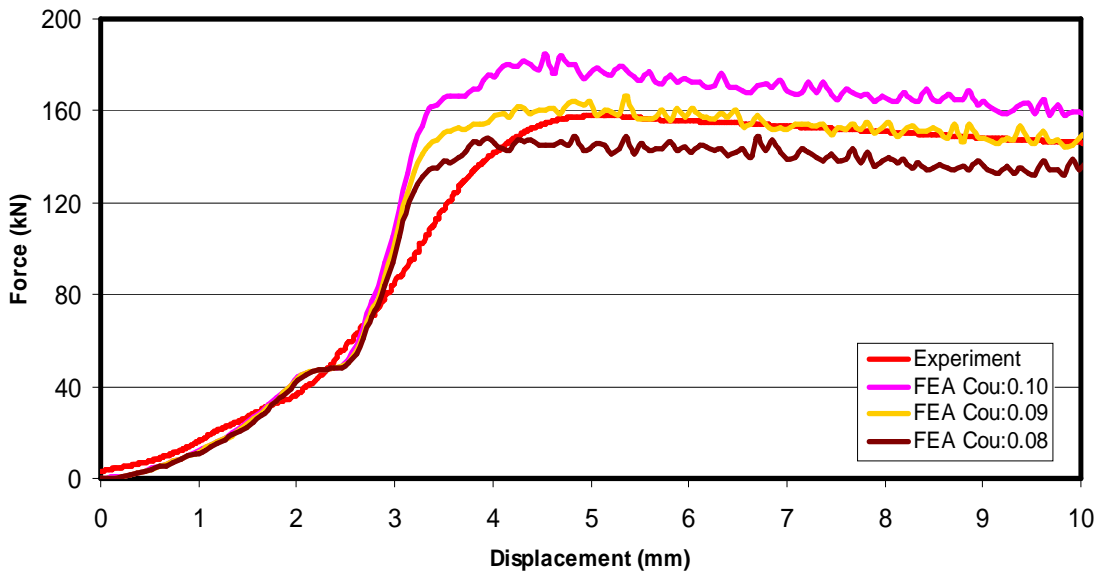
Figure 5.35. Comparison of calculated extrusion force by using Coulomb friction model with experiment data for $h/d = 2.5$ and $\varphi = 1.2$
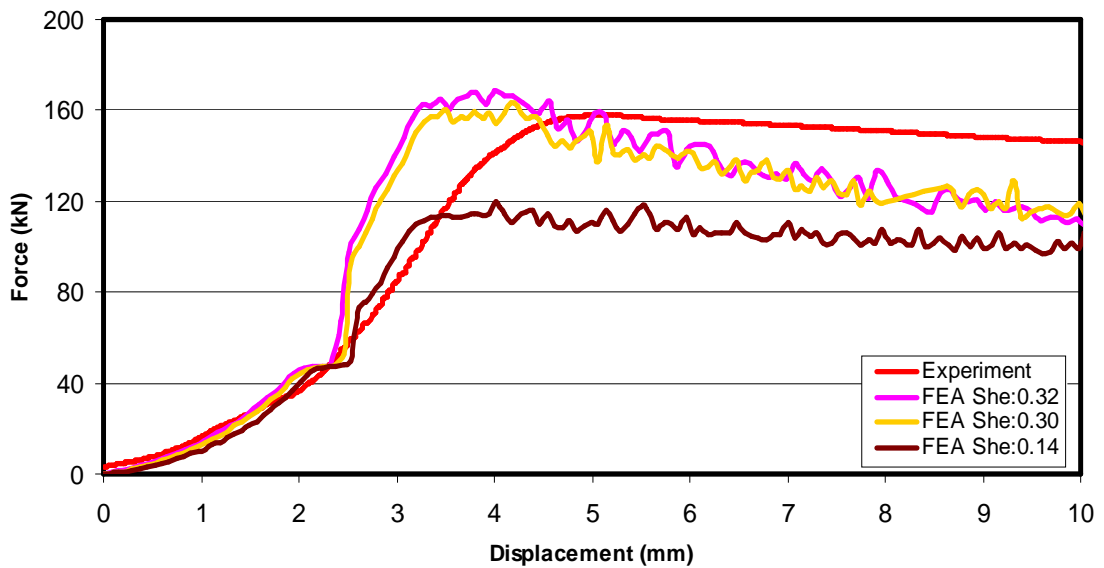
Figure 5.36. Comparison of calculated extrusion force by using shear friction model with experiment data for $h/d = 2.5$ and $\varphi = 1.2$
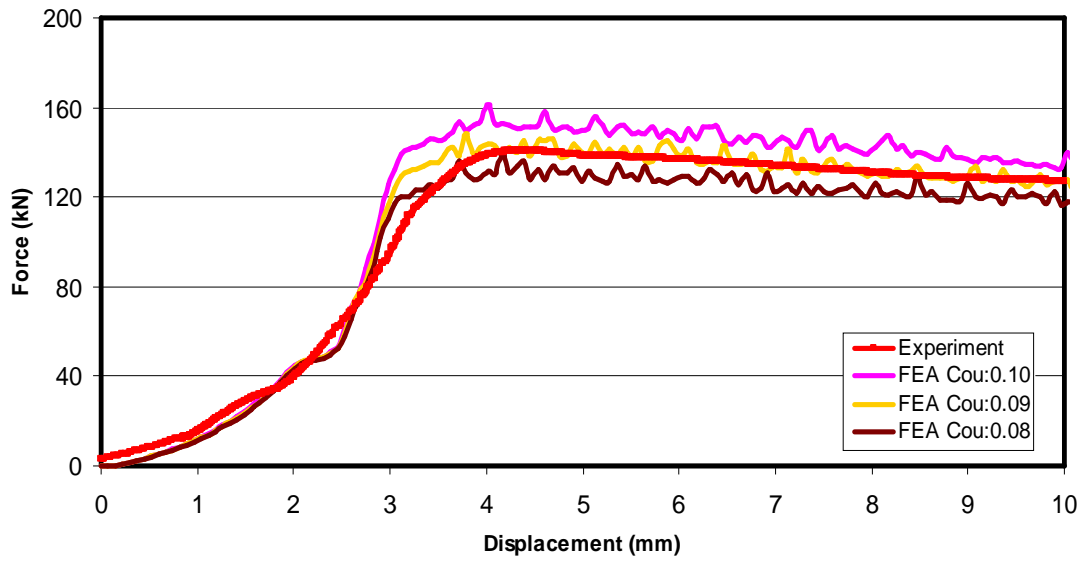
Figure 5.37. Comparison of calculated extrusion force by using Columb friction model with experiment data for $h/d = 2.0$ and $\varphi = 1.2$
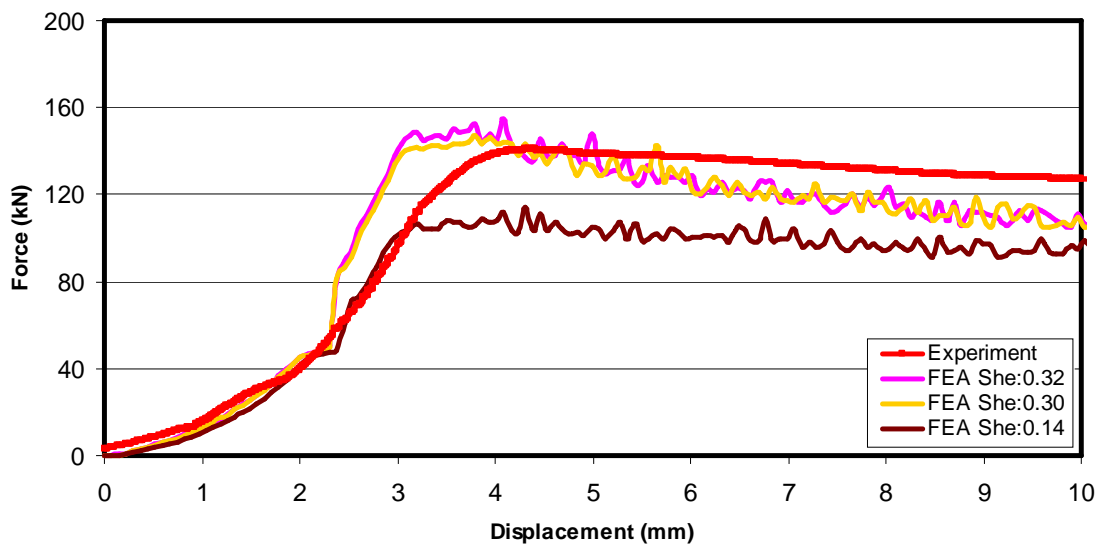
Figure 5.38. Comparison of calculated extrusion force by using shear friction model with experiment data for $h/d = 2.0$ and $\varphi = 1.2$

199
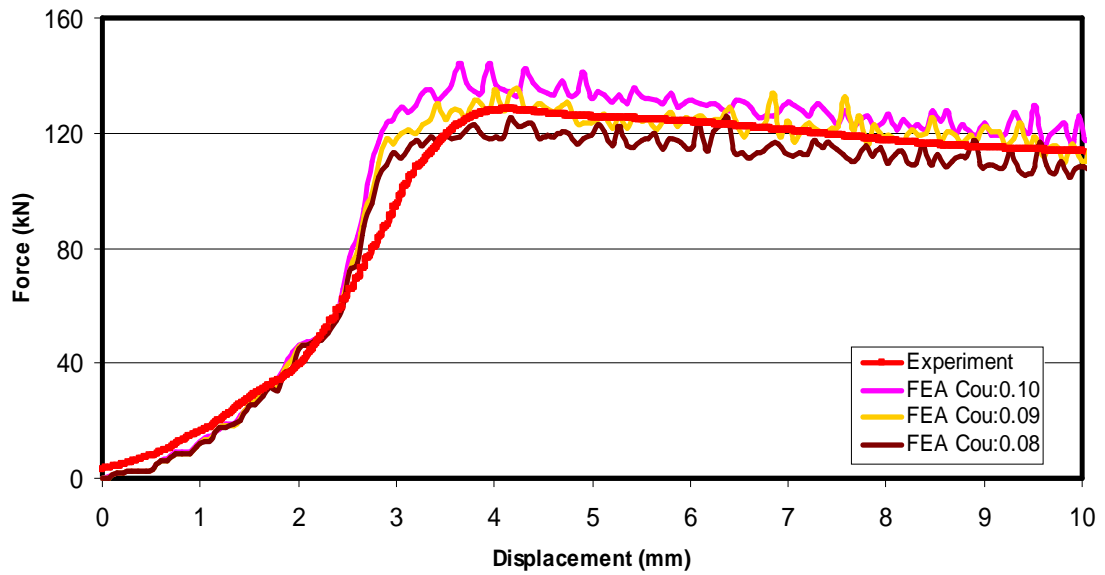
Figure 5.39. Comparison of calculated extrusion force by using Coulomb friction model with experiment data for $h/d = 1.5$ and $\varphi = 1.2$
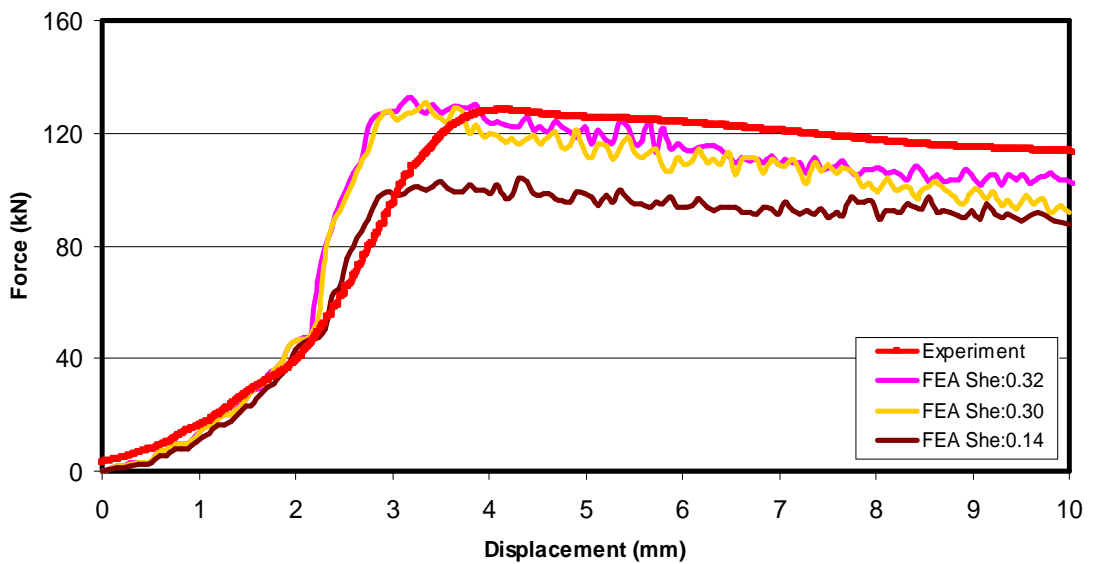
Figure 5.40. Comparison of calculated extrusion force by using shear friction model with experiment data for $h/d = 1.5$ and $\varphi = 1.2$

200

Determined friction constants for Coulomb model by making analytical calculations where equivalent plastic strain is 0.68 are almost the same with the coefficient determined by FE analyses. However this is not the case for the equivalent plastic strain 1.2 where the friction coefficient is calculated approximately 0.23 which is much bigger then the one determined by numerical analyses. This deviation occurred due to the wrong normal stress assumption used in the analytical approach. In Figure 5.41, normal stress distribution along the container is shown for both equivalent plastic strains. The normal stress values for the equivalent plastic strain 0.68 is very close to initial yield stress of material which is 390 MPa. However, the normal stress values are increasing up to 1400 MPa. Therefore, taking the initial yield stress value as the internal pressure while performing analytical calculations to find extrusion force will lead to wrong results.
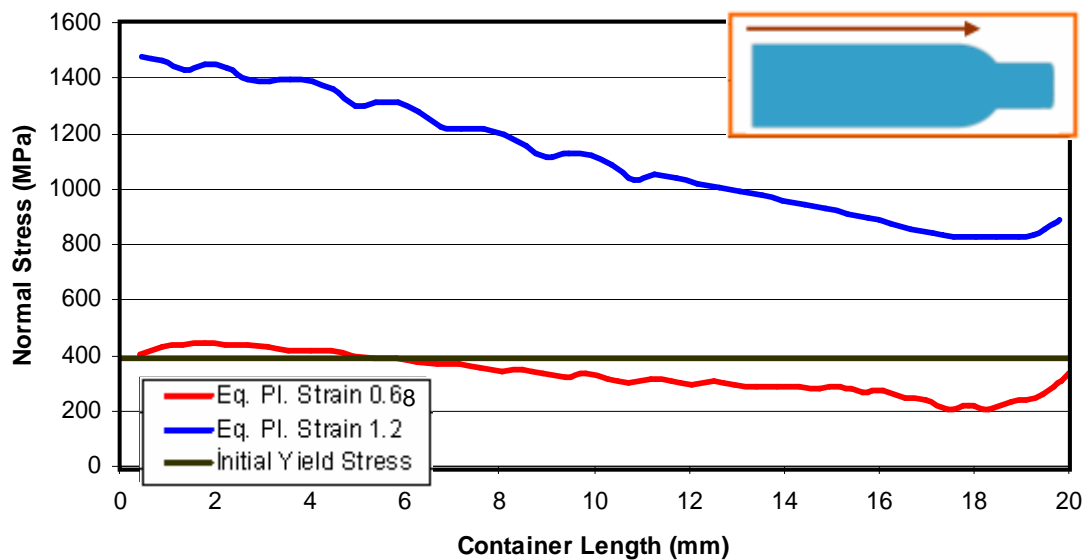
Figure 5.41. Comparison of normal stress distribution along the container for different equivalent plastic strain values with initial yield stress of material

When all the plots are reviewed, two main differences are defined between the FEA results and the experimental data. The first difference is the variation of the force values during the force increase before reaching the maximum value. It is seen in both conditions but more evident for the case when the equivalent plastic strain is 1.2 (Fig. 5.42). The reason for this difference is due to the elastic deflection of the tensile test machine. Since the displacement sensor is located on the top of the machine, this sensor measures both displacement of the punch and elongation of the columns of the machine.
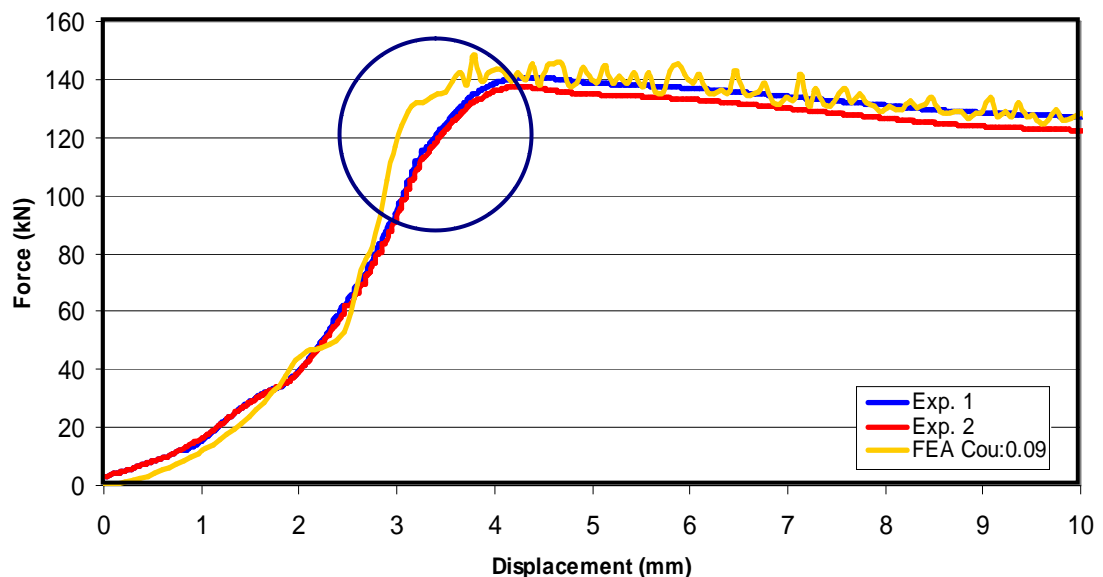
Figure 5.42. Difference in the force due to the elastic effects on test machine

Secondly, there exists a difference in the force path close to maximum value, which is seen more evident in the force – displacement plots of the extrusion process with equivalent plastic strain 0.68. In Figure 5.43 an example of this case is shown for the height / diameter ratio 2.5. It is clearly shown that, FEA result gives a lower value than the measured force during the experiment.
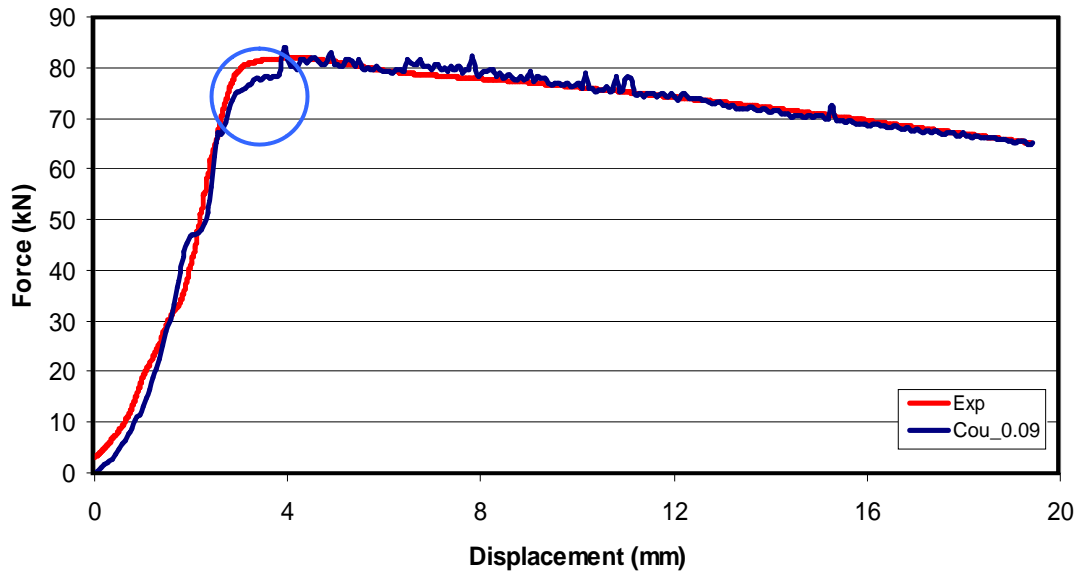
Figure 5.43. Dfference between the measured and calculated maximum extrusion force

This phenomenon is studied by C. Onder [75] and reason for this variation is explained with the high friction on the uncoated shear surface on the billet faces. In the FE analyses, same friction coefficient is defined on the all surfaces of the workpiece whereas shear surface on the specimen is uncoated and results in more

Figure 5.44. Extruded specimens **a)** Phosphate and soap layer on the shear surface **b)** Shiny surface at the tip of the specimen means this region had exposed to high friction [75]

203

severe friction while the material flows through the die shoulder where the extrusion force reaches to a maximum value (Figure 5.44). Due to the increase in the friction force, total forming force becomes higher then the calculated force with numerical methods.

5.4.3 Force Variation with Height/Diameter Ratio

Container friction is the only factor which causes force difference between billets with different lenghths. So that extrusion force increases with the increasing billet length.

Difference in the calcualted forces for rigid and deformable tools are explained before in Chapter 4. The same situation is also observed in the analyses of extrusion process performed for friction analyses. In Figure 5.45 and 5.46, calculated forces from the FE analyses with rigid and deformable tools are shown for two different equivalent plastic strains. Higher force values are obtained from the rigid tool analyses.
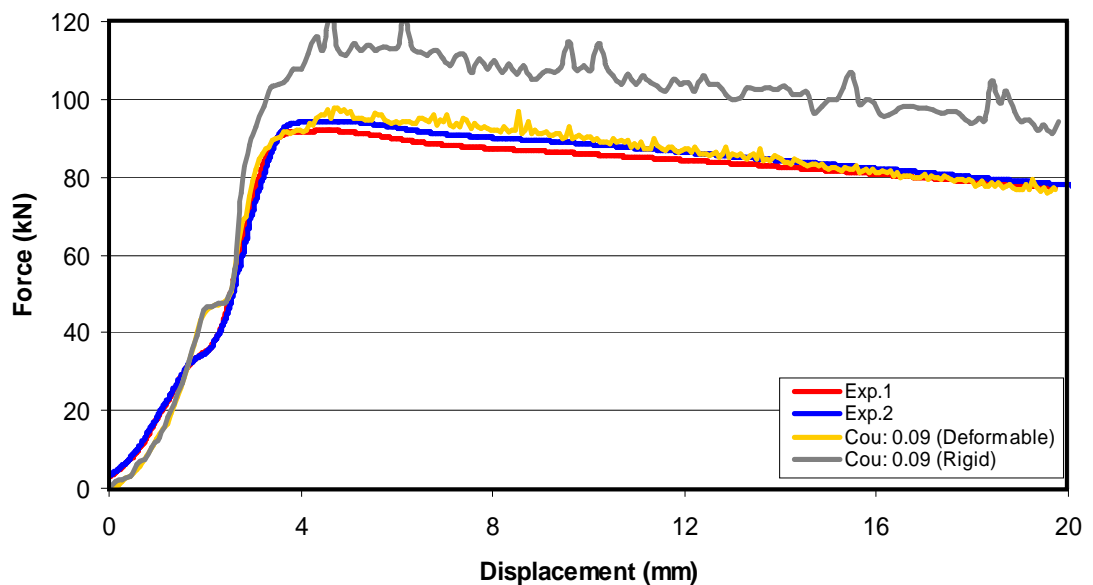
Figure 5.45. Extrusion force obtained from experiment and FE analyses performed with two different die models for $\varphi = 0.68$ and $h/d = 3.5$
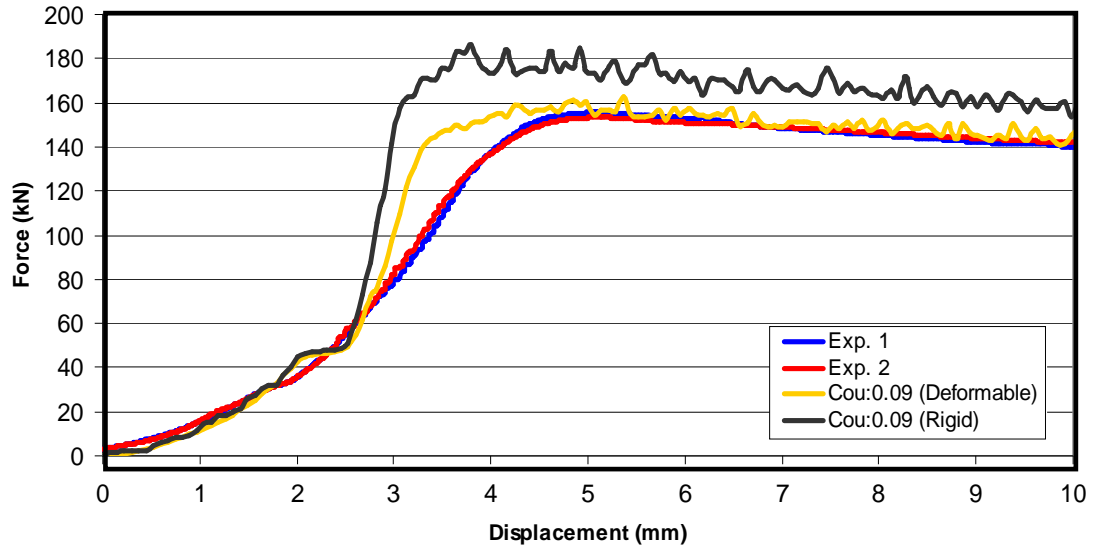
Figure 5.46. Extrusion force obtained from experiment and FE analyses performed with two different die models for $\varphi = 1.2$ and $h/d = 2.5$

Appropriate friction coefficient value for Coulomb model is also determined by performing FE simulations using rigid tools. All the process parameters are taken the same with the analyses performed with deformable tools except die model. Force – displacement curves obtained from FE analyses are fitted on the experimental data for different friction coefficient values. As it can be seen in Figures 5.47 – 5.54, friction coefficient 0.07 is giving the closest results for the equivalent plastic strain 0.68. However for the extrusion process with equivalent plastic strain value 1.2, the most appropriate friction coefficient is found as 0.08. Although the same friction coefficient is determined for both equivalent plastic strain values by using deformable tool models, two different values are determined by using rigid tools. This result explains that FE analyses performed with deformable tool models provide more reliable results than the ones performed with rigid tools.
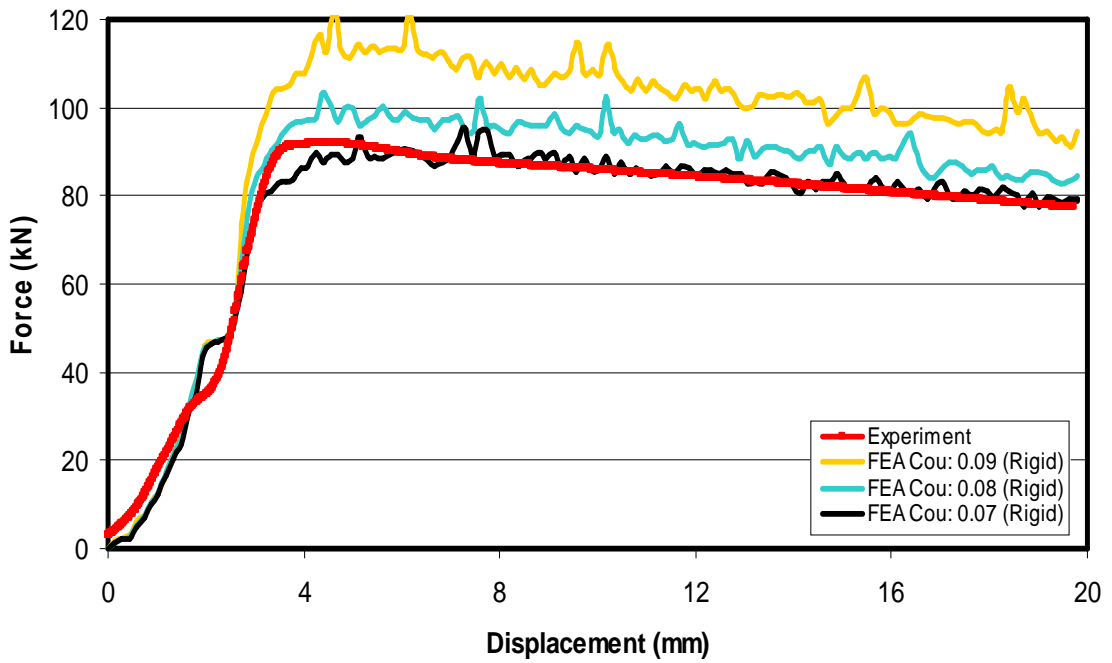
Figure 5.47. Comparison of calculated extrusion force by using Columb friction model with experimental data for $h/d = 3.5$ and $\varphi = 0.68$ (Rigid Die)
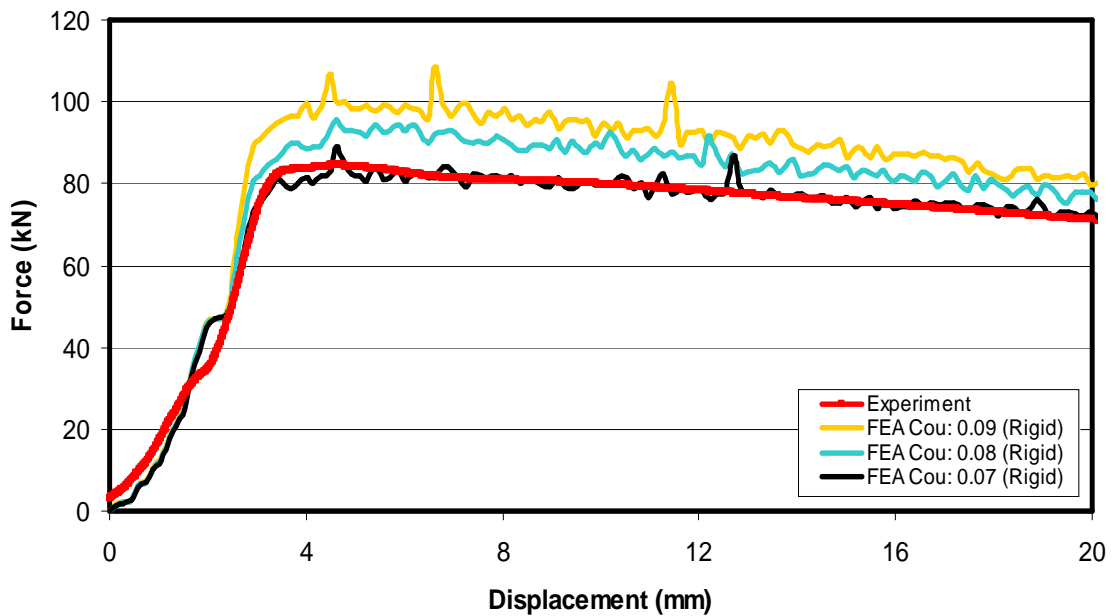
Figure 5.48. Comparison of calculated extrusion force by using Columb friction model with experimental data for $h/d = 3.0$ and $\varphi = 0.68$ (Rigid Die)
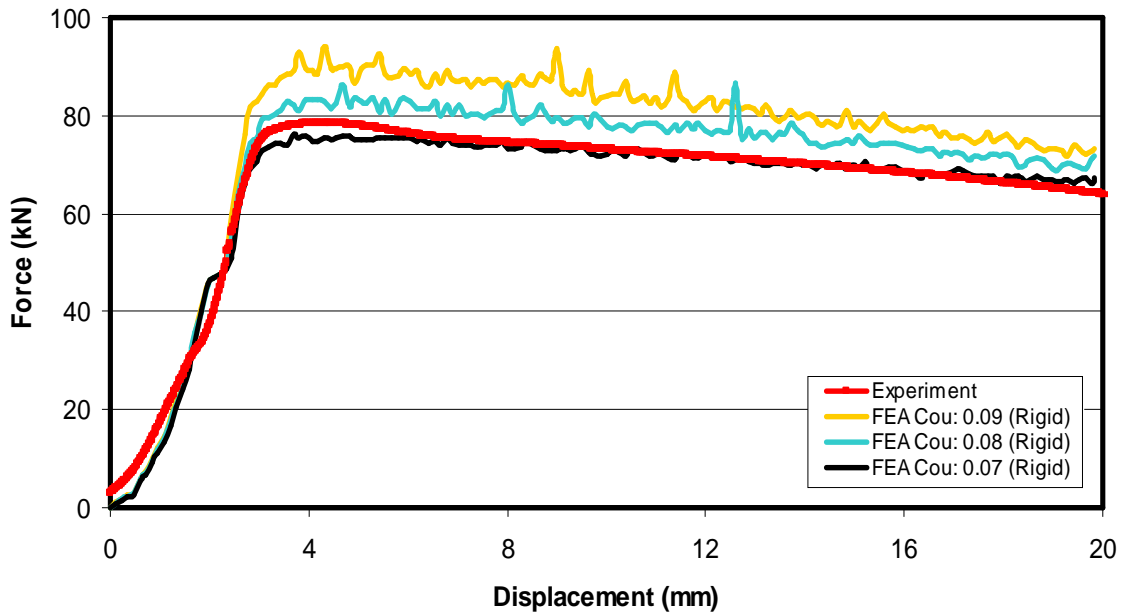
Figure 5.49. Comparison of calculated extrusion force by using Columb friction model with experimental data for $h/d = 2.5$ and $\varphi = 0.68$ (Rigid Die)
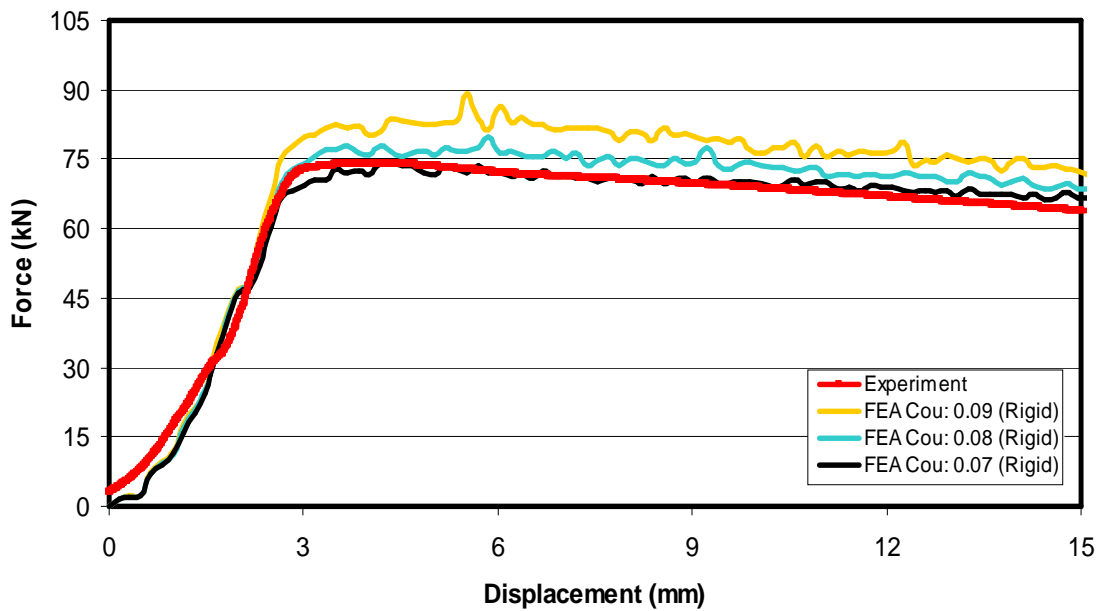
Figure 5.50. Comparison of calculated extrusion force by using Columb friction model with experimental data for $h/d = 2.0$ and $\varphi = 0.68$ (Rigid Die)
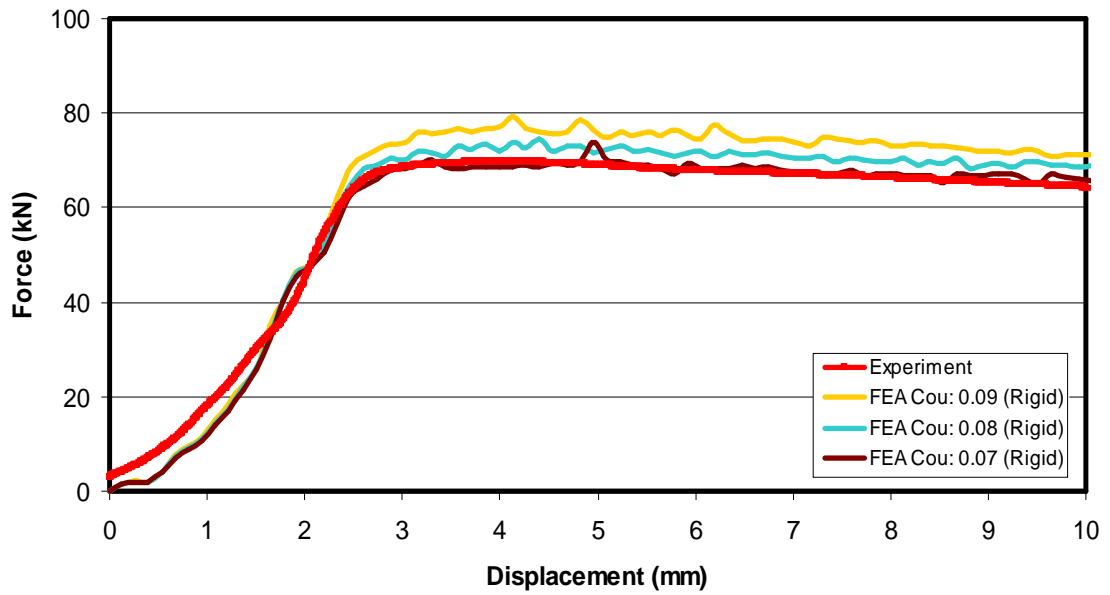
Figure 5.51. Comparison of calculated extrusion force by using Columb friction model with experimental data for $h/d = 1.5$ and $\varphi = 0.68$ (Rigid Die)
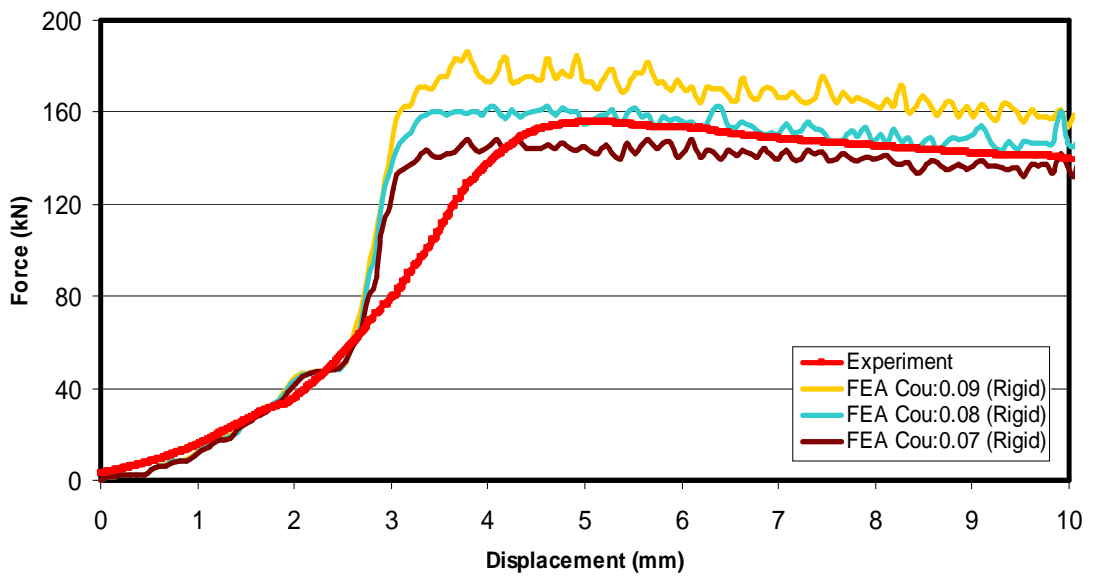
Figure 5.52. Comparison of calculated extrusion force by using Columb friction model with experimental data for $h/d = 2.5$ and $\varphi = 1.2$ (Rigid Die)

208
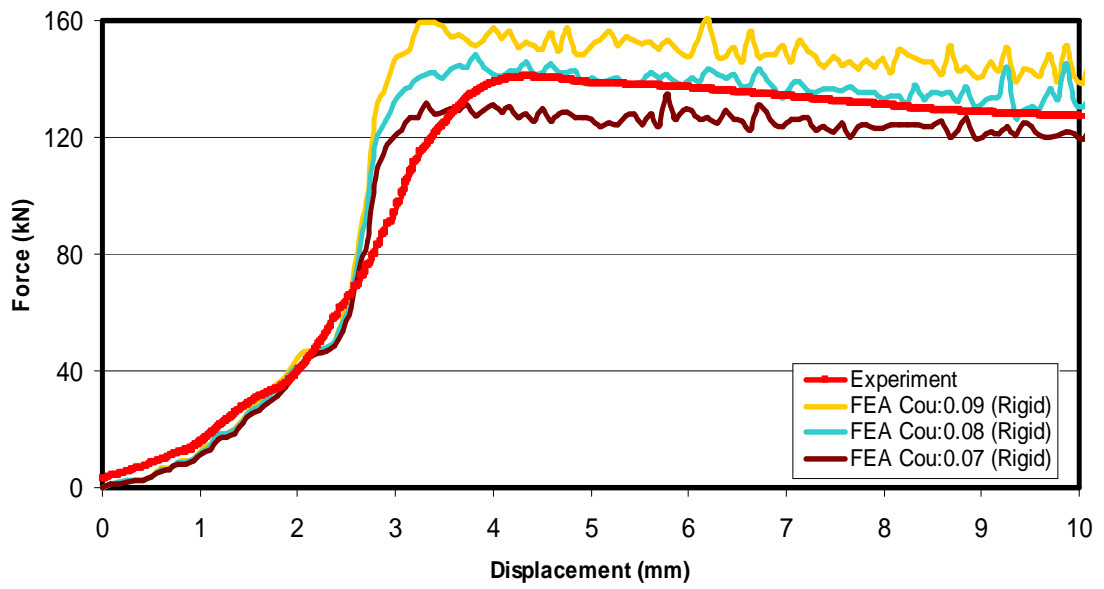
Figure 5.53. Comparison of calculated extrusion force by using Columb friction model with experimental data for $h/d = 2.0$ and $\varphi = 1.2$ (Rigid Die)
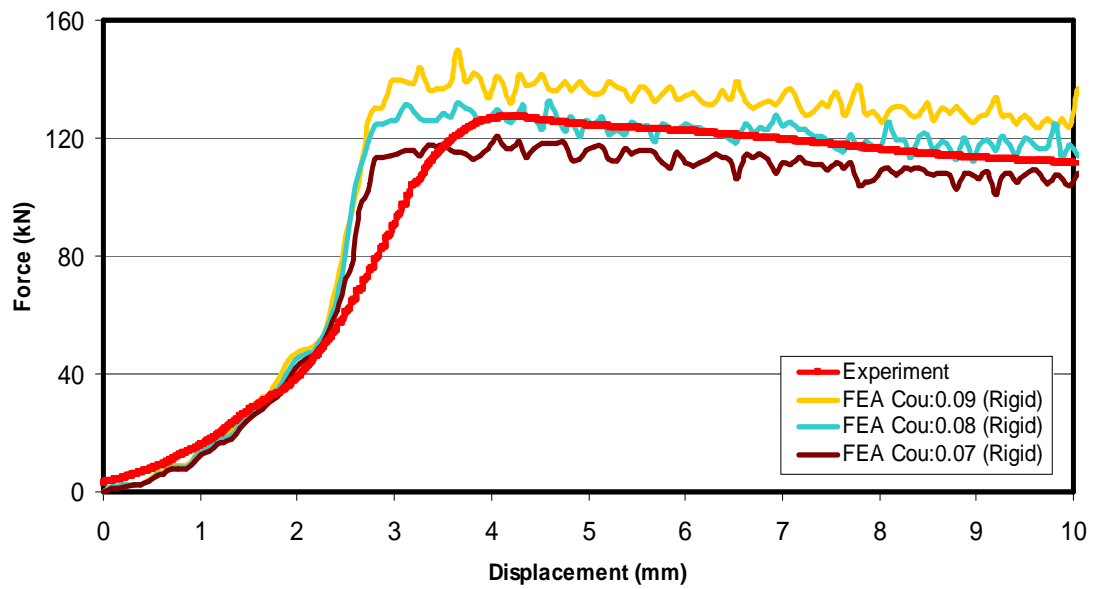
Figure 5.54. Comparison of calculated extrusion force by using Columb friction model with experimental data for $h/d = 1.5$ and $\varphi = 1.2$ (Rigid Die)
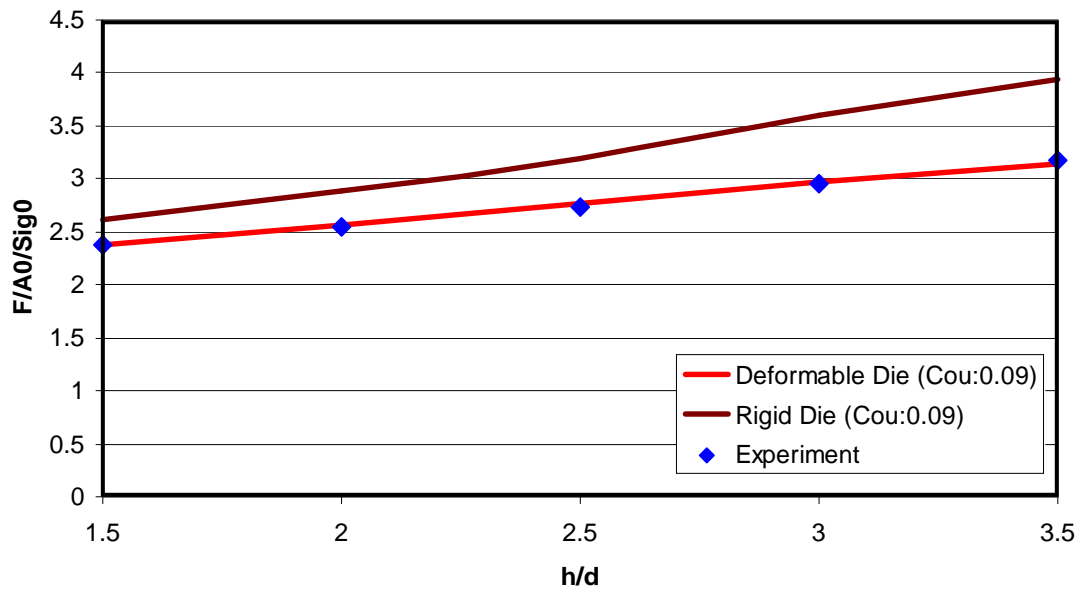
Figure 5.55. Normalized extrusion force vs. h/d ratio for $\varphi = 0.68$
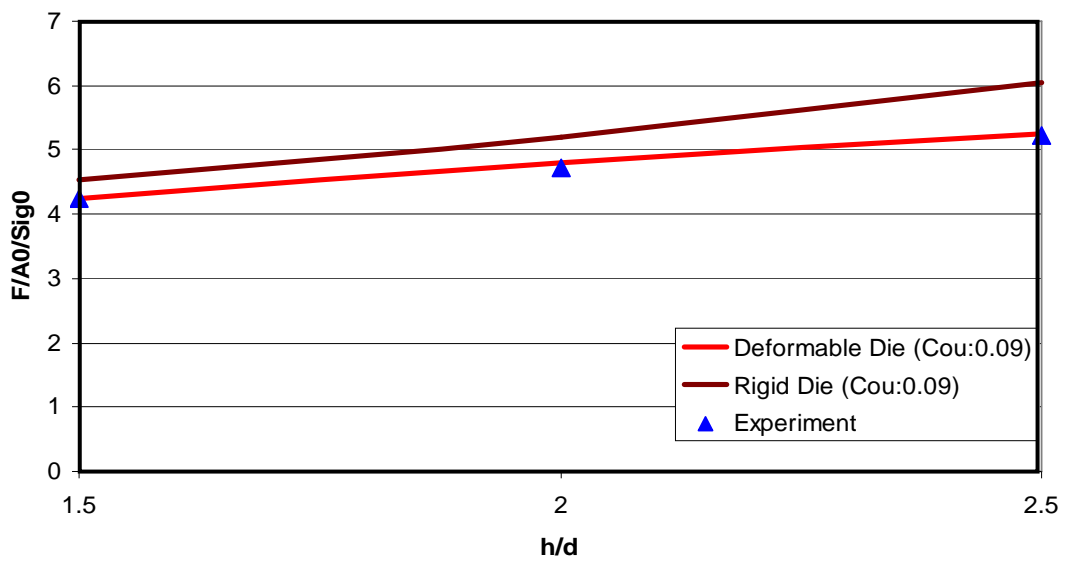
Figure 5.56. Normalized extrusion force vs. h/d ratio for $\varphi = 1.2$

In Figure 5.55 and 5.56, normalized extrusion force ($F/A_0/\sigma_{f0}$) versus billet height/diameter ratio is ploted for FE analyses and experiments for equivalent plastic strains 0.68 and 1.2 respectively where F is the maximum extrusion force and A_0 is the inlet cross section area.

According to the plots, it is clear that difference between the forces calculated by using two different die models increases as the h/d ratio gets higher. This will yield significant errors during the analyses of long extruded parts (Fig. 5.57). When the curves in the above graphs are extended, it has been observed that deviations will reach up to 40% when h/d ratio is 9.

Figure 5.57. Extruded part with h/d = 8.5 and $\varphi = 1.05$

CHAPTER 6

DISCUSSION, CONCLUSION
AND
FURTHER RECOMMENDATIONS

In this study, two main subjects are studied. In the first part, stress analyses are performed on prestressed dies used in bolt forming. In the second part, appropriate friction model and constant are investigated to obtain the most accurate FE analyse results.

Die stress analyses are started with modeling the fundamental application which is the shrink fit assembly of die insert and stress ring. Since all the stresses formed during forging depend on the initial stress state on the prestressed dies, detailed analyses are performed in order to prove the correctness of the FE results.

Since the real process of assembly includes heating and cooling of the stress ring, the same conditions are created by applying proper boundary conditions. Alternatively, commercial finite element software program MSC Superform has a special feature to represent the interference between the tool components by overlapping the nodes. Although both of the methods give the same results, overlapping methods provides ease in modeling and shorter solution time.

Analytical solutions obtained from the theory of elasticity almost coincide with the FE results of prestressing dies with one and two stress rings. The reliability of the FE analyses is enhanced when results are in good agreement with the experimental results.

The simple geometry of tools which are used in the verification of shrink fit simulations did not cause any difficulties in the meshing with quadrilateral elements. However, during meshing the dies with complex geometry, problems arise especially at small fillet radii. Triangular elements provide better mesh quality at these locations as compared to the quadrilateral elements. The prestressing analyses performed with triangular elements give the same results as with quadrilateral elements.

In the real assembly process to prevent material shaving between the die insert and stress ring, a taper angle is formed on both components in the range of 0.2º - 1.5º. The stress distribution is changing significantly compared to straight assembly when taper angle becomes greater than 1.0º. So that, this parameter should be included in the analyses when it gets greater than the defined threshold value.

One of the most important parameters during the die design is the determination of the suitable prestressing condition on die insert to prevent early failure. This can be achieved by selecting the optimum tool diameter and interference value depending on the pressure acting on the die insert. By using the developed optimization tool, die insert diameter and interference values can be determined according to the normal pressure obtained from the FE analyses.

Addition to prestressing dies with stress ring, a second prestressing is applied in the axial direction on the split dies which are placed in a casing. This application is necessary, where axial force is high enough to separate split dies, to prevent shaving of formed material. Hence, in the forming operations like extrusion or shoulder formation on the shaft of the bolt, axial prestressing should be applied.

Performing die stress analyses by using the deformable tool models in the forming analyses instead of transferring the load will provide more accurate results. Since the die expansion is neglected in the presence of rigid tools, normal stresses acting on the die insert are calculated higher compared to analyses in which deformable tools are used. This will result in higher force prediction in the analyses where friction has direct influence on the forming force. Moreover, in complex tooling systems and die profiles, using the force transfer method will not be feasible to perform die stress analyses due to high number of contact areas.

Case studies in the last section of the Chapter 4 show how FEM is beneficial in predicting and preventing tool failures. Use of this technology in industry will provide improvement in production efficiency and cost reduction. Especially integration of tool design with FE simulations will lead to robust production.

For friction analyses, two different processes are investigated. One of them is the ring compression test which is a frequently used test method to determine the friction coefficient. Forward rod extrusion process is the second type of analyses performed to verify the results obtained from the ring compression test.

Convergence study performed prior to the FE analyses shows that, relative sliding velocity constant has a significant effect on the results of ring compression simulations. As the constant value gets bigger effect of friction get less. So that, this constant value should be kept as small as possible.

In ring compression tests, although calibration curves created by using both friction models (shear and Coulomb) fits on the experimental results, shear friction model agrees better with the obtained data. Standard deviation value is taken as the criterion during this evaluation. On the other hand, Coulomb friction model gives highly consistent results in the forward rod extrusion tests for both equivalent plastic strain values. Difference between the shear friction constant is almost 100% between the extrusion processes with equivalent plastic strains 0.68 and 1.2.

The effect of using rigid tools in the analyses is also clearly observed in the results of extrusion analyses. In the presence of deformable tools, friction coefficient constant is found as 0.09 for both equivalent plastic strain values while two different friction coefficients (0.07 and 0.08) are determined for each equivalent plastic strain value when rigid tools are used.

For the extrusion processes with high length/diameter ratio, there will be a big difference in the calculated forces between the analyses performed by using rigid and deformable tools. For instance, this difference will be around 40% for processes where length/diameter ratio is 9. According to these results, Coulomb friction model is more appropriate for cold forming operations. Addition to that use of rigid tools will always cause an error in the FE analyses.

Recommendations for future studies about these subjects are given as follows:

Currently in industry, H13 (1.2344) hot working steel is used as stress ring material in conventional prestressing systems. Various materials with different hardness values can be tested and analysed for improved performance that provide longer tool life. Also effects of using different materials for inner and outer rings in multi-ring systems can be investigated for obtaining higher prestressing on die insert.

As another subject, in addition to the optimization program developed in this study for one ring systems, a new code can be developed to optimize process parameters for multi-ring systems.

Since the correct assembly of insert and ring has great influence on tool life, new techniques can be investigated for this process. For instance, instead of heating stress ring, insert can be cooled down to ease the assembly. In such a study effects of cooling and heating operation on die insert must be well analysed. Evaluating the performance of different lubricants (dry or liquid) used in the assembly process can be another topic that deserves attention.

In extrusion tests, the highest normal stress value was found as 1400 MPa and this corresponds to 126 MPa shear stress on the contact surface. Since the shear yield stress of the material is 225 MPa, sticking friction condition could not be observed in the conducted tests. This study can be carried one step further by performing forward extrusion tests with higher area reduction to obtain high normal stresses acting on the tool surface which will cause sticking friction.

In this study FEM results showed that, assumption of normal stress action on container as σ_{f0} in elementary force computation models is not giving correct results especially for processes with high area reduction. Since the normal stresses become higher than σ_{f0} in these processes, new formulation should be derived by considering deformable die models.

REFERENCES

[1] **Blake, Alexander:** "Threaded Fasteners, Materials and Design"; Markel Dekker Inc; 1986

[2] **K. Lange:** "Hanbook of Metal Forming", Society of Manufacturing Engineers, McGraw Hill, 1985

[3] DIN 8580 Fertigungsverfahren: Begriffe; Einteilung. Entwurf vom Juli 1985. Deutsches Institut für Normung

[4] **A.E. Tekkaya:** ME 453 Metal Forming Technology, Lecture Notes, METU (2001), Ankara

[5] **Forging Facts;** *Retrieved* 13.06.2006, *from* Forging Industry Association Web site: http://www.forging.org

[6] **C. M. Dolezalek:** "The Engineer's View of Industrial Production", (in German), Tech. Rundsch, 35, 1965

[7] **B. Yavuz:** "Correlation between vickers hardness number and yield stress of cold-formed products", M.S. Thesis, METU, Ankara, 2001

[8] **K. Lange, L. Cser, M. Geiger, J.A.G. Kals:** "Tool Life and Tool Quality in Bulk Metal Forming"; Annals of CIRP 41/2 (1992), pp. 667-676

[9] **T. Altan:** "Design and Manufacture of Dies and Molds"; Annals of the CIRP 36/2 (1987) pp: 455-462

[10] **R. Geiger:** "System zum Erfassen und Senken des Werkzeugverbrauchts beim Kaltmassivumformen". Wt −Z.ind Fertig 69/12 (1979), pp:763-769

[11] **B. Bhushan, B.K. Gupta:** "Handbook of Tribology", Mc. Graw-Hill, New York (1991)

[12] **N. Bay:** "Friction and Adhesion in metal Forming"; Doctoral Thesis, University Lyngby, Denmark (1985)

[13] **W. H. Sillekens:** "Backward can extrusion and material behaviour"; Thesis Ph.D., University of Technology Eindhoven, Netherlands (1992)

[14] **W. Reiss:** "Untersuchungen des Werkzeugbruch beim Voll-Vorwarts-Fliespressen"; Berichte aus dem Inst. für Umformtechnic Nr. 94, Univ. Stuttgart, Berlin etc., Springer-Verlag (1987)

[15] **A. Hettig:** "Einflusgrosen des Werkzeugbruch beim Voll-Vorwarts-Fliespressen"; Berichte aus dem Inst. für Umformtechnic Nr. 106, Univ. Stuttgart, Berlin etc., Springer-Verlag (1990)

[16] **M. Geiger, M. Hansel, Th. Rebhan:** "Improving the Fatigue Resistance of Cold forging Tools by FE-Simulation and Computer Aided Die Shape Optimization"; Journal of Engineering Manufacture, Part B, Proc. of the Institution of Mechanical Engineers , Vol. 206 (1992), pp:143-150

[17] **M. Hansel, A. Mesner, U. Engel, M. Geiger:** "Local Energy Approach − an Advanced Model for FEM Simulation of Multiaxial Fatigue", in: Aliabadi, M.H. Nisitani, H., Cartwright, D.J.: Localized Damage II, Vol:2, Computational Methods in Fracture Mechanics, New York: Elsevier Appl. Sci. London (1992), pp: 263-282

[18] **M. Hansel, U. Engel, M. Geiger:** "FEM Simulation of Fatigue crack growth in Cold Forging Dies"; Proc. Int. Conf. On Mixed Mode Fracture and Fatigue, Austria, Special Technical Publication of ESIS (1992)

[19] **A.Sonsöz, A.E. Tekkaya:** "Service Life Estimation of Extrusion Dies by Numerical Simulation of Fatigue Crack Growth"; International Journal of Mechanical Sciences, Vol:38 No:5 (1996), pp:527-538

[20] **K. Lange, A.E. Tekkaya, A. Sonsoz:** "Life estimation of extrusion dies"; A. Prof. Conf. Annals of the International Institute for Production Engineering Research, Manufacturing Technology, Enschede, Netherlands (1995), pp. 231−234

[21] **M.S. Joun, M.C.Lee, J.M. Park:** "Finite element analyses of prestressed die set in cold forging"; International Journal of Machine Tools & Manufacture 42 (2002), pp:1213-1222

[22] **S. Takashi, C.A. Brebbia:** "Forging Die Stress Analyses Using Boundary Element Method", Advanced Technology of Plasticity, 1, (1990), pp: 203-210

[23] **E. B. Nielsen:** "Strip Winding – Combined Radial and Axial Prestressing of Cold Forging Die Insert"; PhD. Thesis, Technical University of Denmark & Strecon Technology Danfoss A/S (1994)

[24] **V. Vasquez, D. Hannan, T. Altan:** "Tool Life in Cold Forging – an Example of Design Improvement to Increase Service Life"; Journal of Material Processing Technology, Vol 98 (2000), pp:90-95

[25] **C.S. Goh, C. M. Choy:** "Pre-stressing od Forging Die To Improve Tool Life"; Forging Technology Group, SIMTech Technical Report (PT/02/037/FT)

[26] **Strecon A/S:** "Limits of conventional stress rings for the prestressing of forging dies" Technology note P6552

[27] **J. Groenbaek, T. Birker:** "Innovations in cold forging die Design"; Journal Of Material Processing Technology vol.98/2 (2000), pp:155-161

[28] **P. Brondsted, P. Skov-Hansen:** "Fatigue Properties of high strength materials used in cold forging tools", International Journal of Fatigue vol. 20/5 (1998), pp: 373-381

[29] **S.Y.Lin:** "Upsetting of a Cylindrical Specimen Between Elastic Tools" Journals of Material Processing Technology vol:86 (1999), P:73-80

[30] **Y. Lee, J. Lee, Y. Kwon, T. Ishikawa:** "Modeling approach to estimate the elastic characteristics of workpiece and shrink-fitted die for cold forging";Journal of Materials Processing Technology vol:147 (2004) pp:102–110

[31] **Y. Lee, J. Lee, Y. Kwon, T. Ishikawa:** "Experimental and analytical evaluation for elastic deformation behaviors of cold forging tool"; Journal of Materials Processing Technology vol:127 (2002), pp:73–82

[32] **Y. Lee, J. Lee, Y. Kwon, T. Ishikawa:** "Analysis of the elastic characteristics at die and workpiece to improve the dimensional accuracy for cold forged part"; Journal of Materials Processing Technology, vol:153–154 (2004), pp:1081–1088

[33] **Y. Lee, J. Lee, T. Ishikawa:** "Analysis of the elastic characteristics at forging die for the cold forged dimensional accuracy"; Journal of Materials Processing Technology, vol:130–131 (2002), pp:532–539

[34] **M.Arbak, A. Putz, U. Engel, M. Geiger:** "Industrial Ceramics in Cold Forging: Increasing Surface Quality and Dimensional Accuracy";Proceedings of the 4th JSTP International Seminar on Precision Forging (2006), pp: 83-86

[35] **K.Kuzman:** "Problems of Accuracy Control in Cold Forming"; Journal of Materials Processing Technology, vol:113 (2001), pp: 10-15

[36] **K.Kuzman:** "Some Research and Development Efforts in Cold Forging"; Umformtechnik Plus, Meisenbach Verlag, Bamberg, (1999), pp:199-206

[37] **K. Osakada, M. Shiraishi, K. Kawasaki:** "Precision Cold Extrusion with Controlled Elastic Deformation"; Wire, vol:45-4 (1995), pp:229-232

[38] **F. Jütte:** "Aktive Matrize zur Prozeβregelung in der Umformtechnik"; Umformtechnik vol:27/3 (1993), pp:207-210

[39] **V. Krusic, C. Hinsel, D. Lavrencic, M. Mervic:** "Tool Life Improvement at Precision Cold Extrusion of Pinions for Automotive Starter Motors", Proceedings of 4th ICIT – International Conference on Industrial Tools (2003), pp: 63-68

[40] **E.-G.Yoh, Y.-I. Kim, Y.-S. Lee, H.-J. Park, K.-H. Na:** "Integrated Analyses for Die Design Including Brittle Damage Evolution", Journal of Material Processing Technology vol:130-131 (2002), pp:647-652

[41] **B. Falk, U. Engel, M. Geiger:** "Estimation of tool life in bulk metal forming based on different failure concepts"; Journal of Materials Processing Technology vol:80–81 (1998), pp:: 602–607

[42] **P. Hansena, N. Bay, J. Gronbaek, P.Brondsted:** "Fatigue in cold-forging dies: tool life analysis"; Journal of Materials Processing Technology vol:95 (1999), pp:40-48

[43] **T. O. Pedersen:** "Numerical studies of low cycle fatigue in forward extrusion dies"; Journal of Materials Processing Technology vol:105 (2000), pp:359-370

[44] **J. Gronbaek, E.B. Nielsen:** "New developments in the design and high performance of strip-wound cold forging tools"; Journal of Materials Processing Technology vol:46 (1994), pp: 87 - 97

[45] **J. Gronbaek, E.B. Nielsen:** "Strip-wound containers for combined radial and axial pre-stressing"; Journal of Materials Processing Technology vol:71 (1997), pp:30 - 35.

[46] **H.T. Yeo, Y.Choi, K.D. Hur:** "Analyses and Design of the Prestressed Cold Extrusion Die", International Journal of Advance Manufaturing Technology, vol:18 (2001), pp: 54-61

[47] **International Cold Forging Group:** "Calculation Methods for Cold Forging Tools", ICFG Document No: 5/82

[48] **Edward M. Mielnik:** "Metal Working Science and Engineering"; McGraw-Hill, 1991

[49] **T. Altan, S. I. Oh, H. Gegel:** "Metal Forming: Fundamentals and Applications"; ASM International, Metal Park, OH, 1983

[50] **X. Tan:** "Comparisons of Friction Models in Bulk Metal Forming"; Tribology International, vol:35 (2002), pp: 385 - 393

[51] **Thomsen, E.G.:** "Mechanics of Plastic Deformation in Metal Processing", Macmillan Co., NewYork, 1965

[52] **T. Wanheim:** "Friction at High Normal Pressures"; Wear, vol:25 (1973), pp: 225-244

[53] **T. Wanheim, N. Bay, A. S. Petersen:** "A Theoretically Determined Model for Friction in Metal Working Processes", Wear, vol:28 (1974), pp: 251-258

[54] **S.B. Petersen, P.A.F. Martins, N. Bay:** "Friction in bulk metal forming: a general friction model vs. the law of constant friction"; Journal of Material Processing Technology, vol:66 (1997), p: 186-194

[55] MSC. SuperForm 2004 Command Reference

[56] **C. Chen, S. Kobayashi:** "Rigid Plastic Finite Element Analyses of Ring Compression, Applications of Numerical Methods of Forming Processes", ASME − AMD, 28 (1978), pp:163

[57] **A. E. Tekkaya:** "A Guide for Validation of FE − Simulations in Bulk Metal Forming", The Arabian Journal of Science, vol:30, Number:1C, pp:113-136

[58] **J.B. Hawkyard, W. Johnson:** "An Analyses of the Changes in Geometry of Short Hollow Cylinders During Axial Compression"; International Journal of Mechanical Sciences, vol:9 No: 163 (1967), p:163-182

[59] **T. Schrader, M. Shirgaokar, T.Altan:** "Analyses of the Double Cup Extrusion Test for Evaluation of Lubricants"; Proceedings of the 4th JSTP International Seminar on Precision Forging, 2006, pp: 77 − 82

[60] **C. Önder:** "Analysis of Bolt Production by Metal Forming", M.S. Thesis, METU, Ankara, 2004

[61] **D.R. Hayhurst, M.W. Chan:** "Determination of friction models for metallic die −workpiece interfaces"; International Journal of Mechanical Sciences, vol: 47 (2005), pp:1–25

[62] **A. Behrens, H. Schafstall:** "2D and 3D Simulation of Complex Multistage Forging Processes by Use of Adaptive Friction Coefficient"; Journal of Materials Processing Technology, vol: 80–81 (1998), p: 298–303

[63] **P. Becker, H.J. Jeon, C.C. Chang, A. N. Bramley:** "A Geometric Approach to Modelling Friction in Metal Forming"; Annals of CIRP, vol:52/1 (2003), pp: 209 − 212

[64] **N. Bay:** "Modelling of friction in Cold Metal Forming Processes", In: Proceedings of the 2nd Workshop of Process Simulation in Metal Forming Industry, DIMEG, Padova, Italy, 2002

[65] **K. Osakada, R. Matsumoto:** "Fundamental Study of Dry Metal Forming with Coated Tools"; Annals of CIRP vol. 49/1 (2000) pp: 161-164

[66] **L.D. Yu, G.W. Shuy, T. Vilaithong:** "Friction Modification of WC-Co by Ion Implantation"; Surface and Coatings Technology, vol:128-129 (2000), pp:404 − 409

[67] **Z. Z. Fang:** "Correlation of Transverse Rupture Strength of WC–Co with Hardness"; International Journal of Refractory Metals & Hard Materials, vol:23 (2005), pp: 119–127

[68] **G.A. Roberts, R.A. Cary;** "Tool Steels", Fourth Edition, American Society for Metals, 1980

[69] **John D. Verhoeven;** "Metallurgy of Steel for Bladesmiths & Others Who Heat Treat and Forge Steel", Iowa State University, 2005

[70] **PVD − CVD Coatings;** *Retrieved* 26.08.2006, *from* WALTER AG Web site http://www.walter-ag.com/

[71] **J. W. Dally, W. F. Riley:** "Experimental Stress Analysis", McGraw-Hill, 1991, 3rd Edition

[72] **L.Parnas:** "ME 543 Theory of Elasticity , Lecture Notes", 2004, METU, Ankara

[73] **A. C. Ugural and S. K. Fenster:** "Advanced Strength and Applied Elasticity", Prentice Hall, New York, 1995

[74] **E. Siebel**, "Die Formebung im Bildsamen Zustande", Düsseldorf: Verlag Stahleisen, 1931

[75] **C. Önder. A. E. Tekkaya:** "Anomalies in Forward Rod Extrusion Process", Proceedings of the 4th International Seminar on Precision Forging, Nara, Japan, 2006, pp.183-86

[76] **J. Vernon:** "Introduction to Engineering Materials", London : Macmillan Press, 3rd edition, 1992

[77] **H. D. Moore:** "Manufacturing, materials and processes", Columbus, Ohio Grid Pub., 3rd edition, 1982

[78] **K. J. A.Brookes:** "Hardmetals and Hard Materials", International Carbide Data, 2nd edition, 1992

APPENDIX A

CEMENTED CARBIDES

Cemented carbide also known as cermets and hardmetal are composed of tungsten (in the form of tungsten carbide, WC), titanium, niobium and other materials, in a matrix of cobalt and are made by powder metalurgy processing involving compaction and sintering [76]

The combination of WC and metallic cobalt as a binder is a well-adjusted system not only with regard to its properties, but also to its sintering behaviour. The high solubility of WC in cobalt at high temperatures and a very good wetting of WC by the liquid cobalt binder result in an excellent densification during liquid phase sintering and in a pore-free structure. As a result of this, a material is obtained which combines high strength, toughness and high hardness.

Before going into the details of production and properties of cemented carbides, first a general information is given about powder metallurgy in the following section.

A.1 Powder Metalurgy

The definition for the term powder metalurgy, as provided by the Committee for Powder Metalurgy of American Society of Metals, is "the art of producing metal

powders and objects shaped from individiual, mixed or alloyed metal powders, with or without the inclusions of non metallic constitents, by pressing or molding objects which may be simultaneously or sebsequently heated to produce a coherent mass" [77].
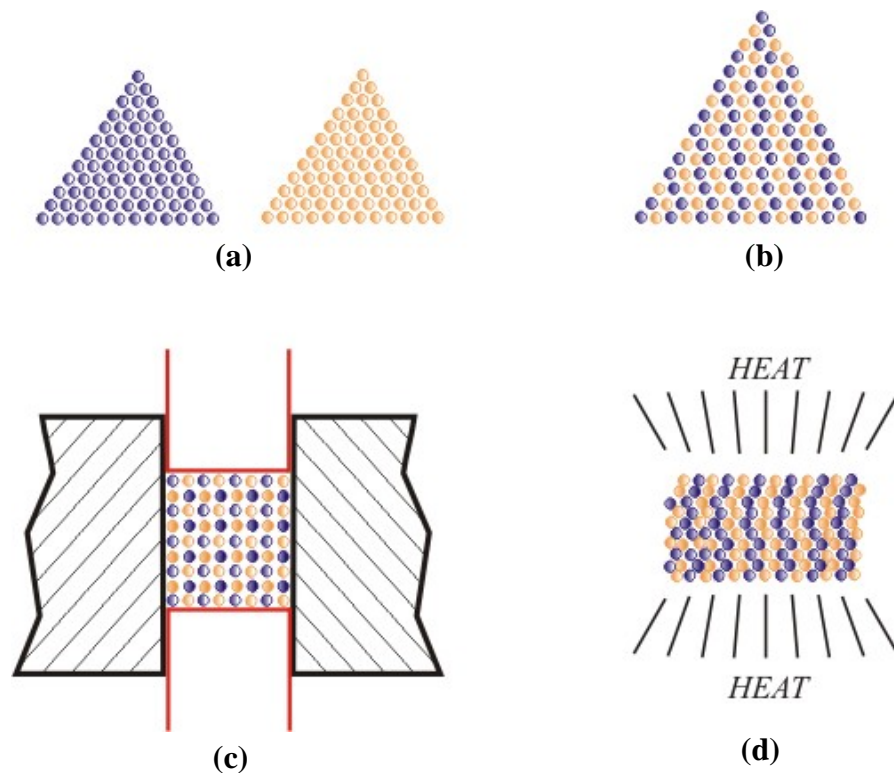
Figure A.1. Powder metallurgy production steps **a)** Preparation of powders **b)** Mix & blend **c)** Pressing **d)** Sintering

Figure A.1 shows the steps ordinarily required in the production of a part by the powder metallurgy process. Suitable powder must be first produced (Fig. A.1a). While theoretically any crystalline material may be fabricated by powder metallurgy, the production of suitable powder has presented restrictions in many cases, either because of difficulty in obtaining adequate purity or because of economic reasons. After selecting and blending of the powder (Fig. A.1b) and manufacture of a die for the shape to be produced, the powder is pressed to size and shape (Fig. A.1c). The application of heat results in crystalline growth and the production of homogenous body (Fig. A.1d).

Various combinations of heat and pressure may be used. Some sintering takes place under high pressure at room temperature. However, cold pressing is usually followed by sintering at room temperature somewhat below the lowest melting point of any of the constitents. An intermediate elevated temperature may be used during pressing, then the shape removed from the press and subjected to higher temperature. In hot pressing, the final sintering temperature is applied with the pressure.

A.1.1 Powders

The charecteristics of any final product of powder metallurgy will depend to a great extent on the properties of the powders used as raw materials. In addition to actual metal of which the powder consists, the properties of greatest importance are particle size, shape, crystalline structure, density, flowability, compactibility and purity. For spherical particles, the diameter is a complete description of the size. However, many particles have flake, needle or jagged shapes and no simple method exists for specifying sizes completely.

Generally, smaller sizes are preferred over coarse sizes because the greater surface to volume ratio produces greater contact area and cohesion between particles, which results in better physical characteristics. Addition to the effect of contact area, particle shape has a large influence on the flowability of particles.

A.1.2 Mixing and Blending

Most powders as initially produced require some further processing before pressing and sintering. Generally, to be satisfactory, powders must be free from stresses to press properly and must contain little or no surface oxides that would inhibit proper bonding during sintering.

A typical procedure for preparing powders starts with washing to remove any foreign chemicals, such as electrolytic acids. Drying is then done at a high enough temperature to produce an annealing action in a reducing atmosphere to further eliminate any oxides present.

Mixing is required for even a single metal powder to promote homogeneity with a random dispersion of particle sizes and shapes. Single materials are often mixed from a variety of sources to develop improved properties. The time required for mixing may vary from a few minutes to several days.

A.1.3 Pressing

The bond that is established between particles in powder metalurgy varies all the way from mechanical interlocking to the growing of new, common crystals across the borders of the initial particles.

Most metals can be plastically deformed and with the applied pressure, contact areas grow in to large areas. The face centered cubic metals such as nickel, copper abd lead do not work harden and can be deformed with comperatively low pressures. The metals that work harden easily such as the body centered cubic structures of iron, tungten and vanadium require much higher pressures to establish suitable contact areas.

A.1.4 Sintering

The term sintering is used to identify the mechanism by which solid particles are bonded by application of pressure or heat or both. Sintering can be accomplished at room temperature with pressure alone but is most often performed at elevated temperatures, either at the same time or after pressure has been applied. With some multiple constitutent compositions, some of the low temperature melting materials may be melted but in most cases sintering is fully solid state process. The two most

common sintering procedures are application of heat and pressure together, called *hot pressing*, and application of heat after the particles have been closely packed by *cold pressing*.

A.2 Manufacture of Sintered Harmetals

Hardmetal manufacture involves a lengty and complex sequence of operations. The original and still the basic, product consists of fine tungsten carbide patricles, the hard and abrasion resistant constituent, bonded with though, comperatively soft, metallic cobalt. Tungsten carbide can be supplemented or substituted by the carbides or nitrides of other refractory metals, typically titanium, tantalum, niobium, chromium, vanadium or molybdenum, independently or in combination, whilst the cobalt may similarly be alloyed with by nickel, nickel-molybdenum or similar metallic elements.

Typical stages of manufacture of sintered hardmetals are;

- Production of tungsten metal powder
- Ppreparation of tungsten carbide
- Preparation of alloyed and other carbides
- Admixture of metallic cobalt to produce grade powders
- Addition of pressing lubricant
- Pressing
- Presintering
- Shaping
- Final sintering
- Hot isostatic pressing

The interrelationship of these manufacturing processes is summarised in Figure A.2. The product is rarely used as sintered, but is generally ground, polished and shot blasted, plated or coated to create a more accurate form or a still harder and more wear resistant surface.

```
                         ┌──────────┐
                         │ Tungsten │
                         │   Ore    │
                         └──────────┘
┌──────────┐                  │
│  Carbon  │               Refine
│  Black   │                  │           ┌──────────┐
└──────────┘            ┌──────────┐      │  Metal   │
                        │ Tungsten │      │  Oxides  │
                        │  Metal   │      └──────────┘
                        └──────────┘

       Carburise                    Carburise

   ┌──────────┐                 ┌──────────┐    ┌──────────┐
   │ Tungsten │                 │  Alloy   │    │  Cobalt  │
   │ Carbide  │                 │ Carbides │    └──────────┘
   └──────────┘                 └──────────┘

                    Mix and Mill

                   ┌──────────┐
                   │  Grade   │
                   │  Powder  │
                   └──────────┘

                      Press

                    Presinter
                      Shape

                      Sinter

               ┌──────────────────┐
               │ Sintered Carbides│
               └──────────────────┘
```
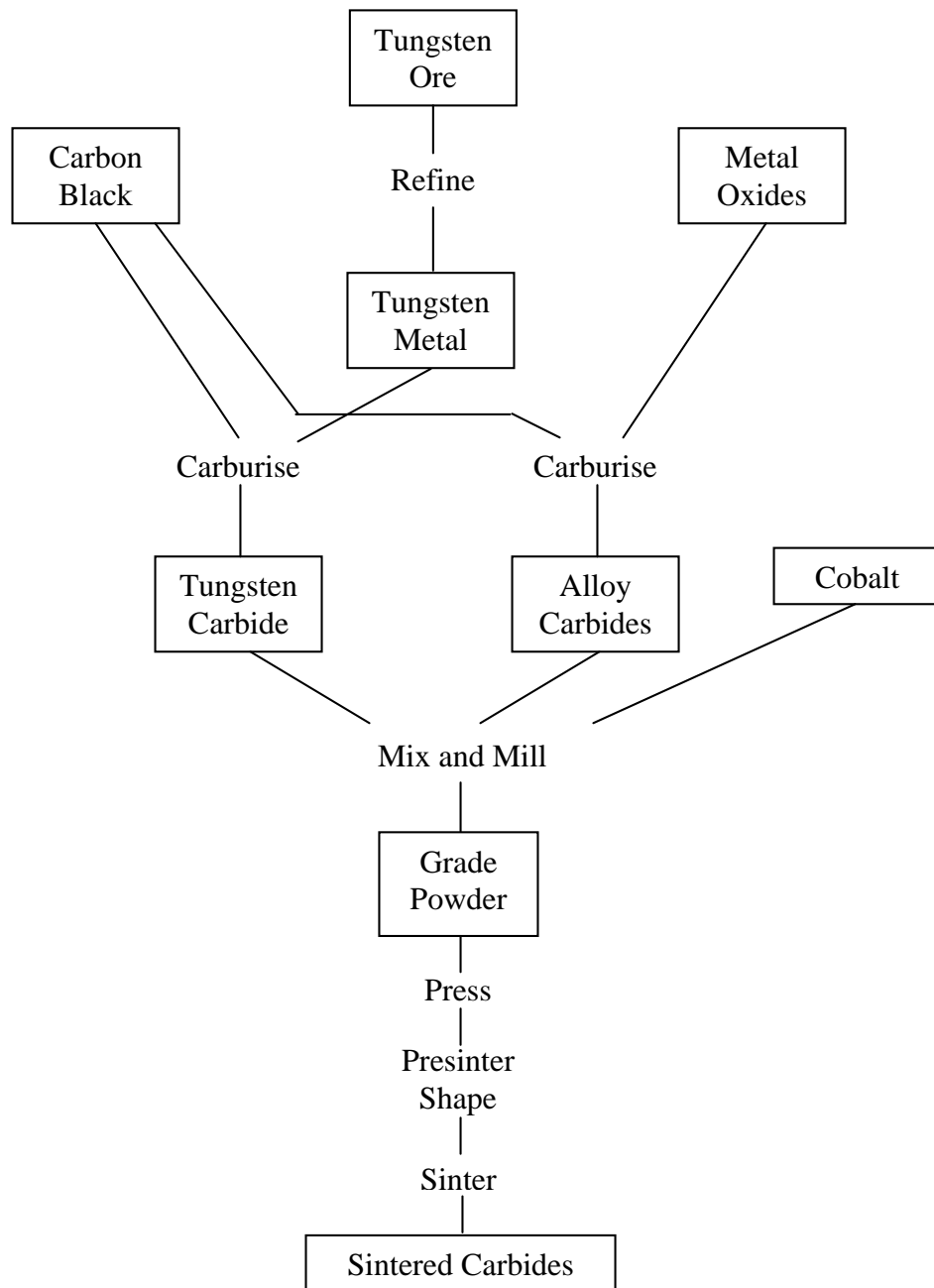
Figure A.2. Schematic flow chart for hardmetal production [78]

These production stages are explained briefly in the following sections.

A.2.1 Tungsten Ore to Metal

Of all carbides employed in hardmetal manufacture only one, tungsten, is usually made by carburising pure metallic powder. In other cases, and occasionally even

with tungsten, carbides are manufactured by direct carburisation of oxides, omitting the intermediate metallic stage. The grain size and other properties of the final product depend on those of the tungsten powder.

The grain size of the tungsten powder can vary from perhaps 0.25 μm to more than 15 μm. Typically less than 0.4 μm is rated as ultrafine up to 0.8 μm as micrograin, around 1 μm as fine, $1.5 - 2$ μm as medium and $3 - 4$ μm or above coarse grain sizes. Ultrafine grain sizes have a very specialised applications and until recently tent to be produced rather different chemical routes. Although they permit the manufacture of very fine and extremely abrasion resistant carbides, ultrafine tungstens are expensive, require special precautions during processing and are consequently ignored by the majority of the manufacturers.

A.2.2 Tungsten Carbide

The progression from tungsten powder to tungsten mono carbide WC (Fig. A.3) is relatively straight forward, entailing the mixture of tungsten and carbon black and firing at a temperature between 1400 and 2650 $^{\circ}$C. The temperature must be high enough to give full carburisation within an acceptable time and also to volatilise most of the residual impurities but not so high as to induce grain growth in the newly formed carbide powder.

Ore

Ammonium paratungstate

Tungstic acid

Heat

Heat

Oxides of tungsten

Mill

Grain growth inhibitors

Carbon black

Tungsten

Titanium oxide

Tantalum-niobium oxides

Mill

Mill

Mill

Carburise

Carburise

Carburise

WC

WC / TiC

WC / TiC / Ta(Nb)C
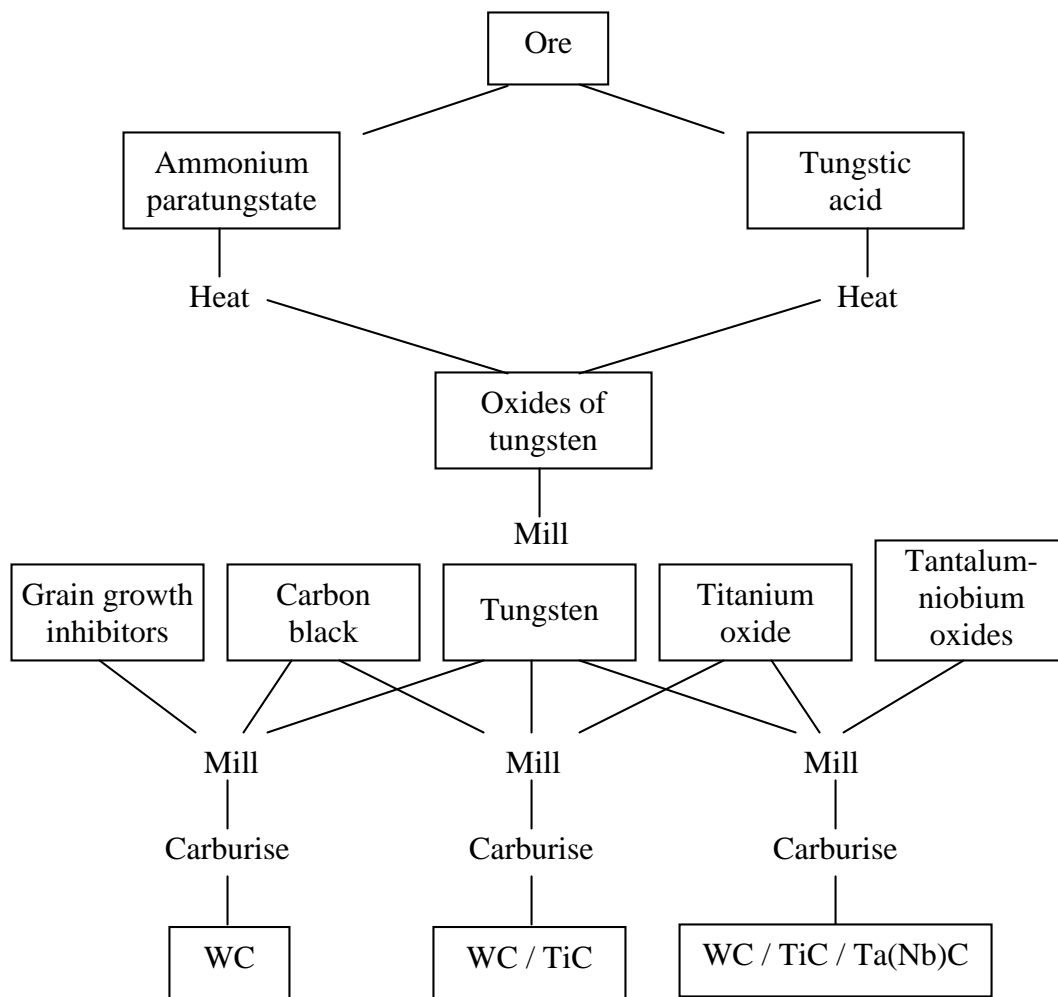
Figure A.3. Simplified flow chart for production of carbide powders

A.2.3 Carbide to Grade Powder

In more than 95 % of all hardmetal production, cobalt is the cement or binder. Strictly, the binder is a cobalt based pseudoeutectic (giving the lowest temperature liquid metals), since tungsten and other carbides dissolve in the molten cobalt during sintering and are only partially reprecipitated during cooling to room temperature.

Grade powders consist of one or more carbide powders, according to the composition and properties required, mixed with appropriate amount of finely divided metallic binder and ball-milled for a sufficiently long time.

A.2.3.1 Milling

A prime object of mixing cobalt and carbide powders is to ensure that every carbide particle is coated with even finer particles of cobalt. To this end the cobalt powder must be initially as fine as possible, and of suitable structure for further

At this stage of process, milling must be considered quite separately from mixing. Straightforward mixing appears to be fully effective after only a few hours ball-milling, yet it is usually extend the milling for days even a week. This extended milling is considered necessary to promote final sintering and to reduce porosity to a satisfactorily low level.

The energy of milling is considerable, and it is therefore necessary to carry out this operation under protective liquid, usually an organic such as acetone or alcohol. The liquid minimises temperature rise, prevents oxidation and frequently also acts as a solvent for the pressing lubricant. After each batch is milled, the liquid is recovered and purified by distillation.

A.2.3.2 Lubricants

Although, when finally sintered cemented carbides have the lowest porosity of any powder metallurgical products, carbide powders mixes have extremely poor pressing properties. In order to avoid interlocking, intermittent voids, variable density, irregular shrinkage and severe distortion during sintering, an efficient pressing lubricant must be employed.

Also lubricated powder in appropriate containers can be stored for lengthy periods or shipped around the world with a little risk of oxidation or contamination.

A.2.4 Pressing

A.2.4.1 Block Pressing

Large blocks, for subsequent cutting or forming, are pressed in rectangular, multi part dies, on a sible or double acting hydrolic presses. Pressure varies from about 50 to 150 MPa. There is little point in exceeding this maximum, since it results only in uneven density within the pressed compact with the possibility of cracking when the pressure is released or severe distortion during sintering.

A.2.4.2 Pressing to Shape or Size

Medium sized or large standard components, for which dies are available, can be produced to finished shape or needing very little additional shaping by simple die pressing.

Because of the considerable shrinkage that takes place during final sintering, it is vitally important to maintain constant properties from one batch of powder to another, in order to obtain components precisely similar in size from different batches produced by using same die.

A.2.4.3 Cold Isostatic Pressing

Cold isostatic pressing (CIP) in which the powder component is subjected to equal pressure from all directions, rather than along a single axis, gives much greater uniformity of density especially in large or lengthy sections. The particular advantage of isostatic pressing is that shrinkage during final sintering takes place equally in all directions, where as uniaxially pressed compact shrinks less along the line of pressing than in the perpendicular directions.

The most common method is employing hydrolic pressure is applied to powder enclosed in a rubber bag, usually within a pressure chamber.

A.2.5 Lubricant Removal and Presintering

In this dual operation, the melting out or volatilisation of the lubricant by moderate heat in a protective atmosphere is usually followed by slight sintering at a progressively higher temperature to a typical maximum of $700 - 750\ ^{\circ}\text{C}$.

The presintering time and temperature are sufficient to cause solid state welding between particles in the pressed compact but not to give liquid phase sintering, consolidation or shrinkage.

A.2.6 Shaping

Preforms for shaping, dewaxed and presintered, come in a variety of simple shapes and sizes, including block pressed round and rectangular sections and isostatically pressed blanks.

The presintered preform has roughly the consistency and strength of chalk and can be cut or shaped with little difficulty. Nevertheless, since the presintered block is composed of highly abrasive powder, any tools used upon it should be of diamond, silicon carbide or other ultra hard material, to give a reasonable service life.

Cylindrical parts are turned, chamfered and otherwise modified on equipment ranging from small manually operated lathes to the most elaborate computerised machining centers.

A.2.7 Final Sintering

This process is the most critical stage in the production of hardmetals. During the sintering, compact shrinks by between 18 and 26 % in each linear direction (40 to 60 % by volume) and virtually all porosity is eliminated. The binder is converted from almost pure metal to a pseudo-binary eutectic, diffusion takes place in the hard

phases and their indivudial compositions may change significantly. New carbide, nitride and other phases may appear. Also mechanical and physical properties of material is affected.

In spite of the complicated reactions taking place, the methods used in sintering are fairly simple. Straight tungsten carbide – cobalt grades are sintered in resistance heated hydrogen atmosphere, semi continious furnaces. Temperatures vary from about 1350 $^{\circ}$C, for extremely tough cemented carbides containing around 30 % cobalt to 1650 $^{\circ}$C and over for some grades with very low cobalt (3 % or less) (Table A.1).

Table A.1. Typical Sintering Temperatures for Hardmetal Grades in Hydrogen-Atmosphere, Semi-Continous Furnaces

Composition – weight %					Sintering Temperature
WC	TiC	Ta (Nb)C	Cr$_3$C$_2$	Co	$^{\circ}$C
94	-	-	-	6	1540
91	-	-	-	9	1480
89	-	-	-	11	1460
87	-	-	-	13	1450
80	-	-	-	20	1400
75	-	-	-	25	1380
70	-	-	-	30	1350
96.5	-	-	0.5	3	1640
95	-	-	0.5	4.5	1620
93.5	-	-	0.5	6	1560
90.5	-	-	0.5	9	1500
85.5	7	3.5	-	4	1640
81.5	7	3.5	-	8	1560
80	14	-	-	6	1620
84	10	-	-	6	1600
87	7	-	-	6	1590
87	5	-	-	8	1550
66	25	-	-	9	1620

A.2.8 Hot Isostatic Pressing

Hot isostatic pressing is a process whereby heat is applied externally to a compact whilst high pressure is applied evenly from all directiongs. The pressure medium is an inert gas, usually argon and helium, which is employed around 1000 to 1500 bars.

The quality produced by hot isostatic pressing is, in terms of imperfections, better by several orders of magnitude than that produced by conventional sintering.

A.3 Properties of Sintered Hardmetals

Although hardmetals are especially noted for their hardness and wear resistance, their other properties, often equally distinctive, are of considerable interest to engineering designers. Explanation and methods used in determination of certain properties are described in following sections.

A.3.1 Density (Fig. A.4)

Measures; mass per unit volume

Unit: g/cm^3

Determined by; comparison of mass (by weighing or acoustic resonance) with volume (by water displacement or manometric balance).

Typical range of values: About 5.5 for TiC base to around 15.4 for lowest cobalt WC-base grades.
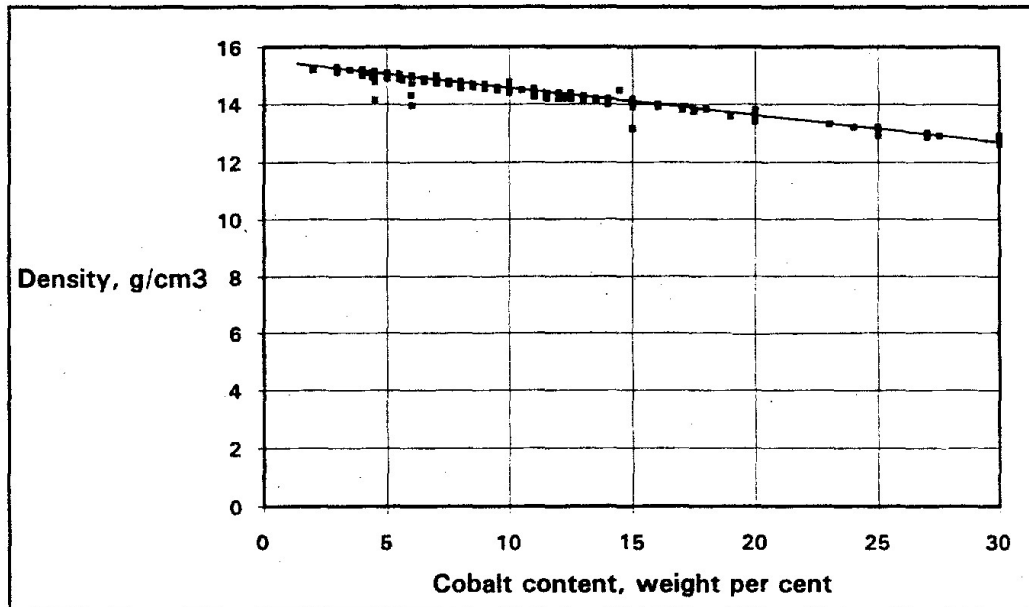
Figure A.4 Density variation with cobalt content of WC/Co

A.3.2 Hardness (Fig. A.5)

Measures; resistance to indentation by a diamond penetrator of special profile

Units: HV or Vickers Hardness (square pyramid indentor): HV value is actually in kgf/mm^2 (load in kilograms force applied to area of indentation in square millimeters), but the unit is nowadays seldom quoted.

HRA or Rockwell 'A' Hardness: (conical indentor with radiused tip): 60kgf (588N) load is applied for measuring the hardness.

HK or Knoop Hardness (elongated pyramid indentor): This test is developed for extremely hard materials though seldom employed for hardmetals. The length of the long diagonal of a very small indentation of this shape is easier to measure than both diagonals of a small square of similar area.

Typical value ranges for hardmetals: HV is 800 to 2400 and HRA is 83 to 94.5

237
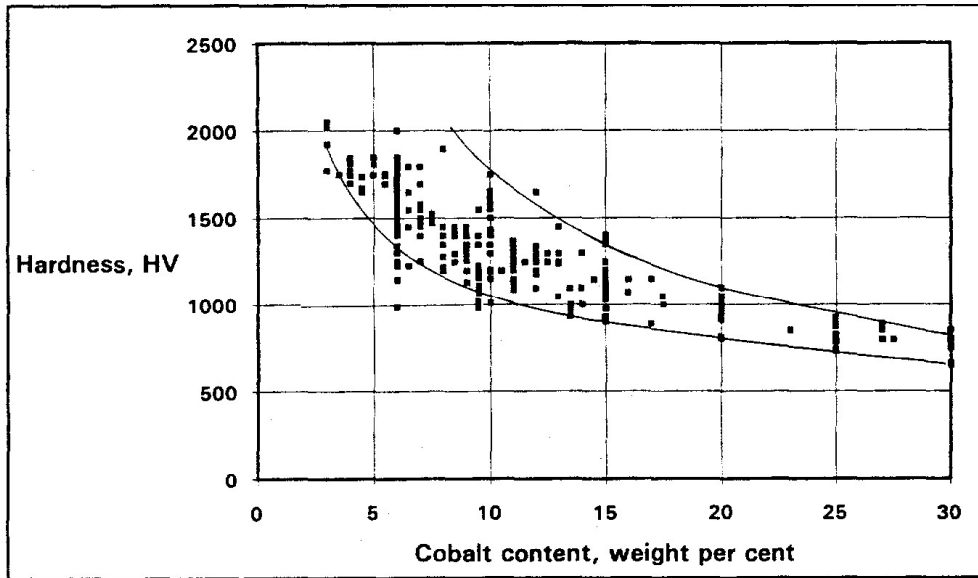
Figure A.5 Vicker's hardness variation with cobalt content of WC/Co

A.3.3 Abrasion Resistance (Fig. A.6)

<u>Measures;</u> surface weight loss due to physical abrasion under prescribed conditions intended to represent operational service.

<u>Units:</u> Arbitrary; for example, mg/rev.
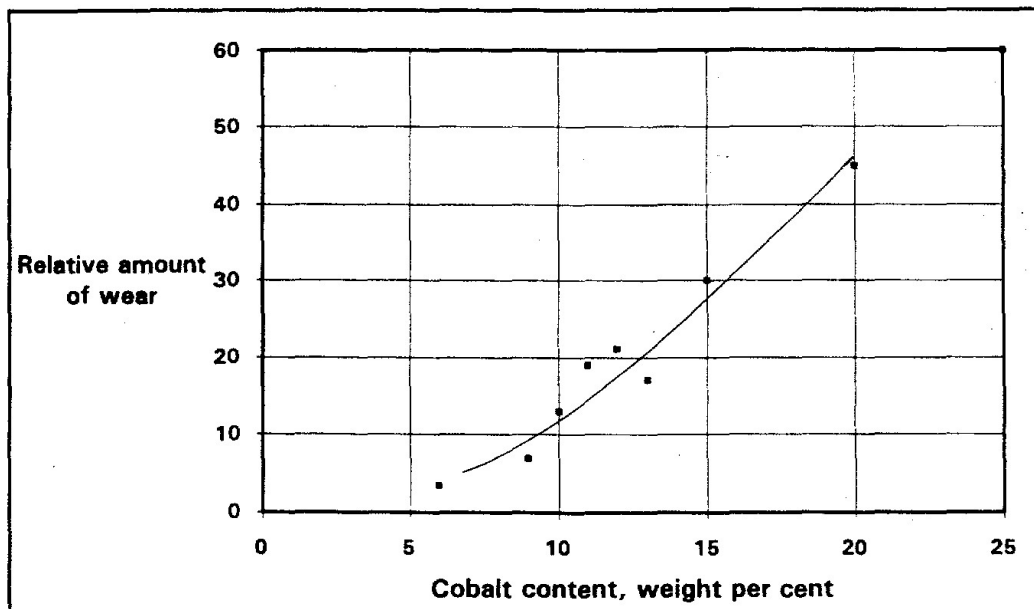
Figure A.6 Relative abrasion resistance variation with cobalt content of WC/Co

238

Determined by; applying a carbide pin or block against an abrasive disc. Revolutions or distance traveled for a predetermined volume or weight loss of carbide.

Range of values: more than 0.25 to 1 for available commercial hardmetals.

A.3.4 Young's Modulus of Elasticity "E" (Fig. A.7)

Measures; stress per unit of strain, linear almost to fracture for typical hardmetals (except the softest high-cobalt grades).

Unit: kN/mm2 or GN/m2

Determined by; dynamic excitation, at ultrasonic frequency or longitudinal oscillations in a test bar.

Typical range of values: 400 to 700 kN/mm2
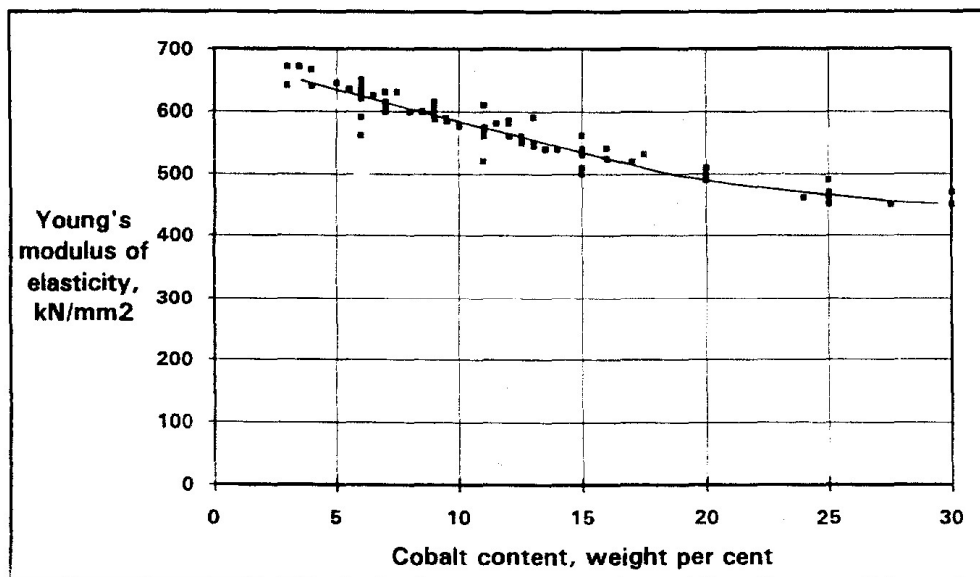
Figure A.7 Young's Modulus of Elasticity "E" variation with cobalt content of WC/Co

A.3.5 Modulus of Rigidity "G"

Unit: kN/mm2 or GN/m2

Determined by; dynamically excited torsional oscillations in a test bar.

Typical range of values: 170 to 280 kN/mm2

A.3.6 Poisson's Ratio "v"

Unit: None

Determined from: By using moduli E and G in the formula;

$$\mu = \frac{E}{2G} - 1 \qquad (A.1)$$

Typical range of values: 0.2 to 0.3

A.3.7 Transverse Rapture Strength (Fig. A.8)

Measures: Maximum normal stress at failure of a carbide rod loaded midway between two supports under standard conditions. Although the commonest strength measurement applied to hardmetals, it can be extremely misleading if taken as a measure of 'toughness' or shock resistance, since no shock or impact is applied during the test.

Units: N/mm2 or kN/mm2

Determined by; placing a rectangular test bar across two sintered carbide support cylinders and applying a gradually increasing force by means of a third carbide cylinder or ball on midway between the supports until the test bar fractures.
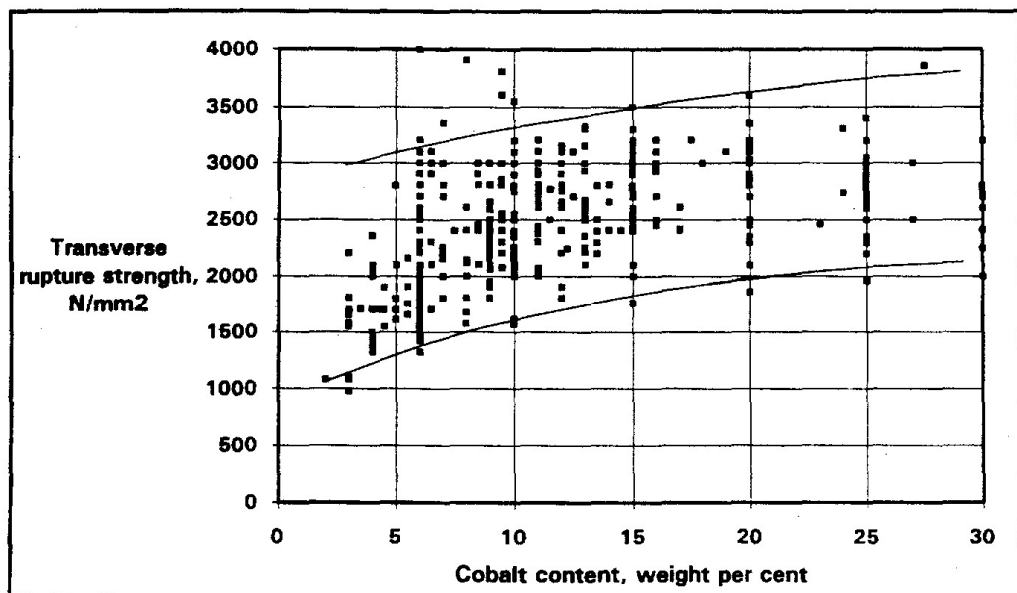
Figure A.8 Transverse rupture strength variation with cobalt content of WC/Co

The transverse rupture strength R_{tr} in N/mm2 is given by the formula:

$$R_{tr} = \frac{3FI}{2bh^2} \cdot K \qquad\qquad (A.2)$$

Where F is the load in Newtons for fracture, l is the length in mm of the test bar at right angles to its height h and b is the thickness in mm of the test bar. K is a correction factor for the chamfer permitted on sintered test bars. Its usual value is between 1.00 and 1.03

Typical range of values: 600 to 3000 N/mm^2

The test is sensitive to test-bar size and surface finish, as well as to other test parameters.

A.3.8 Compressive Strength (Fig. A.9)

Measures; stress per unit area at failure under compression of a cylindrical test piece. Fracture is primarily by shear, but a purely shear failure is prevented by the compressive forces.

Units: N/mm2, kN/mm2 or MN/m2

Determined by; compressing a test-piece between two parallel carbide blocks until failure occurs. In practice the cylinder may be narrowed at the centre to localise fracture.

Typical range of values: 3000 to 7000 N/mm2

Compressive strengths of hardmetals are greater than those of almost any other group of material, metallic or non-metallic.
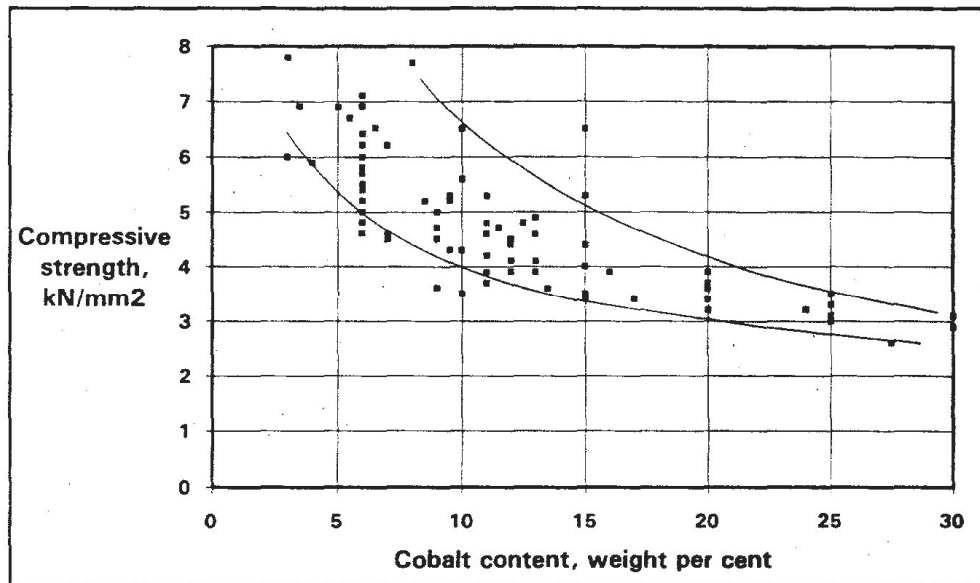
Figure A.9 Compressive stress variation with cobalt content of WC/Co

A.3.9 Tensile Strength

<u>Measures;</u> the tensile stress per unit area at failure of a suitable test piece.

<u>Units:</u> N/mm2

<u>Determined by;</u> calculation as a percentage of transverse rupture strength (45 to 55 %) or by actual test. Genuine tensile tests are very difficult to carry out on hardmetals because of difficulties in gripping the test specimen and in maintaining precise alignment

In practical test, results are very dependent on the size, design and surface finish of the test piece.

<u>Typical range of values:</u> 750 to 1500 N/mm2, about a quarter of the corresponding values for compressive strength.

A.3.10 Impact Strength

<u>Measures;</u> resistance to shock loading or toughness. Although many hardmetal manufacturers seem to regard transverse rupture strength as a measure of shock resistance, in practice the correlation is strictly limited.

242

Units: J or J/cm2

Determined by: drop-weight impact tester, in which a standard weight is dropped on the end of a square test bar secured in a horizontal position by its opposite end. The drop height of the weight is incremented until the bar breaks and the energy required is being recorded.

Various alternative methods of determining impact strength are in use, including some of those used for more ductile materials, such as the Charpy test. The purely subjective and crude method of striking with a hand-held hammer of about 2kg weight is effective for simple evaluation and even production control, but is hardly susceptible to the provision of numerical values. Nevertheless, when certain grades snap at the first hammer tap and others survive up to ten minutes battering before fracture.

Typical range of values:
   0.4 to 6J (Charpy-type test)
   0.3 to 5J/cm2 (drop test with 4.76mm square bar)

A.3.11 Fracture Toughness

A more modern concept is that of fracture mechanics, which studies crack initiation and propagation. Because some kind of discontinuity or stress raiser is required to initiate a crack, it can clearly be understood why hot isostatically pressed carbides with virtually no internal flaws possess such greatly increased shock resistance.

Units: $MN/m^{3/2}$ or $N/mm^{3/2}$

Typical range of fracture toughness values: 5 to 30 $MN/m^{3/2}$

A.3.12 Fatigue Strength

Measures; resistance to repeated stress cycles.

Units: Number of cycles before failure, at a given stress value; or stress (N/mm^2 or MN/m^2) that can be endured without failure for a stated number of cycles.

Determined by; rotating bend test or pulsating compressive test. Higher values are obtained with push-pull compressive stress cycling than with the bend test, which involves alternate tension and compression.

Typical range of values: Endurance limit for 10^8 cycles (reverse bending) 600 to 850 N/mm^2.

A.3.13 Thermal Expansion Coefficient

Measures; mean expansion per unit of length expressed as an average per Kelvin over a set temperature interval.

Units: 10^{-6}/K

Determined by: Dilatometer

Typical range of values: 4.5 to 8.5 x 10^{-6}/K between 0 and 800°C increasing with binder and alloy carbide content.

A.3.14 Thermal Conductivity

Measures; rate of energy transferred per unit distance for unit temperature difference.

Units: W/m K

Determined by: Standard experimental techniques

Typical range of values: 50 to 120 W/m.K for straight tungsten carbide grades

A.3.15 Thermal Capacity

Measures; energy to raise unit weight through unit temperature difference. Also known as specific heat.

Unit: J/kg K

Typical range of values: 200 to 250 J/kg.K for WC/Co grades (around half the corresponding value for a carbon steel).

APPENDIX B

SHRINK FIT PROGRAMS

B.1 Two Rings without Internal Pressure

2 RING CALCULATOR

First Ring's Posion's Ratio $\nu_1 := 0.23$

First Ring's Elastic Modulus (MPa) $E_1 := 450000$

First Ring Yield Stress (MPa) $Y_1 := 3000$

Second Ring's Posion's Ratio $\nu_2 := 0.3$

Second Ring's Elastic Modulus (MPa) $E_2 := 210000$

Second Ring Yield Stress (MPa) $Y_2 := 1250$

Bore Diameter (mm) $d := 10$

First Ring Outer Diameter (mm) $d_1 := 28$

Second Ring Outer Diameter (mm) $D := 50$

Interference (mm) $z := 0.14$

% Interference $\delta = 0.5$ %

CALCULATIONS

$r_{i1} := \dfrac{d}{2}$ $r_{o2} := \dfrac{D}{2}$ $r_{o1} := \dfrac{d_1}{2}$ Calculating Radius Of Rings

$\rho := \dfrac{z}{2}$ Calculating Interference On Radius

$$P_{inter} := \frac{\rho}{r_{o1} \cdot \left[\dfrac{r_{o1}^2 \cdot (v_2 - 1) - r_{o2}^2 \cdot (1 + v_2)}{E_2 \cdot \left(-r_{o2}^2 + r_{o1}^2\right)} - \dfrac{r_{o1}^2 \cdot (1 - v_1) + r_{i1}^2 \cdot (1 + v_1)}{E_1 \cdot \left(-r_{o1}^2 + r_{i1}^2\right)} \right]}$$ Calculating Interference Pressure

$$\sigma_r(r) := \left| \begin{array}{l} \dfrac{P_{inter} \cdot r_{o1}^2}{r_{o1}^2 - r_{i1}^2} \cdot \left(\dfrac{r_{i1}^2}{r^2} - 1 \right) \quad \text{if } r_{i1} \le r \le r_{o1} \\[4mm] \dfrac{P_{inter} \cdot r_{o1}^2 \cdot \left(1 - \dfrac{r_{o2}^2}{r^2}\right)}{r_{o2}^2 - r_{o1}^2} \quad \text{if } r_{o1} < r \le r_{o2} \end{array} \right.$$

Calculating Radial Stress On First Stress Ring Along Radius

Calculating Radial Stress On Second Stress Ring Along Radius

$$\sigma_\theta(r) := \left| \begin{array}{l} \dfrac{-P_{inter} \cdot r_{o1}^2}{r_{o1}^2 - r_{i1}^2} \cdot \left(\dfrac{r_{i1}^2}{r^2} + 1 \right) \quad \text{if } r_{i1} \le r \le r_{o1} \\[4mm] \dfrac{P_{inter} \cdot r_{o1}^2 \cdot \left(1 + \dfrac{r_{o2}^2}{r^2}\right)}{r_{o2}^2 - r_{o1}^2} \quad \text{if } r_{o1} < r \le r_{o2} \end{array} \right.$$

Calculating Hoop Stress On First Stress Ring Along Radius

Calculating Hoop Stress On Second Stress Ring Along Radius

$c_{21} := \left(\dfrac{-P_{inter} \cdot r_{o1}^2}{r_{o1}^2 - r_{i1}^2} \right) \cdot \dfrac{1}{2}$ $c_{31} := \dfrac{r_{i1}^2 \cdot r_{o1}^2 \cdot P_{inter}}{r_{o1}^2 - r_{i1}^2}$

$u_1(r) := \dfrac{1}{E_1} \cdot \left[2 \cdot c_{21} \cdot (1 - v_1) \cdot r - c_{31} \cdot \dfrac{1 + v_1}{r} \right]$ Calculating Radial Dislacement On First Ring

$c_{22} := \left(\dfrac{P_{inter} \cdot r_{o1}^2}{r_{o2}^2 - r_{o1}^2} \right) \cdot \dfrac{1}{2}$ $c_{32} := \dfrac{-1 \cdot r_{o2}^2 \cdot r_{o1}^2 \cdot P_{inter}}{r_{o2}^2 - r_{o1}^2}$

$u_2(r) := \dfrac{1}{E_2} \cdot \left[2 \cdot c_{22} \cdot (1 - v_2) \cdot r - c_{32} \cdot \dfrac{1 + v_2}{r} \right]$ Calculating Radial Dislacement On Second Ring

$$u(r) := \left| \begin{array}{l} u_1(r) \quad \text{if } r_{i1} \le r \le r_{o1} \\ u_2(r) \quad \text{if } r_{o1} < r \le r_{o2} \end{array} \right.$$ Plot Radial Displacement For First and Second Ring

246

Hoop - Radial Stress vs Radius

Equivalent Stress vs Radius

Radius Diameter Change vs Radius
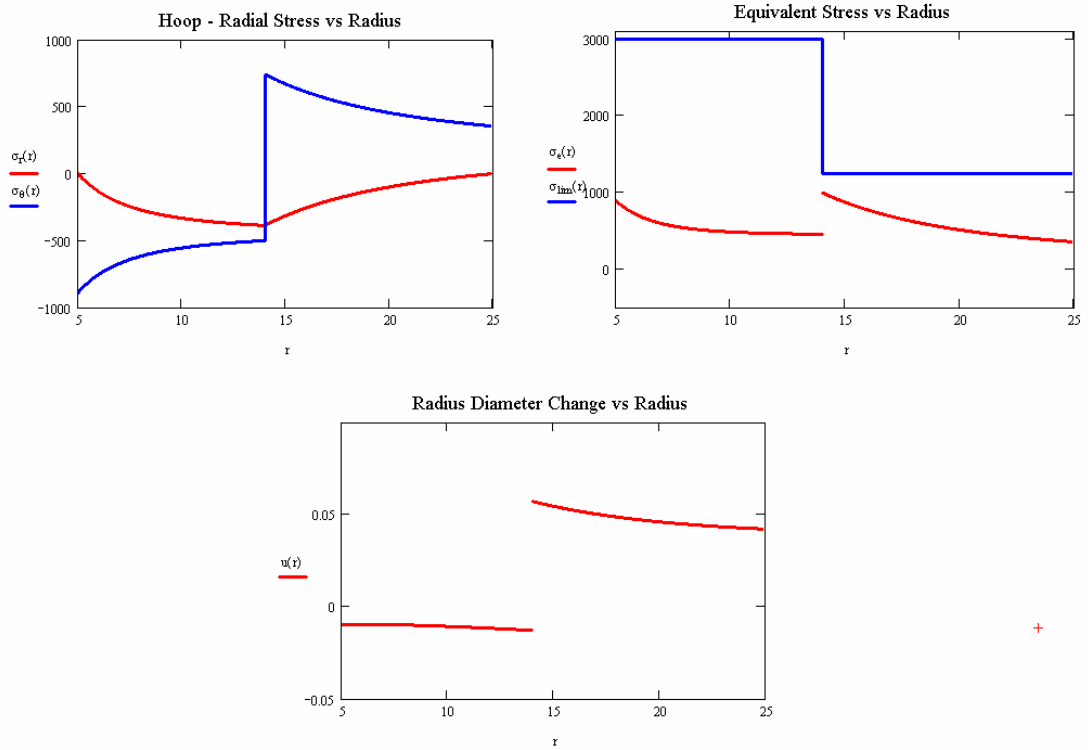
B.2 Three Rings without Internal Pressure

3 RING CALCULATOR

First Ring's Posion's Ratio $\nu_1 := 0.23$

First Ring's Elastic Modulus (MPa) $E_1 := 450000$

First Ring's Yield Stress (MPa) $Y_1 := 3000$

Second Ring's Posion's Ratio $\nu_2 := 0.3$

Second Ring's Elastic Modulus (MPa) $E_2 := 210000$

Second Rings Yield Stress (MPa) $Y_2 := 1250$

Third Ring's Posion's Ratio $\nu_3 := 0.3$

Third Ring's Elastic Modulus (MPa) $E_3 := 210000$

Third Ring's Yield Stress (MPa) $Y_3 := 1250$

Bore Diameter (mm) $d := 10$

First Ring Outer Diameter (mm) $d_1 := 28$

Second Ring Outer Diameter (mm) $d_2 := 40$

Third Ring Outer Diameter (mm) $D := 50$

First Interference (mm) $z_1 := 0.16$

% First Interference $\delta = 0.571$ %

Second Interference (mm) $z_2 := 0.12$

% Second Interference $\delta = 0.429$ %

247

CALCULATIONS

$$r_{i1} := \frac{d}{2} \qquad r_{o1} := \frac{d_1}{2} \qquad r_{o2} := \frac{d_2}{2} \qquad r_{o3} := \frac{D}{2} \qquad \text{Calculating Radius Of Rings}$$

$$\rho_2 := \frac{z_2}{2} \qquad \rho_1 := \frac{z_1}{2} \qquad \text{Calculating Interference On Radius}$$

Given $\qquad$ Solving System of Equations

$$c_{11} := 0.1 \qquad c_{21} := 0.1 \qquad c_{12} := 0.1 \qquad c_{22} := 0.1 \qquad c_{13} := 0.1 \qquad c_{23} := 0.1 \qquad \text{Initial Guess for Iteration}$$

$$c_{12} \cdot r_{o1} + \frac{c_{22}}{r_{o1}} - c_{11} \cdot r_{o1} - \frac{c_{21}}{r_{o1}} = \rho_1$$

$$c_{13} \cdot r_{o2} + \frac{c_{23}}{r_{o2}} - c_{12} \cdot r_{o2} - \frac{c_{22}}{r_{o2}} = \rho_2$$

$$\frac{E_1}{1 - \nu_1^2} \left[c_{11} \cdot \left(1 + \nu_1\right) - c_{21} \cdot \left(\frac{1 - \nu_1}{r_{o1}^2}\right) \right] = \frac{E_2}{1 - \nu_2^2} \left[c_{12} \cdot \left(1 + \nu_2\right) - c_{22} \cdot \left(\frac{1 - \nu_2}{r_{o1}^2}\right) \right]$$

$$\frac{E_2}{1 - \nu_2^2} \left[c_{12} \cdot \left(1 + \nu_2\right) - c_{22} \cdot \left(\frac{1 - \nu_2}{r_{o2}^2}\right) \right] = \frac{E_3}{1 - \nu_3^2} \left[c_{13} \cdot \left(1 + \nu_3\right) - c_{23} \cdot \left(\frac{1 - \nu_3}{r_{o2}^2}\right) \right]$$

$$\frac{E_1}{1 - \nu_1^2} \left[c_{11} \cdot \left(1 + \nu_1\right) - c_{21} \cdot \left(\frac{1 - \nu_1}{r_{i1}^2}\right) \right] = 0$$

$$\frac{E_3}{1 - \nu_3^2} \left[c_{13} \cdot \left(1 + \nu_3\right) - c_{23} \cdot \left(\frac{1 - \nu_3}{r_{o3}^2}\right) \right] = 0$$

$$C := \text{Find}\left(c_{11}, c_{21}, c_{12}, c_{22}, c_{13}, c_{23}\right)$$

248

$$C = \begin{pmatrix} -0.00110778 \\ -0.04423925 \\ 0.00030949 \\ 0.79797642 \\ 0.00135949 \\ 1.57797642 \end{pmatrix}$$

$c_{11} := C_0 \qquad c_{21} := C_1 \qquad c_{12} := C_2$

Equating Values in Constant Matrix to Variables

$c_{22} := C_3 \qquad c_{13} := C_4 \qquad c_{23} := C_5$

$$u(r) := \begin{vmatrix} c_{11} \cdot r + \dfrac{c_{21}}{r} & \text{if } r_{i1} \le r \le r_{o1} \\[3mm] c_{12} \cdot r + \dfrac{c_{22}}{r} & \text{if } r_{o1} < r \le r_{o2} \\[3mm] c_{13} \cdot r + \dfrac{c_{23}}{r} & \text{if } r_{o2} < r \le r_{o3} \end{vmatrix}$$

Calculating Radial Dislacement On First Ring

Calculating Radial Dislacement On Second Ring

Calculating Radial Dislacement On Third Ring

$$\sigma_r(r) := \begin{vmatrix} \dfrac{E_1}{1 - v_1^{\,2}} \cdot \left[c_{11} \cdot (1 + v_1) - c_{21} \cdot \left(\dfrac{1 - v_1}{r^2} \right) \right] & \text{if } r_{i1} \le r \le r_{o1} \\[4mm] \dfrac{E_2}{1 - v_2^{\,2}} \cdot \left[c_{12} \cdot (1 + v_2) - c_{22} \cdot \left(\dfrac{1 - v_2}{r^2} \right) \right] & \text{if } r_{o1} < r \le r_{o2} \\[4mm] \dfrac{E_3}{1 - v_3^{\,2}} \cdot \left[c_{13} \cdot (1 + v_3) - c_{23} \cdot \left(\dfrac{1 - v_3}{r^2} \right) \right] & \text{if } r_{o2} < r \le r_{o3} \end{vmatrix}$$

Calculating Radial Stress On First Ring Along Radius

Calculating Radial Stress On Second Ring Along Radius

Calculating Radial Stress On Third Ring Along Radius

$$\sigma_\theta(r) := \begin{vmatrix} \dfrac{E_1}{1 - v_1^{\,2}} \cdot \left[c_{11} \cdot (1 + v_1) + c_{21} \cdot \left(\dfrac{1 - v_1}{r^2} \right) \right] & \text{if } r_{i1} \le r \le r_{o1} \\[4mm] \dfrac{E_2}{1 - v_2^{\,2}} \cdot \left[c_{12} \cdot (1 + v_2) + c_{22} \cdot \left(\dfrac{1 - v_2}{r^2} \right) \right] & \text{if } r_{o1} < r \le r_{o2} \\[4mm] \dfrac{E_3}{1 - v_3^{\,2}} \cdot \left[c_{13} \cdot (1 + v_3) + c_{23} \cdot \left(\dfrac{1 - v_3}{r^2} \right) \right] & \text{if } r_{o2} < r \le r_{o3} \end{vmatrix}$$

Calculating Hoop Stress On First Ring Along Radius

Calculating Hoop Stress On Second Ring Along Radius

Calculating Hoop Stress On Third Ring Along Radius

$$\sigma_e(r) := \begin{cases} \left(\sigma_r(r)^2 - \sigma_r(r)\cdot\sigma_\theta(r) + \sigma_\theta(r)^2\right)^{0.5} & \text{if } r_{i1} \le r < r_{o1} \\[2mm] \left(\sigma_r(r)^2 - \sigma_r(r)\cdot\sigma_\theta(r) + \sigma_\theta(r)^2\right)^{0.5} & \text{if } r_{o1} \le r \le r_{o2} \\[2mm] \left(\sigma_r(r)^2 - \sigma_r(r)\cdot\sigma_\theta(r) + \sigma_\theta(r)^2\right)^{0.5} & \text{if } r_{o2} < r \le r_{o3} \end{cases}$$

Calculating Equivalent Stress On First Ring Along Radius

Calculating Equivalent Stress On Second Ring Along Radius

Calculating Equivalent Stress On Third Ring Along Radius

$$\sigma_{lim}(r) := \begin{cases} Y_1 & \text{if } r_{i1} \le r \le r_{o1} \\ Y_2 & \text{if } r_{o1} < r \le r_{o2} \\ Y_3 & \text{if } r_{o2} < r \le r_{o3} \end{cases}$$

Yield Stress Of First Ring

Yield Stress Of Second Ring

Yield Stress Of Third Ring

Hoop - Radial Stress vs Radius

Equivalent Stress vs Radius

Radius Diameter Change vs Radius
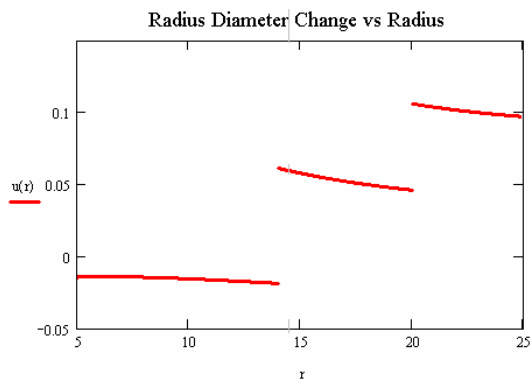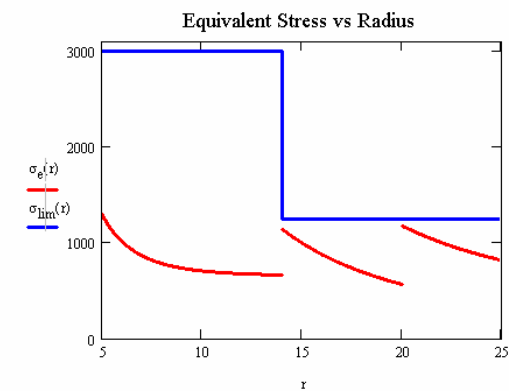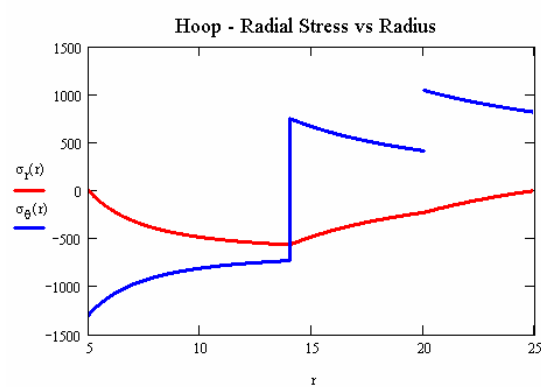
B.3 Two Rings with Internal Pressure

2 RING CALCULATOR WITH INTERNAL PRESSURE

First Ring's Posion's Ratio $\nu_1 := 0.23$

First Ring's Elastic Modulus (MPa) $E_1 := 450000$

First Ring Yield Stress (MPa) $Y_1 := 3000$

Bore Diameter (mm) $d_{i1} := 10$

First Ring Outer Diameter (mm) $d_{o1} := 28$

Second Ring Outer Diameter (mm) $d_{o2} := 50$

Second Ring's Posion's Ratio $\nu_2 := 0.3$

Second Ring's Elastic Modulus (MPa) $E_2 := 210000$

Second Ring Yield Stress (MPa) $Y_2 := 1200$

Internal Pressure (MPa) $P_i := 1000$

Interference (mm) $z := 0.14$

% Interference $\delta = 0.5$ %

CALCULATIONS

$a := \dfrac{d_{i1}}{2}$ $\qquad b := \dfrac{d_{o1}}{2}$ $\qquad c := \dfrac{d_{o2}}{2}$ Calculating Radius Of Rings

$\rho := \dfrac{z}{2}$ Calculating Interference On Radius

$$P := \left(\frac{2 \cdot a^2 \cdot b \cdot P_i}{b^2 - a^2} + \rho \cdot E_1 \right) \cdot \frac{1}{b \cdot \dfrac{E_1}{E_2} \cdot \left(\dfrac{b^2 + c^2}{c^2 - b^2} + \nu_2 \right) + \dfrac{b \cdot \left(b^2 + a^2 \right)}{b^2 - a^2} - \nu_1 \cdot b}$$

Calculating Interference Pressure

$$\sigma_r(r) := \begin{vmatrix} \dfrac{a^2 \cdot P_i - b^2 \cdot P}{b^2 - a^2} - \dfrac{(P_i - P) \cdot a^2 \cdot b^2}{\left(b^2 - a^2 \right) \cdot r^2} & \text{if } a \leq r \leq b \\[3mm] \dfrac{P \cdot b^2 \cdot \left(1 - \dfrac{c^2}{r^2} \right)}{c^2 - b^2} & \text{if } b < r \leq c \end{vmatrix}$$

Calculating Radial Stress On First Stress Ring Along Radius

Calculating Radial Stress On Second Stress Ring Along Radius

251

$$\sigma_\theta(r) := \begin{vmatrix} \dfrac{a^2 \cdot P_i - b^2 \cdot P}{b^2 - a^2} + \dfrac{(P_i - P) \cdot a^2 \cdot b^2}{\left(b^2 - a^2\right) \cdot r^2} & \text{if } a \le r \le b \\[4mm] \dfrac{P \cdot b^2 \cdot \left(1 + \dfrac{c^2}{r^2}\right)}{c^2 - b^2} & \text{if } b < r \le c \end{vmatrix}$$

Calculating Hoop Stress On First Stress Ring Along Radius

Calculating Hoop Stress On Second Stress Ring Along Radius

$$\sigma_e(r) := \begin{vmatrix} \left(\sigma_r(r)^2 - \sigma_r(r) \cdot \sigma_\theta(r) + \sigma_\theta(r)^2\right)^{0.5} & \text{if } a \le r \le b \\[3mm] \left(\sigma_r(r)^2 - \sigma_r(r) \cdot \sigma_\theta(r) + \sigma_\theta(r)^2\right)^{0.5} & \text{if } b < r \le c \end{vmatrix}$$

Calculating Equivalent Stress On First Ring Along Radius

Calculating Equivalent Stress On Second Ring Along Radius

$$\sigma_{lim}(r) := \begin{vmatrix} Y_1 & \text{if } a \le r \le b \\ Y_2 & \text{if } b < r \le c \end{vmatrix}$$

Yield Stress Of First Ring

Yield Stress Of Second Ring

$$u_1(r) := \dfrac{1 - \nu_1}{E_1} \cdot \dfrac{\left(a^2 \cdot P_i - b^2 \cdot P\right) \cdot r}{b^2 - a^2} + \dfrac{1 + \nu_1}{E_1} \cdot \dfrac{(P_i - P) \cdot a^2 \cdot b^2}{\left(b^2 - a^2\right) \cdot r}$$

Calculating Radial Dislacement On First Ring

$$u_2(r) := \dfrac{b^2 \cdot P \cdot r}{E_2 \cdot \left(c^2 - b^2\right)} \cdot \left[(1 - \nu_2) + (1 + \nu_2) \cdot \dfrac{c^2}{r^2} \right]$$

Calculating Radial Dislacement On Second Ring

$$u(r) := \begin{vmatrix} u_1(r) & \text{if } a \le r \le b \\ u_2(r) & \text{if } b < r \le c \end{vmatrix}$$

Plot Radial Displacement For First and Second Ring

252

Hoop - Radial Stress vs Radius

Equivalent Stress vs Radius

Radius Diameter Change vs Radius
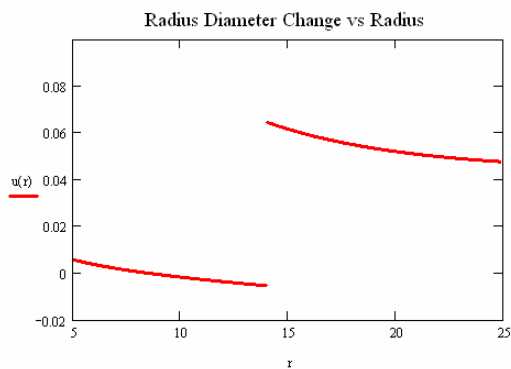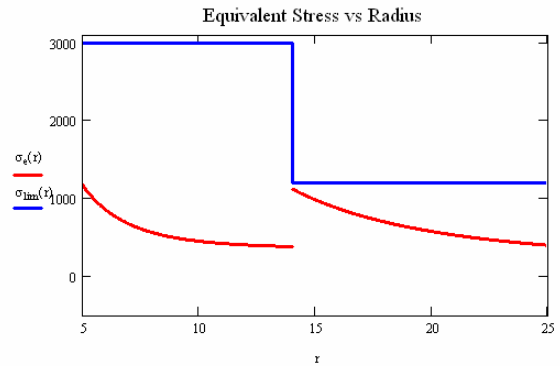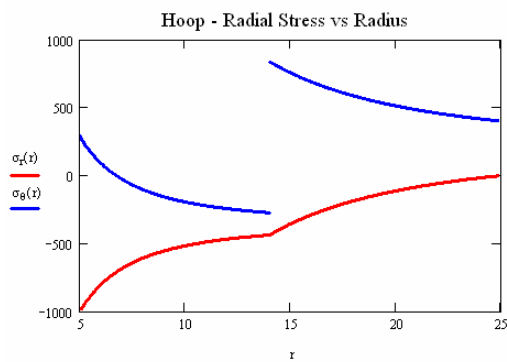
B.4 Three Rings with Internal Pressure

3 RING CALCULATOR WITH INTERNAL PRESSURE

First Ring's Posion's Ratio $\nu_1 := 0.23$

First Ring's Elastic Modulus (MPa) $E_1 := 450000$

First Ring's Yield Stress (MPa) $Y_1 := 3000$

Second Ring's Posion's Ratio $\nu_2 := 0.3$

Second Ring's Elastic Modulus (MPa) $E_2 := 210000$

Second Rings Yield Stress (MPa) $Y_2 := 1250$

Third Ring's Posion's Ratio $\nu_3 := 0.3$

Third Ring's Elastic Modulus (MPa) $E_3 := 210000$

Third Ring's Yield Stress (MPa) $Y_3 := 1250$

Bore Diameter (mm) $d := 10$

First Ring Outer Diameter (mm) $d_1 := 28$

Second Ring Outer Diameter (mm) $d_2 := 40$

Third Ring Outer Diameter (mm) $D := 50$

Internal Pressure (MPa) $P_i := 1000$

First Interference (mm) $z_1 := 0.16$

% First Interference $\delta_1 = 0.571 \%$

Second Interference (mm) $z_2 := 0.12$

% Second Interference $\delta_2 = 0.429 \%$

253

CALCULATIONS

$$r_{i1} := \frac{d}{2} \qquad r_{o1} := \frac{d_1}{2} \qquad r_{o2} := \frac{d_2}{2} \qquad r_{o3} := \frac{D}{2}$$

Calculating Radius Of Rings

$$\rho_1 := \frac{z_1}{2} \qquad \rho_2 := \frac{z_2}{2}$$

Calculating Interference On Radius

Given   Solving System of Equations

$$c_{11} := 0.1 \qquad c_{21} := 0.1 \qquad c_{12} := 0.1 \qquad c_{22} := 0.1 \qquad c_{13} := 0.1 \qquad c_{23} := 0.1$$

Initial Guess for Iteration

$$c_{12} \cdot r_{o1} + \frac{c_{22}}{r_{o1}} - c_{11} \cdot r_{o1} - \frac{c_{21}}{r_{o1}} = \rho_1$$

$$c_{13} \cdot r_{o2} + \frac{c_{23}}{r_{o2}} - c_{12} \cdot r_{o2} - \frac{c_{22}}{r_{o2}} = \rho_2$$

$$\frac{E_1}{1 - \nu_1^2} \left[c_{11} \cdot (1 + \nu_1) - c_{21} \cdot \left(\frac{1 - \nu_1}{r_{o1}^2} \right) \right] = \frac{E_2}{1 - \nu_2^2} \left[c_{12} \cdot (1 + \nu_2) - c_{22} \cdot \left(\frac{1 - \nu_2}{r_{o1}^2} \right) \right]$$

$$\frac{E_2}{1 - \nu_2^2} \left[c_{12} \cdot (1 + \nu_2) - c_{22} \cdot \left(\frac{1 - \nu_2}{r_{o2}^2} \right) \right] = \frac{E_3}{1 - \nu_3^2} \left[c_{13} \cdot (1 + \nu_3) - c_{23} \cdot \left(\frac{1 - \nu_3}{r_{o2}^2} \right) \right]$$

$$\frac{E_1}{1 - \nu_1^2} \left[c_{11} \cdot (1 + \nu_1) - c_{21} \cdot \left(\frac{1 - \nu_1}{r_{i1}^2} \right) \right] = -P_i$$

$$\frac{E_3}{1 - \nu_3^2} \left[c_{13} \cdot (1 + \nu_3) - c_{23} \cdot \left(\frac{1 - \nu_3}{r_{o3}^2} \right) \right] = 0$$

$$C := Find(c_{11}, c_{21}, c_{12}, c_{22}, c_{13}, c_{23})$$

$$C = \begin{pmatrix} -0.00095639 \\ 0.03013996 \\ 0.00038618 \\ 0.88699655 \\ 0.00143618 \\ 1.66699655 \end{pmatrix}$$

254

$$c_{11} := C_0 \qquad c_{21} := C_1 \qquad c_{12} := C_2$$

$$c_{22} := C_3 \qquad c_{13} := C_4 \qquad c_{23} := C_5$$

$$u(r) := \begin{vmatrix} c_{11} \cdot r + \dfrac{c_{21}}{r} & \text{if } r_{i1} \le r \le r_{o1} \\[3mm] c_{12} \cdot r + \dfrac{c_{22}}{r} & \text{if } r_{o1} < r \le r_{o2} \\[3mm] c_{13} \cdot r + \dfrac{c_{23}}{r} & \text{if } r_{o2} < r \le r_{o3} \end{vmatrix}$$

Calculating Radial Dislacement On First Ring

Calculating Radial Dislacement On Second Ring

Calculating Radial Dislacement On Third Ring

$$\sigma_r(r) := \begin{vmatrix} \dfrac{E_1}{1 - v_1^2} \cdot \left[c_{11} \cdot (1 + v_1) - c_{21} \cdot \left(\dfrac{1 - v_1}{r^2} \right) \right] & \text{if } r_{i1} \le r \le r_{o1} \\[4mm] \dfrac{E_2}{1 - v_2^2} \cdot \left[c_{12} \cdot (1 + v_2) - c_{22} \cdot \left(\dfrac{1 - v_2}{r^2} \right) \right] & \text{if } r_{o1} < r \le r_{o2} \\[4mm] \dfrac{E_3}{1 - v_3^2} \cdot \left[c_{13} \cdot (1 + v_3) - c_{23} \cdot \left(\dfrac{1 - v_3}{r^2} \right) \right] & \text{if } r_{o2} < r \le r_{o3} \end{vmatrix}$$

Calculating Radial Stress On First Ring Along Radius

Calculating Radial Stress On Second Ring Along Radius

Calculating Radial Stress On Third Ring Along Radius

$$\sigma_\theta(r) := \begin{vmatrix} \dfrac{E_1}{1 - v_1^2} \cdot \left[c_{11} \cdot (1 + v_1) + c_{21} \cdot \left(\dfrac{1 - v_1}{r^2} \right) \right] & \text{if } r_{i1} \le r \le r_{o1} \\[4mm] \dfrac{E_2}{1 - v_2^2} \cdot \left[c_{12} \cdot (1 + v_2) + c_{22} \cdot \left(\dfrac{1 - v_2}{r^2} \right) \right] & \text{if } r_{o1} < r \le r_{o2} \\[4mm] \dfrac{E_3}{1 - v_3^2} \cdot \left[c_{13} \cdot (1 + v_3) + c_{23} \cdot \left(\dfrac{1 - v_3}{r^2} \right) \right] & \text{if } r_{o2} < r \le r_{o3} \end{vmatrix}$$

Calculating Hoop Stress On First Ring Along Radius

Calculating Hoop Stress On Second Ring Along Radius

Calculating Hoop Stress On Third Ring Along Radius

$$\sigma_e(r) := \begin{vmatrix} \left(\sigma_r(r)^2 - \sigma_r(r) \cdot \sigma_\theta(r) + \sigma_\theta(r)^2 \right)^{0.5} & \text{if } r_{i1} \le r < r_{o1} \\[3mm] \left(\sigma_r(r)^2 - \sigma_r(r) \cdot \sigma_\theta(r) + \sigma_\theta(r)^2 \right)^{0.5} & \text{if } r_{o1} \le r \le r_{o2} \\[3mm] \left(\sigma_r(r)^2 - \sigma_r(r) \cdot \sigma_\theta(r) + \sigma_\theta(r)^2 \right)^{0.5} & \text{if } r_{o2} < r \le r_{o3} \end{vmatrix}$$

Calculating Equivalent Stress On First Ring Along Radius

Calculating Equivalent Stress On Second Ring Along Radius

Calculating Equivalent Stress On Third Ring Along Radius

$$\sigma_{lim}(r) := \begin{vmatrix} Y_1 & \text{if } r_{i1} \le r \le r_{o1} \\ Y_2 & \text{if } r_{o1} < r \le r_{o2} \\ Y_3 & \text{if } r_{o2} < r \le r_{o3} \end{vmatrix}$$

Yield Stress Of First Ring

Yield Stress Of Second Ring

Yield Stress Of Third Ring

Hoop - Radial Stress vs Radius

Equivalent Stress vs Radius

Radius Diameter Change vs Radius

256

APPENDIX C

SHRINK FIT OPTIMIZATION PROGRAM CODE

2 RING OPTIMIZER WITH INTERNAL PRESSURE

First Ring's Posion's Ratio $\nu_1 := 0.23$

First Ring's Elastic Modulus (MPa) $E_1 := 450000$

First Ring Yield Stress (MPa) $Y_1 := 3000$

Second Ring's Posion's Ratio $\nu_2 := 0.3$

Second Ring's Elastic Modulus (MPa) $E_2 := 210000$

Second Ring Yield Stress (MPa) $Y_2 := 1200$

Bore Diameter (mm) $d_{i1} := 10$

Second Ring Outer Diameter (mm) $d_{o2} := 50$

Internal Pressure (MPa) $P_{int} := 1000$

Interference (mm) z will be optimized

First Ring Outer Diameter (mm) d_{o1} will be optimized

CALCULATIONS

$i := 0..99$ Iteration index number is defined

$j := 0..99$ Iteration index number is defined

$a := \dfrac{d_{i1}}{2}$ Bore radius

$b_i := \dfrac{d_{i1}}{2} + 1 + \dfrac{d_{o2} - d_{i1} - 1}{100} \cdot i$ Incremental increased insert outer radius

$c := \dfrac{d_{o2}}{2}$ Ring outer diameter

$\rho_i := 0.02 + \dfrac{i}{260}$ Incremental increased interference

257

$$P_{i,j} := \left[\frac{2 \cdot a^2 \cdot b_i \cdot P_{int}}{\left(b_i\right)^2 - a^2} + \rho_j \cdot E_1\right] \cdot \frac{1}{b_i \cdot \dfrac{E_1}{E_2} \cdot \left[\dfrac{\left(b_i\right)^2 + c^2}{c^2 - \left(b_i\right)^2} + \nu_2\right] + \dfrac{b_i \cdot \left[\left(b_i\right)^2 + a^2\right]}{\left(b_i\right)^2 - a^2} - \nu_1 \cdot b_i}$$

Pressure on the contact surface

$$\sigma_{r\_inner_{i,j}} := \frac{a^2 \cdot P_{int} - \left(b_i\right)^2 \cdot P_{i,j}}{\left(b_i\right)^2 - a^2} - \frac{\left(P_{int} - P_{i,j}\right) \cdot a^2 \cdot \left(b_i\right)^2}{\left[\left(b_i\right)^2 - a^2\right] \cdot a^2}$$

Radial stress distribution on die insert

$$\sigma_{r\_inner_{i,j}} := \frac{a^2 \cdot P_{int} - \left(b_i\right)^2 \cdot P_{i,j}}{\left(b_i\right)^2 - a^2} - \frac{\left(P_{int} - P_{i,j}\right) \cdot a^2 \cdot \left(b_i\right)^2}{\left[\left(b_i\right)^2 - a^2\right] \cdot a^2}$$

Radial stress distribution on die insert

$$\sigma_{\theta\_inner_{i,j}} := \frac{a^2 \cdot P_{int} - \left(b_i\right)^2 \cdot P_{i,j}}{\left(b_i\right)^2 - a^2} + \frac{\left(P_{int} - P_{i,j}\right) \cdot a^2 \cdot \left(b_i\right)^2}{\left[\left(b_i\right)^2 - a^2\right] \cdot a^2}$$

Circumferential stress distribution on die insert

$$\sigma_{r\_interface_{i,j}} := \frac{P_{i,j} \cdot \left(b_i\right)^2 \cdot \left[1 - \dfrac{c^2}{\left(b_i\right)^2}\right]}{c^2 - \left(b_i\right)^2}$$

Radial stress on the inner surface of stress ring

$$\sigma_{\theta\_interface_{i,j}} := \frac{P_{i,j} \cdot \left(b_i\right)^2 \cdot \left[1 + \dfrac{c^2}{\left(b_i\right)^2}\right]}{c^2 - \left(b_i\right)^2}$$

Circumferential stress on the inner surface of stress ring

$$\sigma_{eq\_interface_{i,j}} := \sqrt{\left(\sigma_{r\_interface_{i,j}}\right)^2 - \sigma_{r\_interface_{i,j}} \cdot \sigma_{\theta\_interface_{i,j}} + \left(\sigma_{\theta\_interface_{i,j}}\right)^2}$$

Equivalent stress on the inner surface of stress ring

$$\sigma_{eq\_interface_{i,j}} := \sqrt{\left(\sigma_{r\_interface_{i,j}}\right)^2 - \sigma_{r\_interface_{i,j}} \cdot \sigma_{\theta\_interface_{i,j}} + \left(\sigma_{\theta\_interface_{i,j}}\right)^2}$$

Equivalent stress on the inner surface of stress ring

$$\text{MIN\_SIGMA\_}\theta\text{\_INNER} := \begin{vmatrix} i \leftarrow 0 \\ j \leftarrow 0 \\ temp \leftarrow 5000 \\ \text{for } i \in 0..99 \\ \begin{vmatrix} j \leftarrow 0 \\ \text{for } j \in 0..99 \\ \begin{vmatrix} index\_1 \leftarrow i \quad \text{if } \sigma_{\theta\_inner_{i,j}} \leq temp \wedge \sigma_{eq\_interface_{i,j}} < Y_2 \\ index\_2 \leftarrow j \quad \text{if } \sigma_{\theta\_inner_{i,j}} \leq temp \wedge \sigma_{eq\_interface_{i,j}} < Y_2 \\ temp \leftarrow \sigma_{\theta\_inner_{i,j}} \quad \text{if } \sigma_{\theta\_inner_{i,j}} \leq temp \wedge \sigma_{eq\_interface_{i,j}} < Y_2 \end{vmatrix} \end{vmatrix} \\ \begin{pmatrix} index\_1 \\ index\_2 \\ temp \end{pmatrix} \end{vmatrix}$$

Iterative solver to calculate optimum interference and insert diameter

$$\text{MIN\_SIGMA\_}\theta\text{\_INNER} = \begin{pmatrix} 25 \\ 9 \\ 126.178 \end{pmatrix}$$

Index output of interference and insert outer diameter with lowest circumferential stress

$$z := 2 \cdot \rho_{\text{MIN\_SIGMA\_}\theta\text{\_INNER}_1}$$

Optimum interference

$$dia := 2 \cdot b_{\text{MIN\_SIGMA\_}\theta\text{\_INNER}_0}$$

Optimum insert outer diameter

$$\sigma_\theta := \text{MIN\_SIGMA\_}\theta\text{\_INNER}_2$$

Circumferential stress at bore surface

RESULTS

Insert outer diameter (mm) $dia = 21.5$

Interference (mm) $z = 0.109$

% Interference $\delta = 5.081$

Circumferential Stress (MPa) $\sigma_\theta = 126.178$

APPENDIX D

EXTRUSION FORCE COMPARISON FOR RIGID AND DEFORMABLE DIE MODELS

D.1 Force vs. stroke curves for 20MnB4
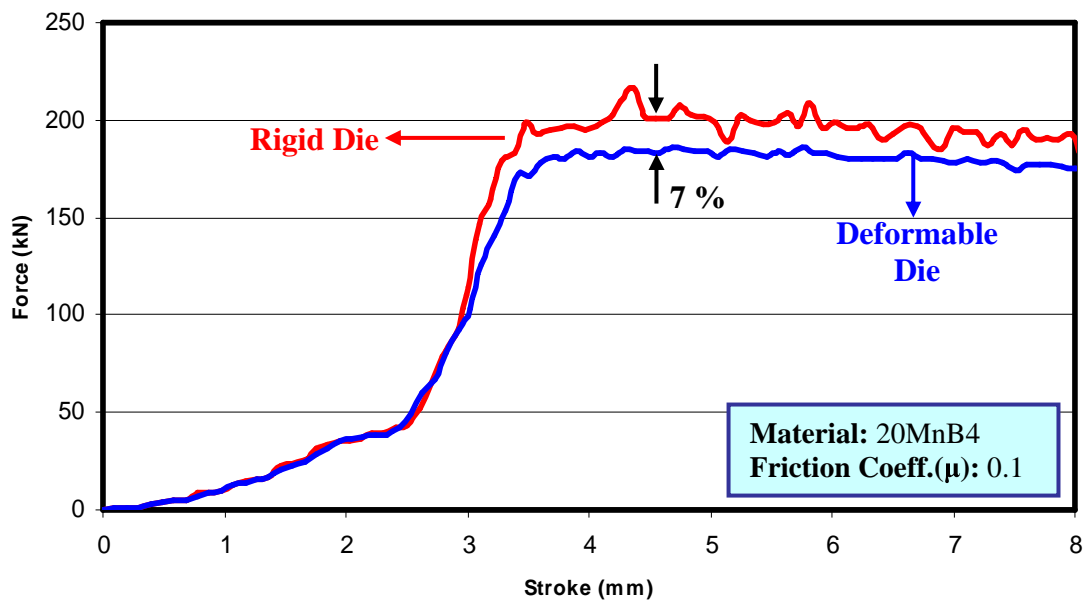
Figure D.1. Force vs. stroke curve for $\varepsilon = 0.85$ (20MnB4)
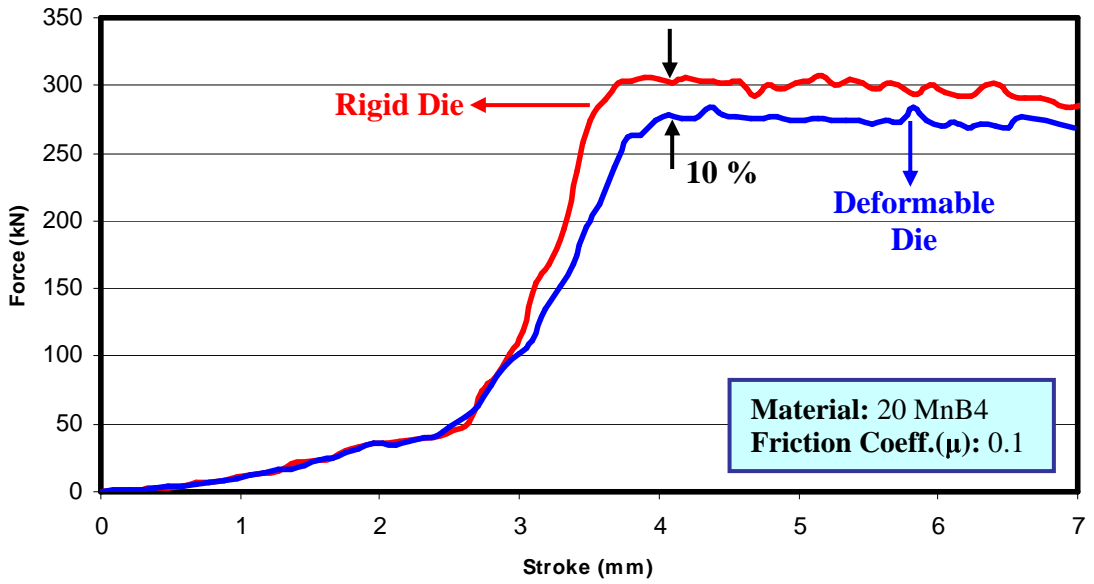
Figure D.2. Force vs. stroke curve for $\varepsilon = 1.2$ (20MnB4)
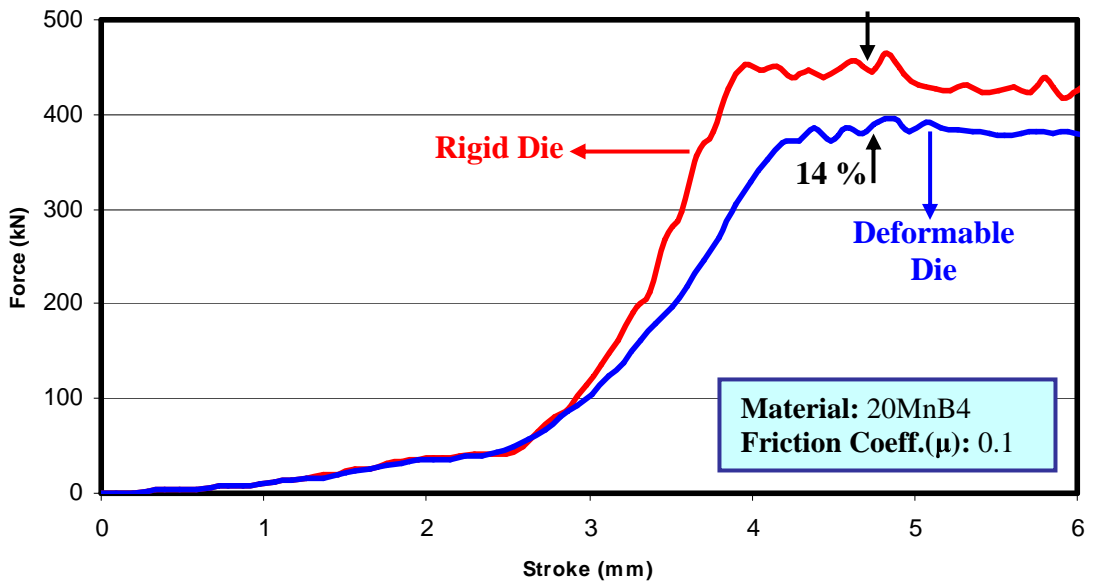
Figure D.3. Force vs. stroke curve for $\varepsilon = 1.6$ (20MnB4)

D.2 Force vs. stroke curves for QST 36-3
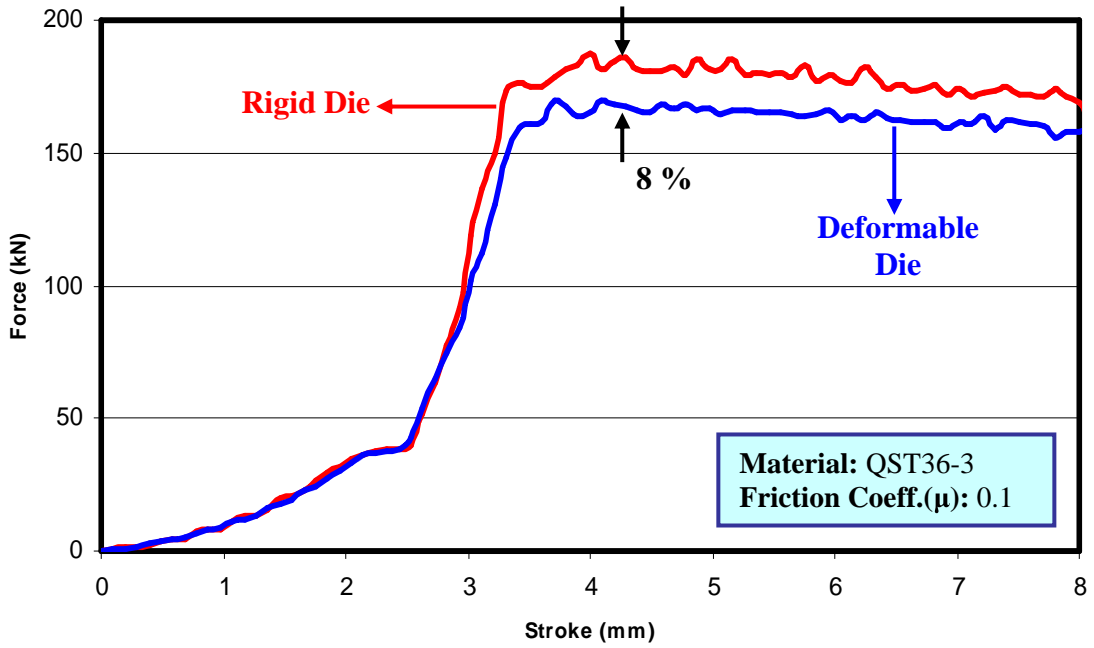
Figure D.4. Force vs. stroke curve for $\varepsilon = 0.85$ (QST 36-3)
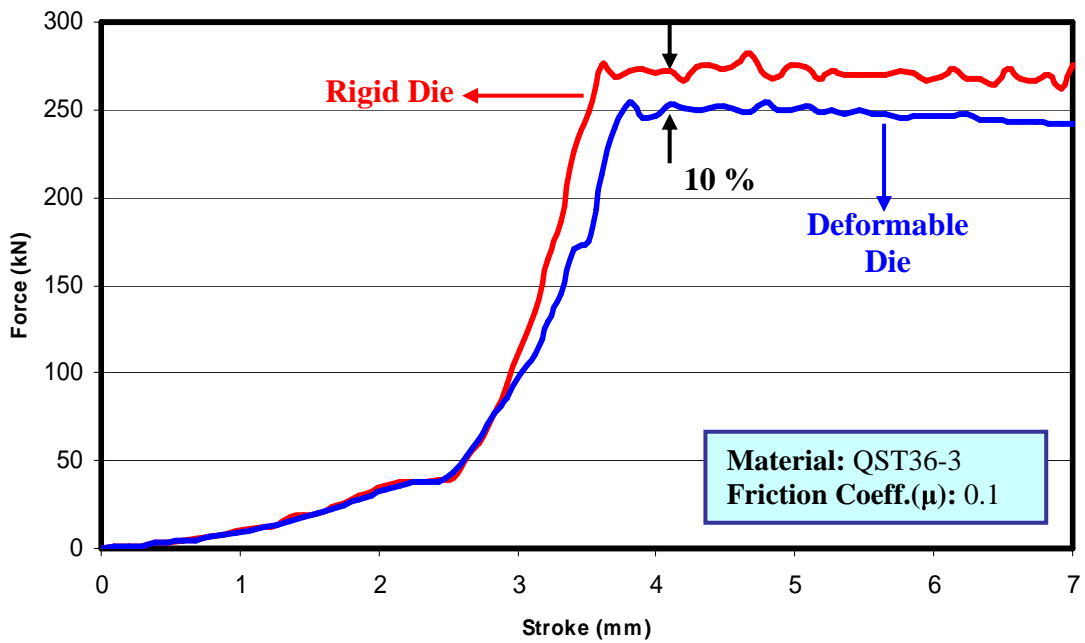
Figure D.5. Force vs. stroke curve for $\varepsilon = 1.2$ (QST 36-3)
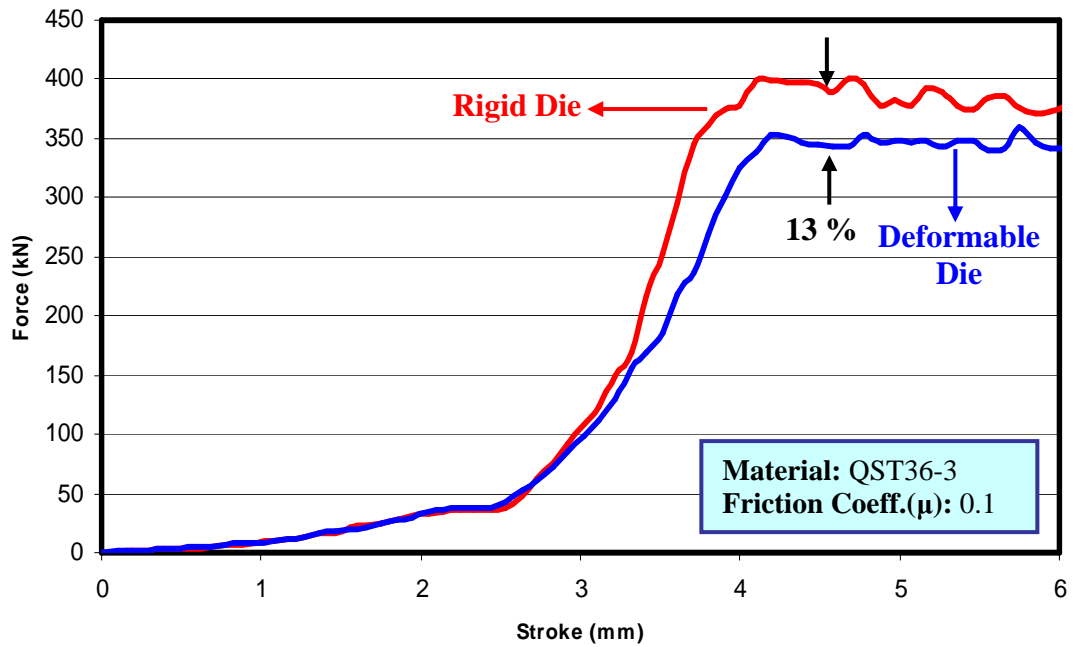
Figure D.6. Force vs. stroke curve for $\varepsilon = 1.6$ (QST 36-3)

D.3 Normal Stress distribution for 20MnB4
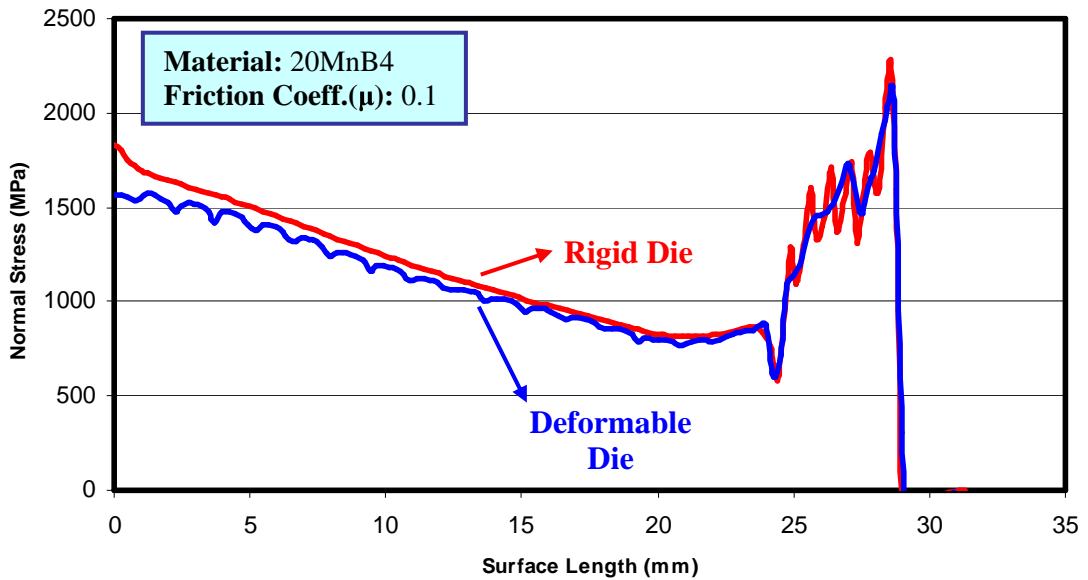
Figure D.7. Normal stress distribution for $\varepsilon = 0.85$ (20MnB4)
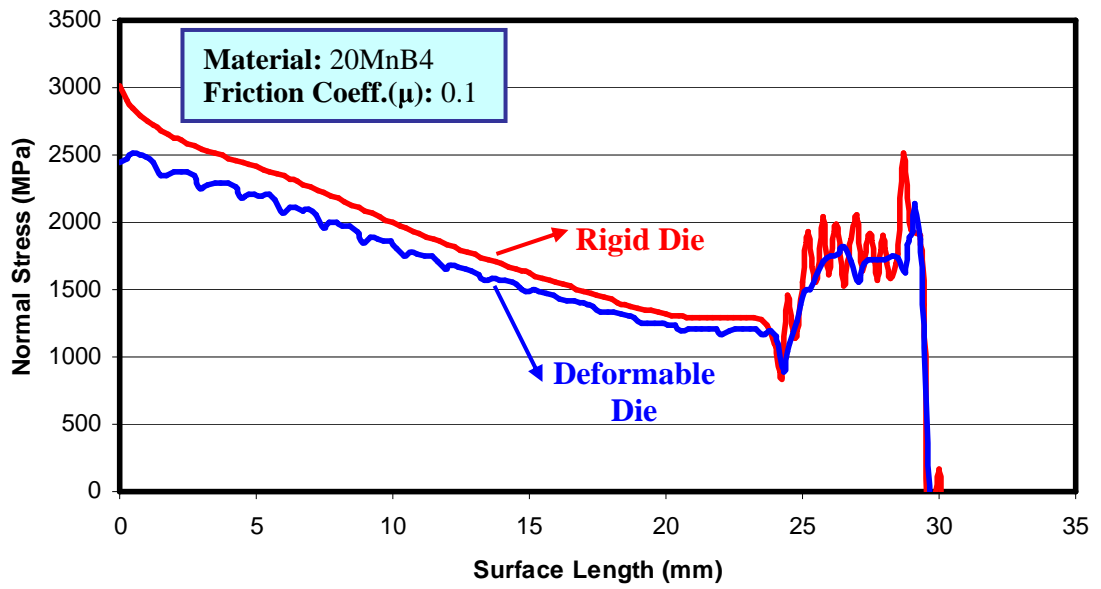
Figure D.8. Normal stress distribution for $\varepsilon = 1.2$ (20MnB4)
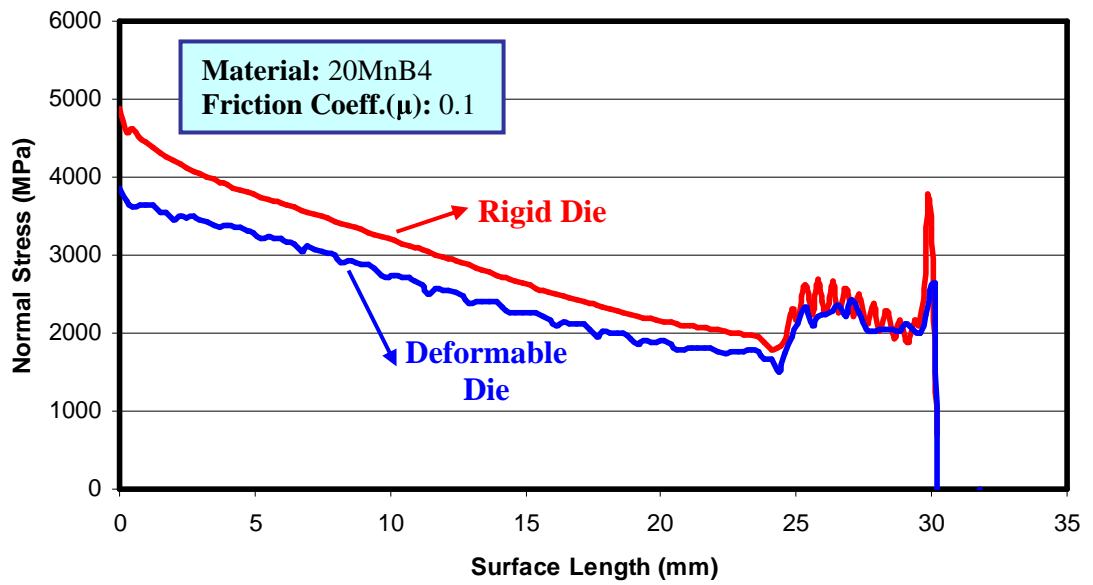
Figure D.9. Normal stress distribution for $\varepsilon = 1.6$ (20MnB4)

D.4 Normal Stress distribution for QST 36-3
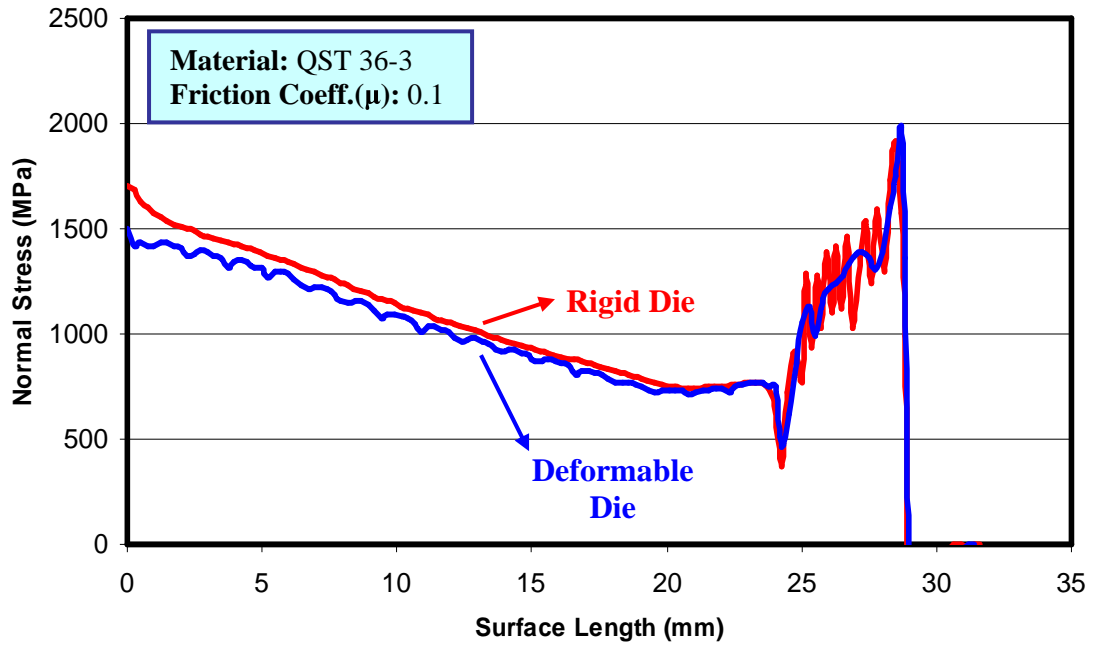
Figure D.10. Normal stress distribution for $\varepsilon = 0.85$ (QST36-3)
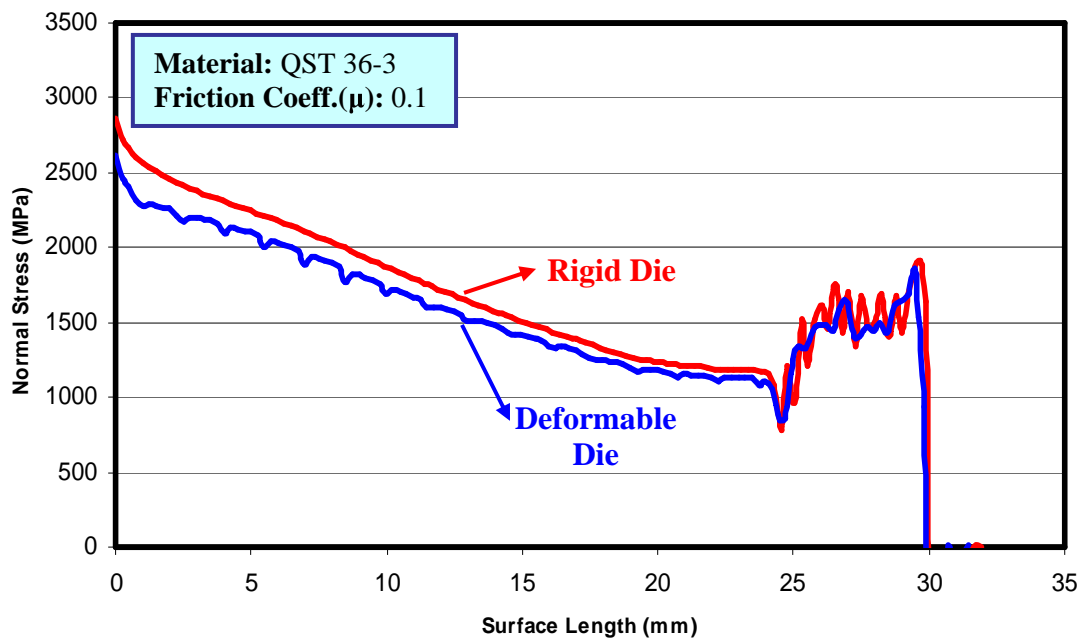
Figure D.11. Normal stress distribution for $\varepsilon = 1.2$ (QST36-3)
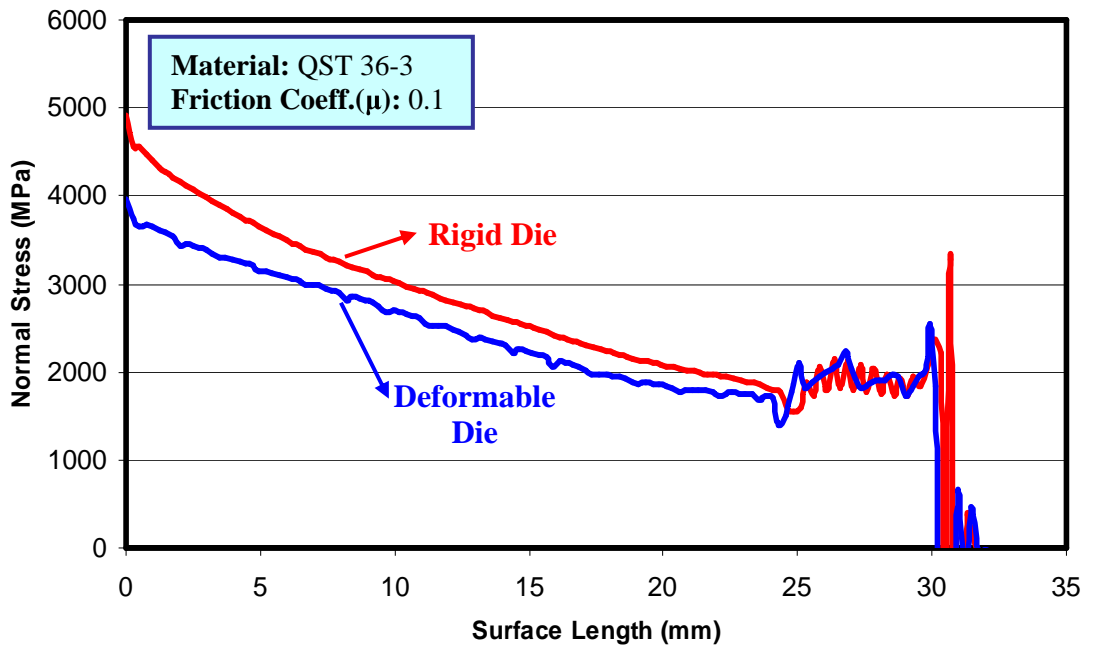
Figure D.12. Normal stress distribution for $\varepsilon = 1.6$ (QST36-3)

APPENDIX E

LOCAL REMESHING SUBROUTINE CODE

```fortran
      subroutine usizeoutl(nbody,idiere,xcent,ycent,inc,cptim,
     &                     ellen,esize,xyz,numout)
      implicit real*8 (a-h,o-z)
      dimension esize(*),xyz(2,*),xcent(4),ycent(4)
      dimension pos(5)
C augument list
C nbody - number of contact bodies (=0,if no there is no contact)
C idiere - current body number for remeshing
C xcent - x reference center of rigid contact bodies
C ycent - y reference center of rigid contact bodies
C inc   - current increment number
C cptim - current analysis time
C ellen - input element length for remeshing
C esize - edge length array on outline
C xyz   - outline point coordinates
C
C user routine to define 2D outline edge length
c define the refinement window
c    (x1,y1) ----- (x2,y2)
c       |           |
c    (x3,y3) ----- (x4,y4)


      if(nbody.gt.0.and.idiere.eq.1)then
         x1=163.0d0
         y1=12.0d0
         x2=165.0d0
         y2=12.0d0
         x3=163.0d0
         y3=10.9d0
         x4=165.0d0
         y4=10.9d0
      else
c skip
         goto 9999
      endif
      dl_mine=0.02d0*ellen
      do i=1,numout
c box 1
         if((xyz(1,i).gt.x1.and.xyz(1,i).lt.x2.and.
     &      (xyz(2,i).gt.y3.and.xyz(2,i).lt.y1))then
            esize(i)=dl_mine
         endif
      enddo

9999  continue
      return
      end
```

APPENDIX F

NODE COORDINATE DETERMINATION SUBROUTINE CODE

```fortran
      SUBROUTINE IMPD (N,DD,TD,XORD,F,V,A,NDEG,NCRD)
c* * * * * *
c
c     user subroutine for output of "displacements".
c
c     lnode(1)      user node number
c     lnode(2)    = 1 structural
c                 = 2 thermal
c                 = 3 fluids
c                 = 4 joule
c                 = 5 pore pressure / diffusion
c                 = 6 electrostatic
c                 = 7 magnetostatic
c                 = 8 electromagnetic
c                 =10 acoustics
c
c     dd            array of incremental displacements of this node
c     td            array of total displacements of this node
c     xord          array of coordinates of this node
c     f             array of reaction forces/residuals
c     v             array of velocity (dynamics only)
c     a             array of acceleration (dynamics only)
c     ndeg          number of degrees of freedom per node
c
c* * * * * *
      include '../common/implicit'
      include '../common/form'
      include '../common/spaceco'
      dimension lnode(2)
      dimension dd(ndeg),td(ndeg),xord(ncrd),f(ndeg),
     *          v(ndeg),a(ndeg)
      dimension txord(2)
      Open (3, FILE='fric.txt')
      if (N.gt.2.and.N.lt.18) then
C     TXORD WILL BE THE COORDS + TOTAL DISPLACEMENTS
      DO 1 I = 1,2
1     TXORD(I) = XORD(I) + 1.0*TD(I)
C     WRITE COORDS FOR EACH NODE IN SAME ROW
      write (3,605) txord(2)
605   format (F7.4$)
c
      end if
C     MOVE TO NEXT ROW IN OUTPUT FILE
      if (N.eq.104) then
      write (3,606)
606   format ()
      end if
      return
      end
```

268

APPENDIX G

EXTRUSION TEST
FORCE – DISPLACEMENT CURVES
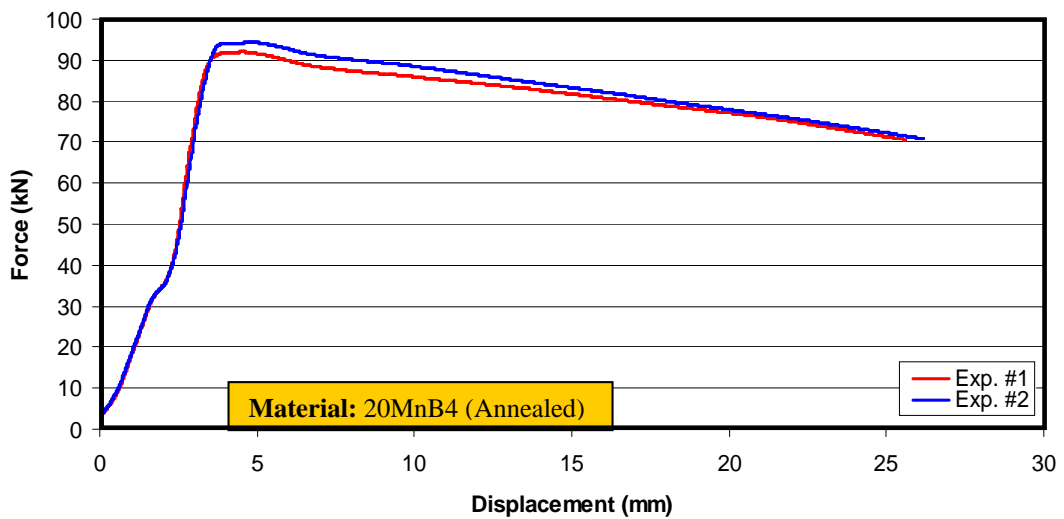
Figure G.1. Force vs. displacement curve of 35mm billet for equivalent plastic strain $\varepsilon = 0.68$
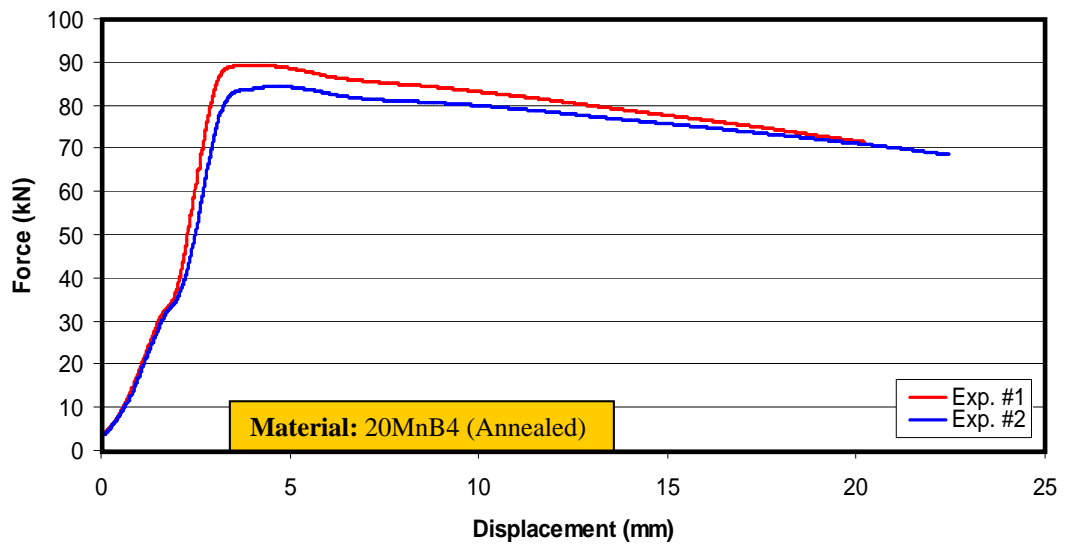
Figure G.2. Force vs. displacement curve of 30mm billet for equivalent plastic strain $\varepsilon = 0.68$
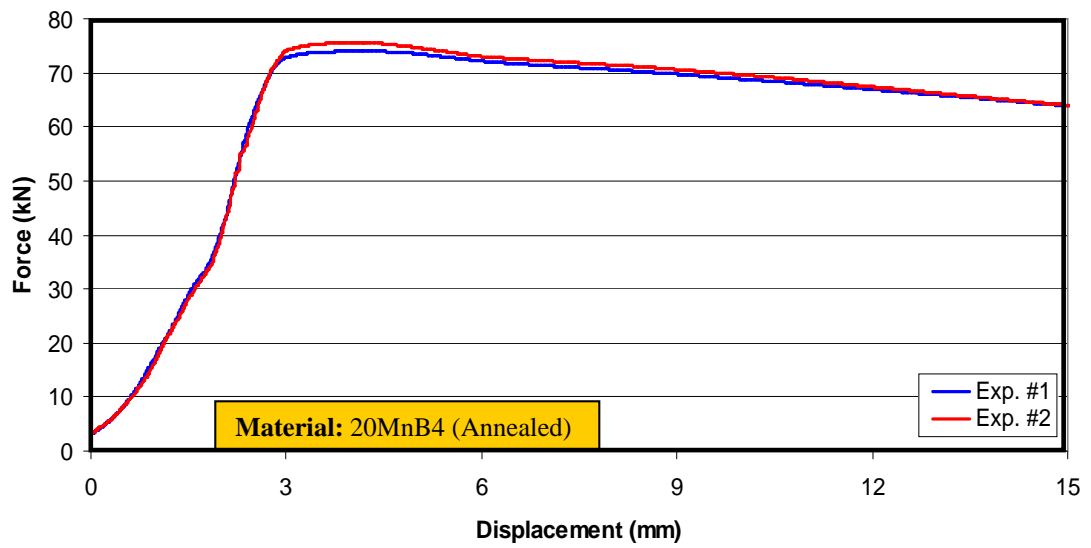
Figure G.3. Force vs. displacement curve of 20mm billet for equivalent plastic strain $\varepsilon = 0.68$
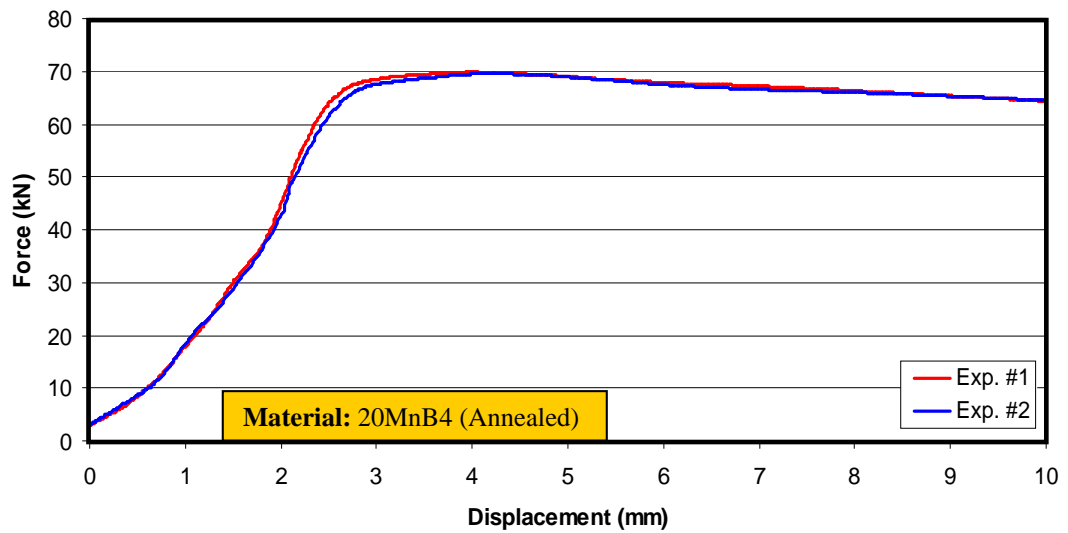
Figure G.4. Force vs. displacement curve of 15mm billet for equivalent plastic strain $\varepsilon = 0.68$
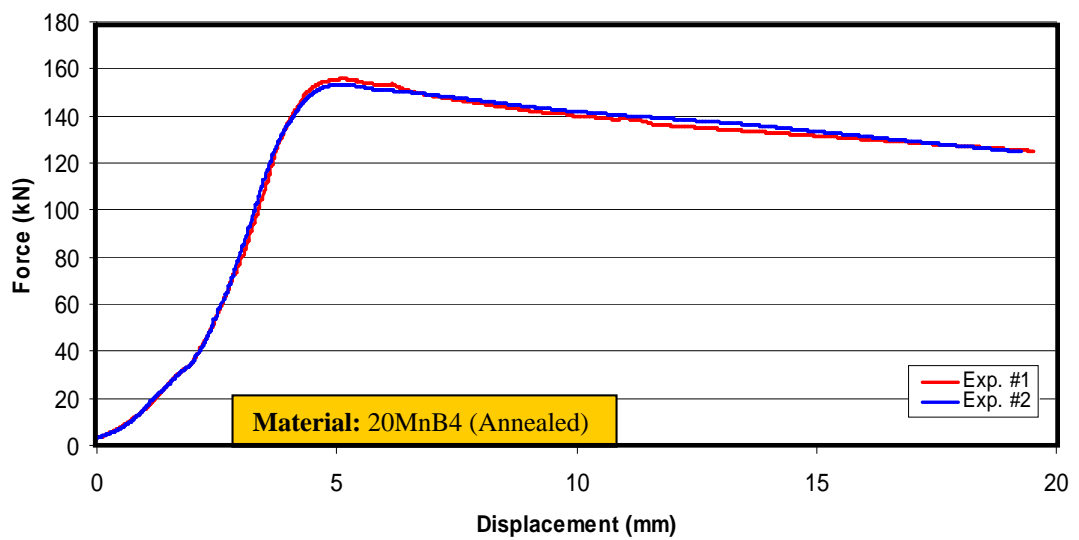
Figure G.5. Force vs. displacement curve of 20mm billet for equivalent plastic strain $\varepsilon = 1.2$
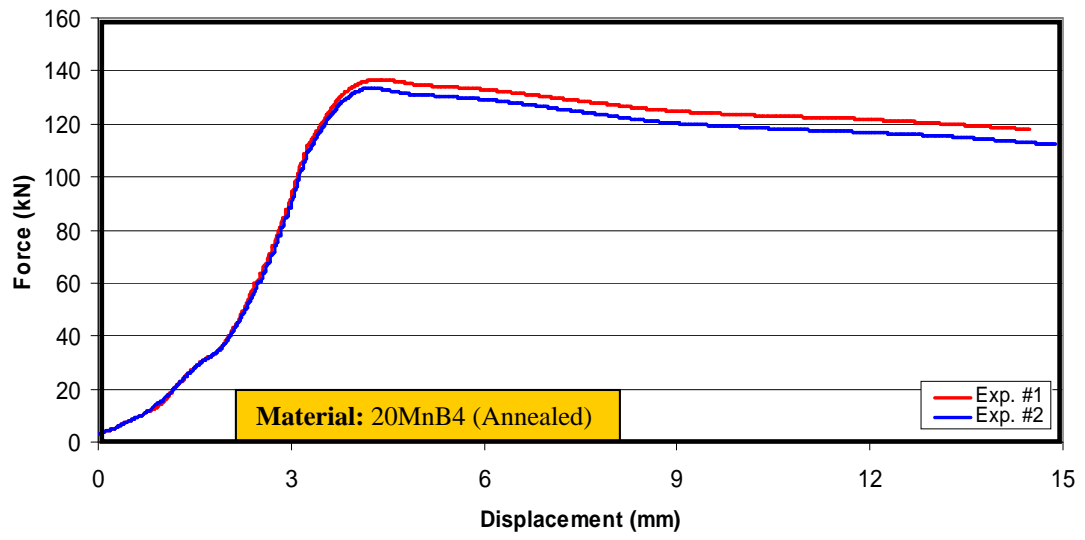
Figure G.6. Force vs. displacement curve of 15mm billet for equivalent plastic strain $\varepsilon = 1.2$